



Development of an Add-On Electrode for Non-Invasive Monitoring in Bioreactor Cultures and Medical Devices

Entwicklung einer Zusatzelektrode für das nicht-invasive Monitoring von Bioreaktorkulturen und Medizinprodukten

Doctoral thesis for a doctoral degree
at the Graduate School of Life Sciences,
Julius-Maximilians-Universität Würzburg,
Section: Biomedicine

submitted by

Jihyoung Choi

From
SEOUL, Republic of Korea

Wuerzburg, 2024



Submitted on:

Office stamp

Members of the Thesis Committee

Chairperson: Prof. Dr. Knut Kirmse

Primary Supervisor: Prof. Dr.-Ing. Jan Hansmann

Supervisor (Second): Prof. Dr. Heike Walles

Supervisor (Third): Priv.-Doz. Dr. Vladimir Soukhoroukov

Date of Public Defence:

Date of Receipt of Certificates:

Declaration

I hereby declare that some of the results presented in this thesis have been previously published in Choi, Jiyoung, Sanjana Mathew, Sabrina Oerter, Antje Appelt-Menzel, Jan Hansmann, and Tobias Schmitz. 2022. "Online Measurement System for Dynamic Flow Bioreactors to Study Barrier Integrity of hiPSC-Based Blood–Brain Barrier In Vitro Models" *Bioengineering* 9, no. 1: 39. <https://doi.org/10.3390/bioengineering9010039>, which is published under the terms of the Creative Commons Attribution (CC BY) license. Permission to include these published results in this thesis has been obtained in accordance with the license requirements.

Abstract

Electrochemical impedance spectroscopy (EIS) is a valuable technique analyzing electrochemical behavior of biological systems such as electrical characterization of cells and biomolecules, drug screening, and biomaterials in biomedical field. In EIS, an alternating current (AC) power signal is applied to the biological system, and the impedance of the system is measured over a range of frequencies.

In vitro culture models of endothelial or epithelial barrier tissue can be achieved by culturing barrier tissue on scaffolds made with synthetic or biological materials that provide separate compartments (apical and basal sides), allowing for further studies on drug transport. EIS is a great candidate for non-invasive and real-time monitoring of the electrical properties that correlate with barrier integrity during the tissue modeling. Although commercially available transendothelial/transepithelial electrical resistance (TEER) measurement devices are widely used, their use is particularly common in static transwell culture. EIS is considered more suitable than TEER measurement devices in bioreactor cultures that involve dynamic fluid flow to obtain accurate and reliable measurements. Furthermore, while TEER measurement devices can only assess resistance at a single frequency, EIS measurements can capture both resistance and capacitance properties of cells, providing additional information about the cellular barrier's characteristics across various frequencies. Incorporating EIS into a bioreactor system requires the careful optimization of electrode integration within the bioreactor setup and measurement parameters to ensure accurate EIS measurements. Since bioreactors vary in size and design depending on the purpose of the study, most studies have reported using an electrode system specifically designed for a particular bioreactor. The aim of this work was to produce multi-applicable electrodes and established methods for automated non-invasive and real-time monitoring using the EIS technique in bioreactor cultures. Key to the electrode material, titanium nitride (TiN) coating was fabricated on different substrates (materials and shape) using physical vapor deposition (PVD) and housed in a polydimethylsiloxane (PDMS) structure to allow the electrodes to function as independent units. Various electrode designs were evaluated for double-layer capacitance and morphology using EIS and scanning electron microscopy (SEM), respectively. The TiN-coated tube electrode was identified as the optimal choice. Furthermore, EIS measurements were performed to examine the impact of influential parameters related to culture conditions on the TiN-coated electrode system. In order to demonstrate the versatility of the electrodes, these electrodes were then integrated into in different types of perfusion bioreactors for monitoring barrier cells. Blood-brain barrier (BBB)

cells were cultured in the newly developed dynamic flow bioreactor, while human umbilical vascular endothelial cells (HUVECs) and Caco-2 cells were cultured in the miniature hollow fiber bioreactor (HFBR). As a result, the TiN-coated tube electrode system enabled investigation of BBB barrier integrity in long-term bioreactor culture. While EIS measurement could not detect HUVECs electrical properties in miniature HFBR culture, there was the possibility of measuring the barrier integrity of Caco-2 cells, indicating potential usefulness for evaluating their barrier function. Following the bioreactor cultures, the application of the TiN-coated tube electrode was expanded to hemofiltration, based on the hypothesis that the EIS system may be used to monitor clotting or clogging phenomena in hemofiltration. The findings suggest that the EIS monitoring system can track changes in ion concentration of blood before and after hemofiltration in real-time, which may serve as an indicator of clogging of filter membranes. Overall, our research demonstrates the potential of TiN-coated tube electrodes for sensitive and versatile non-invasive monitoring in bioreactor cultures and medical devices.

Zusammenfassung

Die elektrochemische Impedanzspektroskopie (EIS) ist eine nützliche Methode, um das elektrochemische Verhalten von biologischen Systemen zu analysieren, wie z.B. die elektrische Charakterisierung von Zellen und Biomolekülen, Drug Screening und Biomaterialien im biomedizinischen Bereich. Für die EIS wird ein Wechselstrom an das biologische System angeschlossen und die Impedanz des Systems über einen Frequenzbereich gemessen.

In vitro-Modelle von Gewebekulturen epithelialer Barrieren können mithilfe künstlicher oder biologischer Materialien, die über unterschiedliche Kompartimente (apikale und basolaterale Seite) verfügen, hergestellt werden und ermöglichen weitere Untersuchungen zum Transport von Arzneistoffen. Die EIS bietet dabei eine hervorragende Methode für das nicht-invasive Echtzeit-Monitoring der elektrischen Eigenschaften, die mit der Barriere-Integrität während der Gewebeentwicklung korreliert. Obwohl kommerziell erhältliche Geräte zur Messung des transendothelialen/transepithelialen elektrischen Widerstands (TEER) umfangreich verwendet werden, ist ihre Verwendung besonders bei statischen Transwell-Kulturen verbreitet. Durch die EIS kann im Gegensatz zur TEER-Messung für Bioreaktor-Kulturen, die einen dynamischen Medienfluss aufweisen, genauere und verlässliche Messungen erhalten werden. Zudem können EIS-Messungen anders als die TEER-Messung, die nur den Widerstand einer einzelnen Frequenz misst, gleichzeitig den elektrischen Widerstand und die Kapazität von Zellen erfassen und damit zusätzliche Informationen über die zellulären Barriereigenschaften über verschiedene Frequenzen hinweg liefern. Der EIS-Einbau in ein Bioreaktor-System bedarf einer sorgfältigen Optimierung der Elektrodenintegration in das Bioreaktor-Setup und der Messparameter, um akkurate EIS-Messungen durchführen zu können. Da Bioreaktoren abhängig vom Untersuchungszweck in ihrer Größe und ihrem Design variieren, verwenden die meisten Studien speziell entwickelte Elektrodensysteme für einzelne Bioreaktoren. Das Ziel dieser Arbeit war die Herstellung von vielseitig anwendbaren Elektroden und etablierten Methoden für das automatisierte nicht-invasive Echtzeit-Monitoring von Bioreaktor-Kulturen mithilfe der EIS. Entscheidend für das Elektrodenmaterial war die Titanitrid (TiN)-Beschichtung, die auf verschiedenen Substraten (Materialien und Formen) durch Physical Vapor Deposition (PVD) hergestellt und in einer Polydimethylsiloxan (PDMS)-Struktur untergebracht wurde, damit die Elektroden unabhängig voneinander arbeiten können. Verschiedene Elektrodendesigns wurden auf Doppelschicht-Kapazität mithilfe der EIS bzw. auf die Morphologie mit Rasterelektronenmikroskopie untersucht. Die TiN-beschichteten

Elektroden in Röhrenform erwiesen sich als optimal. Weiterhin wurden EIS-Messungen durchgeführt, um die Auswirkung von beeinflussenden Parametern auf die Kulturbedingungen durch das TiN-beschichtete Elektrodensystem zu untersuchen. Um die Vielseitigkeit der Elektroden aufzuzeigen, wurden diese anschließend zum Monitoring von Barriere-bildenden Zellen in unterschiedliche Perfusionsbioreaktoren integriert. Zellen der Blut-Hirn-Schranke (BHS) wurden im neu entwickelten dynamischen Flussreaktor kultiviert, wohingegen humane umbilikale vaskuläre Endothelzellen (HUVEC) und Caco-2-Zellen in Hohlfaserbioreaktoren (HFBR) in Miniaturform kultiviert wurden. Das TiN-beschichtete Röhrenelektrodensystem ermöglichte die Untersuchung der BHS-Barrieren-Integrität in einer Langzeit-Bioreaktorkultur. Während die EIS-Messung in der Miniaturform-HFBR-Kultur keine elektrischen Eigenschaften der HUVECs detektieren konnte, war es möglich, eine Barriere-Integrität der Caco-2-Zellen zu messen, die den potentiellen Nutzen für die Evaluierung deren Barrierefunktion aufzeigt. Nach den Bioreaktorkulturen wurde die Anwendung der TiN-beschichteten Röhrenelektrode auf die Hämofiltration erweitert, auf Grundlage der Hypothese, dass das EIS-System ein Gerinnen oder Verstopfen während der Hämofiltration überwachen könnte. Die Ergebnisse zeigen, dass das EIS-Monitoring-System Veränderungen in der Ionenkonzentration des Blutes vor und nach Hämofiltration in Echtzeit verfolgen kann, welches eventuell als Messgröße für ein Verstopfen der Filtermembranen genutzt werden kann. Insgesamt weisen TiN-beschichtete Röhrenelektroden unseren Forschungen zufolge ein großes Potential für ein empfindliches und vielfältiges nicht-invasives Monitoring von Bioreaktorkulturen und Medizingeräte auf.

Table of Contents

Declaration.....	I
Abstract.....	II
Zusammenfassung.....	IV
Table of Contents	VI
List of Figures.....	X
List of Tables	XII
List of Acronyms.....	XIII
List of Symbols.....	XV
1. Introduction	1
1.1. Electrochemical Impedance Spectroscopy Basics.....	1
1.2. Electrochemical Impedance Spectroscopy for Investigating the Integrity of Barrier Tissue <i>in vitro</i> Culture	7
1.2.1. Single Frequency Transendothelial/Transepthelial Electrical Resistance measurement.....	10
1.2.2. Electrochemical Impedance Spectroscopy	12
1.3. Titanium Nitride Coating as an Electrode Material	14
1.4. State-of-the-art of Electrochemical Impedance Spectroscopy Setup for Cellular Barrier Culture in Perfusion Bioreactors	18
1.5. Electrochemical Impedance Spectroscopy Niche for Hemofiltration	25
1.6. Aim of Thesis	28
2. Materials.....	30
3. Methods	37
3.1. Electrode Fabrication.....	37
3.1.1. Substrate Preparation for Physical Vapor Deposition	37
3.1.2. Physical Vapor Deposition	37
3.1.3. Design of Modular Electrode Models.....	37
3.1.3.1. Different Design of Electrode.....	37

3.1.3.2. Polydimethylsiloxane Casting	40
3.2. Electrode Characterization	41
3.2.1. Scanning Electron Microscope	41
3.2.2. Electrical Double Layer Characterization of Electrodes	42
3.2.3. Impedance Spectroscopy for Investigating the Impact Parameters	43
3.3. Electrode Application 1: Chip Bioreactor	43
3.3.1. Chip Bioreactor Preparation	43
3.3.1.1. Polydimethylsiloxane Chambers	43
3.3.1.2. Three-Dimensional-Printed Culture Membrane Frames	44
3.3.1.3. Bioreactor Clamps, Stand, and Medium Bottle Silicone Holder.....	45
3.3.2. Generation of Human Induced Pluripotent Stem Cell-derived Brain Capillary Endothelial Cells	46
3.3.3. Static Culture of Brain Capillary Endothelial Cells.....	47
3.3.4. Dynamic Flow Culture of Brain Capillary Endothelial Cells.....	49
3.3.4.1. Sterilization.....	49
3.3.4.2. Bioreactor Set Up and Cell Culture.....	49
3.3.4.3. Electrochemical Impedance Spectroscopy Measurement	49
3.3.4.4. Fitting and Simulation of Impedance Data.....	50
3.3.5. Histology and Image Analysis	51
3.3.5.1. Immunofluorescence Staining and Microscopy	51
3.3.5.2. Image J Analysis.....	52
3.4. Electrode Application 2: a Miniature Hollow Fiber Bioreactor	53
3.4.1. Passaging and Cryopreservation of Cell lines	53
3.4.2. Reference Transwell Culture of Cell lines.....	53
3.4.2.1. Electrochemical Impedance Spectroscopy Analysis	53
3.4.2.2. Immunofluorescence Staining and Microscopy	54
3.4.3. Miniature Hollow Fiber Bioreactor culture of Cell lines.....	55

3.4.3.1. Miniature Hollow Fiber Bioreactor Culture Setup and Sterilization.....	55
3.4.3.2. Extracellular Matrix Protein Coating and Equilibrium	55
3.4.3.3. Cells Seeding and Electrochemical Impedance Spectroscopy analysis	57
3.4.3.4. Immunofluorescence Staining and Microscopy	58
3.5. Electrode Application 3: Hemofiltration	58
3.5.1. Setup of a Hemofilter with Titanium Nitride-Coated Electrodes	58
3.5.2. Hemofiltration and Electrochemical Impedance Spectroscopy Analysis	59
3.6. Statistical Analysis	60
4. Results.....	61
4.1. Add-on Electrode Development	61
4.1.1. Examine Applicability of TiN Coating on Various Substrates.....	61
4.1.2. Various Designs of Electrode Models and Leak Test.....	63
4.1.3. Electrical Double Layer Characterization of Electrode Models	64
4.1.4. Investigating Influential Parameters Impact on Impedance Measurement	66
4.2. Electrode Application 1: A Chip Bioreactor	70
4.2.1. Optimization of Chip Bioreactor System with TiN-Coated Tube Electrodes ...	71
4.2.2. Electrochemical Impedance Spectroscopy Analysis of Blood Brain Barrier ...	73
4.2.2.1. Electrochemical Impedance Spectroscopy Data Analysis in Static and	
Dynamic Culture	74
4.2.2.2. Quantification of Barrier Integrity of Blood Capillary Endothelial Cells ..	76
4.2.3. Analysis of Immunofluorescent Images	79
4.3. Electrode Application 2: A Miniature Hollow Fiber Bioreactor.....	80
4.3.1. Barrier Integrity of Human Umbilical Vein Endothelial Cells.....	81
4.3.1.1. Reference Impedance Spectroscopy measurement for Barrier Integrity of	
Human Umbilical Vein Endothelial Cells.....	81
4.3.1.2. Assessment of Barrier Integrity of Human Umbilical Vein Endothelial	
Cells in Miniature Hollow Fiber Bioreactor.....	85
4.3.2. Barrier Integrity of Cancer coli-2	87

4.3.2.1. Reference Impedance Spectroscopy Measurement in Transwell Culture ..	87
4.3.2.2. Assessment of Barrier Integrity in Miniature Hollow Fiber Bioreactor.....	91
4.4. Electrode Application 3: Hemofiltration	94
4.4.1. Analysis of Electrochemical Impedance Spectroscopy and Pressure Data	95
5. Discussion	101
6. Conclusion and Outlook	113
7. Bibliography.....	115
8. Appendix	128
Publications	136
Acknowledgement	137
Curriculum Vitae	139
Affidavit	141

List of Figures

Figure 1.1. Illustration of sinusoidal graph.....	1
Figure 1.2. Two types of graphical representation of EIS	4
Figure 1.3. Example of equivalent circuit modeling in EIS	6
Figure 1.4. Electrical properties of biological tissue	8
Figure 1.5. Transport pathways of endothelial and epithelial cell layer.....	9
Figure 1.6. Illustration of the <i>in vitro</i> transwell based cell culture	11
Figure 1.7. TEER measurement in transwell culture system.....	12
Figure 1.8. EIS measurement of cellular barrier.....	13
Figure 1.9. Schematic diagram of PVD coating process	17
Figure 1.10. Different probe configurations	19
Figure 1.11. State-of-the-art of EIS system (1).....	20
Figure 1.12. State-of-the-art of EIS system (2).....	21
Figure 1.13. State-of-the-art of EIS system (3).....	23
Figure 1.14. A schematic diagram of hemofiltration.....	26
Figure 3.1. Graphical illustration of various designs of TiN-coated electrodes	38
Figure 3.2. PDMS casting steps for add-on electrodes	41
Figure 3.3. The electrode system setup for electrical double layer characterization.....	42
Figure 3.4. Chip insert fabrication	45
Figure 3.5. EIS measurement setup with TiN electrodes for static culture	48
Figure 3.6. Equivalent circuit modeling for the chip bioreactor system.....	50
Figure 3.7. Miniature HFBR setup for protein coating and cell seeding.....	56
Figure 3.8. Implementing TiN-coated tube electrodes into the hemofiltration circuit	59
Figure 4.1. Photograph of pre- and post-coating on different substrates.....	62
Figure 4.2. SEM images of TiN-coated surfaces on different substrates	62
Figure 4.3. Photographs of various electrode designs	64
Figure 4.4. Characterization of double-layer capacitance of electrodes.....	65
Figure 4.5. Electrodes setup for investigating impact parameters on EIS measurement.....	67
Figure 4.6. EIS results from the investigation of impact parameters (1).....	68
Figure 4.7. EIS results from the investigation of impact parameters (2).....	69
Figure 4.8. 3D graphical view of a chip bioreactor	71
Figure 4.9. Schematic diagram of chip bioreactor system with EIS.....	72
Figure 4.10. Photographs of the chip bioreactor system.....	73

Figure 4.11. Comparing EIS data over 48 h in dynamic and static culture	75
Figure 4.12. Illustration of the equivalent circuit model for bioreactor culture	76
Figure 4.13. Barrier integrity of BCECs cultured in dynamic and static culture.....	77
Figure 4.14. Immunofluorescence analysis of BCECs	79
Figure 4.15. Referencing EIS results for HUVECs cultured in a transwell system	82
Figure 4.16. Fit and simulation of EIS data from HUVECs in static culture	83
Figure 4.17. Immunofluorescence images of HUVECs in transwell culture	84
Figure 4.18. Miniature HFBR system setup incorporating TiN-coated tube electrodes	85
Figure 4.19. EIS analysis of HUVECs culture in miniature HFBR.....	86
Figure 4.20. Referencing EIS results for Caco-2 cultured in a transwell system	88
Figure 4.21. Fit and simulation of EIS data from Caco-2 in static culture	90
Figure 4.22. Immunofluorescence images of Caco-2 cells in static culture	91
Figure 4.23. Error in EIS measurement during miniature HFBR culture of Caco-2.....	92
Figure 4.24. EIS monitoring of Caco-2 cells cultured in a miniature HFBR	93
Figure 4.25. Immunofluorescence images of Caco-2 culture in miniature HFBR	94
Figure 4.26. EIS and pressure measurement during hemofiltration	96
Figure 4.27. Comparison of ΔZ_{V-A} and TMP as function of time	99

List of Tables

Table 1.1. Equivalent circuit elements.....	5
Table 2.1. Chemicals.....	30
Table 2.2. Laboratory devices.....	31
Table 2.3. Disposable materials	32
Table 2.4. Laboratory equipment.....	34
Table 2.5. Software	34
Table 2.6. List of Cells.....	35
Table 2.7. Caco-2 and BCECs culture media and supplements	35
Table 2.8. HUVECs culture media and supplements	36
Table 2.9. ECM coating solution	36
Table 3.1. Post processing of Dental SG resin.....	39
Table 3.2. Post processing of Dental Model resin	40
Table 3.3. Immunofluorescence procedure for BCECs	52
Table 3.4. Immunofluorescence procedure for HUVECs and Caco-2	55
Table 4.1. Comparison of <i>CPE</i> parameters of TiN-coated electrodes.....	66
Table 4.2. <i>CPE</i> parameters obtained from dynamic culture	78
Table 4.3. Analysis of DAPI counting of hiPSCs-derived BCECs	80

List of Acronyms

Acronyms	Definition
2D	Two Dimensions
3D	Three Dimensions
AC	Alternating Current
AF	Along Fiber
AKF	Acute Kidney Failure
AKI	Acute Kidney Injury
AM	Across Membrane
BBB	Blood-Brain Barrier
BCECs	Brain Capillary Endothelial Cells
P	Cell Passage
C	Counter probe/electrode
Caco-2	Cancer Coli-2
CAD	Computer-Aided Drawing
CPE	Constant Phase Element
DAPI	4',6-diamidino-2-phenylindole
DIV	Dynamic <i>in vitro</i>
DMSO	Dimethyl Sulfoxide
EC	Extracapillary
ECM	Extracellular Matrix
EDTA	Ethylene-Diamine-Tetraacetic Acid
EIS	Electrochemical Impedance Spectroscopy
EtOH	Ethanol
FFT	Fast Fourier Transform
FSC	Fetal Calf Serum
GLUT-1	Glucose Transporter 1
hCMEC	Human Brain Endothelial Cells
HFBR	Hollow Fiber Bioreactor

hiPSCs	Human Induced Pluripotent Stem Cells
HSA	Human Serum Albumin
HUVECs	Human Umbilical Vein Endothelial Cells
IC	Intracapillary
ID	Inner Diameter
IF	Immunofluorescence
OD	Outer Diameter
PBS	Phosphate Buffered Saline
PDMS	Polydimethylsiloxane
PVD	Physical Vapor Deposition
R	Reference Probe/electrode
RF	Radio Frequency
RMS	Root Mean Square
RRT	Renal Replacement Therapy
SD	Standard Deviation
SEM	Scanning Electron Microscope
SLA	Stereo Lithography Apparatus
SS	Stainless Steel
TEER	Transendothelial/Transepithelial Electrical Resistance
TJ	Tight Junction
TMP	Trans-Membrane Pressure
W	Working probe/electrode
WC	Working Sensing probe/electrode
ZO-1	Zonula Occludens 1

List of Symbols

Symbols	Meaning	Unit
ω	Angular frequency	rad/s
C	Capacitance	F
Q	Constant phase element	$S \cdot s^n$
Y_0	CPE admittance	$S \cdot s^n$
n	CPE exponent	
I	Current	Ampere
\emptyset	Diameter	mm
f	Frequency	Hz
h	Hour	
Z	Impedance	Ω
L	Inductance	H
min	Minute	
N	Number	
ε	Permittivity	$F \cdot m^{-1}$
ϕ	Phase angle	$^\circ$
P	Pressure	mmHg
R	Resistance	Ω
A	Surface area	m^2
T	Temperature	$^\circ C$
V	Voltage	volt
W	Watt	W

1. Introduction

1.1. Electrochemical Impedance Spectroscopy Basics

Electrochemical impedance spectroscopy (EIS) is a prompt electrochemical technique used extensively in fields, such as biochemistry [1-3], materials science [4-8], and biomedical science [9-15]. The basic concept of EIS is to measure the electrical impedance of an electrochemical cell as a function of frequency. This impedance data can then be used to analyze various electrochemical properties, including resistance, capacitance, double-layer capacitance, and mass transfer, among others [16-22].

Impedance is defined as the total opposition to the flow of alternating current (AC) in a circuit, and it extends the concept of electrical resistance by including not only the measure of resistance of a resistor but also the reactance of a capacitor or an inductor.

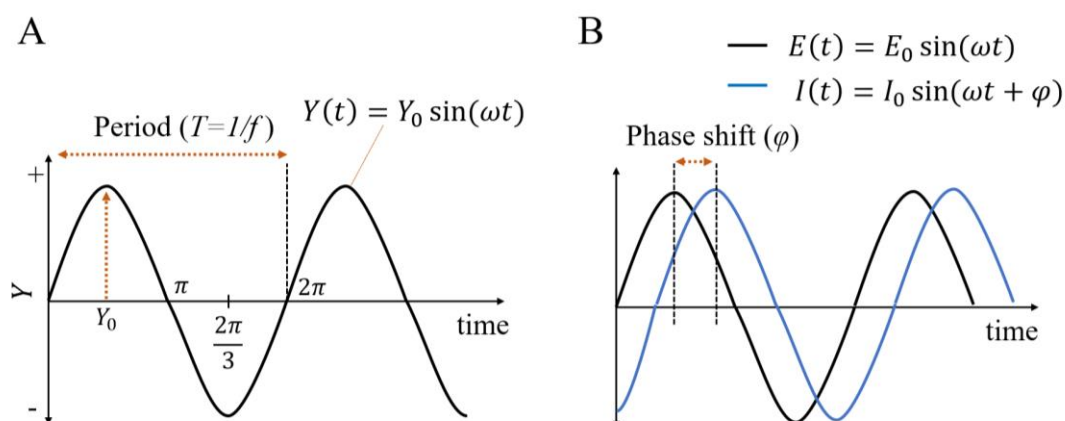


Figure 1.1. Illustration of sinusoidal graph. (A) Sinusoidal graph represents instantaneous value of sinusoidal signal, $Y(t)$, as function of time. Y_0 represents the amplitude, indicating the maximum values of the waveform. Period (T) refer to time for one complete cycle of waveform. T is inverse proportional to frequency (f), additionally, angular frequency (ω) is equal to $2\pi f$. (B) When one waveform leads or lags behind another waveform due to a time shift, the amount of this time shift is defined as the phase shift (φ) in sinusoidal functions. Example (B) illustrates a situation where the potential sinusoidal signal wave ($E(t)$) lead the current sinusoidal signal wave ($I(t)$) by a certain phase shift. This figure has been adapted from Gamry Instruments with permission [23].

EIS devices are operated either in potentiostatic mode or galvanostatic mode [24]. In potentiostatic mode, an input signal in the form of a sinusoidal potential is applied to the electrochemical system, and the resulting output signal in the form of a sinusoidal current is

measured, and it is referred to as potentiostatic EIS. In contrast, in galvanostatic mode, using sinusoidal current as an input signal and measuring the output sinusoidal potential. In the case of potentiostatic EIS, the applied potential as function of time, $E(t)$ is represented to the form in Equation 1.1.

$$E(t) = E_0 \sin(\omega t) \quad 1.1$$

Where, E_0 is amplitude of the potential wave, ω is the angular frequency, and t is the time. Thus, the basic sinusoidal graph is represented in Figure 1.1.

The angular frequency, ω , is equal to the constant value 2π multiplied by the frequency, f (Equation 1.2).

$$\omega = 2\pi f \quad 1.2$$

The output signal in the form of sinusoidal current, $I(t)$, may have phase shift and varying with the amplitude of current signal, and that express in Equation 1.3.

$$I(t) = I_0 \sin(\omega t + \varphi) \quad 1.3$$

Where, $I(t)$ is current signal as a function of time, I_0 is amplitude of current signal, φ is phase angle (Figure 1.1).

The total impedance (Z) of the electrochemical system is calculated by Ohm's law equation.

$$Z = \frac{E(t)}{I(t)} = \frac{E_0 \sin(\omega t)}{I_0 \sin(\omega t + \varphi)} = Z_0 \frac{\sin(\omega t)}{\sin(\omega t + \varphi)} \quad 1.4$$

As a result, the impedance is described by the magnitude of impedance (Z_0) and the phase angle (φ) [23].

There is another way to represent impedance using a complex number, allowing for the easy expression of both magnitude and phase [25,26]. In general, complex number is represented by z , and included real part and imaginary part.

$$z = a + bj = |z|(\cos \varphi + j \sin \varphi) \quad 1.5$$

The a represents real part, bj denotes the imaginary part, and j is the imaginary unit (where $j = \sqrt{-1}$). Both a and b are the real number.

Also, the complex number can be expressed in polar form with respect to absolute value (modulus or magnitude) of complex number $|z|$.

$$a = |z| \cos \varphi \quad 1.6$$

$$b = |z| \sin \varphi \quad 1.7$$

$$|z| = \sqrt{a^2 + b^2} \quad 1.8$$

Additionally, a complex number can be represented using Euler's formular (Equation 1.9).

$$e^{j\varphi} = \cos \varphi + j \sin \varphi \quad 1.9$$

Where e is the base of the natural logarithm, j is the imaginary unit (where $j = \sqrt{-1}$), and φ can be any real numbers. Equation 1.5 can be expressed in exponential form, as shown in Equation 1.10.

$$z = |z|e^{j\varphi} \quad 1.10$$

Furthermore, Equation 1.9 can be rearranged to Equation 1.11.

$$\cos \varphi = e^{j\varphi} - j \sin \varphi \quad 1.11$$

The equation is expressed using real portion of complex number to remain only the real number as followed (Equation 1.12). The real portion of complex number is denoted by Re .

$$\cos \varphi = Re(e^{j\varphi}) \quad 1.12$$

In this regard, potential and current sinusoidal signals can be expressed using the following forms.

$$E(t) = E_0 \cos(\omega t) = Re(E_0 e^{j\omega t}) \quad 1.13$$

$$I(t) = I_0 \cos(\omega t - \varphi) = Re(I_0 e^{j(\omega t - \varphi)}) \quad 1.14$$

Thus, the impedance is calculated using Ohm's law, as represented by Equation 1.15.

Consequently, the impedance can be expressed as a complex number with magnitude $|Z|$ and phase φ (Equation 1.15).

$$\underline{Z} = \frac{\underline{E}}{\underline{I}} = \frac{E_0}{I_0} e^{j\varphi} = |Z| e^{j\varphi} \quad 1.15$$

$$\underline{Z} = |Z| e^{j\varphi} = |Z| (\cos \varphi + j \sin \varphi) = Z_r + jZ_i \quad 1.16$$

\underline{Z} represents the complex impedance, \underline{E} denotes the complex potential, and \underline{I} stand for the complex current. The exponential form can be extended to compose real impedance (Z_r or Z') and imaginary impedance (Z_i or Z'') (Equation 1.16).

Hence, EIS results including impedance magnitude ($|Z|$), real (Z_r) and imaginary (Z_i) impedance, and phase angle (φ) are commonly presented using Bode and Nyquist plots. A Bode plot is a graph that depicts impedance magnitude and phase angle as functions of frequency (Figure 1.2A). Consequently, a Bode plot provides a simple and comprehensive representation of the complex impedance data as a function of frequency. Unlike the Bode plot, the Nyquist plot can be obtained by plotting Z_r (or Z') on the x-axis and Z_i (or Z'') on the y-axis, as demonstrated in the example plot shown in Figure 1.2B.

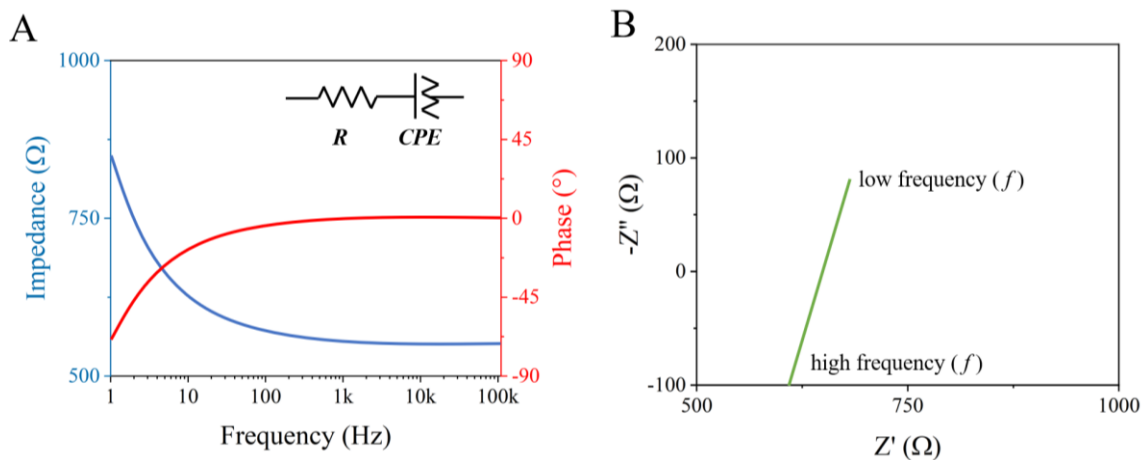



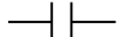
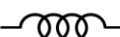

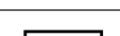
Figure 1.2. Two types of graphical representation of EIS. (A) An example of a Bode plot involves plotting the impedance and phase as functions of frequency. (B) An example of a Nyquist plot involves plotting the complex impedance as a function of frequency. The imaginary part ($-Z''$) of the complex impedance is plotted on the y-axis, while the real part (Z') is plotted on the x-axis. This figure was generated as a reference to the impedance data measured in my work using the Nova software program and Autolab PGSTAT 204.

Even though frequency values are not directly indicated on the Nyquist plot, it offers a simple and comprehensive representation of the electrochemical system [27]. Both graphical

representations enable the identification of impedance behavior associated with electrochemical systems within given frequency ranges. In terms of equivalent circuit modeling, the impedance response of electrochemical system can be further analyzed to acquire useful information. Based on impedance response of electrochemical system, the analogous equivalent circuit elements used to model the electrochemical system.

Table 1.1 shows well-known electrical circuit elements. A resistor opposes the flow of current in a circuit, resulting in an impedance, Z_R . This impedance is independent of frequency and comprises only a real number contrast to other elements. The phase angle is zero, indicating that current passing through a resistor and voltage applied across resistor are in phase. As an example, the resistor is used to represent the electrolyte resistance [28,29], a polarization resistance applied coating analysis study [30-33], and a transendothelial/transepithelial electrical resistance (TEER) applied in biological analysis [34-37].

Table 1.1. Equivalent circuit elements [41]

Circuit elements	Electronic symbol	Impedance formular
Resistor (R)		$Z_R = R$
Capacitor (C)		$Z_C = \frac{1}{j\omega C}$
Inductor (L)		$Z_L = j\omega L$
Constant phase element (CPE)		$Z_{CPE} = \frac{1}{Y_0(j\omega)^n}$
Warburg element (W)		$Z_W = \frac{1}{(j\omega)^{0.5}}$

The impedance of capacitor, Z_C , is occurred when the current passing through the capacitor because the capacitor stored the electrical charge. The impedance of capacitor is dependant of frequency, and phase shifted of -90° . As represented in Table 1.1, it includes imaginary number, and a angular frequency and capacitance are inversely proportional to the Z_C . The example use of capacitor elements are to define double-layer capacitance [38,39] and coating capacitance [5,40]. An inductor impedes the current flow as storing energy in a magnetic field in an electrical circuit. Opposite to capacitor, the impedance of inductor (Z_L) increases by increasing frequency and is proportional to inductance. The current and voltage waveform in a circuit containing inductor are out of phase as $+90^\circ$.

In reality, the ideal capacitor does not exist in the most cases. Constant phase element (*CPE*) is useful to examine inhomogeneity of a capacitor [42,43]. The impedance of *CPE* (Z_{CPE}) equal to inverse proportional to the Y_0 parameter carrying capacitance information and to the frequency. The fractional exponent, n , ranges from $0 < n < 1$. When n is equal to 1 indicating a pure capacitor, on the other hand, $n = 0$ describes a pure resistor. The $n = 0.5$ corresponds to the Warburg element. Several researches reported using *CPE* elements to model the double-layer capacitance [21,44] and coating capacitance [45,46] of their electrochemical circuits rather than capacitor element. The Warburg element represents diffusion phenomena in electrochemical system. Warburg impedance is frequency dependant and inverserly propotional to Warburg constant and $(j\omega)^{0.5}$. The phase is constant at 45° which is independent of frequency. Most commonly, Warburg elements are used to model semi-infinite linear diffusion layers, often accompanied by a charge-transfer resistance and a double-layer capacitance [47- 49].

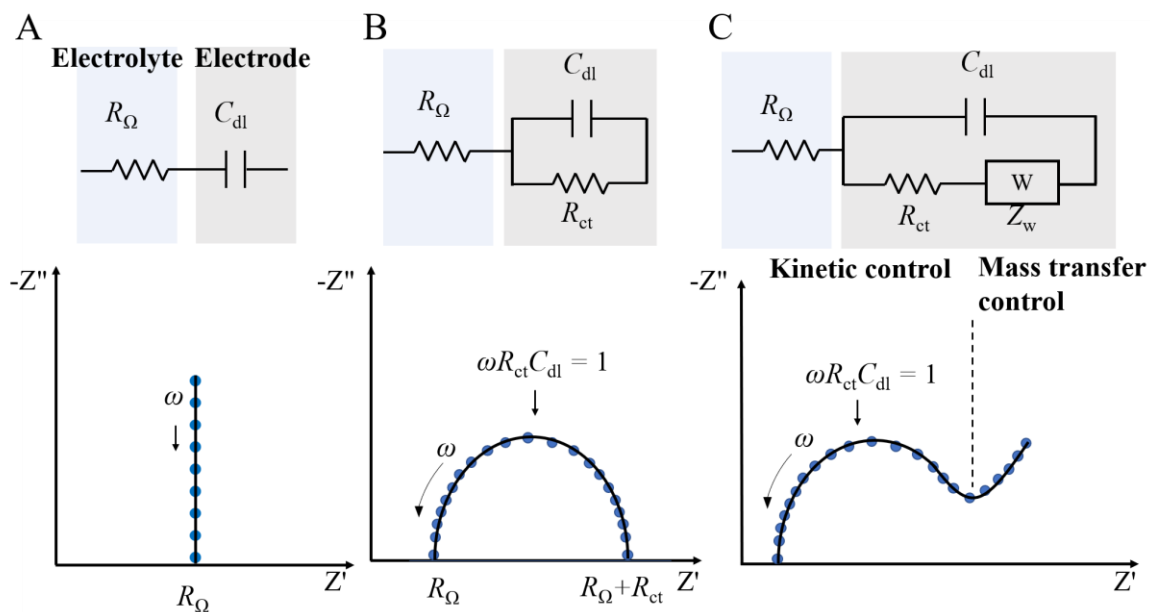


Figure 1.3. Example of equivalent circuit modeling in EIS. The modeling is based on Nyquist plot associate electrochemical system. (A) EIS responds to non-faradaic process where no electron transfer occurs at the interface of the electrode and electrolyte. (B) EIS responds to faradaic process, which involves electron transfer between electrode and electrolyte, is controlled by kinetics, such as redox chemical reactions. (C) EIS responds to faradaic process is controlled by kinetics and mass transfer, such as diffusion. This figure has been reconstructed from Brett (2022) under the terms and conditions of the Creative Commons Attribution (CC BY) license [50].

Figure 1.3 provides an illustrative example of modeling and fitting an equivalent circuit based on impedance responses, specifically using a Nyquist plot, and employing elements analogous to those found in an electrochemical system. This illustration demonstrates how diverse electrochemical phenomena can be effectively modeled and investigated through the application of an equivalent circuit. The line in Nyquist plots (Figure 1.3A, B, and C) are the impedance response to the electrochemical system, where an inert metallic electrode is immersed in an electrolysis composed of electroactive species.

Figure 1.3A describes the case of non-faradaic process which doesn't involve the electron transfer between electrode and electrolyte, the impedance response is depicted by a vertical straight line. Considering the electrochemical system, circuit models with a resistor (R_{Ω}) analogous to the electrolyte and a capacitor (C_{dl}) analogous to the electrical double layer of electrode are connected in series. Thus, an equivalent circuit can be fitted to the impedance spectra. The choice of the equivalent circuit model would result in a different quality of fitting. The Figure 1.3B represents the faradaic process which involves the transfer of the electron between electrode and electrolyte, resulting semicircular form in Nyquist plot. Thus phenomena, electron transfer, represents to charge transfer resistance (R_{ct}), and R_{ct} element is connected in parallel with C_{dl} . When larger the electroactive surface area of electrode because of modifying to have nanostructure, the R_{ct} becomes smaller. This is because the larger the electroactive area is equivalent to increasing number of active sites available. Consequently, when the charge transfer rate is controlled by diffusion at low frequencies, it is revealed as a straight line in the Nyquist plot (Figure 1.3C), unlike Figure 1.3B. Thus, the diffusion process is modeled by the Warburg element, and as a result, the circuit models in Figure 1.3B can be extended to a more complex model, as shown in Figure 1.3C.

Hence, equivalent circuit modeling and fitting to impedance responses enable further investigation and interpretation of the electrochemical system, providing quantitative parameters such as resistance, capacitance, Y_0 , and σ , among others.

1.2. Electrochemical Impedance Spectroscopy for Investigating the Integrity of Barrier Tissue *in vitro* Culture

The electrical properties of tissues have been investigated since the 1900s, alongside the development of suitable electrical measurement devices. In particular, Herman P. Schwan reported on the dielectric properties of cell membranes in relation to cell suspension [51]. When an electric field is applied to biological materials such as biological tissue or cell suspension,

dielectric polarization occurs within the biological materials, opposing the electric current. The study focused on the passive electrical properties, such as resistance, capacitance, and inductance, of biological tissue in response to external electrical signals in low frequency ranges where Ohm's law applies.

Consequently, Schwan demonstrated that the dielectric properties of biological tissue possess three dispersion characteristics (α , β , and γ -dispersion) across a wide frequency range. The Figure 1.4 is the graph of the frequency dependent permittivity of muscle cells proposed by Schwan [51]. Permittivity (ϵ) is a physical constant that measures the ability of a material to store electric charge in an electric field [52,53]. α -dispersion was observed at low frequency ranges (below 10 kHz), where the permittivity was relatively high, and this correlated to the counter-ion polarization along the cell membrane surface.

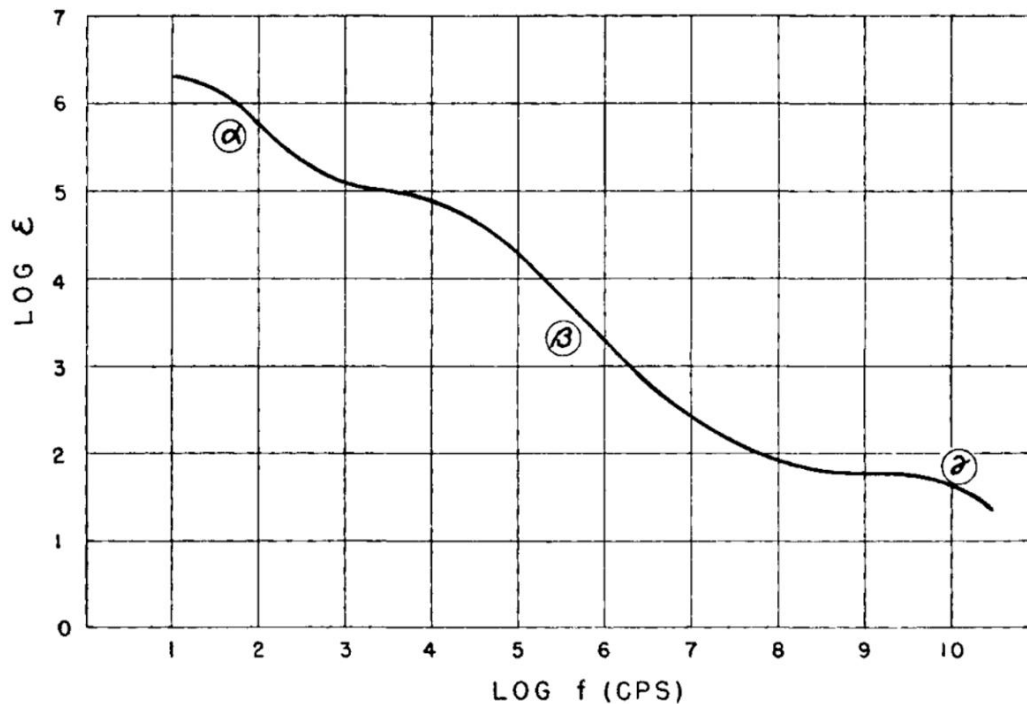


Figure 1.4. Electrical properties of biological tissue. Three steps, α , β , and γ -dispersion, of dielectric constant as a function of frequency in muscle tissue. This figure has been reprinted from Schwan's original data with permission from publisher Elsevier [51].

As the frequency range increases (from 10 kHz to 1 MHz), the permittivity became lower than that observed in α -dispersion, and this was referred to as β -dispersion. β -dispersion is caused by the polarization of cellular structures, such as the cell membrane, proteins, and

macromolecules, and as the frequency increases, the current begins to pass through the cell membrane. Lastly, water polarization contributes to the γ -dispersion at the high frequency (over 1 GHz) [51,52].

Barrier tissue plays an important role as a physical barrier of two different compartments in the body [54]. The major function of barrier tissue is to control the passage of substances, such as pathogens, toxins, and foreign particles, from one side of the tissue to the other. The two compartments that have the barrier tissue placed in the middle are called the apical (or luminal) and basolateral (or abluminal) sides (Figure 1.5A). The endothelial tissue, which lines the inner surface of blood vessels [55], and the epithelial tissue, which lines various organs such as the skin, lungs, and intestines, are the most common barrier tissues in the body.

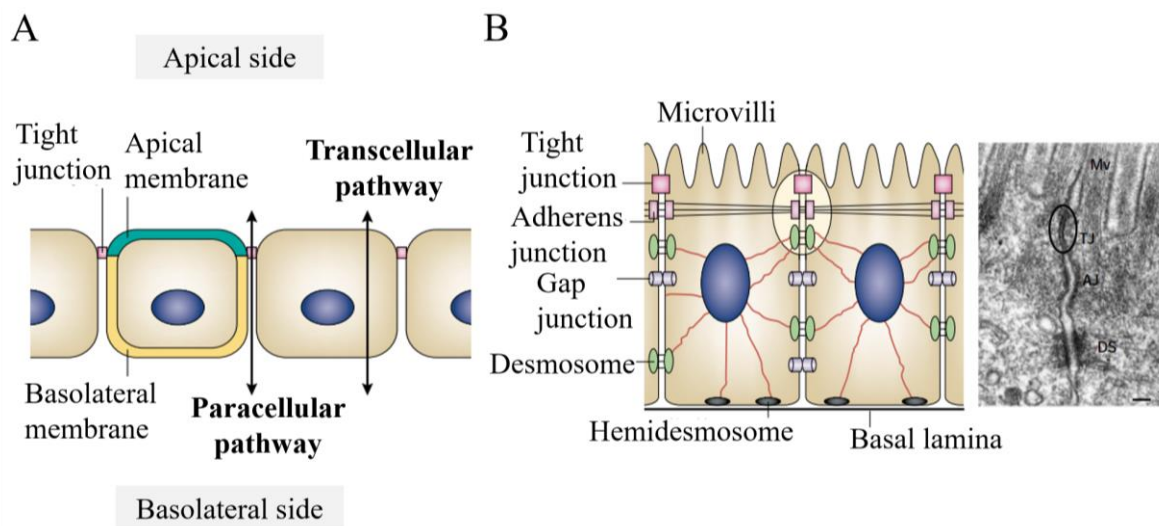


Figure 1.5. Transport pathways of endothelial and epithelial cell layer. (A) Molecules are transported between the apical and basolateral sides of cells through two distinct pathways: the transcellular pathway and the paracellular pathway. (B) (Left) Schematic depiction of intercellular junctions within the epithelial cell layer. The circular mark indicates junctions located at the most apical membrane. (Right) Electron micrograph showing intercellular junctions, including microvilli (Mv), tight junctions (TJ), adherens junctions (AJ), and desmosomes (DS). Scale bar 200 nm. This figure has been adapted from Tsukita et al. under permission Springer Nature [60].

The endothelial and epithelial cell layer have a unique feature in the form of specialized intercellular junctions that connect adjacent cells. As shown in Figure 1.5B, intercellular junctions are divided into four distinct types: gap junctions, desmosomes, adherens junctions, and tight junctions (TJ) [56,57]. TJ consist of transmembrane proteins such as occludin, claudin, and zonula occludens-1 (ZO- 1), which form interconnected strands between adjacent cells.

Understanding of the transport mechanisms in barrier tissues began with Ussing's work [58,59], which distinguished between passive and active transport by observing the transport of Cl^- and Na^+ across a frog skin model. The conclusion drawn from the flux ratio analysis was that the passive transport of Cl^- across the skin was determined by the difference in electrical potential between the two sides (apical and basolateral membranes). On the other hand, it has been demonstrated that Na^+ undergoes active transport by confirming the electrical asymmetry of Na^+ across the skin using the short-circuit method. The amount of Na^+ transported was exactly equal to the current measured through the short-circuiting method [61]. Subsequently, the transport mechanism has been expanded to demonstrate that solutes can be transported across barrier tissues via either intercellular or paracellular pathways (Figure 1.5A). Transcellular transport refers to the movement of molecules and ions across the cellular membrane from one compartment to another. Alternatively, molecules and ions can move through TJs via the paracellular pathway. Therefore, the selectively permeable cell layer enables the maintenance of homeostasis by regulating solute movement through transcellular or paracellular routes using active or passive transport.

1.2.1. Single Frequency Transendothelial/Transepthelial Electrical Resistance measurement

Transwell cell cultures are widely accepted and used as an *in vitro* cell culture such as blood brain barrier (BBB) endothelial cells and intestinal epithelial cells. Cells are cultured on semi-permeable membrane inserts in a transwell plate, separating the apical and basolateral compartments (Figure 1.6). Closely mimicking an intact *in vivo* barrier is crucial when modeling *in vitro* cell barrier especially for transport studies [62,63]. There are several methods that can be used to examine paracellular or transcellular permeability, including the use of fluorescent dye molecules such as fluorescein isothiocyanate (FITC)-dextran and lucifer yellow, radioactively labeled sucrose, and TEER measurement. Among them, TEER measurement is a direct and non-destructive method to investigate barrier integrity, unlike other methods that require the addition of fluorescent dyes or contrast agents [64-67]. The Figure 1.7 shows the general setup of most commonly used and commercially available TEER measurement device (EVOM and Millicell ESR-2). The fixed pair of double electrodes, made out of silver/silver-chloride pellets, is immersed into each of the apical and basolateral compartments filled with culture medium of inserts placed in a transwell plate. An AC current with a frequency of 12.5 Hz is applied between the two electrodes, and the resulting output

signal (voltage) is measured. As a result, total electrical resistance of transwell culture is quantified using Ohm's law.

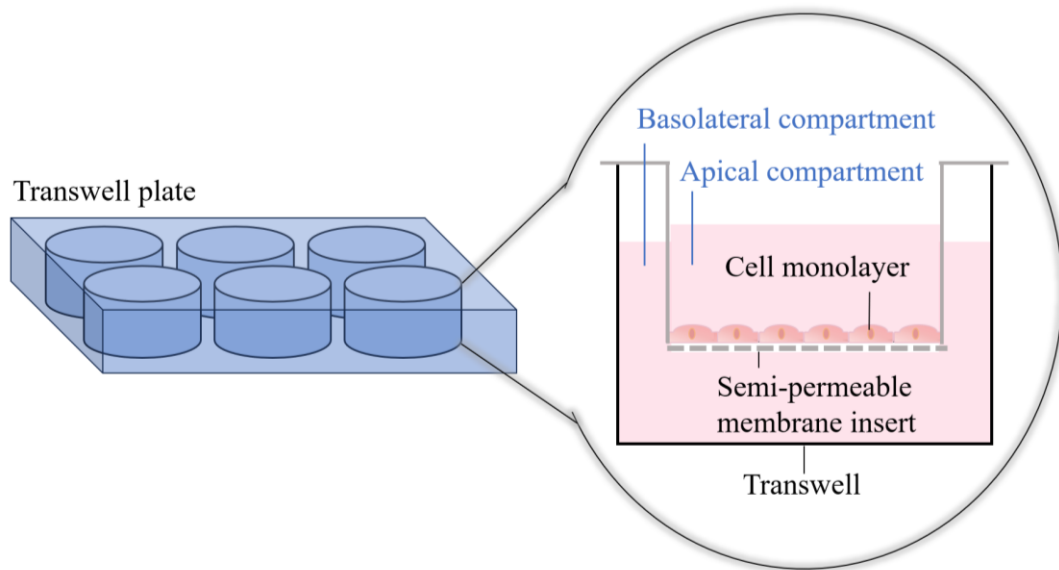


Figure 1.6. Illustration of the *in vitro* transwell based cell culture. Cells are cultured on a semi-permeable membrane within the insert. The inner part of the insert constitutes the apical compartment, while the outer part is designated as the basolateral compartment.

The circuit diagram includes two series-connected resistors: one represents the TEER and the other represents the resistance of the culture medium (R_M), electrode (R_E), and porous membrane (R_{PM}) (Figure 1.7). Therefore, the R_{TEER} can be extracted using the Equation 1.17 from obtained total resistance (R_{Total}) [69].

$$R_{TEER}[\Omega \cdot cm^2] = (R_{Total}[\Omega] - R_{Blank}[\Omega]) \times A_{Porous\ membrane}[cm^2] \quad 1.17$$

$$R \propto \frac{1}{A} \quad 1.18$$

Here, R_{Blank} represents the TEER measurement without a cell layer, R_{Total} represents the TEER measurement with a cell layer, and $A_{Porous\ membrane}$ is the geometrical surface area of the porous membrane on which the cells are cultured. Since resistance is inversely proportional to surface area (A) as per Equation 1.18 [70], the TEER value is multiplied by the surface area for normalization, as shown in Equation 1.17. Despite its value as a non-invasive method, TEER measurement is susceptible to errors due to various factors such as temperature changes, electrode damage, and positioning [68,69,71].

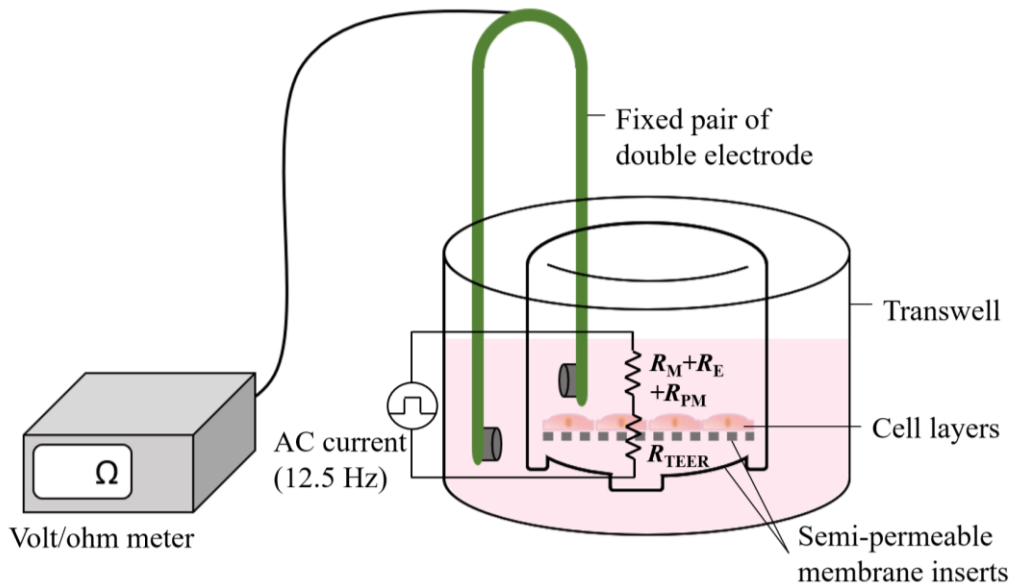


Figure 1.7. TEER measurement in transwell culture system. Illustration of TEER measurement device that is commonly used in transwell culture. The device operates by allowing an AC current with a constant amplitude to flow between two electrodes, while measuring voltage changes in order to display the ohmic resistance at a frequency of 12.5 Hz. The equivalent circuit represents electrochemical elements in transwell culture system that includes cell layer resistance (R_{TEER}), culture medium resistance (R_M), electrode resistance (R_E), and porous membrane resistance (R_{PM}). This Figure has been reconstructed from 2013 Benson et al.; license BioMed Central Ltd [68].

Therefore, it is important to carefully control these conditions during TEER measurement. Furthermore, a volt-ohm meter exclusively measures resistance, implying that equivalent circuits can be modeled to incorporate only resistors (Figure 1.7). However, this approach lacks specific information, particularly regarding electrode characteristics such as CPE or W , as introduced in Table 1.1.

1.2.2. Electrochemical Impedance Spectroscopy

Unlike single-frequency TEER measurements, EIS offers the advantage of monitoring electrical impedance across a wide range of frequencies. This capability enables the capture of electrical impedances from different components within an electrochemical system in a single measurement. Consequently, potential sources of error in single-frequency TEER measurements, such as electrode damage and changes in medium resistance due to variations in concentration or temperature, can be monitored or further eliminated, as R , CPE , and W can be extracted from the given system. This leads to the attainment of more precise results.

Figure 1.8 represents an equivalent circuit model analogous to the barrier tissue models that can be obtained by EIS. Compared to single-frequency TEER measurements (Figure 1.7), not

only does R_T serve as an analogous tight junction protein regulating paracellular transport, but R_{CM} and C_C also represent the polarization function of the lipid bilayer as part of the transcellular pathway. The cell-related circuit elements, R_T , R_{CM} , and C_C , are connected in parallel. Additionally, the electrode impedance is represented by C_E , and the cell culture medium is represented by R_M .

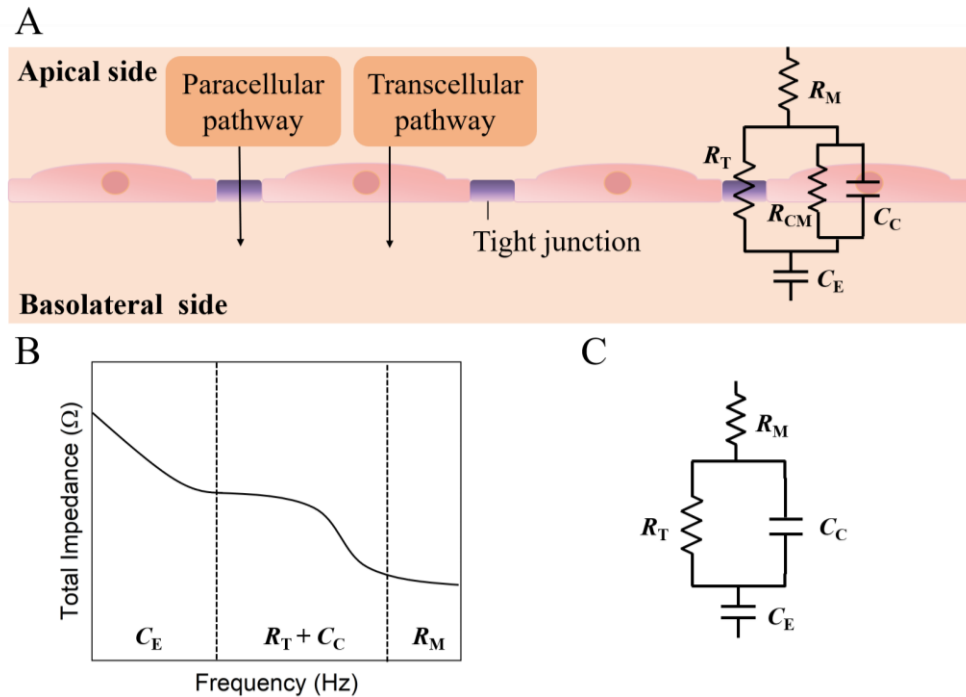


Figure 1.8. EIS measurement of cellular barrier. (A) Typical equivalent circuit model corresponding to electrical properties of cellular barrier system as reflected in EIS measurement. The tight junction that regulates paracellular transport can be modeled with resistor (R_T). The transport through the transcellular pathway is regulated by the cell membrane, which can be modeled with a parallel connection of a resistor (R_{CM}) and a capacitor (C_C). Additionally, the electrode capacitor (C_E) and medium resistance (R_M) is series connected to the circuit. (B) Typical graphical representation of the impedance distribution of the cellular barrier in the frequency spectrum. The electrical barrier parameters, R_T and C_C , contribute dominantly to the total impedance at middle frequencies, while the electrode impedance (C_E) and the medium impedance (R_M) are dominant at low and high frequencies, respectively. (C) The equivalent circuit of the cellular barrier can be simplified. This figure has been reconstructed from Benson et al. under the terms of the Creative Commons Attribution License, published by BioMed Central Ltd [68].

The impedance of each component in an electrochemical system becomes dominant at a particular frequency range. As shown in Figure 1.8B, the electrode impedance (C_E) dominates the total impedance at low frequencies, while the cell-related impedance, composed of parallel connected R_T and C_C , becomes predominant at middle frequencies. Figure 1.8C depicts the

simplified equivalent circuit commonly utilized. At high frequency ranges, the permittivity of both the electrode and the cell membrane decreases [52], causing the medium impedance (R_M) to become the dominant factor contributing to the total impedance. The obtained EIS data can be used to quantify the electrical parameters of barrier integrity, including resistance of tight junction and capacitance of the cell membrane, by fitting an equivalent circuit using software. The quantified R_T and C_C out of fitting program can be normalized to porous membrane surface area and used.

$$R_{T,normalized} [\Omega \cdot cm^2] = R_{T,Fitting}[\Omega] \times A_{Porous\ membrane}[cm^2] \quad 1.19$$

The parameter $R_{T,Fitting}$ represents the resistance of tight junction quantified by fitting the equivalent circuit to EIS data, and $A_{Porous\ membrane}$ denotes the geometrical surface area of the porous membrane.

While resistance is inversely proportional to surface area, capacitance is directly proportional to surface area (Equation 1.20).

$$C \propto A \quad 1.20$$

Therefore, the capacitance can be normalized using Equation 1.21.

$$C_{C,normalized}[F/cm^2] = \frac{C_{C,Fitting}[F]}{A_{Porous\ membrane}[cm^2]} \quad 1.21$$

Where $C_{C,normalized}$ represents the normalized value of C_C , $C_{C,Fitting}$ denotes C_C obtained from fitting the equivalent circuit, and $A_{Porous\ membrane}$ signifies the surface area of the porous membrane. Hence, through the use of equivalent circuit fitting, accurate results can be obtained regarding barrier integrity, effectively eliminating the impact of undesired background factors like electrode and medium resistance. Moreover, the advanced measurement of EIS, when compared to single-frequency TEER measurement, has been considered advantageous for application in perfusion bioreactor cultures operating under fluid flow condition. Further discussion on their utilization within bioreactor systems will be presented in the subsequent sections.

1.3. Titanium Nitride Coating as an Electrode Material

EIS measurements rely on the electrodes as an essential link between the measurement device and the electrochemical system. By subjecting the electrode to AC voltage and measuring the resulting current, valuable information regarding the impedance response of the electrochemical system can be obtained. In simpler terms, the sensitivity of the electrodes holds

importance. At the same time, since the impedance of the electrode affects EIS results, as shown in the Figure 1.8, lowering electrode impedance becomes a crucial goal when employing EIS for biological applications. Therefore, the choice of materials should be decided depends on the specific electrochemical system along with preliminarily examination of electrode properties to obtain meaningful results. In terms of studying electrical impedance of biological tissue, the electrode should be conductive, biocompatible, and exhibiting no chemical reactivity or degradation during the experiment.

Titanium nitride (TiN), a ceramic material possessing great hardness, is an excellent candidate for use as an electrode in bioimpedance studies. TiN is mainly coated onto other materials such as steel, titanium alloy, and aluminum for use. Even though the conductivity of TiN ($\sim 4 \times 10^6$ S/m) is relatively low compare to noble metals such as gold (Au, 4.52×10^7 S/m) and platinum (Pt, 9.44×10^6 S/m) [72,73], TiN coating possesses other superior material properties that make it more suitable for use in EIS measurements with biological tissue rather than those materials. The biocompatibility and wear resistance of TiN coating has been extensively demonstrated in biomedical research, to the extent that it is being used as a coating for medical implants [74-79]. Another advantageous material property of TiN coating is corrosion resistance. To ensure accurate bioimpedance measurements and prevent harm to biological tissue, it is important to choose electrodes with high corrosion resistance. This is because chemical reactions at the electrode/electrolyte interface can cause material degradation, resulting in inaccurate EIS readings and the release of harmful corrosion debris. Khatkhatay et al. [80] discovered that the TiN coating on Zircaloy-4 tubes stayed stable and intact even after being exposed to supercritical water for 48 h, while the uncoated tubes showed significant oxidation and corrosion. In general, supercritical water is defined as water at a beyond critical point (above a temperature of 374 °C and a pressure of 22.1 Mpa) in a phase equilibrium curve, and served as severe oxidizing agent [81]. Their corrosion test involved exposing the samples to aerated water for 48 h at a temperature of 500 °C and a pressure of 25 MPa. They confirmed that TiN coating revealed high corrosion resistance due to the formation of an oxide film. Also, Subramanian et al. [82] performed three TiN coatings (TiN, TiON, and TiAlN) on CP-Ti substrates and compared their corrosion rates to the substrate using EIS. Their findings showed a greater decrease in corrosion rate for all three TiN coatings in simulated body fluid compared to the substrate. Lastly, another beneficial property of TiN coating is its relatively low electrode impedance. Minimizing the contribution of electrode impedance to the total impedance has been emphasized to obtain accurate results [51,83-85].

Higher electrode impedance might lead to signal distortion, making it difficult to accurately detect the electrical properties of biological tissue, which are the main focus of EIS measurements in biology field. Preliminarily, electrode double-layer capacitance can be defined using EIS measurement as it is significant factor deciding the electrode impedance. Double-layer capacitance is an electrochemical property of the electrical double layer at the electrode-electrolyte interface, where charges of opposite signs align, with one at the electrode surface and the other in the electrolyte, resulting in the storage of electrical energy. Thus, if the electrode has high double-layer capacitance, it results in low electrode impedance. The equation that defines the relationship between double-layer capacitance and capacitor impedance (where the electrode essentially acts as a capacitor) is explained in Table 1.1. Several studies have investigated that TiN coating has a relatively higher double-layer capacitance than other commonly used electrode materials. Norlin et al. compared the double-layer capacitance of pure platinum (Pt) and Titanium (Ti), and TiN-coated electrode (TiN coating on Ti substrate) using EIS [32]. The TiN coating electrode showed a double-layer capacitance of value $3.5 \times 10^{-2} \text{ F/cm}^2$, which is hundred times higher than the capacitance values of Pt and Ti, which are $6.0 \times 10^{-5} \text{ F/cm}^2$ and $1.6 \times 10^{-4} \text{ F/cm}^2$, respectively. Their study indicated the rough surface of TiN coating causes a high effective surface area, leading to an increase in double-layer capacitance. Schmitz et al. [86] reported a comparison of the interfacial capacitance between smooth and rough TiN coating surfaces using EIS measurement. Hence, they showed that the interfacial capacitance of rough TiN coating ($309 \times 10^{-6} \text{ F/cm}^2$) was higher than smooth TiN coating ($11.1 \times 10^{-6} \text{ F/cm}^2$). Moreover, interfacial capacitance of the rough TiN coating was higher than the gold ($35.3 \times 10^{-6} \text{ F/cm}^2$) and stainless steel ($6 \times 10^{-6} \text{ F/cm}^2$).

To apply TiN onto substrates, physical vapor deposition (PVD) is a commonly used coating method. It includes various processes, such as vacuum evaporation, sputter deposition, and ion plating [88-92]. Among these processes, the sputter deposition is commonly used for producing thin film of compound materials such as TiN, silicon dioxide (SiO_2), titanium carbide (TiC), and so on.

The Figure 1.9 shows an example of sputtering process, specifically the radio frequency (RF) magnetron sputtering process. RF power supply is connected to the vacuum chamber using a matching network, and an AC electric field with a frequency of 13.56 MHz is applied to the low-pressure gas in the chamber. Inert gases such as argon (Ar) are commonly used as process

gases. Other process gases, such as nitrogen and oxygen, can also be used for specific applications. Plasma is generated when gas atoms become ionized by an electromagnetic field.

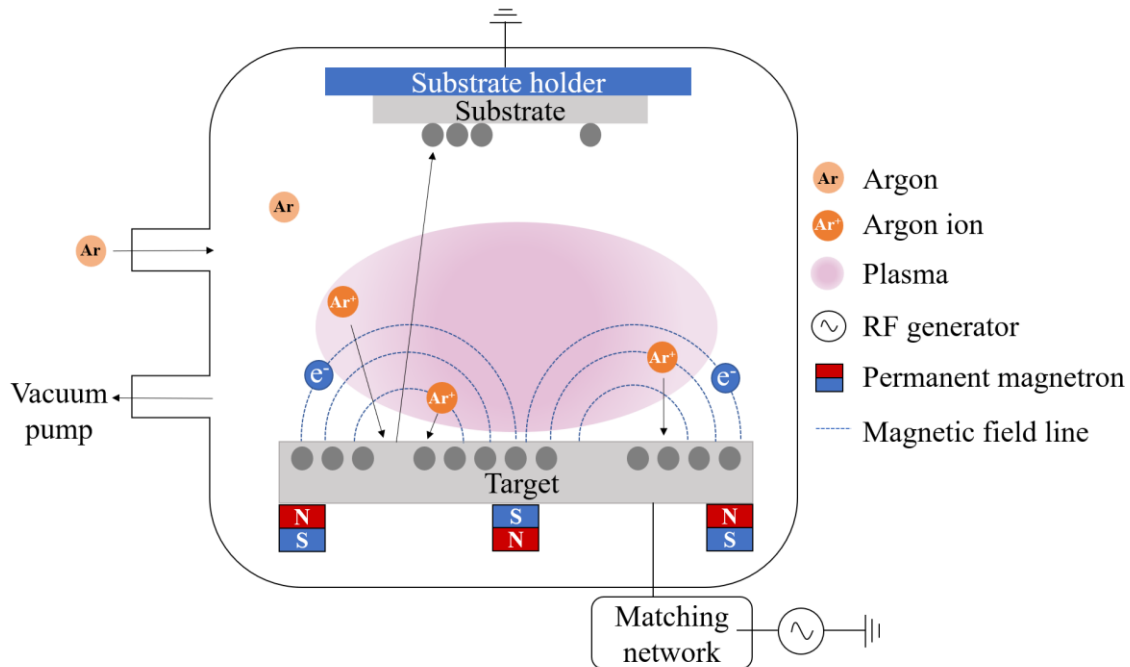


Figure 1.9. Schematic diagram of PVD coating process. The diagram illustrates PVD process using RF magnetron sputtering. A low-pressure process gas such as argon is ionized by an RF energy source to form a plasma. High-energy ions (Ar^+) from the plasma bombard a target material, causing atoms to be ejected and deposited onto a substrate. This figure has been adapted from Schmitz's doctoral dissertation [87].

The gaseous ions from the plasma collide with the target surface, causing the surface atoms and ions of the target to be bombarded. The sputtered materials are then deposited onto a substrate. The magnetron traps electrons in a magnetic field, increasing the ionization of the process gas and protecting the substrate from damage caused by ion bombardment. In magnetron sputtering, the deposition parameters are highly linked to the characteristics of thin films, thereby it is important to find optimized parameters depending on the demands [93-99]. Regarding RF magnetron sputtering specifically, Vasu et al. [100] found that the crystal structure and optical properties of TiN thin films were influenced by substrate temperature in RF magnetron sputtering, resulting in a transition from a non-stoichiometric, tetragonal Ti_2N phase to a nitrogen-deficient, cubic TiN phase. According to Kim et al. [101], reducing the Ar/ N_2 ratio (to 20:30, 10:30, and 0:30 ratios) during RF magnetron sputtering caused a decrease

in the grain size of the TiN coating. They also observed that increasing the flow rate of N₂ led to an increase in both the hardness and elastic modulus of the coating possibly because of a fine dispersion of TiN nano crystals. This is consistent with results reported by Dhanaraj et al. [102].

The TiN coating has shown promise as an electrode material for use in biological applications. Furthermore, by optimizing the PVD coating deposition process, the surface properties of TiN coating can be further improved to meet the requirements for electrode use.

1.4. State-of-the-art of Electrochemical Impedance Spectroscopy Setup for Cellular Barrier Culture in Perfusion Bioreactors

The transwell culture is a widely used *in vitro* cell culture for studying the BBB and intestinal barrier due to its ease of use and reproducibility [103-105]. However, the model lacks some of the dynamic conditions found in the *in vivo* environment, such as shear stress, continuous nutrient supply, and pressure [106-111]. Bioreactor culture is one of alternatives providing mechanical stimuli to approach to advance *in vitro* barrier cell culture. However, the use of fixed double electrodes is limited to transwell cell culture, and obtaining reliable TEER measurements under dynamic conditions, particularly under fluid flow, can be challenging. EIS is a particularly suitable technique to be used in bioreactor culture, as it enables automated long-term monitoring of tissue barrier integrity.

When integrating the EIS system into a perfusion bioreactor where a cellular barrier is being cultured, several factors need to be considered to ensure that the system operates more precisely and effectively. One of factors is electrode numbers. Most of impedance analyzer are four probe instruments consisting working (W), counter (C), working sensing (WS), and reference (R) probe. Working and counter probe are current carrier, and working sensing and reference probe participate to measure the potential. The number of electrodes required for the experiment may vary between two, three, or four, and the probes must be configured accordingly [112]. In a two-electrode setup, the same electrodes participate for both carrying the current and measuring the potential hereby, the working and working sense probe connect to one electrode and the counter and reference probe to another electrode (Figure 1.10A). The whole electrochemical cell contributes to the measurement results. The main difference between the three- and the two-electrode setup is that in the former, a third electrode is used to connect the reference probe (Figure 1.10B). This allows the potential change caused by the counter electrode to be excluded. In a four-electrode setup, four probes are connected to

individual electrodes (Figure 1.10C). The working sense and reference probes, what measure the potential, are not connected to the working and counter electrodes, and therefore any potential changes that may occur due to polarization or chemical reactions on the working and counter electrodes will not be detected.

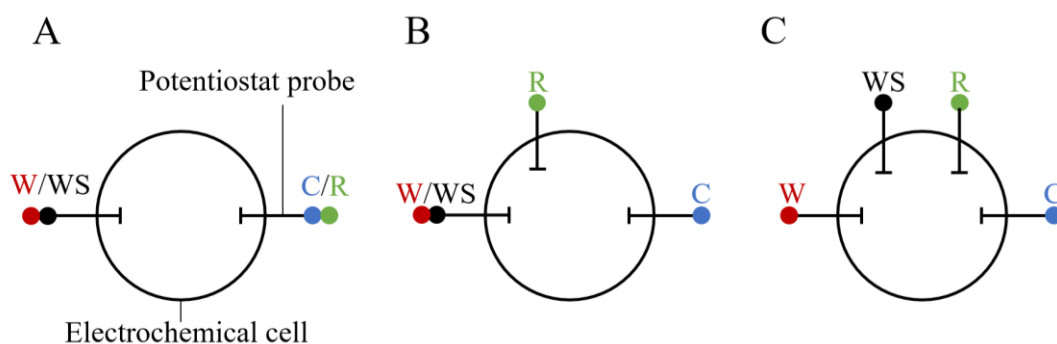


Figure 1.10. Different probe configurations. (A) Two-, (B) Three-, and (C) Four- electrode setup. (A) Connection of working (Red) and working sense (Black) probe to one electrode, and counter (Blue) and reference (Green) probe connected to another. (B) Connection of a working and working sense probe to one electrode, a counter probe to another electrode, and a reference probe to a third electrode. (C) Four probes are connected to individual electrodes. This figure has been reconstructed with permission from Gamry Instruments [112].

The measurement results involve information on potential differences from the electrolyte or some barrier present within the electrolyte. In addition to considering the number of electrodes, the electrode position also needs to be taken into account. Furthermore, various methods can be used to integrate electrodes to bioreactor system, such as sputtering, printing, or inserting metal wires. Another factor that needs to be considered is an impedance meter that performs the actual measurement. The selection of impedance meters for biological impedance research should be based on the specific characteristics of the biological samples under investigation. This is because different impedance meters provide varying frequency ranges, impedance ranges, automatic measurement options, and resolutions. In addition, the availability of fitting and simulation programs for equivalent circuit modeling may also be considered when choosing an impedance meter.

In the following paragraphs, an overview is presented of the state-of-the-art EIS system integrated into a perfusion bioreactor, where cellular barriers are cultured. In their 2013 study, Griep et al. [113] presented a microfluidic model designed for the cultivation of BBB, which specifically utilized immortalized human brain endothelial cells (hCMEC/D3) and enabled the measurement of TEER. As you can see in the Figure 1.11A, their BBB chip comprised a top

and bottom part made out of polydimethylsiloxane (PDMS), with the main channel for cell culture and a side channel for the electrode. They embedded the two inert platinum (Pt) electrodes on the side channels (top and bottom) and connected the HP4194A impedance/gain phase analyzer to electrodes for TEER measurement. TEER measurement was performed within 100 Hz to 10 MHz controlled by LabVIEW 7.1 software.

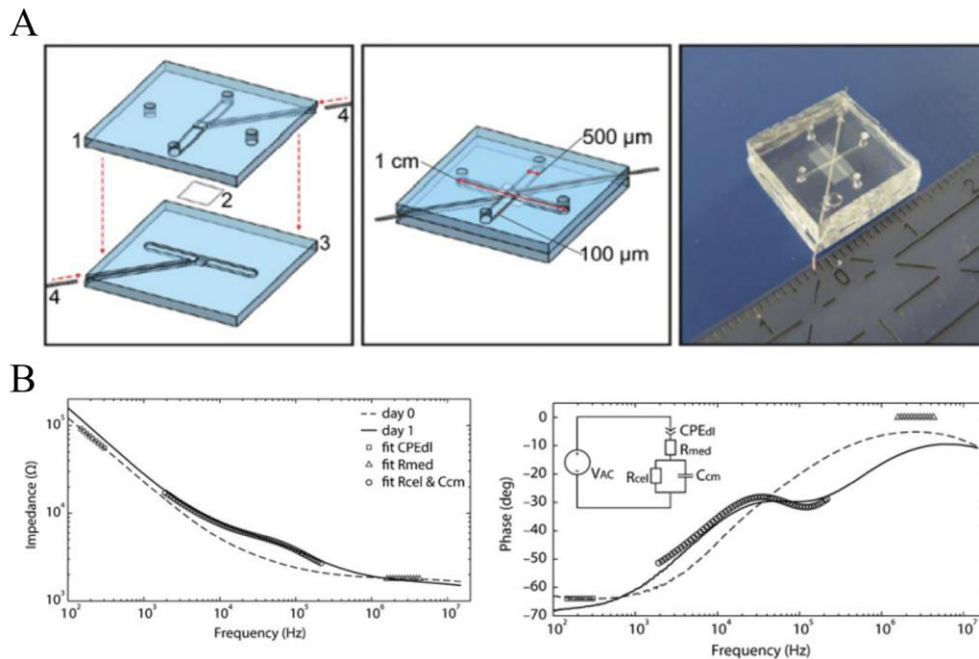


Figure 1.11. State-of-the-art of EIS system (1). Griep et al. proposed a microfluidic BBB chip integrating electrodes to examine BBB barrier integrity. (A) BBB on chip is composed of top part (1) and bottom part (3), and porous membrane (2). The device consists of a main channel for microfluidic culture and a side channel (4) that contains an electrode integrated on both the top and bottom parts. The image on the far right displays a photograph of the BBB chip. (B) Obtained EIS data represents to impedance and phase bode plot. The results show a comparison of EIS measurements between the BBB chip without cells (day 0) and with cells (day 1). Furthermore, the EIS data were fitted to equivalent circuits, where each circuit element represents a specific frequency range. The electrode impedance (CPE_{dl}) is represented at low frequencies, the medium resistor (R_{med}) at high frequencies, and the electrical barrier function resistor and capacitor (R_{cel} and C_{cm}) at intermediate frequencies. The figure has been reprinted from publication of Griep et al. with permission from Springer Nature [113].

Also, based on the obtained bode plots (Figure 1.11B), they have done equivalent circuit modeling which is represented upper left corner in Figure 1.11B (phase plot), subsequently fitting the equivalent circuit modeling on impedance data using external program (EC-lab V10.02). They were able to analyze and quantified the TEER value of hCMEC/D3 in microfluidic model. However, they found that the electrode positions differed slightly between

batches during fabrication, which had an influence on the TEER value. Therefore, they recommended the use of sputter electrodes with a higher surface area in future designs. Griep et al. [113] used a two-electrode setup, while Van der Helm et al. [114] and Linz et al. [115] have employed a four-electrode setup for monitoring electrical barrier function. The advantage of using the four-electrode setup is that it can eliminate the electrode impedance, which is not a focus in monitoring barrier function. Van der Helm et al. fabricated thin metal layers on polycarbonate (PC) by sequentially depositing titanium, gold, and titanium using e-beam evaporation (Figure 1.12A). They then integrated four electrodes by bonding two of these films to the top PDMS channel and two to the bottom PDMS channel of an organ-on-chip device using silane chemistry.

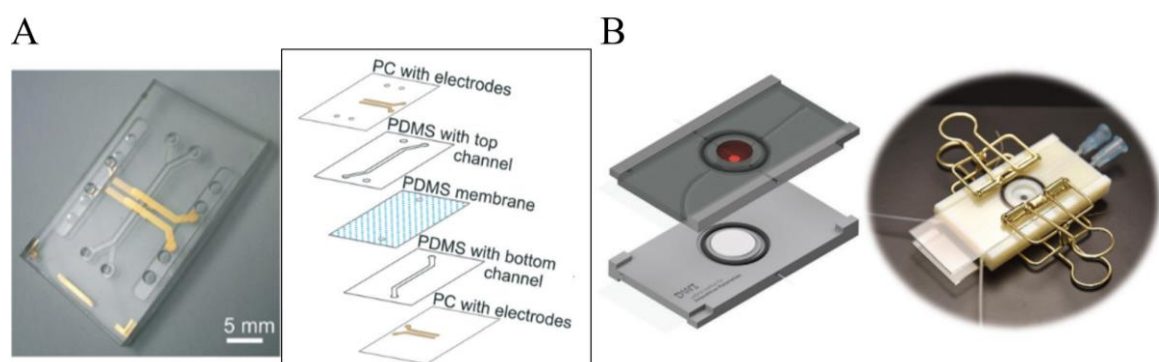


Figure 1.12. State-of-the-art of EIS system (2). (A) Gut-on-chip, as proposed by Van der Helm et al. is composed of PDMS top and bottom channels, a PDMS membrane where cells are cultured, and a polycarbonate films on which electrodes were deposited. The figure has been reprinted from Van der Helm et al. licensed under a Creative Commons Attribution Non-Commercial 3.0 Unported Licence [114]. (B) Linz et al. presented a 3D-printed bioreactor for organ-on-chip applications. A cell culture membrane is placed in between of 3D-printed two half cells, and the conductive glasses on below and upper chambers and inserted Pt electrodes in each half cells participate for EIS measurement. This figure has been reprinted of the work by Linz et al. and it is licensed under a Creative Commons Attribution-Non-Commercial License. Copyright belongs to the authors and Advanced Materials Technologies, published by Wiley-VCH GmbH [115].

The organ-on-chip device was used to culture Caco-2 cells under dynamic culture, and the barrier function and differentiation were demonstrated using EIS. EIS measurement was performed in galvanostatic mode by applying a constant AC current in the frequency range of 1 Hz to 100 kHz and measuring the potential difference using Autolab PGSTAT 204.

The impedance spectra graph indicated the detection of cell layer impedance between 100 Hz and 10 kHz. Furthermore, it was observed that the measurement of the electrical properties of

the cell layers remained unaffected by the double-layer capacitance with the use of a four-electrode setup. Using obtained data, they quantified the cell layer resistance and capacitance using mathematic equations. Additionally, Linz et al. [115] presented a 3D-printed micro-bioreactor (Figure 1.12B) that included electrodes, enabling the culture of epithelial cells, specifically Caco-2 cells, and online monitoring of cellular barrier function using EIS. Their 3D-printed bioreactor was composed of two identical half-cells with a 3 mm drilled area for cell culture. The cell membrane was placed between half-cells and the Pt wire electrodes are inserted in each half-cell. The indium tin oxide (ITO) glass of two half cells played a role of current injecting electrodes while the Pt wire electrodes served as a pick-up voltage during EIS.

The positioning of the electrodes was intended to minimize any phase shift between voltage and current that may result in measurement errors. They carried out EIS measurement in galvanostatic mode applying constant current of 10 μA at a frequency range 10 Hz to 30 kHz. The impedance data was fitted with the equivalent circuit using the fitting software Zview 2, resulting in the quantification of TEER and cell layer capacitance.

Carcopardo et al. [116] described the integration of an EIS system into a milli-fluidic double flow bioreactor, which is capable of real-time monitoring of the barrier functions of Caco-2 cells (Figure 1.13A). Their bioreactor is composed of a the apical and the basolateral chambers, separated by the cell culture membrane equipped in membrane holder. They intended to produce modular type of electrodes and has transparency for optical monitoring of cell culture area. Hence, electrodes were fabricated by dispensing a silver-enriched epoxy paste on a glass slide using a dispensing computer numerical control (CNC) machine. Two glass slides with Ag-printed electrodes were placed, one on the basolateral side of the chamber and the other on the apical side, creating four-electrode configuration. The EIS measurement performed both in low frequency 40 Hz to 1.04 kHz and high frequency ranges from 2 kHz to 100 kHz. To calculate the TEER, the impedance values within the range of 401.04 kHz were averaged, and the resulting average value was subtracted by the respective blank impedance value (without cells). This value was then normalized by the cell culture area.

In addition to the planar culture bioreactor, the hollow fiber bioreactor (HFBR) is widely used for culturing barrier tissues that can mimic the vascular system of various tissues and organs, such as the liver tissue [118-120], blood-brain barrier (BBB) [121,122] and renal tubule [123-127]. The hollow fiber bioreactor is composed of bundles of tubular, porous membranes made out of materials such as polypropylene, polysulfone, or polyethylene. Thus, bundles of hollow fibers

are housed within cylindrical housing creating HFBR. The bioreactor has inlet and outlet ports that are dedicated for the intracapillary (IC) space and extracapillary (EC) space in the HFBR.

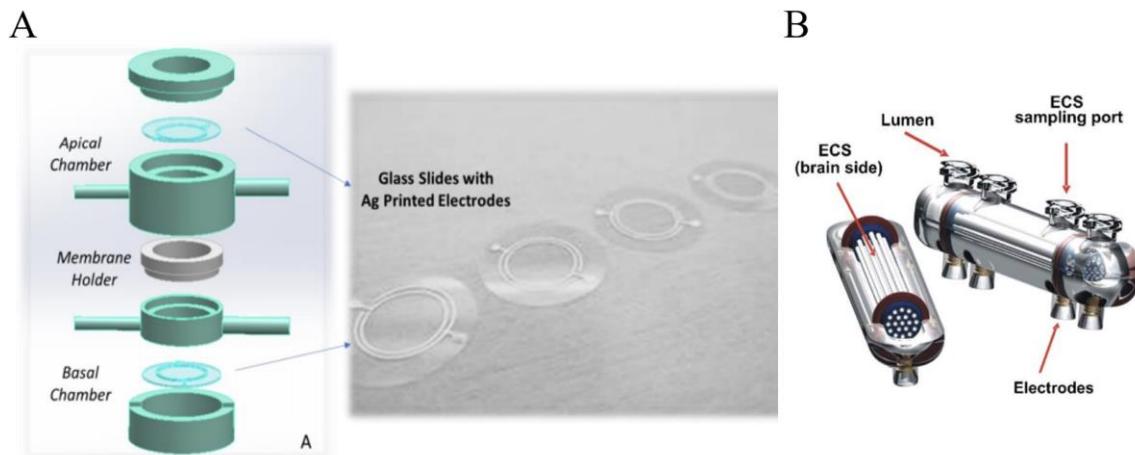


Figure 1.13. State-of-the-art of EIS system. (3). Perfusion bioreactors with module electrodes. (A) A dual flow membrane bioreactor presented by Carcopardo et al. The schematic view represents the components of the bioreactor, where the apical and basal chambers are separated by a membrane holder, and a glass slide with Ag-printed electrodes is assembled in each chamber. The figure has been reprinted from Carcopardo et al., Elsevier Publishers, with permission [116]. (B) DIV-BBB model proposed by Santaguida et al. A bundle of porous polypropylene hollow fibers is fixed inside the cartridge. Two extraluminal space (ECS) ports and two lumen ports for medium flow are located on the upper side, while four electrodes for TEER measurement are embedded on the lower side of the cartridge. This figure has been reprinted from Santaguida et al. with permission from the publisher Elsevier [117].

Due to their capillary structure with high surface area, hollow fiber reactors offer a great mass transfer rate, which is advantageous for the exchange of nutrients and gases compared to conventional tissue culture. Furthermore, perfusing medium culture or blood through EC space and IC space enable to mimic microenvironment of living tissue giving relative shear stress and pressure [128,129]. The use of commercially available HFBR is common, but they are designed as closed systems, so it is not possible to open for microscopic observation during cell culture. Thus, it is essential to have a non-invasive and real-time monitoring system to evaluate cell growth, function, and differentiation in a hollow fiber bioreactor during tissue culture. Resazurin assay is one of non-invasive methods to assess the cell viability using for hollow fiber bioreactor culture [130,131]. In principle, resazurin, which is initially blue and non-fluorescent, is reduced by the reducing agents produced during the metabolic processes of cells, resulting in the formation of the pink-colored and fluorescent dye called resorufin. Cell viability can be examined by measuring the fluorescence emitted by the dye.

However, substances used during cell treatment can disturb the redox reaction, potentially affecting the assay results [132]. Therefore, interpretation of the results should be done carefully. Santaguida et al. [117] demonstrated the barrier integrity of the BBB cultured in a commercially available HFBR from Flocel Inc (Figure 1.13B). The four embedded electrodes in the extra ports of the cartridge, apart from the fluid flow ports, to measure TEER. The excitation voltage of 0.06 V was applied through the excitation electrodes connected to the IC and EC spaces, and the resistivity and capacitance per cm^2 were obtained by a microcontroller. Although further details about electrode materials and frequency ranges were not described, the study shows the possibility of real-time monitoring of barrier integrity during HFBR culture. Subsequently, in 2013, their research group presented a TEER measurement study for a dynamic *in vitro* (DIV)-capillary-venule model using the same TEER measurement setup [133]. However, the commercially available bioreactor with embedded electrodes may increase costs, limiting practicality for parallel experiments or high-throughput screening.

Therefore, several crucial factors need to be carefully considered and designed to ensure the success of EIS measurements in a perfusion bioreactor system. These factors include aspects such as the number of electrodes, the positioning of electrodes within the bioreactor system, and the input parameters of EIS. Two- or four-electrodes setup has been commonly used for biological impedance measurement. A four-electrode setup has the advantage of eliminating the contribution of electrode impedance to the total impedance, thereby preventing influence of electrode impedance on the measurement of biological cell impedance. However, Grimmes and Martinsen [134] have been reported that four-electrode setup (tetrapolar electrode system) is possible to bring measurement errors because of several phenomenon such as negative sensitivity regions, separate current paths and common-mode signals. Furthermore, their findings showed that even dipolar electrode systems (two-electrode setup) exhibited higher sensitivity zone that contribute to total impedance, compared to four electrode system in their experimental design. Therefore, when the four-electrode setup is used, the electrode size and placement must be carefully considered. On the other hand, although the influence of electrode impedance cannot be neglected in measurements using a two-electrode system, it can be eliminated through equivalent circuit modeling at a later stage. Additionally, the use of two electrodes is cost-effective and less complicated for bioreactor designs compared to four-electrode systems. Whether electrodes can be positioned either within the perfusion bioreactor where cell cultures are present or in the tubing system outside of the bioreactor. Electrodes are often integrated into bioreactors to reduce noise during EIS measurements by bringing them in

close proximity to biological tissue. However, this integration can complicate the bioreactor design and fabrication process, and the size of the integrated electrodes may vary between batches, which could affect measurements. Furthermore, the integration can impede visual inspections of cell culture during bioreactor operation, especially if the bioreactor has transparency such as PDMS. Lastly, because the electrical properties of cells differ depending on the cell types, it is important to optimize input parameters such as frequency range and applied AC signal to obtain accurate and reliable measurements that are not harmful to biological cells.

1.5. Electrochemical Impedance Spectroscopy Niche for Hemofiltration

The utilization of a HFBR can be extended to medical devices, such as hemofilter. In order to accommodate the demanding high-volume molecular transfer necessary for effective medical treatment, the HFBR possesses a substantial surface area, achieved through the configuration of a bundle of hollow fibers. In this section, the utilization or necessity of EIS within the context of hemofiltration based on HFBR for monitoring purposes will be discussed. Hemofiltration is a form of renal replacement therapy (RRT) that can be used to treat acute kidney injury (AKI) or kidney failure (AKF) in patients. While hemofiltration will be the focus of this study, it should be noted that RRT also includes other treatments such as hemodialysis and hemodiafiltration. Hemofiltration uses a semi-permeable membrane filter to allow solutes and fluid from the blood to pass through by convection, whereas hemodialysis relies on diffusion. On the other hand, hemodiafiltration uses both convection and diffusion. During hemofiltration, the patient's blood is circulated through an extracorporeal circuit that incorporates a hemofilter (Figure 1.14). The blood exits the patient and enters the hemofilter, where waste products and excess fluid are removed via a semi-permeable membrane through convection. This process clears both small and large molecular weight waste products at similar rates [135,136]. The filtrate is discarded, and replacement fluid is infused into the filtered bloodstream before returning the blood to the patient. There are intermittent hemofiltration and continuous hemofiltration. Intermittent hemofiltration requires 3 h to 5 h per session, which is done several times per week, while continuous hemofiltration runs for 8 h to 12 h or more per treatment. Continuous hemofiltration is most commonly used in the intensive care unit [135,137,138]. There are several factors, such as filter clotting, blood line or sensor kinking, and hypotension, that can occur during hemofiltration and lead to treatment failure. If measures are not taken promptly, these factors can directly affect the patient's health. Among the factors, clotting is a

common factor that can arise within the hemofilter, typically on the fiber membranes and within the venous 'air-trap' chamber [139].

Clotting occurs when platelets become activated and trigger a cascade of coagulation events that result in the formation of a clot while circulating in the extracorporeal circuit [141,142]. Initial clotting is often induced at the entrance of the hemofilter, which can lead to further clotting and accumulation of debris and proteins on the filter fibers, resulting in the clogging of the filter membranes. Clotting and clogging of the fiber membranes, which is related to the filter's life time, can result in inefficient treatment.

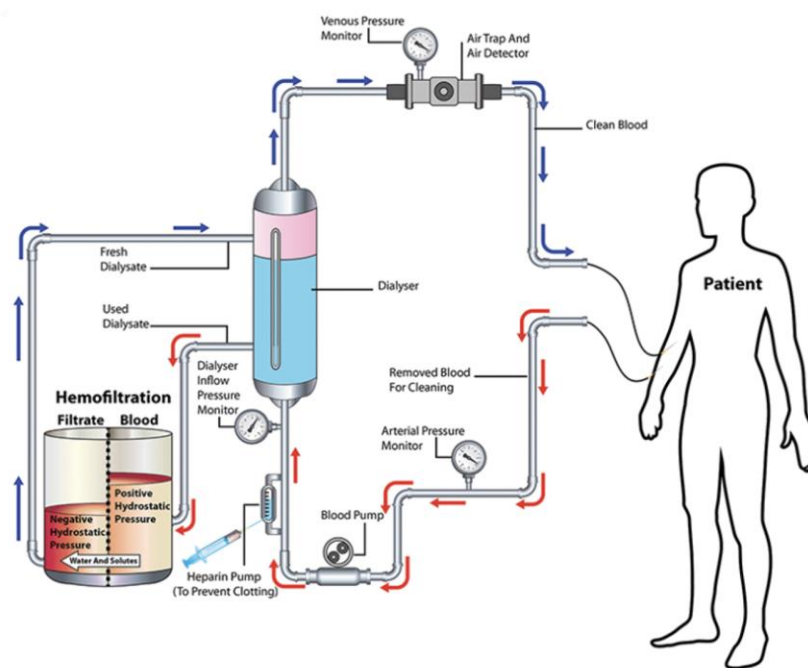


Figure 1.14. A schematic diagram of hemofiltration. The patient's blood is directed out of the body via a peristaltic pump and enters the extracorporeal circuit, where it passes through the hemofilter. Waste products and water are separated from the blood through the semi-permeable fibers in the hemofilter by convection. Fresh dialysate is infused back into the blood to maintain a consistent blood volume that is returned to the patient. This figure has been reprinted from Alhazmi et al. under the terms of the Creative Commons Attribution 3.0 License [140].

Clotting in the venous 'air-trap' chamber, where blood passes before returning to the patient, occurs due to the continuous blood oscillation generated by turbulent flow in the chamber. Consequently, the clotting causes resistance to blood flow, reducing the blood flow rate. Overall, the clotting and clogging in extracorporeal circuit increased circuit costs and overload of medical staff. Studies have been attempted to reduce clotting, such as adjusting the dose of

anticoagulation [143-147], predilution of the filter [148,149], and improving the filter membrane materials [150-152]. Furthermore, monitoring is also necessary to provide prompt feedback on the right moment when the filter becomes clogged. The hemofiltration system possesses a pressure monitoring function that measures arterial, venous, and effluent pressure during hemofiltration, displaying the readings that can be interpreted by medical staff. Moreover, an alarm is activated when the pressure readings exceed the input pressure limit, enabling the medical staff to take appropriate action. An increase in post-pump arterial pressure may indicate clotting problems in the hemofilter, whereas higher venous pressure denotes clotting at the venous drip chamber. Additionally, a negative effluent pressure may also indicate that the filtration is being driven by a pump instead of convection due to clotting or clogging in the hemofilter. Moreover, the transmembrane pressure (TMP) can be calculated using measured pressures (Equation 1.22), and it is commonly used as an indicator of clogging in hemofiltration [153].

$$TMP = \frac{Arterial P + Venous P}{2} - Effluent P \quad 1.22$$

However, these pressures are not definitive indicators of clotting or clogging on the fiber membranes in the hemofilter, as other phenomena can contribute to an increase in pressure [154]. For example, a kink, clamp, or occlusion in the arterial or venous line may increase post-pump arterial or venous pressure, respectively. Additionally, clotting in the venous catheter can also influence venous pressure. Consequently, there is a risk of taking action with a misinterpretation based on pressure values. Thus, an absolute indicator that monitors clotting or clogging of a hemofilter in real-time remains a niche area, enabling earlier detection of clotting or clogging in hemofiltration and facilitating correct actions. This not only contributes to beneficial cost efficiency by avoiding inappropriate interventions but also promotes optimal patient health outcomes.

1.6. Aim of Thesis

EIS is a cutting-edge technique that enables non-invasive monitoring of the electrical behaviors of biological cells and biomolecules within a perfusion bioreactor. Several attempts have been made to integrate electrodes into perfusion bioreactor systems for EIS measurements, but these electrodes are exclusively designed for a specific bioreactor. The aim of this thesis is to design and develop a versatile add-on electrode that can be seamlessly integrated into various types of perfusion bioreactors and medical devices, thereby simplifying the fabrication process and reducing design complexity. Additionally, using the electrode system, the objective is to enable the evaluation of barrier cell integrity in two different types of perfusion bioreactors and the monitoring of clotting or clogging phenomena in biomedical devices during hemofiltration. The research objectives are specifically designed to achieve the aims outlined in this thesis.

To fabricate electrode material. The electrode material is considered a critical factor that brings stable and accurate results in electrical measurement. Furthermore, it must be biocompatible due to its direct contact with the cell culture environment. A TiN coating will be fabricated using the PVD method previously optimized by Schmitz et al. [86]. Also, various electrode substrates with different materials will be compared to optimize the electrode. In addition to the analysis of surface chemistry and structure, the double-layer capacity, a reflection of the electrical impedance of the TiN coating, will be compared across various electrode substrates.

To find optimum design for producing add-on types electrodes. To achieve versatile applications of electrodes in a perfusion bioreactor system, various electrode designs will be attempted during the production process. PDMS casting and 3D printing techniques support modifying the structure to find an optimum design of add-on type electrodes. The electrode structure will undergo characterization by subjecting it to varying flow rates. This characterization aims to evaluate the extent to which the structure is prone to leakage under conditions of fluid flow. By means of this evaluation, the objective is to further refine and enhance the electrode design to achieve optimal functionality.

To explore how influential parameters of a fluidic culture system impact electrochemical impedance spectroscopy. Before integrating electrodes into perfusion bioreactors, electrode system was examined as varying influential parameters of a fluidic culture system using EIS. This step aims to analyze the impedance response of the electrode system across a broad frequency range (1 Hz to 100 kHz) under various parameters such as temperature, flow rate,

and other controlled factors during dynamic flow culture. The objective is to determine how each parameter influences EIS results across the frequency range.

To test applicability of a non-invasive monitoring system in perfusion bioreactor systems.

This step involves optimizing the overall bioreactor setup, while considering the number and placement of electrodes. Additionally, it includes conducting EIS online monitoring under dynamic flow conditions. The impedance data obtained through online monitoring is subsequently analyzed and quantified to assess cell barrier integrity using equivalent circuit fitting and simulation. This evaluation will cover essential indicators, including tight junction resistance and cell membrane capacitance. In detail, the first application is implementing the electrodes on a novel chip bioreactor designed by Dr. Tobias Schmitz, and aims to verify online monitoring of cellular barrier integrity during long-term dynamic flow culture. The transwell-based human induced pluripotent stem cells (hiPSC)-BBB *in vitro* model established by Appelt-Menzel et al. [155] will be adapted to dynamic flow bioreactor culture. The second application is to set the electrodes in a miniature HFBR to examine the effectiveness of implemented non-invasive monitoring system in monitoring cell barrier integrity. Cell lines, such as HUVECs or Caco-2, will be cultured within the HFBR system for the test.

To test of applicability a non-invasive monitoring system into hemofiltration. The testing of the electrodes will be expanded to a medical device operated using a HFBR. This expansion will aim to assess the hypothesis that impedance spectroscopy can reliably detect instances of hemofilter clogging. The number of participating electrodes will be adjusted based on the specific measurement focus within the system, including impedance across the fiber, blood impedance, and effluent impedance. The focus of the study is to develop a method for interpreting the EIS data that reflects the hemofiltration system across a wide range of frequencies. This interpretation aims to establish a connection with phenomena related to hemofiltration, such as clogging in the hemofilter.

2. Materials

Table 2.1. Chemicals

Chemicals	Company
Antibody Diluent, AL120R500	DCS Innovative Diagnostik-Systeme GmbH & Co. KG (Hamburg, Germany)
B27 supplement	Life Technologies (Darmstadt, Germany)
Citric acid	Sigma Aldrich
Clear resin (FLGPCL02)	Formlabs (Berlin, Germany)
Collagen-1(rat tail)	TERM Wuerzburg
Dental SG (FLDGOR01)	Formlabs (Berlin, Germany)
Dental Model (FLDMB01)	Formlabs (Berlin, Germany)
Dimethyl sulfoxide (DMSO)	Sigma-Aldrich GmbH (Taufkirchen, Germany)
Donkey serum, 31965080	Life Technologies GmbH (Darmstadt, Germany)
Dublisil® 15	Dentalversender(Cologne, Germany)
Dulbecco's Modified Eagle Medium (DMEM) (high glucose, Hepes)	Gibco/life Technologies GmbH (Darmstadt, Germany)
Endothelial Cell Growth Medim (CatC-22215), Supplements (CatC-39210)	Promo Cell (Heidelberg, Germany)
Ethanol 96 %, denatured	Carl Roth GmbH & Co. KG (Karlsruhe, Germany)
Fetal calf serum (FCS), FCS.ADD.0500	Bio & Sell e.K. (Feucht, Germany)
Fluoromount-G DAPI™	Life Technologies GmbH (Darmstadt, Germany)
human basic fibroblast growth factor (hbFGF, 100-18B)	PeproTech (Cranbury, NJ, USA)
Human Endothelial SFM [+] L-Glutamine	Gibco/Thermofisher
Human plasma fibronectin (F0895-1MG)	Sigma-Aldrich GmbH (Taufkirchen, Germany)
hydrogen peroxide 200 (1561563)	Fisher scientific UK
Isopropanol	Carl Roth GmbH (Kalsruhe, Germany)
Leit-C	Plano GmbH (Wetzlar, Germany)
Nacl 0.9 % 182778001	B.Braun (Melsungen, Germany)
Non-Essential Amino Acid (NEAA)	Gibco/life Technologies GmbH (Darmstadt, Germany)

Penicillin/Streptomycin	Sigma-Aldrich Chemie GmbH (Taufkirchen, Germany)
Phosphate buffered saline (PBS without Mg ²⁺ and Ca ²⁺) (PBS ⁻)	Sigma-Aldrich Chemie GmbH (Taufkirchen, Germany)
Retinoic acid	Sigma-Aldrich GmbH (Taufkirchen, Germany)
Roti [®] Histofix, 4 % Paraformaldehyde	Carl Roth GmbH & Co. KG (Karlsruhe, Germany)
Sodium pyruvate	Life Technologies (Darmstadt, Germany)
Sylgard [®] 184 silicone, DOWSIL [™]	DowDuPont, Inc. (Wilmington, Delaware, US)
Triton [™] X-100, BioUltra	Sigma-Aldrich Chemie GmbH (Taufkirchen, Germany)
Trypan blue solution, 0.4 %	Sigma-Aldrich GmbH (Taufkirchen, Germany)
Trypsin 0.5 % 10 ×, 15400-054	Invitrogen GmbH (Darmstadt, Germany)
Tween [®] 20, viscous liquid	Sigma-Aldrich GmbH (Taufkirchen, Germany)
Vasculife EnGS-Mv Endothelial Medium Complete Kit (LS-1035)	Cellsystems (Troisdorf, Germany)

Table 2.2. Laboratory devices

Laboratory devices	Company
Aspiration Device Vacusafe	Integra Biosciences GmbH (Fernwald, Germany)
Autoclave DX-45 Bench-top Technoclav	Systec GmbH (Wettenberg, Germany)
Autoclave Steam sterilizer (Varioklav)	HP Medizintechnik GmbH (Oberschleissheim, Germany)
Autoclave Technoclav	Biomedis Laborservice GmbH (Giessen, Germany)
Autolab, Impedance spectroscopy (PGSTAT 204)	Metrohm Autolab, Utrecht, Netherland
Centrifuge Heraeus Multifuge X1R	Thermo Fisher Scientific GmbH (Dreieich, Germany)
Centrifuge Micro SD 220 V AC	Carl Roth GmbH & Co. KG (Karlsruhe, Germany)
Cold storage room 4 °C	Genheimer KKT GmbH (Hoechberg, Germany)
Confocal-microscope TSC SP8	Leica Microsystems (Wetzlar, Germany)
Form 2	Formlabs GmbH (Berlin, Germany)
FormWash device	Formlabs GmbH (Berlin, Germany)

Freezer Comfort, 513 l, -20 °C	Liebherr-International Deutschland GmbH, (Biberach an der Riss, Germany)
Freezer TS Series TS 588e, -80 °C	Thermo Fisher Scientific GmbH (Dreieich, Germany)
Freezing container Mr. Frosty	VWR International GmbH (Darmstadt, Germany)
Hot plate 062	Labotect (Göttingen, Germany)
Ice machine AF-80	Scotsman Ice Systems Frimont S.P.A. (Milan, Italy)
Incubator Heraeus BBD 6220 37 °C, 5 %	Thermo Fisher Scientific GmbH (Dreieich, Germany)
Inverse Fluorescence Microscope BZ-9000	Keyence Deutschland GmbH (Neu- Isenburg, Germany)
Laminar flow hood safe 2020 1.8	Thermo Fisher Scientific GmbH (Dreieich, Germany)
Liquid nitrogen storage tank	German-cryo® (Juechen, Germany)
Microscope EVOS® XL Core	Thermo Fisher Scientific GmbH (Dreieich, Germany)
Oven	Thermo Fisher Scientific GmbH (Dreieich, Germany)
Plasma chamber Pico LF PC 115656	Diener Electronics (Ebhausen, Germany)
Sputter coater	Leica Microsystem (Wetzlar, Germany)
SEM microscope DSM 940	Zeiss (Oberkochen, Germany)
Ultrasonic bath	Branson Ultraschall Nierlassung der EMERSON Technologies GmbH & Co. KG (Dietzenbach, Germany)
Water bath	Memmert GmbH & Co. KG (Schwabach, Germany)
Water purification system Milli-Q Advantage A10	Millipore GmbH (Schwalbach, Germany)

Table 2.3. Disposable materials

Disposable materials	Company
Aluminum Foil	Carl Roth GmbH & Co. KG (Karlsruhe, Germany)
Autoclave bag	A. Hartenstein GmbH (Wuerzburg, Germany)
Black PVC EHT cable, Ø 5.2 mm, 7/0.3 mm strands	RS Components GmbH (Frankfurt am main, Germany)
BRAND plates for 24 well plate (1478060)	Omnilab (Bremen, Germany)

Centrifuge tubes Cellstar® Blue Cap, 15 mL, 50 mL	Greiner Bio-One GmbH (Frickenhausen, Germany)
Cover slips for object slides, 24×60 mm	Gerhard Menzel Glasbearbeitungswerk GmbH & Co. KG (Braunschweig, Germany)
CryoTubes® 1.8 mL	Nunc® GmbH & Co. KG (Wiesbaden, Germany)
Disposable pipettes, 5 mL, 10 mL, 25 mL, 50 mL	Greiner Bio-One GmbH (Frickenhausen, Germany)
Econ connect KS4 Bananenstecker Stift-Ø: 4 mm Metall 1 St.	Conrad Electronic (Hirschau, Germany)
Flexible silicone tubing (ID: 3.2 mm, OD: 6.2 mm)	Saint-Gobain Performance Plastics (Charny, France)
Lamellenstecker Stecker, Einbau vertikal Stift-Ø: 4 mm	Conrad Electronic (Hirschau, Germany)
Luerlock connectors, various shapes and sizes	Mednet GmbH (Münster, Germany)
Microscopic slides 76×26×1 mm, uncoated	Gerhard Menzel Glasbearbeitungswerk GmbH & Co. KG (Braunschweig, Germany)
Microscopic slides Polysine™	R. Langenbrinck (Emmendingen, Germany)
Microscopic slides Super Frost® Plus Object slides	R. Langenbrinck (Emmendingen, Germany)
Millicell culture inserts, 0.4 µm PCF, 12 mm diameter	Merck Millipore Ltd. (Darmstadt, Germany)
Minisart® single-use filter unit	Sartorius (Goettingen, Germany)
Parafilm laboratory film Parafilm®M	Carl Roth GmbH & Co. KG (Karlsruhe, Germany)
Parafilm® M	Carl Roth GmbH (Karlsruhe, Germany)
Pasteur pipettes, glass, 120 mm, 2 mL	Brand GmbH & Co. KG (Wertheim, Germany)
Peristaltic pump tubing	IDEX Health& Science (Wertheim, Germany)
Petri dishes, plastic, various sizes	Greiner Bio-One GmbH (Frickenhausen, Germany)
Pipette tips 0.5 µl – 10 µl, 10 µl –100 µl, 100 µl – 1000 µl	Greiner Bio-One GmbH (Frickenhausen, Germany)
SiC wet sandpaper	Schmitz-Metallographie GmbH, (Herzogenrath, Germany)
Stainless steel tube (4249598)	Gust. Alberts GmbH&Co. KG (Herscheid, Germany)
Steel Slotted Hex Bolt Drive, 7 – 9 mm inside diameter (27428912)	RS components (Frankfurt am main, Germany)
Test lead connectors socket diameter 4 mm	Voltcraft (Hirsau, Germany)
Tissue culture flasks, growth area 175 cm (T175)	Greiner Bio-One GmbH (Frickenhausen, Germany)

Tissue culture flasks, growth area 75 cm (T75) 90076, 150 cm 90151 (T150)	TPP Techno Plastic Products AG (Trasadingen, Switzerland)
Tissue culture plates 6 well, 24 well	TPP Techno Plastic Products AG (Trasadingen, Switzerland)
Unique-Mem® Track-Etched Membrane (A4 sheets, 210401U4)	Oxyphen (Lottstetten, Germany)

Table 2.4. Laboratory equipment

Laboratory equipment	Company
Centrifuge tube racks, various sizes	NeoLab Migge GmbH (Heidelberg, Germany)
Eppendorf pipettors, Research plus, 0.5 µl – 10 µl, 10 µl – 100 µl, 100 µl – 1,000 µl	Eppendorf AG (Hamburg, Germany)
Fine tweezers	Fine Science Tools GmbH (Heidelberg, Germany)
Forceps, various sizes	Karl Hecht GmbH & Co KG (Sondheim, Germany)
Glass cutter (diamond)	A. Hartenstein GmbH (Wuerzburg, Germany)
Laboratory glass bottles Duran® with thread, various sizes	Schott AG (Mainz, Germany)
Neubauer cell counting chamber, depth 0.1 mm, area 0.0025 mm ²	A. Hartenstein GmbH (Wuerzburg, Germany)
Pipettor accu-jet® pro	Brand GmbH & Co. KG (Wertheim, Germany)
Scalpel blade handles, stainless steel	C. Bruno Bayha GmbH (Tuttlingen, Germany)
3M™ MicroPES® TF10 (Polyethersulfon) 3M™ Plasmaphan® P1 LX (Polypropylen)	3M science. Applied to life.™ (Wuppertal, Germany)
FX80 dialyzer (Fresenius Helixone® High Flux, ref.5008881)	Fresenius Medical Care (Bad Homburg, Germany)

Table 2.5. Software

Software name	Version	Company
BZ-9000/-II Analyzer		Keyence Deutschland GmbH (Neu-Isenburg, Germany)
ImageJ/Fiji	Java 1.8.0_172[64-bit]	Rasband, W.S., ImageJ, U. S. National Institutes of Health, Bethesda, Maryland, USA, https://imagej.nih.gov/ij/ , 1997-2018.
Microsoft office (Excel, Word, PowerPoint)	2019	Microsoft Corporation (Redmond, WA, USA)
Nova	Nova 2.1.4	Metrohm Autolab B.V. (Utrecht, Netherlands)

Origin	OriginPro 2021b (64-bit) SR2	1991-2021 OriginLab Corporation
Photo View 360 for Solid- Works		Dassault Systèmes SolidWorks Corporation (Waltham, MA, USA)
PreForm	PreForm 3.15.0	2012-2021 Form labs inc.
SolidWorks	Education Edition 2017 SP5.0	Dassault Systèmes SolidWorks Corporation (Vélizy-Villacoublay, France)

Table 2.6. List of Cells

Cells	Source
Caco-2 (ACC 169)	DSMZ, Braunschweig
Human Induced pluripotent stem (IPSC(IMR-90-4)-4-DL-01)	WiCell, USA
Human Umbilical Vein Endothelial Cells	Lonza Cologne GmbH, Koeln
Human Umbilical Vein Endothelial Cells (FC-0003)	Lifeline Cell Technology

Table 2.7. Caco-2 and BCECs culture media and supplements

Cell culture media	Composition
Caco-2 culture media (Transwell and bioreactor culture)	DMEM [+] high glucose, [+] hepes (500 mL)
	10 % FCS
	1 % NEAA
	1 % Sodium-pyruvate
BCECs culture media (Transwell and bioreactor culture)	Human Endothelial SFM [+] L-Glutamine (500 mL)
	1:200 B27 supplement

Table 2.8. HUVECs culture media and supplements

Cell culture media	Composition
HUVECs culture media (Transwell culture)	VascuLife Basal Medium (500 mL)
	50 µg/mL Ascorbic Acid LifeFactor (0.5 mL)
	10 mM L-Glutamine LifeFactor (25 mL)
	5 ng/mL rh EGF LifeFactor (0.5 mL)
	0.2 % rh EnGS LifeFactor (1 mL)
	5 % FBS LifeFactor (25 mL)
HUVECs culture media (Bioreactor culture)	Endothelial cell Basal Medium (500 mL)
	Fetal Calf Serum (0.02 mL/mL)
	Endothelial Cell Growth Supplement (0.004 mL/mL)
	Epidermal Growth Factor (0.1 ng/mL)
	Basic Fibroblast Growth Factor (1 ng/mL)
	Heparin (90 µg/mL)
	Hydrocortisone (1 µg/mL)

Table 2.9. ECM coating solution

ECM coating solution	Final concentration	Composition
Fibronectin	10 µg/mL	1 mg/mL Human plasma fibronectin
		DMEM
Collagen	100 µg/mL	Collagen I coating solution (rat tail)
		0.1 % acetic acid

3. Methods

3.1. Electrode Fabrication

3.1.1. Substrate Preparation for Physical Vapor Deposition

In the process of electrode fabrication, multiple electrodes were manufactured to explore an optimal electrode design suitable for use within a dynamic fluidic system. A range of substrates, characterized by distinct shapes, sizes, and materials, were employed in the fabrication of the electrodes. These substrates included Luer lock connectors, stainless-steel (SS) mesh, glass plates, and SS tubes. No size modification was necessary for the other substrates before TiN coating, except for the SS tubes. With the use of a saw, the length of the SS tube, having an outer diameter (OD) of 8 mm and an inner diameter (ID) of 6 mm, was subsequently adjusted to 15 mm. Afterwards, the cut surface was polished using ascending grits of polishing paper, starting from number 8 and progressing up to number 4000. All substrates were ready by washing with isopropanol and placing them in holders. These holders, along with the substrates, were then positioned within a custom-made vacuum chamber designed for PVD coating.

3.1.2. Physical Vapor Deposition

The custom-made vacuum chamber consisted of an RF generator and a titanium target (with a height of 10 mm and a diameter of 120 mm). First, the chamber was evacuated to achieve a pressure of 5×10^{-7} mbar. Second, the mixture of argon (Ar) and nitrogen (N₂) gas were filled in vacuum chamber under pressure set 4.0×10^{-3} mbar. The magnet sputtering was processed with 800 W generated by a 13.56 MHz RF generator for 3 min and with 500 W for 60 min sequentially. The TiN coating process was performed by Dr. Tobias Schmitz, employing an optimized method outlined in a previous study by Schmitz et al. [86].

3.1.3. Design of Modular Electrode Models

The TiN-coated electrodes with different substrates were combined with silicone tubes in unique ways, enabling easy assembly with a tubing system. This structure is referred to as the core structure, which was then covered with a PDMS shell using a PDMS casting method.

3.1.3.1. Different Design of Electrode

The following paragraph provides a detailed description of the geometry and the specific fabrication process for the core structure of different electrodes, as well as the geometry of the PDMS shell. The PDMS casting method for the PDMS shell will be further described in the

following section 3.1.3.2. The Luer lock connector used for tubing connections does not require a PDMS housing. It can be directly used without any additional modifications.

TiN-Coated Stainless Steel Mesh Electrode

TiN-coated SS meshes were cut in in rectangular 5 mm wide and 25 mm long using scissors. Also, the silicone tube was cut perpendicular to its axis for electrode insertion, but not all the way through. Then the cut meshes were inserted, covering the cut cross-sectional area of the tube, and the outer parts were glued with PDMS. Thus, the core structure was covered by a cylindrical-shaped PDMS shell that was 13 mm wide and 23 mm in length using the PDMS casting method as described in the following section 3.1.3.2, except for some parts of the meshes electrode that were left uncovered for electrical connection with external devices (Figure 3.1A).

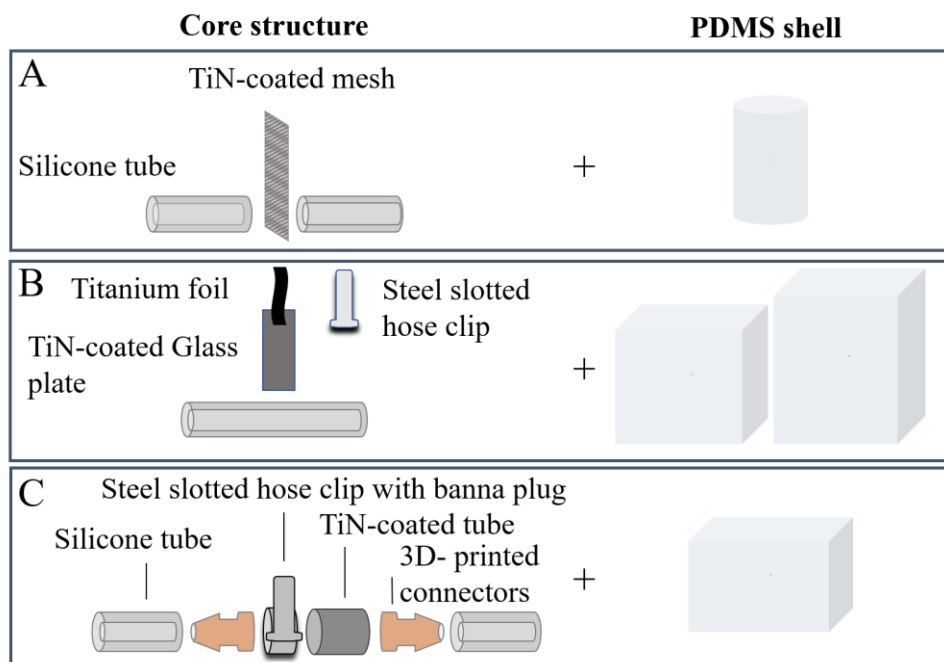


Figure 3.1. Graphical illustration of various designs of TiN-coated electrodes. (A) TiN-coated SS mesh electrode, (B) TiN-coated glass plate electrode, and (C) TiN-coated SS tube electrode. The core structure's components were assembled, and the assembly was housed by PDMS.

TiN-Coated Glass Electrode

TiN-coated glass plates were cut in rectangular 5 mm wide and 25 mm long using glass diamond cutter. Similar to the TiN-coated mesh electrode, the silicone tube was cut to insert the TiN-coated glass plate electrode, but this time the glass plate was placed attached to the

wall. The cut parts were glued with Biopor AB Xtreme silicone. Additionally, titanium foil was glued to glass plate using Leit-C plast for electrical connection. The glass plate electrode ultimately had two PDMS shells that were rectangular in shape. The inner shell measured 30 mm in height, 15 mm in length, and 30 mm in width, while the outer shell measured 50 mm in height, 28 mm in length, and 30 mm in width (Figure 3.1B).

TiN-coated SS Tube electrode

TiN-coated SS tube electrodes, length with 15 mm and 6 mm in diameter, were connected to a silicone tube using 3D-printed Luer lock connectors. This is for eliminating the need to cut the silicone tube in order to insert the electrodes, as required with TiN-coated SS mesh and glass plate electrodes. The Luer lock connectors for 3D printing were designed utilizing SOLIDWORKS™ Premium 2017 software. The process began with sketching 2D drawings on a plane, followed by the creation of 3D features mainly using revolved boss/base and fillet functions. Dr. Tobias Schmitz performed the 3D design. The design of 3D-printed Luer lock connectors has the exact same geometry as 30 mm diameter commercial Luer lock connectors. Thus, completed 3D design was imported into the Preform software for SLA 3D printing.

Table 3.1. Post processing of Dental SG resin

Steps	Conditions	Time (min)
Washing	Solution: Isopropanol	5 min
Curing	Temperature: 60 °C	30 min

Since the culture medium passes through the 3D-printed Luer lock connectors in bioreactor culture, the Dental SG resin (FLDGOR01), which is autoclavable and biocompatible, was chosen as the material, and the layer thickness was set to 0.5 mm. After completing the 3D print, the printed parts underwent post-processing, including washing and curing steps, for further hardening. The details of post-processing for Dental SG resin (FLDGOR01) are provided in Table 3.1. Also, a banana plug was attached to the electrode using a steel slotted hose clip on the outer surface for electrical connection. The core structure was housed in a PDMS shell that had a height, length, and width of 25 mm, 25 mm, and 30 mm, respectively (Figure 3.1C).

3.1.3.2. Polydimethylsiloxane Casting

The Figure 3.2 shows a general overview of the steps involved in the PDMS casting method. The positive mold was produced by 3D printing technique. The positive mold design was created using SOLIDWORKS™ Premium 2017 software, incorporating specific geometries for the electrodes as mentioned in the previous section 3.1.3.1. Briefly, for the 3D design of the positive mold for the mesh electrodes, a 2D sketch of a circle was created, and a 3D feature was formed using the extrude function. Afterward, a hole was created in the center of the cylindrical configuration using the extruded cut function, allowing for the secure placement of the core structure within the 3D feature. Unlike the cylindrical shape used for the positive mold of mesh electrodes, a rectangular column was designed for the positive mold for the glass plate and tube electrode. For 3D design, a square shape was drawn using a 2D sketch, and a 3D feature was created using the extrude function. A hole was formed using the extrude cut function. The designs were subsequently exported to the Preform software program for SLA 3D printing. Dental Model resin (FLDMB01) was used for the printing, and the layer thickness was set to 0.5 mm. After completing the 3D printing, the 3D-printed part underwent post-processing steps such as washing and curing step. The detailed parameters for washing and curing, especially for Dental Model resin (FLDMB01), are presented in the Table 3.2. After ready the 3D-printed positive mold, the PDMS casting was performed (Figure 3.2). The 3D- printed positive mold, prepared as described, was first placed inside a container, and then a mixture of the DUBLISIL®15 duplicating silicone rubber, which consists of resin and hardener in a 1:1 ratio, was poured into the container.

Table 3.2. Post processing of Dental Model resin

Steps	Conditions	Time (min)
Washing	Solution: Isopropanol	10 min
Curing	Temperature: 60 °C	30 min

After the mixture was left to cure and harden for 30 min at room temperature, the silicone negative mold was detached from the container and positive mold. To prevent bonding with PDMS in the next steps, the surface of the silicone negative mold required an oxygen plasma treatment for surface deactivation. The oxygen plasma treatment was performed using 500 W RF for 2 min with an oxygen pressure of 0.3 mbar in plasma vacuum chamber.

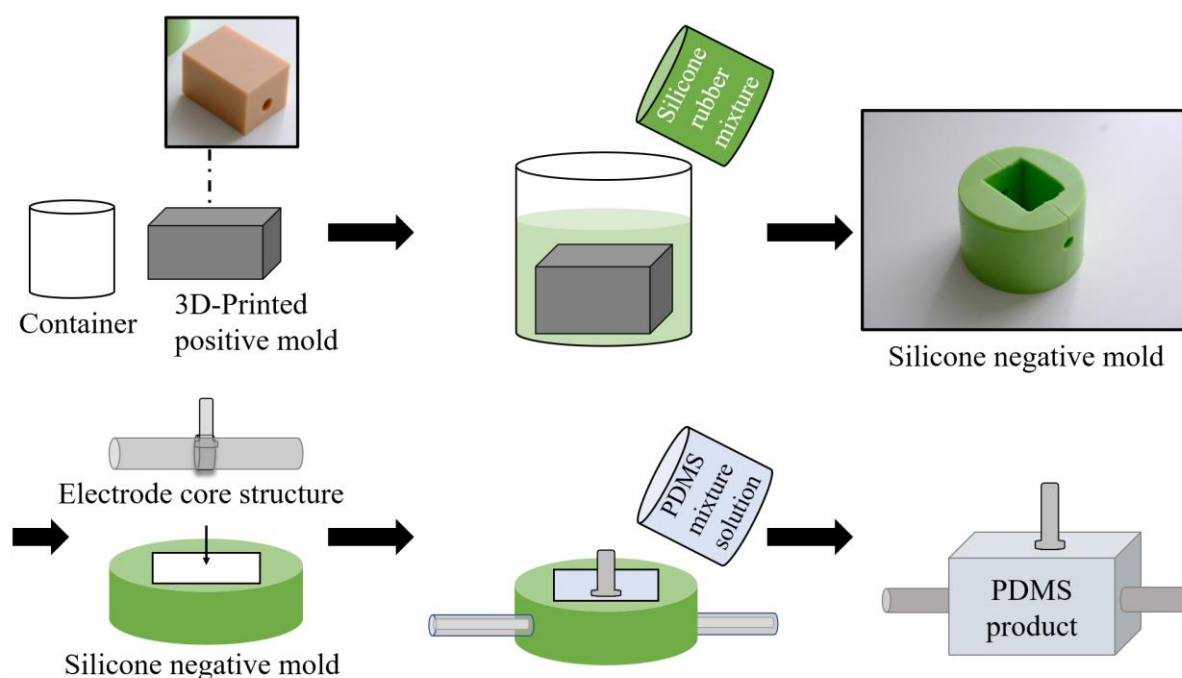


Figure 3.2. PDMS casting steps for add-on electrodes. This specific figure illustrates the TiN-coated tube electrode process. The fabrication of various substrate electrodes also involves the PDMS casting step with their respective designs. The 3D-printed positive mold, which has the same design as the desired product, is placed in a container for primary molding. Next, the silicone rubber mixture was poured into the container and allowed to harden, creating a negative silicone mold. In the following steps, the electrode core structure (Figure 3.1) is assembled within silicone negative mold. The PDMS mixture solution was added to the mold cavity of the negative mold and left to cure. This resulted in the final PDMS product after undergoing a second hardening process.

Meanwhile, a PDMS mixture solution was prepared by mixing the pre-polymer and cross-linker components of PDMS polymer (Sylgard[®] 184) in a ratio of 10:1, and any gas bubbles generated during mixing were removed under vacuum conditions. Each core structure of electrodes was placed inside the mold cavity of the negative mold, and the PDMS mixture solution was poured into the mold cavity and primary cured at 55 °C for 3 h in an oven. The completed electrodes were detached from the negative mold and underwent heat treatment at 80 °C for 1 h.

3.2. Electrode Characterization

3.2.1. Scanning Electron Microscope

SEM was carried out to examine the surface topography of TiN coatings on substrates (SS meshes, glass plates, and SS tubes) with high resolution. Each sample was cut into small

pieces to fit onto the SEM specimen stub, and then washed with acetone and dried with compressed air. Before SEM imaging, a 4 nm thick platinum coating was applied to the samples using a sputter coater for higher quality of SEM images. Finally, the surface topography of the TiN-coated SS meshes, glass plates, and SS tube electrodes was captured using SEM (Zeiss DSM 940).

3.2.2. Electrical Double Layer Characterization of Electrodes

Using EIS, the electrical double layer characteristics of different substrate electrodes, including TiN-coated SS mesh, glass slides, and SS tubes, were compared.

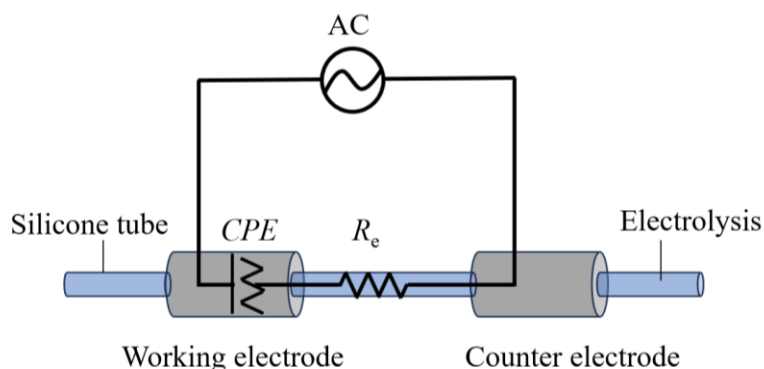


Figure 3.3. The electrode system setup for electrical double layer characterization. The equivalent circuit, representing the electrode system, is depicted. In this circuit, a resistor (R_e) represents the electrolyte, and a constant phase element (CPE) represents for both electrodes, which are connected in series.

Figure 3.3 represents the electrochemical cell for electrical double layer characterization, and depicts the equivalent circuit. Two electrodes of each substrate were connected using silicone tubes and Luer lock connectors. The distance between the two electrodes was 30 mm, and they were filled with phosphate-buffered saline without calcium and magnesium (PBS^-) electrolytes. Impedance measurement was performed by applying sinusoidal AC signal with $0.2 V_{RMS}$ in a frequency range of 1 Hz to 100 kHz using electrochemical impedance analyzer (Autolab PGSTAT 204), and the results were displayed in Nova 2.1.4 software. The temperature was sustained at room temperature ($20\text{ }^\circ\text{C}$) during impedance measurement. Afterward, obtained EIS data were fitted in an equivalent circuit model composed of a series-connected resistor (R_e) and constant phase element (CPE) using the Nova 2.1.4 software program to quantify electrical parameters (Figure 3.3). The impedance of electrolyte and electrodes were represented by R_e and CPE in equivalent circuit respectively.

3.2.3. Impedance Spectroscopy for Investigating the Impact Parameters

Before applying TiN-coated tube electrodes to a dynamic fluidic system, the electrochemical characterization of the electrode system was evaluated by testing various parameters that could influence impedance spectroscopy measurements. The electrical characterization was performed by varying four different parameters; distance between two electrodes, temperature, flow rate, and electrolyte concentration. The basic experimental setup was that two electrodes were connected at particular distances and filled with electrolytes. To check the effect of varying distance between two electrodes on impedance spectroscopy, the distances set with 30, 60, 100, 150, and 200 mm for testing. Furthermore, two different temperature 20 °C (room temperature) and 37 °C (optimal culture of human cells) were tested with 60 mm distance electrodes. To carry on the test about the effects of flow rate, a 60 mm distance between two electrodes was connected to a peristaltic pump. Impedance measurements were then performed at differing flow rates of 0, 7, 5, 140, and 280 mL/min. Finally, different electrolyte concentrations; 20, 40, 60, 80, and 100 % of PBS⁻ were diluted with distilled water. The different concentrations of PBS⁻ were filled in 60 mm distance electrodes connected tube for impedance spectroscopy. AC signal with 0.2 V_{RMS} were applied in frequency range of 1 Hz to 100 kHz for impedance measurement.

3.3. Electrode Application 1: Chip Bioreactor

The TiN-coated tube electrodes were applied to two different types of perfusion bioreactor systems and a medical device to assess their versatility. This section presents the initial application of electrodes to a custom-made chip bioreactor, originally designed by Dr. Tobias Schmitz, with subsequent applications described in sections 3.4 and 3.5.

3.3.1. Chip Bioreactor Preparation

A chip bioreactor is primarily composed of two PDMS chambers and 3D-printed culture membrane frames. These main components are securely assembled using 3D-printed bioreactor clamps. Additionally, several pieces of equipment, such as bioreactor stands and a bottle holder, are used to support the operation of the bioreactor system. In this section, the preparation of these essential components of the bioreactor will be discussed.

3.3.1.1. Polydimethylsiloxane Chambers

The bioreactor chamber was made out of PDMS, and accordingly, the fabrication of PDMS chambers was based on polymer casting method developed by Dr. Tobias Schmitz. First, the body and head parts of each chamber design drawn using SOLIDWORKS™ Premium 2017

software program was imported to Preform software for 3D printing. The printing material is set as Dental Model resin (FLDMB01), and subsequently, the parts were 3D-printed using an SLA 3D printer (Form 2, Formlab GmbH, Germany). Afterward, the 3D printed-parts were through post-processing steps according to Table 3.2. The PDMS casting for the chip bioreactor has been described in a previous publication by Choi et al. [156]. Briefly, the 3D-printed parts were placed in containers, forming the mold cavity to produce negative molds. The duplicating silicon rubber (DUBLISIL[®]15, Dentalversender, Germany) was used for negative molds, and the resin and hardener of dublil[®]15 were mixed in a ratio of 1:1 and poured into container. The rubber mixture was placed for 30 min in room temperature for hardening. The negative molds were separated from 3D-printed parts and container, and underwent an oxygen plasma treatment for surface deactivation. The plasma chamber evacuated; the oxygen gas filed up to 0.3 mbar with a flow rate 12 sccm. Once the chamber pressure became stable at 0.3 mbar, 500 W RF was operated for 2 min causing oxygen plasma. Finally, the negative molds were ready for fabrication of PDMS chambers. The pre-polymer and cross linker of PDMS polymer (Sylgard[®] 184, Dow Corning, Germany) were mixed in ratio 10:1. Before pour PDMS polymer mixture into negative molds, the air bubbles generated during mixing were removed with a vacuum chamber. Prepared some PDMS polymer was transferred to 50 mL syringes and injected into negative molds of body parts of each chamber with 1 mL/min using syringe pumps. The rest was poured into negative molds of head parts of each chamber otherwise. The negative molds filed with PDMS polymer kept in oven at 37 °C for 10 h. Each chamber's body and head parts were adhered to by applying a thin layer of PDMS on the contact surface and completed treating heat 100 °C for 2 h in the oven. Finally, the PDMS chambers underwent oxygen plasma treatment for surface modification. The vacuum plasma chamber was filled with 0.3 mbar of oxygen gas at a flow rate of 12 sccm. Subsequently, 350 W of RF power was applied for 40 seconds. This plasma treatment was performed to convert the hydrophobic PDMS surface into a hydrophilic one.

3.3.1.2. Three-Dimensional-Printed Culture Membrane Frames

The chip bioreactor was designed to accept an insertable frame fixed cell culture membrane called chip inserts. Two compartments of membrane frames were designed using 3D design software (SOLIDWORKS[™] Premium 2017) by Dr. Tobias Schmitz. Subsequently, for 3D printing, the part file was imported into Formlab software, which was configured to print using a biocompatible resin (Dental SG FLDGOR01). Consequently, membrane frames were

printed using an SLA 3D printer (Figure 3.4A and B). The 3D-printed parts of membrane frame underwent post-processing according to the Table 3.2.

Additionally, ultrasonication was conducted by treating them in an ultrasonic bath for 15 min at least twice to remove any surface contaminants. Also, they were incubated in 70 % EtOH for 15 min and then autoclaved at 120 °C for 30 min for chemical disinfection.

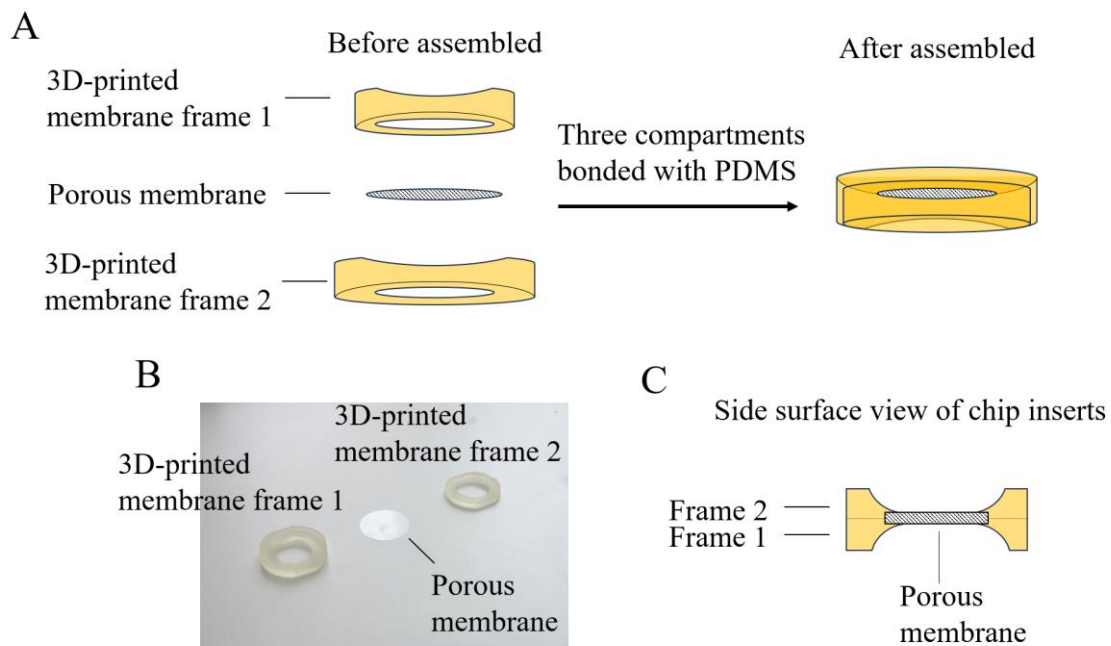


Figure 3.4. Chip insert fabrication. (A) Three components of chip inserts, two 3D-printed frames and a porous membrane, were bonded using PDMS. (B) Photograph of the three chip insert components. (C) Illustrated side view of the assembled chip inserts.

Chip inserts were prepared to be used for cell culture by sandwiching the cell culture membrane (Oxyphen, 0.4 μm pore size) between two membrane holders. A thin layer of PDMS polymer was applied to the inner surfaces of the membrane frames, precisely at the location where the cell membrane adheres. (Figure 3.4A and C). Thus, sandwiched chip insert was gently pressed and given heat 65 °C for 3 h. Completed chip inserts were gamma sterilized to be ready for cell culture. Consequently, chip inserts provide a surface area of 0.95 cm^2 on which cells can be seeded.

3.3.1.3. Bioreactor Clamps, Stand, and Medium Bottle Silicone Holder

Some glitches are commonly encountered while running the perfusion bioreactor systems. For example, leakage is the one causing contamination. Furthermore, an air bubble can cause cell

culture damage and flow instability. Thereby, additional equipment such as clamp and holder were designed to prevent thus glitches. Their designs, created using 3D design software (SOLIDWORKS™ Premium 2017), were imported into Preform software for 3D printing. A layer thickness of 0.5 mm and clear resin (FLGPCL02) were selected as the materials for clamps and holders. Following SLA 3D printing, the components underwent the post processing steps detailed in Table 3.2. To enhance ease of handling and prevent contamination, a medium bottle holder was crafted using silicon casting. Openings placed at the bottom of the bottle for fluid flow were connected with silicone tubes and then positioned inside the container. The height of the container was half of the bottle height. A mixture of DUBLISIL®15 in a 1:1 ratio was poured into the container. The rubber mixture was left to harden at room temperature for 30 minutes. After hardening, the silicone bottle holder was detached from the container and the bottle.

3.3.2. Generation of Human Induced Pluripotent Stem Cell-derived Brain Capillary Endothelial Cells

The differentiation of the hiPSC line IMR90-4 to BCECs was carried out by Dr. Sanjana Mathew following the described procedure [155]. The hiPSC cell line (IMR90-4) was obtained from Wicell (USA). The donor details include fetal lung fibroblasts and the donor is female. For differentiation, the dissociated single cells of hiPSCs were seeded on 10 cm² plate coated with matrigel. The initial cell density was 7.5×10^3 cells/cm². For the first 24 h, mTeSR™1 medium, including 10 µM dihydrochloride was treated after that daily medium change was conducted with mTeSR™1 medium until reaching the cell density at $2.5 - 3.5 \times 10^4$ cells/cm². Once the cells reached desired density, the mTeSR™1 medium was switched to an unconditioned medium, and the day was designated as day 0 of differentiation. During day 0 to day 5 of differentiation, the medium change was performed with unconditioned medium every day. Afterwards, the 4 mL EC++ medium (+B27 (1:200), +RA (10 µM), +hbFGF (20 ng/mL)) was treated on each dish on day 6 of differentiation instead of unconditioned medium, and then there was no medium change on day 7 of differentiation. Before cells seeding on chip inserts for bioreactor and transwell inserts for 2D static culture on day 8 of differentiation, the inserts were coated with 200 µg/mL matrigel and incubated for 1 h at room temperature (20 °C). Cells were detached using Accutase™ and seeded in chip and transwell inserts with cell density 10^6 cells/cm² in EC++ medium. On day 9, medium change was performed with EC medium (+B27, -RA, -hbFGF). Finally, on day 10, the BCECs cultured in chip inserts were transferred to a chip bioreactor for long-term dynamic flow culture,

accompanied by EIS measurements. Meanwhile, cells cultured in Transwell inserts continued their static culture in a specialized transwell plate for EIS measurements.

3.3.3. Static Culture of Brain Capillary Endothelial Cells

To examine the effect of flow conditions, especially shear stress, on the barrier integrity of BCECs, EIS measurements were conducted simultaneously on cells in static culture within a transwell plate. This served as a control for the dynamic flow culture. On day 10 of differentiation, as described in section 3.3.2, the transwell inserts with BCECs were transferred to 24-well specialized plate for EIS measurement. Day 10 of differentiation is subsequently referred to as day 0 of the extended long-term culture.

EIS Measurement

For EIS measurement, the custom-made measuring device equipped with nanostructured TiN electrodes previously described by Schmitz et al. [86] was sterilized with 70 % EtOH under a safety cabinet. The EC medium was filled freshly on the apical side (400 μ L) and basolateral side (850 μ L) of the insert in 24 well-specialized plates. Then, the transwell plate was closed with the sterilized measuring device and incubated for 40 min in an incubator (Figure 3.5A). After that, the plate closed with measuring device was moved to a tailored incubator system and connected to an electrochemical impedance analyzer (Figure 3.5B).

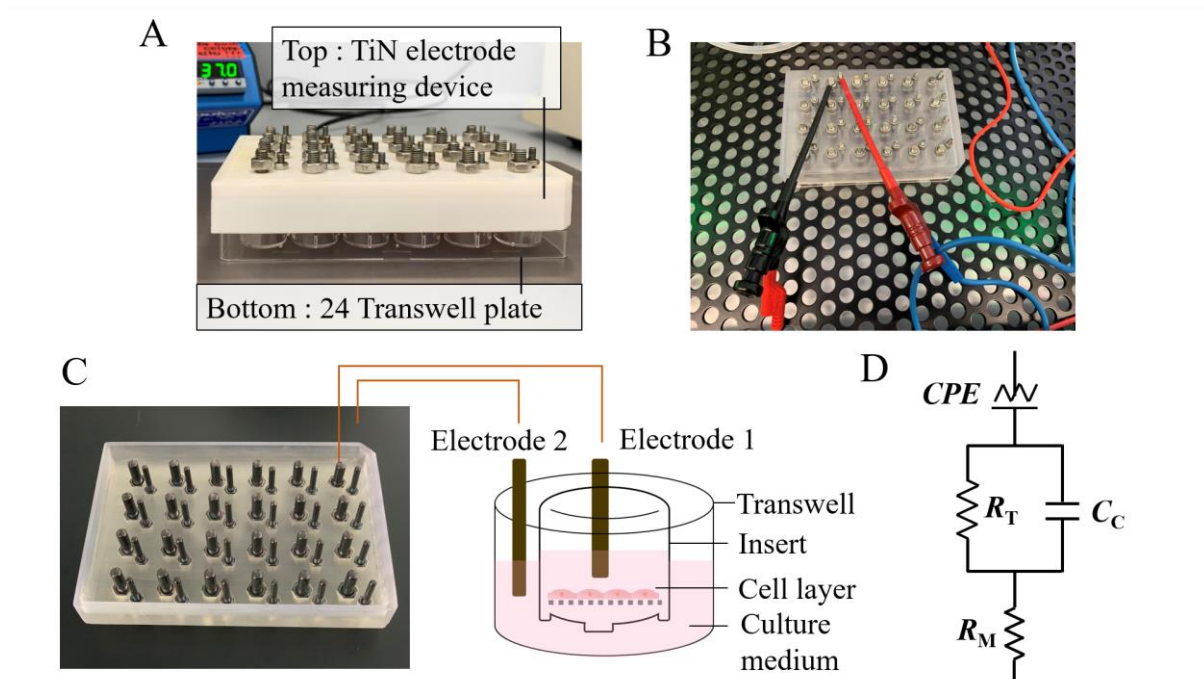


Figure 3.5. EIS measurement setup with TiN electrodes for static culture. (A) A 24-well transwell culture plate equipped with a TiN electrode measuring device. (B) Each pair, comprising two electrodes, is connected to a potentiostat for EIS measurements. (C) An internal view of the TiN electrode measuring device (Left photo) is shown. One electrode is positioned inside the insert (apical compartment), while the other electrode is located outside the insert (basolateral compartment). (D) The equivalent circuit model used for fitting and simulation is represented. R_M stands for the impedance of the cell culture medium, while R_T denotes the impedance to tight junction protein. C_C represents the impedance of the cell membrane, and CPE is used to indicate the impedance associated with the electrode.

EIS measurement was conducted at 0, 2, 4, and 6 h on day 0, followed by subsequent measurements every 24 h. A voltage amplitude of $0.05 V_{RMS}$ was applied for EIS measurement within a frequency range 1 Hz to 100 kHz.

Fitting and Simulation of Impedance data

The impedance data obtained (Bode plot and Nyquist plot) were further analyzed using the fit and simulation commands in the Nova 2.1.4 software program to quantify the desired electrical parameters (R_T , C_C , and CPE). Designed equivalent circuit model (Figure 3.5D) for static culture was inserted in equivalent circuit editor, and the fitting and simulation operations were conducted. Afterward, the fitting and simulation results were overlaid onto an impedance graph, and parameters for each component of the equivalent circuit were quantified.

3.3.4. Dynamic Flow Culture of Brain Capillary Endothelial Cells

3.3.4.1. Sterilization

The chip bioreactor system was aimed to have two flow circuits through each chamber. Before sterilizing bioreactor system, the components of each flow circuit were connected; a medium bottle (capacity 50 mL), a pump tube, three pieces of silicone tubes (two with length 400 mm and one with 450 mm), and Luer lock connectors. For convenience, the two chambers and two electrodes were prepared separately. Finally, the assembled and not yet assembled parts were autoclaved at 120 °C for 30 min.

3.3.4.2. Bioreactor Set Up and Cell Culture

The assembly of the chip bioreactor system was completed under a biosafety cabinet. In the state of vacancies of electrodes and two bioreactor chambers in the assembly of the flow circuit, the TiN-coated tube electrode was first connected to the pre-assembled part in sterilization steps. Two TiN-coated tube electrodes were attached to where they could place diagonally opposite each other, right next to each chamber. Before the chip bioreactor joined the flow circuit, the pre-cultured chip inserts with hiPSC-derived BCECs were equipped in the middle of two PDMS chambers. Then, the PDMS chambers were closed tightly with clamps and then connected to the rest of the assembly. Before filling the EC medium, the checkpoint was to block the way of EC medium out in the bottle using screw clamps to prevent uncontrol medium flow into the bioreactor system before controlled flow started. Also, the culture medium should have been warm enough (37 °C) to avoid any air bubble generation after bioreactor culture begins. Lastly, air filter was equipped on the medium bottle, 45 mL EC medium was filled in each medium bottle. Finally, all the assembly of the chip bioreactor system completed under a biosafety cabinet was transferred to the tailored incubator system equipped with a peristaltic pump. The pump tube of the chip bioreactor system was installed on the peristaltic pump, and the screw clamps were taken off to start the pump. The flow rate was set at 0.3 mL/min, and the whole bioreactor system with hiPSC-derived BCECs was incubated at 37 °C and 5 % CO₂ in a tailored incubator system during cell culture. The initial culture running time was 48 h intending to validate the bioreactor system. After that, the culture period was even prolonged to 7 days.

3.3.4.3. Electrochemical Impedance Spectroscopy Measurement

In order to make continuous non-invasive online monitoring possible during dynamic flow culture, the two Black PVC EHT cables were installed on the tailored incubator system.

The electrochemical impedance analyzer was linked to electrodes of the bioreactor system located in the incubator using Black PVC EHT cables. The EIS measurement of dynamic flow culture has been begun as soon as the whole bioreactor system was filled up with EC medium. On day 0, the dynamic flow culture was monitored for 0, 2, 4, and 6 h and then measured every 24 h. For EIS monitoring of hiPSC-derived BCECs, the voltage amplitude $0.05 V_{RMS}$ was applied with a frequency range of 1 Hz to 100 kHz.

3.3.4.4. Fitting and Simulation of Impedance Data

After EIS measurement, the obtained impedance data were further analyzed using Nova 2.1.4 software program. Since Nova software program enables both measurement and analysis, easily and immediately the analysis can be carried out.

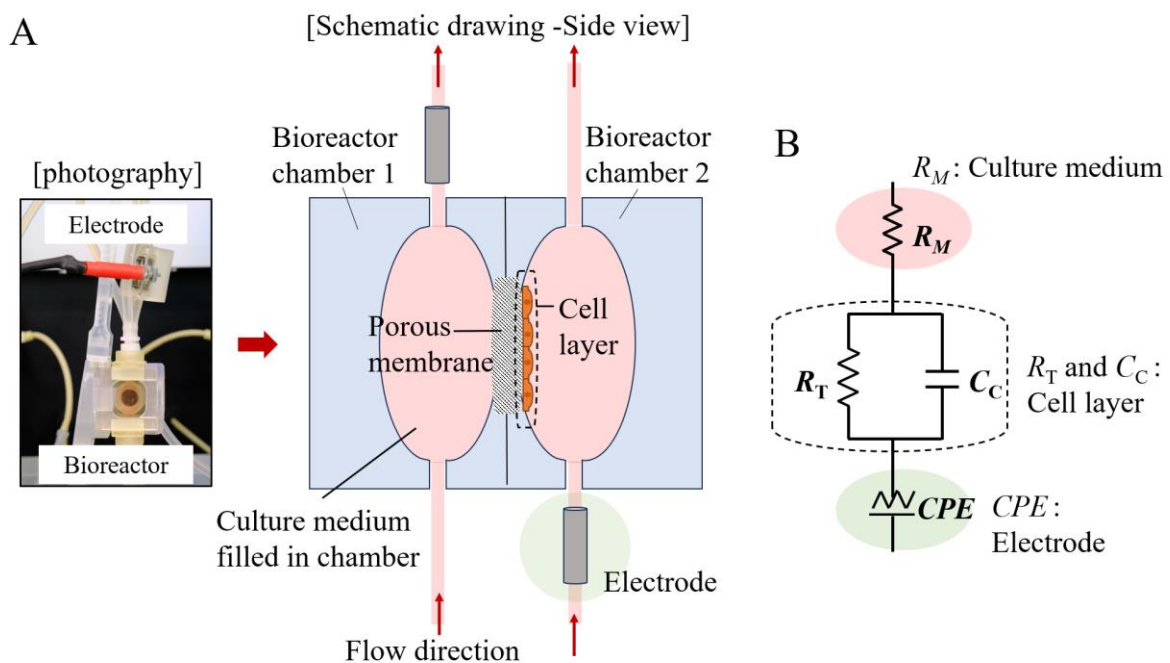


Figure 3.6. Equivalent circuit modeling for the chip bioreactor system. (A) A real photograph (on the left) and schematic side view (on the right) of the chip bioreactor with an electrode (B) Equivalent circuit was modeled for impedance data fit and simulation in the chip bioreactor system. R_M (Pink) represents the impedance of the cell culture medium, R_T (Dashed line) indicates the impedance of tight junction barrier integrity, C_C (Dashed line) corresponds to the impedance of the cell membrane, CPE (Green) signifies the impedance of the electrode.

The analysis was performed using fit and simulation command. An equivalent circuit that is corresponds to the bioreactor culture model (Figure 3.6A) is represented in Figure 3.6B. The equivalent circuit model included a series connection of CPE for electrode impedance and R_M

for culture medium impedance, with an additional series connection of a parallel combination of C_C for cell membrane and R_T for the tight junction barrier. Thus, the designed equivalent circuit model is added to the equivalent circuit editor in the fit and simulation command within the Nova 2.1.4 software program. Consequently, the fitting and simulations were carried out, and the results were overlaid on the impedance graph. Furthermore, the electrical parameters of the cell layers, such as the capacitance of the cell membrane (C_C) and the resistance of the tight junction (R_T), were quantified using the equation introduced in Table 1.1.

3.3.5. Histology and Image Analysis

3.3.5.1. Immunofluorescence Staining and Microscopy

Immunofluorescence was conducted to observe the cell morphology with tight junction proteins of hiPSCs-derived BCECs after dynamic flow culture and 2D static culture. The BCECs cultured on chip inserts and transwell inserts were washed with PBS⁻ and fixated with 4 % Roti Histofix for 15 min at room temperature. The fixated samples were rinsed and filled again with PBS⁻ for storing at 4 °C when it is not the case for immediate use.

After fixation, the permeabilization step was carried out to enable antibody penetration through the lipid membrane. Consecutively, non-specific antigen was blocked using host serum to avoid non-specific binding causing background fluorescence signal in the blocking step. Then, the incubation of primary antibodies having high specificity of interest proteins (Occludin, ZO-1, Glucose transporter-1 (GLUT-1)) was performed overnight. In the next step, secondary antibodies conjugated with fluorophore were bonded with the primary antibody in secondary antibody incubation. For the final steps, the samples were placed on microscope slides.

Table 3.3. Immunofluorescence procedure for BCECs

Procedure	Solution	Time (min)
Fixation	4 % paraformaldehyde	10 min
Permeabilization	Permeabilization buffer: 0.2 % Triton-X 100 in PBS	5 min
Blocking	Washing buffer: 0.5% Tween-20 in PBS (3 times)	5 min
	Blocking buffer: 5 % donkey serum +0.02 % Saponin + 0.1 % Triton-X 100	20 min
Primary antibody	Primary antibody solution: ZO-1, Occludin, and GLUT-1	Overnight (4 °C)
Secondary antibody	Washing buffer: 0.5% Tween-20 in PBS (3 times)	5 min
	Secondary antibody solution Alexa Fluor 488 and 647	60 min
Cover cells	Fluoromount-G TM with DAPI	mount a cover slip

Finally, the nuclei were stained using DAPI including mounting solution, and the sample was covered with coverslips for microscopy. The details of immunofluorescence steps are described in the Table 3.3. Following, the immunofluorescence staining was imaged using Leica SP8 confocal laser scanning microscope. Dr. Sanjana Mathew performed the sample preparation and image acquisition.

3.3.5.2. Image J Analysis

The microscopic image was analyzed to quantify the nuclei number. It was for comparing of the nuclei number of three different culture conditions, 2D static culture (0 h and 7 days) and dynamic flow culture (7 days). The samples from three biological replicates of each condition were taken for microscopy. The microscopic photo (magnification 40×) captured three different areas of each sample. As a consequence, 9 photos of each condition were used for Fiji analysis. The microscopic images were converted to 8-bit and thresholded to binary images in black and white, using Fiji [157]. Then, the ‘Watershed’ command was applied to separate touching objects from images. The minimum and maximum surface area pixel size needed to be defined to exclude counting the not-interest objects. Thereby, the surface area of the smallest nuclei was measured in pixels and input into the minimum size setting. The maximum size was set to infinity. The default value was used for the circularity setting. Finally, the particle analyzer was run for particle counting.

3.4. Electrode Application 2: a Miniature Hollow Fiber Bioreactor

The second application object of TiN-coated tube electrode was a miniature HFBR to monitor cell growth. Microscopic observation during cell culture in a commercial miniature HFBR presents challenges, non-invasive monitoring is required for cell viability and growth assay. TiN-coated tube electrode availability was tested individually on a miniature HFBR with cell cultures of two different cell lines, such as HUVECs and Caco-2.

3.4.1. Passaging and Cryopreservation of Cell lines

Passage numbers 3 to 5 were used for HUVECs, while passages 30 to 35 were employed for Caco-2 cells in conducting transwell plate cultures and miniature HFBR experiments. Cells were cultured until reaching 70 % confluency of cell density in the T75 culture flask. Once the cell density was about 70 %, the cells were rinsed with 10 mL PBS⁻, and then the ethylenediaminetetraacetic acid (EDTA) solution (0.05 %) was treated for 3 to 5 min at 37 °C for cell detachment. After observing the cell detachment using microscope, 10 % fetal calf serum (FCS) and 10 mL PBS⁻ were added to stop further enzyme reaction. The cell suspension was transferred to a 50 mL centrifuge tube and centrifuged at 1200 rpm for 5 min. The supernatant was discarded carefully by not touching cell pallets, and the cell pellets were mixed with a fresh cell-specific culture medium. Afterward, total cell numbers were verified by cell counting. Depending on cell culture surface area, the desired density of cells was taken from the cell suspension. The residue cells in cell suspension were preserved using cryopreservation technique for long-term storage. As soon as the mixture of 1 mL cell suspension (cell density of 0.5 million/mL), 10 % FCS, and 10 % dimethyl sulfoxide (DMSO) was prepared in cryotube, the tubes were put into Mr. Frosty for cooled down step at - 80 °C for 24 h. Afterwards, the cryotubes transferred to liquid nitrogen tank for long-term storage.

3.4.2. Reference Transwell Culture of Cell lines

Before monitoring Huvecs and Caco-2 cell cultures in a miniature HFBR, the electrical and morphological characterizations of HUVECs and Caco-2 cells in transwell cultures were performed. HUVECs (FC-0003) and Caco-2 cells (ACC 169) were used for transwell culture (Table 2.6). These characterizations served as a reference for EIS measurements in the miniature HFBR.

3.4.2.1. Electrochemical Impedance Spectroscopy Analysis

Transwell culture of HUVECs and Caco-2 cells was performed before miniature HFBR culture to investigate the barrier integrity of the cells in a simple setup using EIS.

The porous membrane 24 well inserts were coated with 10 $\mu\text{g}/\text{mL}$ fibronectin overnight and with 100 $\mu\text{g}/\text{mL}$ collagen in 0.1 % acetic acid for 30 min in the incubator for HUVECs and Caco-2 cells culture, respectively. HUVECs (FC-0003) were seeded onto the fibronectin-coated inserts at a density of 60000 cells/ cm^2 , while the Caco-2 cells (ACC 169) were seeded onto the collagen-coated inserts at a density of 100000 cells/ cm^2 .

The EIS measurements of the transwell cultures followed the same method that was used in the BCECs transwell model, as mentioned in the previous section 3.3.3. Briefly, the 2D static measuring device with TiN electrodes were sterilized with 70 % EtOH under a safety cabinet. Meanwhile, the medium on the apical and basolateral sides was replaced with 450 μL and 600 μL of fresh medium, respectively. The transwell plates were closed with a measuring device equipped with TiN-coated electrode, and incubated for 40 min in incubator (Figure 3.5). The EIS measurement was conducted under controlled temperature conditions, with an applied AC voltage of 0.05 V_{RMS} in a frequency range 1 Hz to 1 MHz for HUVECs and 1Hz to 100 kHz for Caco-2 cells. For further analysis, EIS data were analyzed through fit and simulation using an equivalent circuit model applied to the BCECs transwell culture (Figure 3.5D).

3.4.2.2. Immunofluorescence Staining and Microscopy

Immunofluorescence staining was performed on HUVECs on day 0 and day 9, and Caco-2 cells on day 21, to assess the morphology of the tight junctions in both cell types. The same protocol described in section 3.3.5.1 for immunofluorescence staining of BCECs was followed for HUVECs and Caco-2 cells.

The details of the immunofluorescence steps are described in the Table 3.4. HUVECs histology images were captured at magnification 20 \times using Keyence fluorescence microscope.

Table 3.4. Immunofluorescence procedure for HUVECs and Caco-2

Procedure	Solution	Time (min)
Fixation	4 % paraformaldehyde	10 min
Permeabilization	Permeabilization buffer: 0.2 % Triton-X 100 in PBS	5 min
Blocking	Washing buffer: 0.5% Tween-20 in PBS (3 times)	5 min
	Blocking buffer: 5 % donkey serum + 0.1 % Triton-X 100	20 min
Primary antibody	Primary antibody solution: ZO-1	Overnight (4 °C)
Secondary antibody	Washing buffer: 0.5% Tween-20 in PBS (3 times)	5 min
	Secondary antibody solution: Alexa Fluor 488 and 647	60 min
Cover cells	Fluoromount-G™ with DAPI	mount a cover slip

For capturing immunofluorescence images of Caco-2 cells, Leica SP8 confocal laser scanning microscope was used. Maximum projection Z-stack images were taken at 40× magnification with confocal laser scanning microscope, and the images were accessed by Z-stack function in Fiji.

3.4.3. Miniature Hollow Fiber Bioreactor culture of Cell lines

3.4.3.1. Miniature Hollow Fiber Bioreactor Culture Setup and Sterilization

The existing miniature HFBR is connected to a tubing system and a medium bottle for cell culture. Additionally, two TiN-coated tube electrodes were integrated into the existing bioreactor setup. The electrodes were connected to a tubing system to locate at the EC outlet and IC inlet. For sterilization, the miniature HFBR and tubing system with electrodes were packed separately and autoclaved at 120 °C for 30 min.

3.4.3.2. Extracellular Matrix Protein Coating and Equilibrium

The hollow fiber membrane (MicroPES® TF10), was coated with ECM proteins before cell seeding. Two independent experiments with miniature HFBR using distinct cell lines were conducted for HUVECs and Caco-2 cells.

Specifically, fibronectin was used at a concentration of 10 µg/mL for HUVECs, and collagen was applied at a concentration of 100 µg/mL for Caco-2 cells, following the protein coating

protocol provided by our collaboration partner, eXcorLab GmbH. In general, cells can be seeded either in the IC space or EC space. In this study, for the HUVECs culture experiments, cells were seeded in the IC space, while for the Caco-2 culture experiments, cells were seeded in the EC space; the only difference is the initiation of injection, whether it starts in the IC or EC space. Here, the seeding procedure in the EC space will be described.

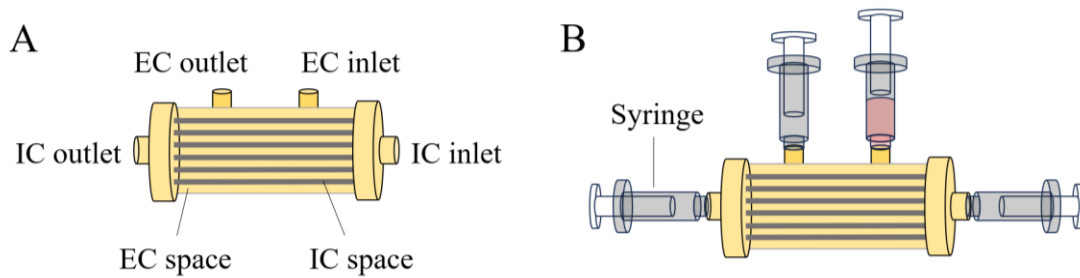


Figure 3.7. Miniature HFBR setup for protein coating and cell seeding. (A) depicts the structure of a miniature HFBR. Solutions can be introduced through the extracapillary (EC) and intracapillary (IC) inlets and outlets, thereby filling the corresponding EC and IC spaces. (B) The illustration of a miniature HFBR setup depicts the initial step of protein coating or cell seeding on the EC surface of hollow fibers.

Briefly, the prepared 3 mL coating solution was put into the syringe (cap 5 mL) and connected to the EC inlet. All other entrances, such as the EC outlet, IC inlet, and IC outlet were linked with empty syringes (cap 5 mL) (Figure 3.7). The coating solution was filled in extracapillary space. Two syringes have cooperated in any cases of injecting or removing a solution, such as ECM coating solution, cell suspensions, etc., in a HFBR. The injection and removal of solutions were led by pulling the plunger of one side syringe while another side syringe was assisted as gently pushing the plunger. This was for achieving a homogenous filling of the solutions without bubbles in a miniature HFBR. To fill the EC space with the coating solution, the first step involves pulling the syringe at the EC outlet, initiating the flow of the solution from the syringe connected to the EC inlet. Subsequently, the same process is performed in a reversible direction and repeated for two rounds. As a result, the EC space is filled with the coating solution, and the remains from the filling process are left in both the syringe at the EC inlet and outlet. In the second step, the remaining solution from the first step in each syringe, including the EC inlet and EC outlet, flows through the membrane to ensure the complete coating of the membrane surface. The flow direction is from the EC inlet to the IC outlet and from the EC outlet to the IC inlet, respectively. Afterward, the miniature HFBR was incubated at 37 °C and 5 % CO₂ for 1 h for both fibronectin and collagen coating.

During the incubation time, the bioreactor rotated along the cylinder axis by 180 ° every 15 min to ensure a uniform coating on the membrane fibers. After the incubation, the coating solution was removed from the bioreactor, and the bioreactor was connected to a pre-assembled tubing system composed of silicone tube, Luer lock connectors, and medium bottle. The ECM protein-coated hollow fiber membrane was equilibrated by given culture medium flow with a flow rate of 0.15 mL/min under 37 °C and 5 % CO₂ for 30 min before cell seeding.

3.4.3.3. Cells Seeding and Electrochemical Impedance Spectroscopy analysis

The concentration of each cell line being seeded on a miniature HFBR was 60000 cells/cm² (Total of 0.42 milion cells in 3mL suspension) for HUVECs (Lonza Cologne GmbH, Koeln) culture experiment and 100000 cells/cm² (Total of 1.4 milion cells in 3mL suspension) for Caco-2 cells (ACC 169) culture experiment. The cell seeding was performed similarly to the protein coating of fibers. The protocol for cell seeding was supplied by our collaborative partner, eXcorLab GmbH. HUVECs culture was carried out by Dr. Moritz Tulke in eXcorLab GmbH. To seed the cells, the prepared 3 mL cell suspension was put in a syringe (cap 5 mL) and connected to an EC inlet. The three empty syringes were linked to the IC inlet, IC outlet, and EC outlet. The cell suspensions were filled into the bioreactor following the same procedures as those described for treating the coating solution in the hollow fiber bioreactor in section 3.4.3.2. Then, the miniature HFBR with cells was incubated for 3 h. Every 15 min, the bioreactor was turned 180 ° during incubation to achieve homogeneous cell seeding on the surface. The miniature HFBR seeded with cells were taken out from incubator to biosafety cabinet for assembly with electrodes and tubing system. The assembly were connected to the pump, then placed in incubator at 37 °C, 5 % CO₂, and humidity about 95 % for long term dynamic flow culture. The medium flow was constantly controlled with a flow rate of 0.15 mL/min for the HUVECs culture experiment and 0.3 mL/min for the Caco-2 culture experiment. EIS measurement was performed with two TiN-coated tube electrodes using EIS measuring device (either Autolab PGSTAT 204 or Sciospec). 0.05 V_{RMS} amplitude AC voltage was constantly applied in frequency range 1 Hz to 100 kHz. Fitting and simulation of obtained impedance data for further analysis were conducted using an equivalent circuit model identical to that in Figure 3.6D and following the same procedures as described in section 3.3.4.4.

3.4.3.4. Immunofluorescence Staining and Microscopy

After the long-term of dynamic flow culture, Hoechst staining was carried out to identify cells on hollow fibers. Our collaboration partner, eXcorLab GmbH, supplied the procedure for Hoechst staining. Briefly, the culture medium in miniature HFBR was rinsed out with 3 mL PBS⁻ using 5 mL syringe very carefully. Then, for fixation of the cells, the 3 mL fixation solution was treated in hollow fiber reactor, and the bioreactor was kept at room temperature for 5 min. Afterwards, it was rinsed again with 3 mL PBS⁻. Subsequently, the hollow fiber bioreactor was filled with 3 mL Hoechst stain solution for cell nuclei staining and incubated for 5 min at room temperature. As last step of Hoechst staining, the bioreactor was washed with 0.5 % human serum albumin (HAS) solution (3 mL) twice. When the Hoechst staining has been done, the hollow fibers were taken out by dismantling hollow fiber bioreactor using saw. Hollow fibers were stored in 10 mL falcon tube filling with 0.5 % HSA solution (3 mL).

3.5. Electrode Application 3: Hemofiltration

3.5.1. Setup of a Hemofilter with Titanium Nitride-Coated Electrodes

To investigate whether EIS enables the monitoring of clogging in hollow fiber membranes during hemofiltration, TiN-coated tube electrodes were tested and characterized into a hemofilter test system operating with blood. Human blood was collected for the study, with explicit consent obtained directly from blood donors carefully selected from a healthy population. Technical support during hemofiltration was provided by Dominik Köhler. The sterilized blood tubing line containing three drip chambers and a hemofilter was installed following the order of the extracorporeal blood circuit on the DBB-05 dialysis device. The extracorporeal blood circuit diagram is described in Figure 3.8. Supplementary the photography of hemofilter setup with TiN-coated tube electrode represented in Appendix G (Figure G.1). The extracorporeal blood circuit is categorized into two sections: designated arterial blood line and venous blood line. The blood taken out from arterial access of blood bags flows along the arterial blood line, and the filtered blood returns through the venous blood line to the blood bags. Briefly explaining the connection of components of extracorporeal blood circuit following order of the blood pathway, the arterial drip chamber and arterial inlet blood pressure chamber were positioned before and after the arterial blood pump of the arterial blood line respectively and connected to pressure sensors. Then, the hemofilter was located next to the hemofilter inlet blood pressure chamber for blood filtration. Finally, the venous drip chamber was placed on the venous blood line, so the filtered blood passed over the drip

chamber connected with the pressure sensor and returned to the blood sample bag. Additionally, a peristaltic pump was linked to a ultrafiltrate line to collect drained ultrafiltrate from the hemofilter and send it to the venous drip chamber for mixing with blood.

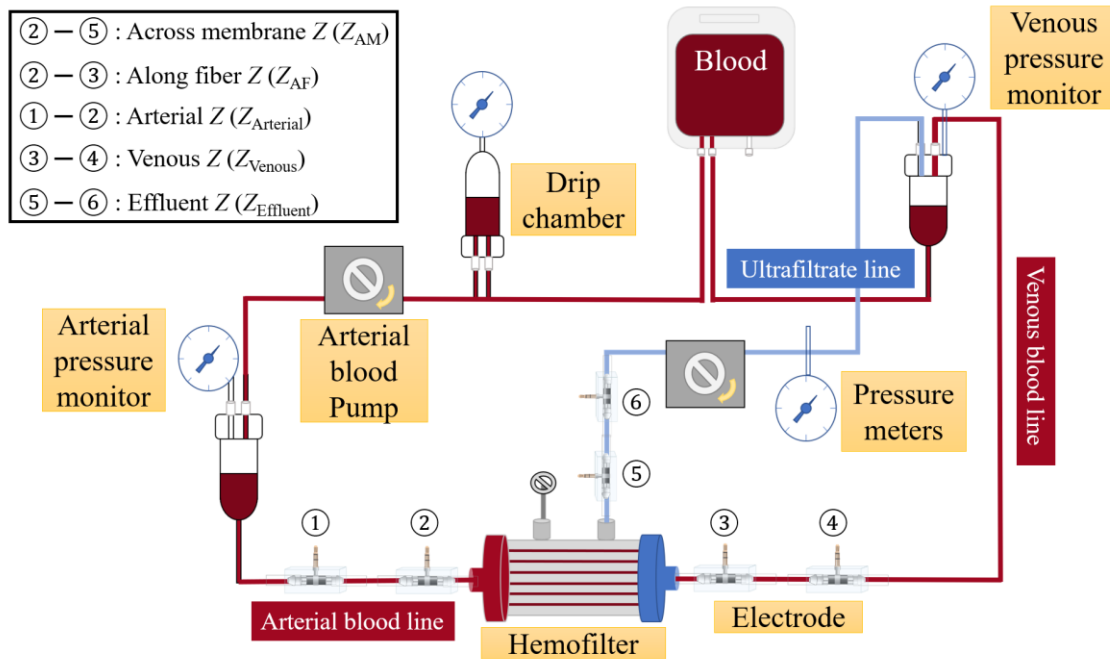


Figure 3.8. Implementing TiN-coated tube electrodes into the hemofiltration circuit. Each two electrodes were placed in the arterial, venous, and ultrafiltrate lines close to the hemofilter. For every EIS measurement, a pair of electrodes was used. The upper left corner box signifies the measurement objective for each electrode pair.

Since the setup was for testing, the filtrate, instead of replacement fluid, returned to the blood sample bag after being mixed with blood for continuous circulation, unlike medical treatment. The six TiN-coated tube electrodes were integrated into the circuit using Luer lock connectors. Two electrodes were placed on the arterial blood line, two on venous blood line, and two on dialysate line near the entrance of the hemofilter.

3.5.2. Hemofiltration and Electrochemical Impedance Spectroscopy Analysis

Before begin hemofiltration, the priming blood circuit was conducted, rinsing the blood circuit with saline solution to check for any blocking and leakage on the circuit pathway. The sample bag with 1 L saline solution (0.9 % NaCl) was connected to the arterial access tubing line and the waste bag to the venous access tubing line. The arterial blood and dialysate pumps were set with flow rates at 200 mL/min and 60 mL/min for priming blood circuits, respectively.

After the 1 L of saline solution circulation, the saline solution sample bag was switched to blood sample bag. Following, the residue of saline solution left on the blood circuit was discharged given a single blood pass and collected in a waste bag. Once the saline solution on blood circuit was completely removed, the venous access tubing line linked with blood sample bag instead of waste bag. Afterward, the blood pump was operated with a 300 mL/min flow rate, and the temperature was kept constant at 37 °C. Also, the dialysate pump ran at a flow rate of 60 mL/min while the arterial blood pump was active. The pressure at hemofilter inlet blood, venous, and ultrafiltrate pressures was monitored and recorded every 1 min during the hemofiltration. Later on, TMP was calculated by adding measured pressure values to Equation 1.22. The EIS measurement was carried out to monitor the hemofiltration. A pair of electrodes were connected to EIS analyzer (Autolab PGSTAT 204) for each EIS measurement, depending on the desired measuring point. The applying voltage was set to 0.05 V_{RMS} and frequency range was 1 Hz to 100 kHz.

3.6. Statistical Analysis

Mean and Standard Deviation (SD)

In order to calculate measures of central tendency and dispersion, mean and standard deviation (SD) were calculated using the mean and STDEV.P functions within Microsoft Excel 2019.

ANOVA Test

A One-Way ANOVA was conducted in the OriginPro 2021b software to investigate significant differences among groups. The Tukey test was applied, and a significance level of 0.05 was chosen. A p-value less than 0.05 (indicated with *) indicated statistically significant differences in population means among the groups.

4. Results

4.1. Add-on Electrode Development

Electrodes play a crucial role in enhancing the accuracy of results of EIS measurement because they represent the physical interface between the measurement system and the biological system. Thereby, electrodes with superior physical properties, such as low electrical impedance and high corrosion resistance etc., are preferred for biological application. Also, electrodes should be biocompatible since electrodes have direct contact with the cell culture medium or even with cells. Furthermore, the placement of electrodes, whether within the bioreactor where tissue is located or in the tubing connected to the bioreactor, would be a consideration depending on the research goal. Progress has been achieved in developing electrodes with various designs to identify the optimal electrode for EIS in dynamic flow culture.

4.1.1. Examine Applicability of TiN Coating on Various Substrates

TiN layers were deposited on four distinct substrates (Polycarbonate Luer lock connector, SS mesh, glass plate, and SS tube) using PVD. Subsequently, the TiN layers on each substrate were examined through visual inspection and SEM. This assessment aims to evaluate the applicability of TiN coating on various substrate materials and geometries. The use of a polycarbonate Luer lock connector as electrode substrates is advantageous, as it is already served as a tubing connector. This means that no additional modifications are required for its application in a bioreactor system. The TiN-coating was deposited on the exterior of the polycarbonate Luer lock connector (Figure 4.1A), and a color change to dark brown was observed after the PVD. Nevertheless, incomplete coating was occasionally observed, particularly at the edges, attributed to the complex 3D structure. Furthermore, both a SS mesh (Figure 4.1B) and a glass plate (Figure 4.1C), featuring flat surfaces, were employed as substrates for electrode. Following the PVD, TiN-coated surface exhibited a dark brown color. For the SS tube substrate, TiN coating was applied to the inner surface of the SS tube. Despite the relatively complex geometry when compared to a flat surface, the SS tube form was chosen as a substrate candidate because it allows for the easy design of electrodes that can be integrated into the tubing system.

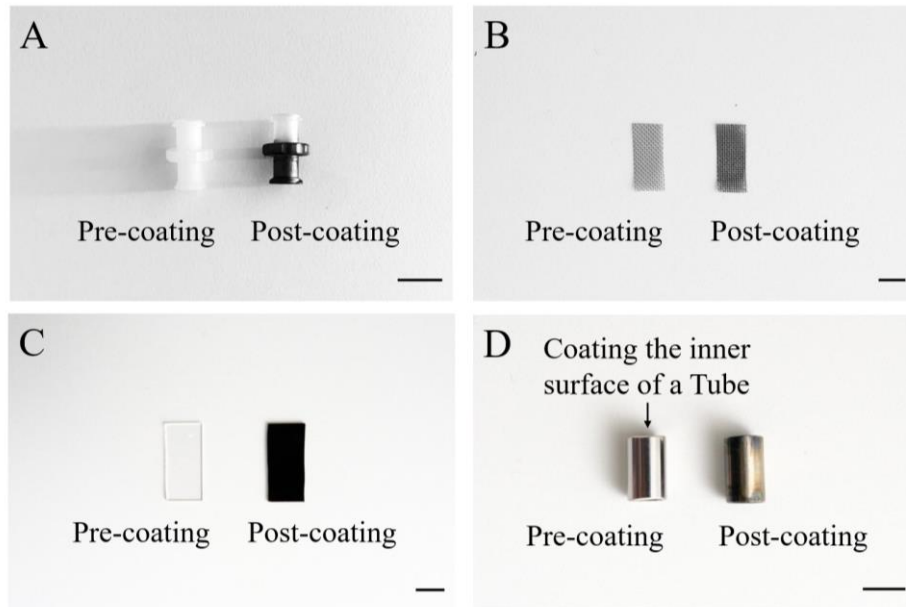


Figure 4.1. Photograph of pre- and post-coating on different substrates: (A) Luer lock connectors, (B) SS mesh, (C) glass plate, and (D) SS tube. Overall, the color change to dark brown was observed in all samples. However, due to the TiN coating being applied to the inner surface of the SS tube, it may not be clearly visible in photograph in Figure D. Each subfigure includes a scale bar representing 10 mm.

Color changes were observed across the entire inner surface of the SS tube, although this change was not clearly visible in the picture (Figure 4.1D) because of the coating being on the inner surface. SEM analysis was conducted on the TiN-coated surfaces of all substrates except the Luer lock connector.

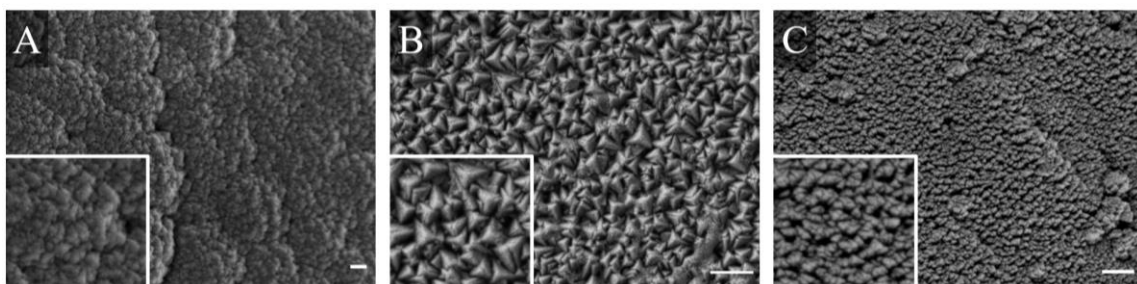


Figure 4.2. SEM images of TiN-coated surfaces on different substrates: (A) SS mesh (scale bar 200 nm), (B) glass plate (scale bar 200 nm), and (C) SS tube (scale bar 200 nm). Nano-scale rough structures were observed in all samples. Philip Stahlhut performed the capturing of the SEM images.

SEM images revealed a rough nanostructure of the TiN coating on SS mesh (Figure 4.2A), glass plate (Figure 4.2B), and SS tube (Figure 4.2C). Due to its highly uniform flat surface, the glass plate displayed relatively consistent and uniformly rough nanostructures.

4.1.2. Various Designs of Electrode Models and Leak Test

Figure 4.3 depicts four different electrode designs developed to find optimum electrodes for applying to bioreactor culture. A thin layer of TiN was deposited on each substrate using PVD, resulting in each TiN-coated electrode having its own unique design. First, TiN-coated Luer lock were initially developed intending to simplify the development process. Except for TiN-coated Luer lock electrodes, TiN-coated electrodes of each substrate were housed using PDMS shell to make electrodes externally attachable. As shown in Figure 4.3B, the TiN-coated SS mesh was inserted through the incision part. The TiN-coated SS mesh inserted in the tube was covered with PDMS casting to prevent leakage, but a portion of the TiN-coated SS mesh remained exposed to connect to the EIS device. In the same way as TiN-coated mesh electrode, the TiN-coated glass plate (Figure 4.3C) was inserted into silicone tube through incision part. However, this time, the whole TiN-coated glass inserted in silicone tube were covered by PDMS shall unlike TiN-coated mesh electrode design. The banana plugs and titanium sheet played a conductive link between the TiN-coated glass electrode and the EIS device. Lastly, the TiN-coated SS tube electrode is shown in Figure 4.3D. The TiN-coated SS tube was connected to a silicone tube using a 3D-printed connectors, and their core structures, including an electrode, 3D-printed connectors, and silicone tubes, were surrounded by a PDMS shell. The banana plug was fixed to the steel hose clip, which was linked to the TiN-coated SS tube, enabling electrical contact between the TiN-coated SS tube and the EIS device.

Each electrode was connected to a fluid flow circuit and tested to see whether it leaked or not. The TiN-coated Luer lock electrode was directly connected to a silicone tube in the fluid circuit. On the other hand, the TiN-coated SS mesh, glass plate, and SS tube electrodes used commercially available Luer lock connectors to connect to silicone tubes. TiN-coated Luer lock electrodes did not have any leakage as expected since it is for joining silicone tubes. Like the TiN-coated Luer lock electrode, the other two, the TiN-coated glass and SS tube electrodes, showed no leakage even at high fluid speed. It was noticed that the TiN-coated SS mesh electrode started to leak as the flow rate increased (up to 280 mL/min). Another important observation was the tendency of air bubbles to become easily trapped on the TiN-coated SS mesh in the flow system which can have an impact on impedance measurements. Nevertheless, there remains an opportunity to utilize the TiN-coated SS mesh electrode without

requiring experiments that demand high flow rates. Additionally, any trapped bubbles can be easily eliminated by gently tapping the electrode.

Furthermore, it was observed that the TiN coating on the Luer lock connector was prone to wearing off during handling, indicating a relatively low wear resistance of the coating.

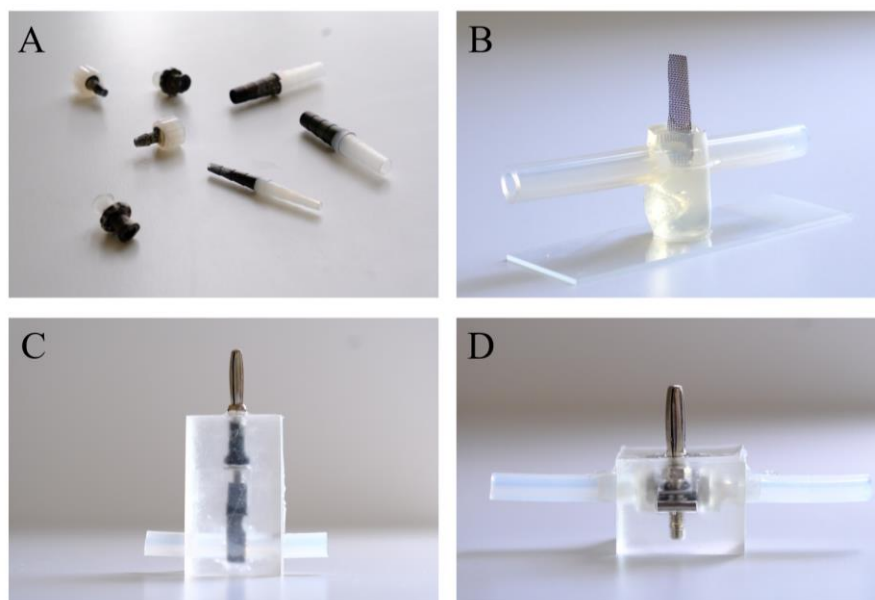


Figure 4.3. Photographs of various electrode designs. (A) TiN-coated Luer lock connectors electrode (B) TiN-coated SS mesh electrode (C) TiN-coated glass plate electrode (D) TiN-coated SS tube electrode

The poor wear resistance causes several issues such as poor electrical connections and high electrode impedance leading inaccurate results. As a result, the TiN-coated Luer lock connector electrode was excluded in the list of candidates. The photo of the Luer lock electrode issues presents in Appendix A (Figure A.1)

4.1.3. Electrical Double Layer Characterization of Electrode Models

Electrochemical double layer capacitance is an indicator related to electrode sensitivity. The electrochemical properties of TiN-coated electrodes with different substrates, SS mesh, glass plate, and SS tube, were demonstrated using impedance spectroscopy. As mentioned in the previous section 4.1.1 and 4.1.2, the TiN-coated Luer lock electrode was excluded because the coating was unstable, causing peeling off easily by friction. The results were plotted on a Bode plot representing total impedance versus frequency range (Figure 4.4A). Electrode impedance was dominantly presented in the low-frequency range (1 Hz to 100 Hz), while the electrolyte

impedance was relatively dominant at the high-frequency range (100 Hz to 10 kHz) in a Bode plot.

All impedance values across the frequency ranges (1 Hz to 10 kHz) were adjusted by subtracting the baseline impedance at 10 kHz. This adjustment enables a concise comparison of electrode impedance among different substrate electrodes. As a result, the baseline at 10 kHz set to 0. When comparing impedance values at 1 Hz, where the electrode impedance is most dominant, the TiN-coated glass plate had the highest impedance with $385.39 \pm 7.12 \Omega$. The TiN-coated SS mesh was lower than the TiN-coated glass plate with $167.31 \pm 1.42 \Omega$. Furthermore, the TiN-coated SS tube electrode impedance was the lowest at $83.97 \pm 1.29 \Omega$.

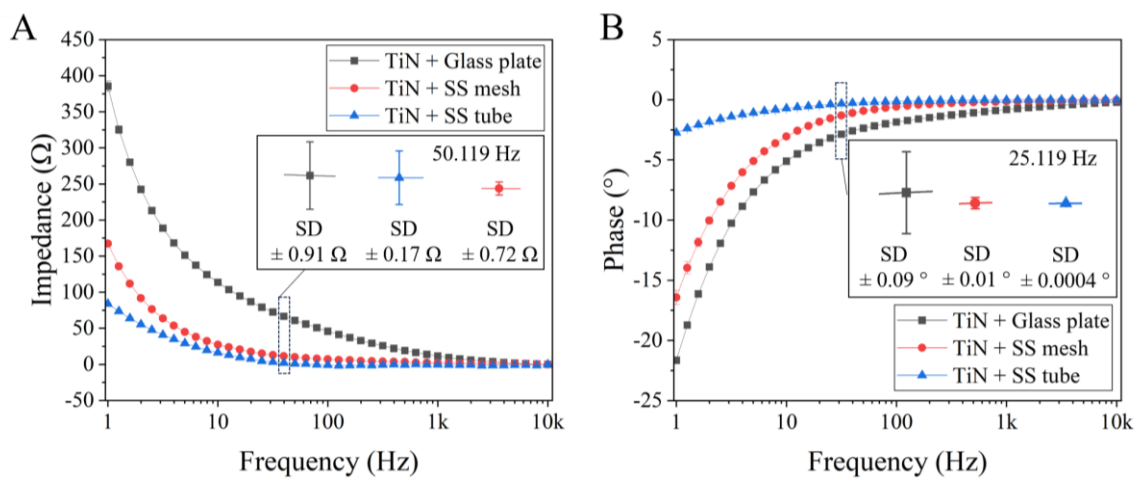


Figure 4.4. Characterization of double-layer capacitance of electrodes. A pair of electrodes connected using Luer lock connectors and filled with PBS⁻ was used for these measurements. (A) The impedance value depicts the function in relation to the frequency range of 1 Hz to 10 kHz. The baseline at 10 kHz indicates that medium resistance was subtracted from the impedance value across the entire frequency range. (B) Phase responses were measured over a frequency range of 1 Hz to 10 kHz for three different substrate electrodes. Each experiment was technically replicated three times, and the mean value with standard deviation (SD) is presented in the graph. Since the SD is relatively small, the error bar representing SD in graph is difficult to perceive. To enhance visibility, a zoomed-in inset of one data point at 50.119 Hz of impedance and 25.119 Hz of phase is provided.

The phase angle as function of frequency was represented in Figure 4.4B. As the input signal frequency lowered (1 kHz to 1 Hz), the phase angle was changed to negative values. The phase angle at 1 Hz was $-2.78 \pm 0.01^\circ$ for SS tube, $-16.43 \pm 0.59^\circ$ for SS mesh, and $-21.65 \pm 0.20^\circ$ for the glass plate. In addition, the impedance data were fitted to an equivalent circuit model to obtain quantitative values relating double layer capacitance.

The electrochemical cell used for the test was represented in Figure 3.3 by a series connection of a constant phase element (*CPE*) and an electrolyte resistor (R_e). The Table 4.1 shows the results of impedance data fitting using Nova 2.1.4 software program, *CPE* admittance (Y_0) is where containing capacitance information, and n represents the inhomogeneity of the coating surface. The TiN-coated SS tube showed the highest *CPE* admittance value with $19.5 \times 10^{-4} \text{ S}\cdot\text{s}^n$. The SS mesh and glass plate values were lower than TiN-coated SS tube as $6.16 \times 10^{-4} \text{ S}\cdot\text{s}^n$ and $3.42 \times 10^{-4} \text{ S}\cdot\text{s}^n$, respectively.

Table 4.1. Comparison of *CPE* parameters of TiN-coated electrodes

Electrode	<i>CPE</i> admittance, Y_0 ($\text{S}\cdot\text{s}^n$)		n ($0 < n < 1$)	
	Mean ($\times 10^{-4}$)	SD ($\times 10^{-5}$)	Mean	SD ($\times 10^{-3}$)
TiN + Glass plate	3.42	0.04	0.74	4.03
TiN + SS mesh	6.16	2.22	0.82	1.02
TiN + SS tube	19.5	1.89	0.65	6.36

In general, n ranges from 0 to 1. $n = 1$ means the *CPE* behaves as a pure capacitor, while $n = 0$ means the *CPE* behaves as a pure resistor. Furthermore, the electrode inhomogeneity of the TiN-coated tube electrode was 0.65, and the TiN-coated glass plate was 0.74. The TiN-coated SS mesh was the closest to a pure capacitor with 0.82, among others.

4.1.4. Investigating Influential Parameters Impact on Impedance Measurement

Based on the leak test and the evaluation of the *CPE* parameter discussed in sections 4.1.2 to 4.1.3, it was determined that the TiN-coated tube electrode was the most optimized choice for application in the bioreactor. Before incorporating the electrodes into the bioreactor system, an assessment of the impact of various influential parameters on EIS measurements was conducted. The electrochemical cell used for the assessment was configured by connecting two electrodes (Figure 4.5). For the flow rate experimentation, the peristaltic pump was additionally connected to the two electrodes. The system was filled with PBS⁻. Four different parameters such as distance between two electrodes (Figure 4.5A), temperature (Figure 4.5B), electrolyte concentration (Figure 4.5C), and flow rate were varied to evaluate the electrical properties of TiN-coated tube electrodes (Figure 4.5D). The results of impedance spectroscopy are represented in the Bode plot in Figure 4.6 and Figure 4.7. In a Bode plot, the magnitude of the impedance (Z) and the phase angle, are displayed as a function of frequency on a plot. Impedance baseline, in this context, refers to the impedance value at the frequency where the phase angle is closest to 0° in each recorded spectrum. In high-frequency conditions, due to

the rapid changes in the supply voltage, capacitors act as short circuits, resulting in very low impedance in EIS. As a consequence, the electrolysis resistance response becomes dominant at high frequencies, representing a minimum value in the impedance spectrum and effectively serving as the baseline. Also, resistance exhibits a frequency-independent response, meaning its phase remains constant at 0° .

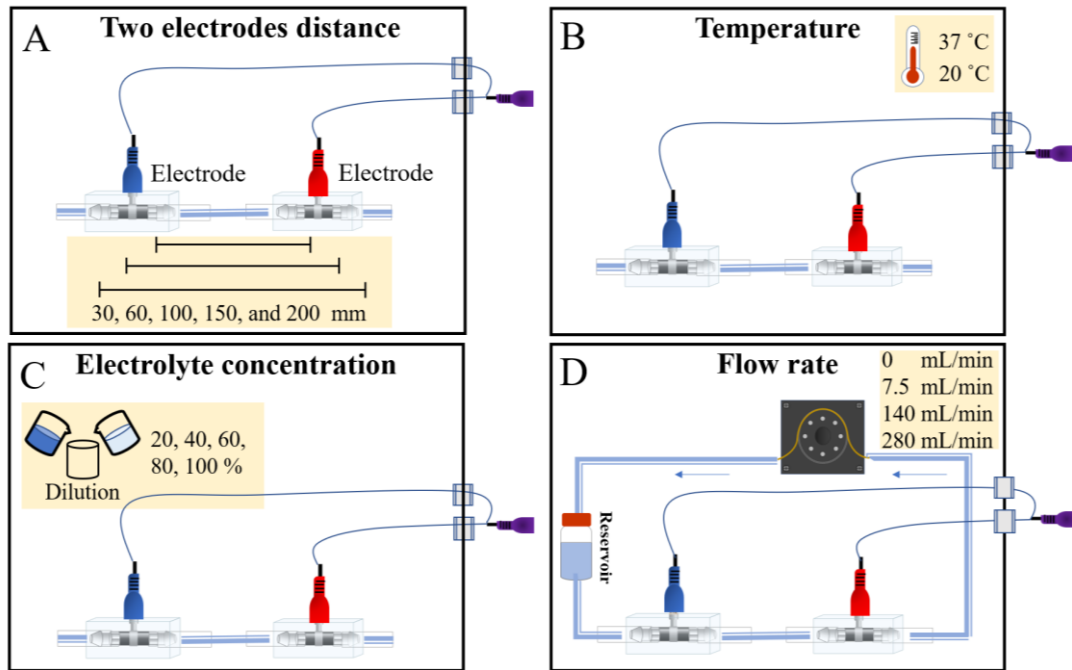


Figure 4.5. Electrodes setup for investigating impact parameters on EIS measurement. The setup includes two electrodes connected using a Luer lock connector and the system filled with PBS^- . Various parameters influencing the impedance response of electrode system were varied, including: (A) distance between two electrodes (30, 60, 100, 150, and 200 mm), (B) temperature (room temperature (20°C) and 37°C), (C) electrolyte concentration (20, 40, 60, 80, and 100 %), (D) flow rate (0, 7.5, 140, and 280 mL/min). Additionally, a peristaltic pump was connected to the two electrodes using a silicone tube to generate fluid flow. The default parameters applied to all experiments, except for the parameter being intentionally varied, include a 60 mm electrode distance, room temperature, 0 rpm flow rate, and 100 % PBS^- concentration. This figure has been adapted from the previous publication by Choi et al., under the terms of the Creative Commons Attribution (CC BY) license [156].

As shown in the Figure 4.6A, the impedance baseline (at frequency 794.33 Hz) was risen with increasing electrode distance from 2.96 $\text{k}\Omega$ at 30 mm to 18.19 $\text{k}\Omega$ at 200 mm distance. An average of $974.15 \pm 61.51 \Omega$ increased by the distance getting 10 mm longer. The electrode impedance became prominent moving into the low frequency range (30 Hz to 1 Hz) at all other distances. Accordingly, the phase between 1 Hz to 30 Hz tended to increase as the distance between the two electrodes increased (Figure 4.6B). The phase at 1 Hz was -2.46° at 30 mm

and rose to -0.40° at 200 mm. Unexpectedly, the impedance increased with increasing frequency at the high frequency range (10 kHz to 100 kHz). Furthermore, the increment was greater as the distance between the electrodes increased. The changes were also observed in phase graph (Figure 4.6B), the phase of the high frequency range (10 kHz to 100 kHz) was decreased by increasing the distance.

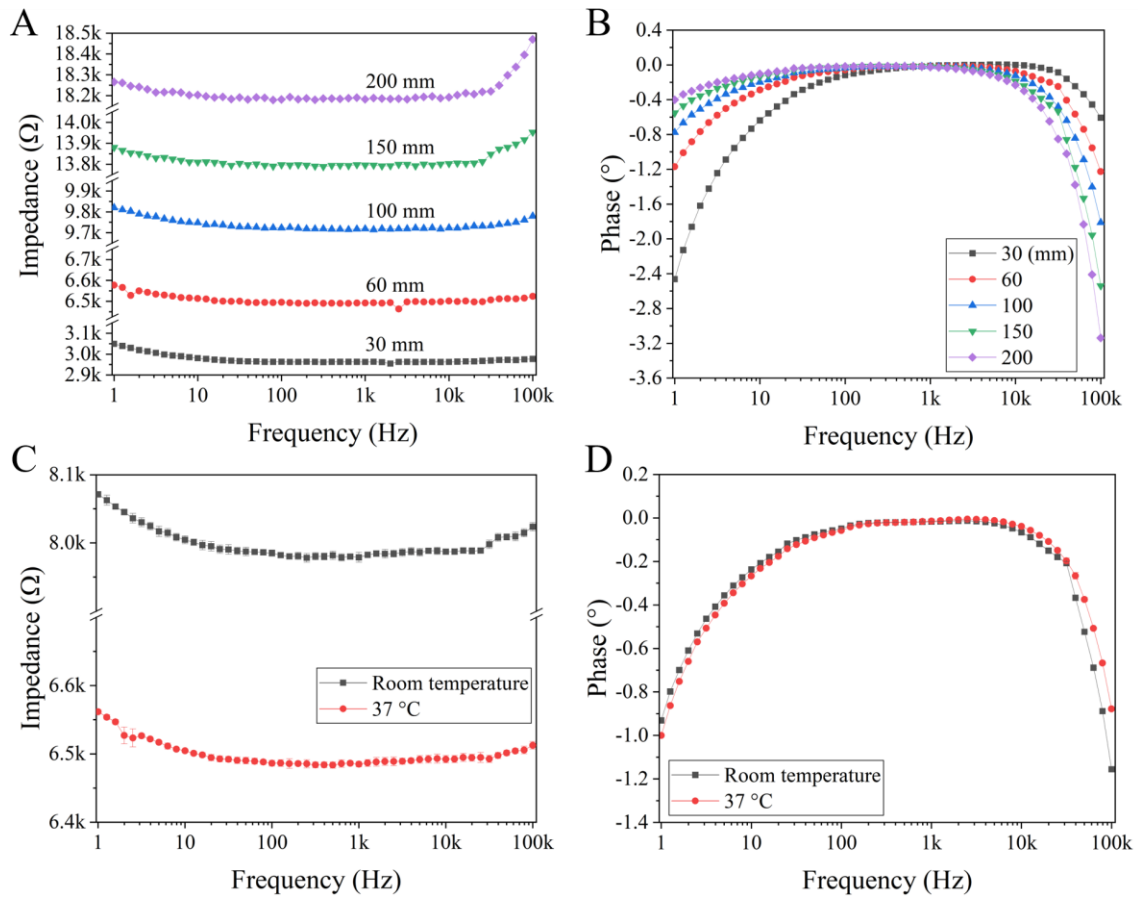


Figure 4.6. EIS results from the investigation of impact parameters (1). The experimental setup is depicted in Figure 4.5. (A and B) EIS measurements were carried out at varying distances between two electrodes: 30, 60, 100, 150, and 200 mm. The (A) impedance and (B) phase Bode plots are presented as a result. (C and D) The EIS measurements were conducted at temperatures ranging from room temperature to 37 $^\circ\text{C}$. The results include Bode plots for (C) impedance and (D) phase. The total impedance increased with increasing distance between the electrodes and decreasing temperature. The results of the electrode distance variation experiments were obtained from a single trial each. The temperature variation experiment was conducted three times for technical replication and was represented by the mean and standard deviation. This figure has been reproduced from the previous publication by Choi et al., under the terms of the Creative Commons Attribution (CC BY) license [156].

The Figure 4.6C shows impedance response according to temperature changes. The baseline (at frequency 2.5119 kHz) of room temperature was $7.98 \pm 0.005 \text{ k}\Omega$ but decreased to $6.48 \pm 0.006 \text{ k}\Omega$ by increasing temperature to $37 \text{ }^\circ\text{C}$. Unlike the electrode distance variation test, the phase angles at both room temperature and $37 \text{ }^\circ\text{C}$ were similar across the frequency ranges (Figure 4.6D). EIS was conducted with the same electrochemical cell while varying electrolyte concentration (Figure 4.7A and B). The impedance at frequency 31.623 kHz, being a baseline, was taken for comparison (Figure 4.7A).

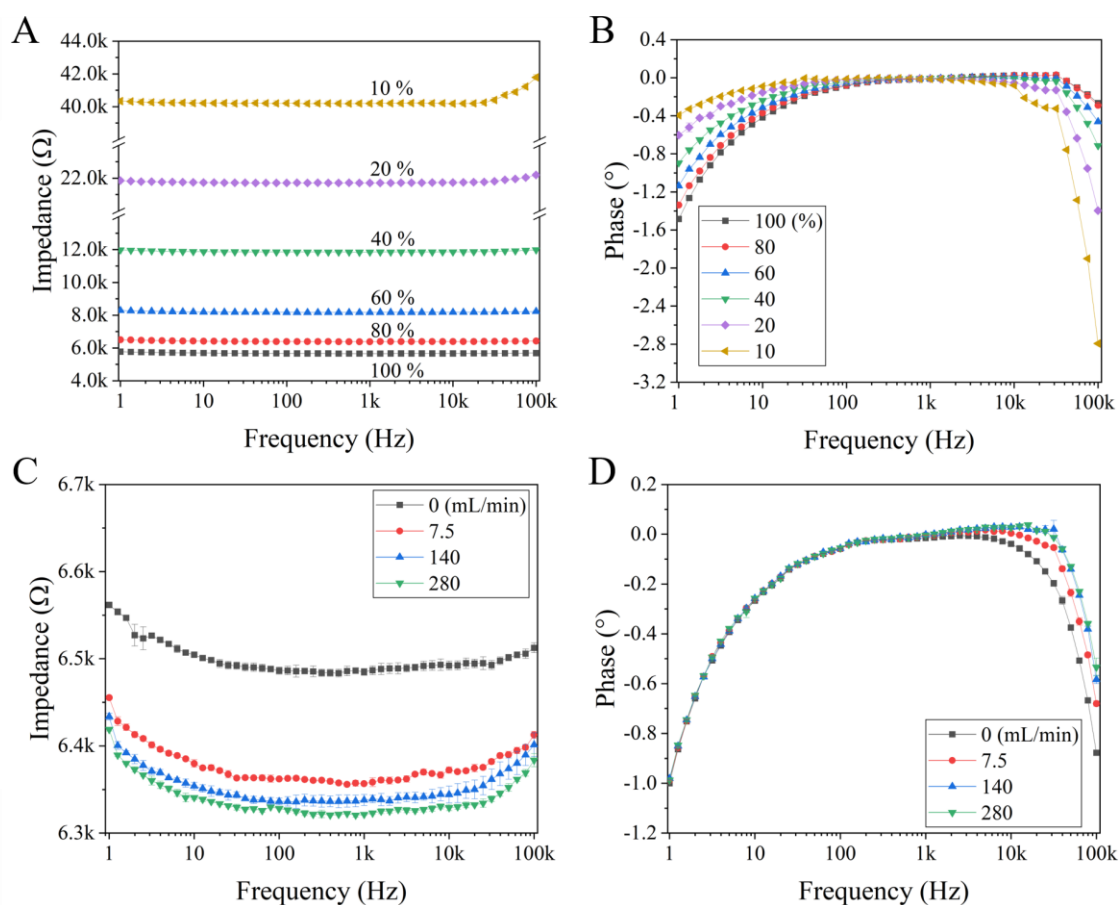


Figure 4.7. EIS results from the investigation of impact parameters. (2). This is a continuation from Figure 4.6. (A and B) EIS measurements were conducted with varying concentrations of the electrolyte (PBS^-): 10, 20, 40, 60, 80, and 100 %. The results include Bode plots for (A) impedance and (B) phase. (C and D) EIS measurements were performed with different flow rates: 0, 7.5, 140, and 280 mL/min. The findings incorporate Bode plots illustrating (C) impedance and (D) phase. Electrolyte concentration and flow rate variations affected impedance and phase shifts with frequency. Each experiment was conducted three times for technical replication, and the mean and standard deviation were calculated from three replicates. The Figure (C) and (D) were reproduced from previous publication Choi et al., under the terms of the Creative Commons Attribution (CC BY) license [156].

As a result, 100 % impedance was started at $5.67 \pm 0.008 \text{ k}\Omega$. Subsequently, the impedance exhibited exponential growth as the concentration of PBS⁻ decreased. The impedance followed an increasing trend, reaching $6.39 \pm 0.003 \text{ k}\Omega$ at 80 %, $8.19 \pm 0.03 \text{ k}\Omega$ at 60%, and $11.88 \pm 0.045 \text{ k}\Omega$ at 40 %. Continuously, the impedance increased to $21.81 \pm 0.108 \text{ k}\Omega$ at 20 % and reached $40.40 \pm 0.158 \text{ k}\Omega$ at 10 %. Like the electrode distance test, phase change at low frequency and high frequency appeared by changing PBS⁻ concentration (Figure 4.7B). The phase at 1 Hz gradually increased from $-1.48 \pm 0.001^\circ$ at 100 % to nearly 0° as the concentration decreased. Oppositely, the phase at 100 kHz decreased from $-0.27 \pm 0.001^\circ$ at 100 % until $-2.79 \pm 0.010^\circ$ at 10 % by reducing concentration. Lastly, EIS was conducted at three different flow rates to investigate the influence of flow rate on the impedance of the electrochemical cell (Figure 4.7C and D). As the pump started at 7.5 mL/min, the impedance dropped by 128.22Ω from $6.48 \pm 0.006 \text{ k}\Omega$ of the static state (0 mL/min) to $6.36 \pm 0.001 \text{ k}\Omega$. Impedance decreased continuously from $6.34 \pm 0.006 \text{ k}\Omega$ at 140 mL/min to $6.32 \pm 0.002 \text{ k}\Omega$ at 280 mL/min. Overall, the results show a decreasing trend. The rate of decrease in each step got lower with increasing flow rate. The phases of each different flow rate were similar within the frequency range of 1 Hz to 10 kHz. In the high frequency range (10 kHz to 100 kHz), the phase appeared to increase with an increase in flow rate.

4.2. Electrode Application 1: A Chip Bioreactor

The first application of TiN-coated tube electrodes was a chip bioreactor. The novel PDMS-based bioreactor was developed to provide a more physiological environment than ordinary culture conditions by stimulating the shear stress-sensitive cells mechanically. On the other hand, a non-invasive monitoring system was required to monitor cells' functionality during bioreactor culture, because of its closed system. EIS is one of the valuable techniques allowing non-invasive methods. Therefore, the TiN-coated tube electrode system was implemented into the chip bioreactor system. As the PDMS-based chip bioreactor, newly developed by Dr. Tobias Schmitz, was implemented, the system setup, including TiN-coated tube electrodes, was optimized for bioreactor culture. Furthermore, the hiPSCs-derived BCECs were cultured in the bioreactor to test the monitoring system whether the real-time monitoring of barrier integrity is possible. In this context, dynamic culture is defined as cell culture in a bioreactor under fluid flow conditions, while static culture refers to cell culture in a transwell plate without fluid flow.

4.2.1. Optimization of Chip Bioreactor System with TiN-Coated Tube Electrodes

Bioreactor manufacturing based on 3D printing technique and PDMS casting caused cost-efficient and reproducible bioreactor for dynamic culture. A sophisticatedly 3D-printed part with defined geometries was reusable and contributed to generating multiplicities of negative silicone molds. Also, it required less than 30 mins for silicone casting. Therefore, according to needs, several bioreactors could be easily produced at the same time. The chip bioreactor was mainly composed of two bioreactor chambers made by PDMS and a chip insert. As shown in Figure 4.8A, the two PDMS bioreactor chambers are symmetric except for the tongue and groove joints. After completing the PDMS bioreactor chambers through PDMS casting, oxygen plasma treatment was applied to render the initially hydrophobic surface hydrophilic.

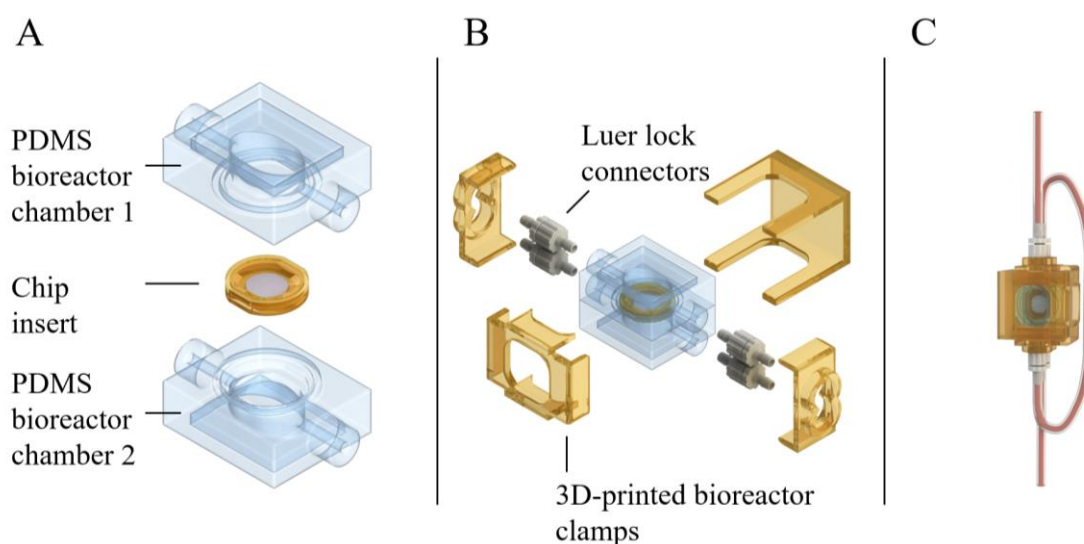


Figure 4.8. 3D graphical view of a chip bioreactor. (A) The chip insert is positioned between two chambers, providing a customizable platform for constructing an experimental setup with two separate compartments. (B) The assembly of the bioreactor involves the tight closure of the two chambers using 3D-printed bioreactor clamps. Luer lock connectors are used to connect the chambers to the tubing. (C) Completed chip bioreactor shown in assembled view. This figure has been reproduced from the previous publication Choi et al., originally created by Dr. Tobias Schmitz, under the terms of the Creative Commons Attribution (CC BY) license [156].

This modification was implemented due to the observed tendency of the hydrophobic surface to readily trap bubbles generated within the bioreactor system. Since the air bubble in the bioreactor interrupts not only the nutrient supply to cells but also EIS measurement, it must be avoided. In the Figure 4.8A, the culture membrane (Oxyphen, 0.4 μm pore size) was glued using PDMS in between two 3D-printed frames by evenly stretching.

Thus, completed framed culture membranes, called chip insert, enabled cell culture in transwell plates and chip bioreactors, which also meant a simple transfer from static culture protocols to the dynamic culture and vice versa. Also, the 3D-printed frame was made of autoclavable material (Dental SG FLDGOR01), giving it an advantage in terms of reusability. Lastly, the 3D-printed bioreactor clamps tightened the main three compartments, two PDMS chambers and a chip insert, thereby avoiding leaks (Figure 4.8B).

The setup of the bioreactor system for cell culture and non-invasive monitoring has been optimized. Figure 4.9 shows the overall flow scheme of bioreactor system. In this study, two flow regime were generated considering future study such as transport study. Each flow circuits were completely separated by inserting the chip inserts in between bioreactor chambers.

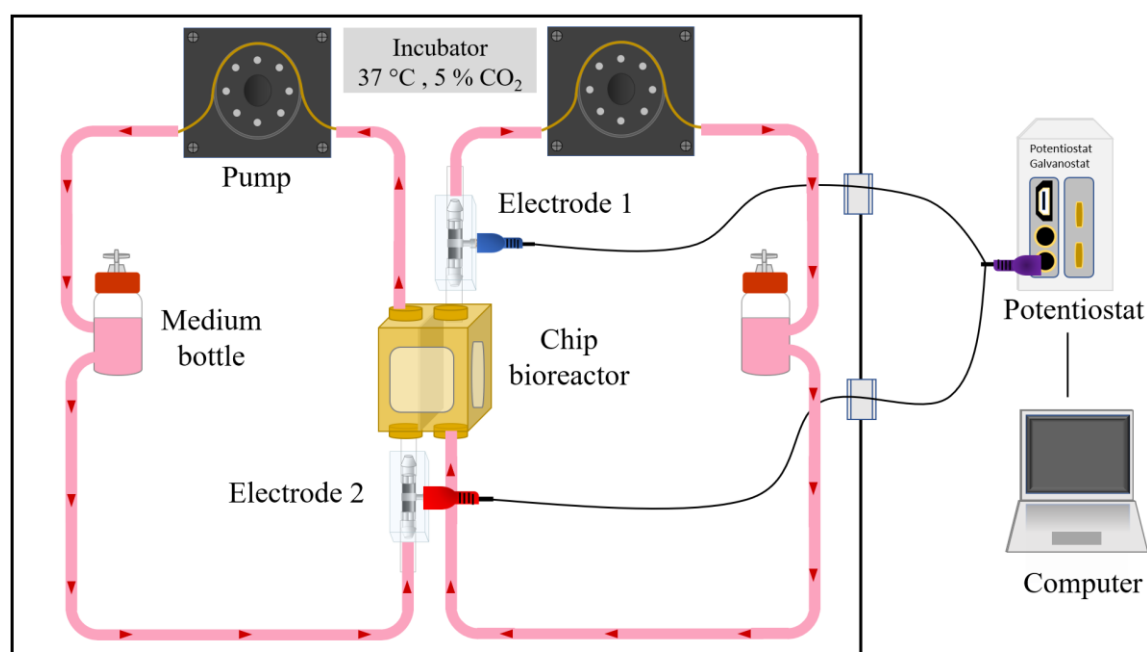


Figure 4.9. Schematic diagram of chip bioreactor system with EIS. Two separate flow circuits pass through the apical and basolateral compartments of the chip bioreactor, with fluid flowing in a co-current pattern. TiN-coated tube electrodes were positioned at the entrance of each compartment. The chip bioreactor systems were operated in an incubator. Electrodes 1 and 2 are connected to external devices, including an Autolab PGSTAT 204 potentiostat and a computer, for measuring EIS. This figure has been modified from the previous publication Choi et al., under the terms of the Creative Commons Attribution (CC BY) license [156].

The TiN-coated tube electrodes were placed next to each PDMS bioreactor chamber and both electrodes stood on a diagonal line with each other. The Figure 4.10 shows a photograph of a

bioreactor with hiPSCs-derived BCECs installed in a tailored incubator system. The bioreactor was positioned on a dedicated bioreactor stander (Figure 4.10A, ③) printed using a 3D printer. The advantage of using a vertical postured bioreactor stander was to prevent bubbles from getting stuck in the bioreactor and electrodes. In very rare cases, if air bubbles became trapped on the bioreactor or electrodes, they could be easily observed through transparent PDMS and removed by tapping (Figure 4.10B). The bottle holder (Figure 4.10A, ⑥) helped to keep the medium bottle stable, reducing the risk of air filter (Figure 4.10A, ⑦) contamination caused by the medium bottle lying or tilting during handling. For EIS measurement, the tailored incubator was modified whereby making holes in the wall and implementing adapters (Figure 4.10A, ⑧).

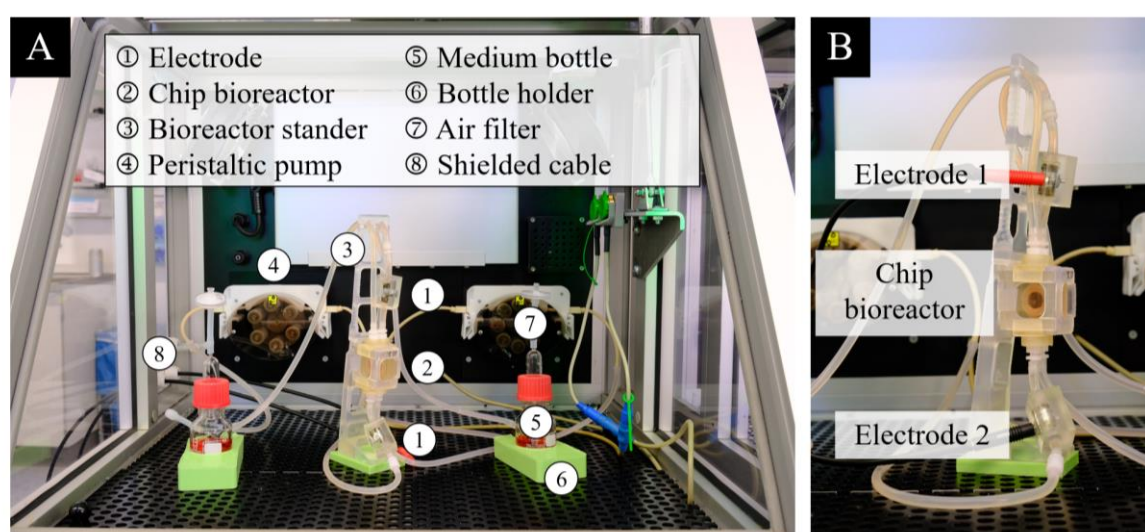


Figure 4.10. Photographs of the chip bioreactor system in a custom incubator system. (A) An overall view. (B) A close-up view focused on the chip bioreactor and electrodes.

The Black PVC EHT cable was threaded through adapters, with one end of the cable connected to the EIS potentiostat on the exterior, while the other end was connected to the electrodes on the interior of the incubator. This enables automated EIS measurements without the need to open the incubator. Furthermore, Black PVC EHT cables help to reduce magnetic field interference.

4.2.2. Electrochemical Impedance Spectroscopy Analysis of Blood Brain Barrier

BCECs were differentiated from hiPSCs line IMR90-4 for 10 days. After day 10 of differentiation, the BCECs culture was extended in the chip bioreactor. The dynamic culture was conducted with a controlled flow rate of 0.3 mL/min. As mentioned in previous section 4.2.1, it was possible to transfer from static to dynamic culture without modifying

conventional static culture protocol by using the chip insert that can be used for both static and dynamic cultures.

EIS measurements were conducted at 0, 2, 4, and 6 h after cell seeding, followed by subsequent measurements every 24 h to monitor the barrier integrity during dynamic culture. Simultaneously, the transwell culture was accompanied to compare cellular barriers in static and dynamic culture conditions. The measuring plate with TiN electrode was used for EIS measurement of a transwell-based model (Figure 3.5), and the EIS measuring time point was the same as dynamic culture. Initially, BCECs were cultured in quadruplicate for 48 h under dynamic and static conditions. After observing that the bioreactor system worked properly with BCECs, the culture time was extended to 7 days (168 h).

4.2.2.1. Electrochemical Impedance Spectroscopy Data Analysis in Static and Dynamic Culture

In this section, the results of a 48 h impedance experiment are presented with the intention of examining how the BCECs dynamic flow culture system is represented across the frequency spectrum through EIS. Furthermore, the study aims to determine whether the impedance responses of each system component are represented in frequency ranges comparable to those of a static culture system, despite the relative complexity of the dynamic culture system. In this context, static culture refers to cell culture in a transwell plate without fluid flow, while dynamic culture is defined as bioreactor culture under fluid flow conditions. Once again, the primary focus here is not on interpreting the integrity of the BCECs barrier using impedance results; instead, this aspect will be addressed in the subsequent section (Section 4.2.2.2). The Figure 4.11 depicts the Bode plots obtained from EIS measurement in a dynamic (Figure A and B) and static culture (Figure C and D), which were conducted in parallel. In Bode plot (impedance versus frequency), the baseline impedance at the frequency where the phase close to 0° , was subtracted over frequency range, then the impedance value was normalized by porous membrane area. The geometrical surface area of the chip membrane was 0.95 cm^2 , and the inserts membrane for static culture was 0.33 cm^2 . In the EIS measurement of dynamic culture (Figure 4.11A and B), the medium culture resistance was dominated at approximately the high frequency range (1 kHz to 10 kHz). In Figure 4.11A, the impedance values of the dynamic culture at 3.1623 kHz were set to 0 through baseline subtraction across all frequency ranges. This adjustment was made as the primary focus of the study was on determining barrier integrity. The impedance reflecting the BCECs was detected across the middle frequency range (approximately 5 Hz to 1 kHz). When compared to the blank, which

represents the bioreactor system without cells, the bioreactor system cultured with BCECs apparently demonstrated an increase in impedance within the middle frequency range.

The electrode impedance started to appear in the spectrum at the frequency approx. 1 Hz to 5 Hz. Each component impedance (electrode impedance, cellular barrier impedance, and cell culture medium impedance) of the static culture system (Figure 4.11C) was plotted on frequency ranges comparable to the dynamic culture system (Figure 4.11A).

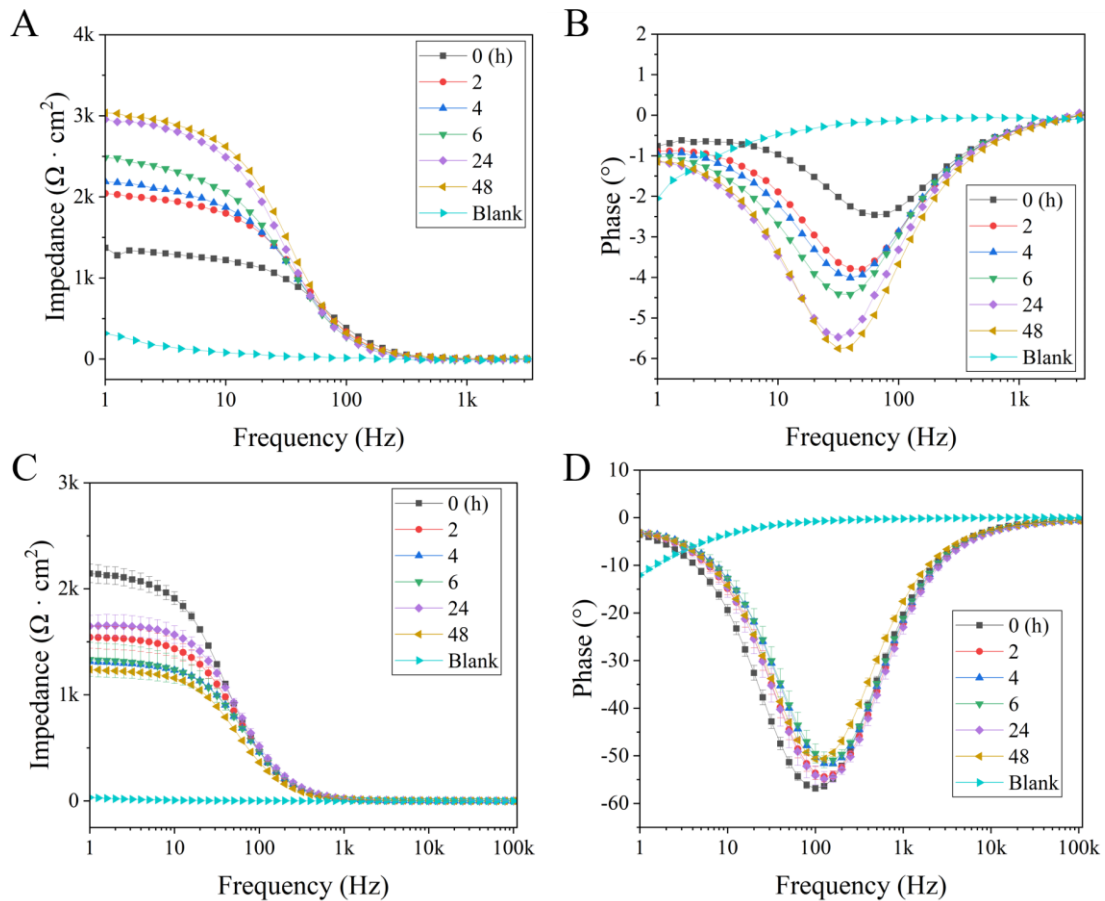


Figure 4.11. Comparing EIS data over 48 h in dynamic and static culture. (A and B) represent EIS results of dynamic culture. (A) Impedance was plotted as a function of frequency (1 Hz to 3.1623 kHz) after subtracting the baseline impedance at 3.1623 kHz and normalizing it by the surface area of the porous membrane (0.95 cm^2) (B) Phase Bode plot was obtained in the frequency range 1 Hz to 3.1623 kHz. (C and D) depict EIS results of static culture. (C) Impedance was plotted as a function of frequency (1 Hz to 100 kHz) after subtracting the baseline impedance at 100 kHz and normalizing it by the surface area of the porous membrane (0.33 cm^2). (D) Phase Bode plot was represented over the frequency range (1 Hz to 100 kHz).

The phase shift in the middle frequency was smaller in dynamic culture than in static culture due to the bigger geometrical surface area of a chip insert of the chip bioreactor than the

membrane of the insert used for static culture. The lowest phase angle over EIS measurement time was approx. -2° to -6° in dynamic culture, on the other hand, approx. -45° to -60° in static culture.

4.2.2.2. Quantification of Barrier Integrity of Blood Capillary Endothelial Cells

After the verification that electrode system enabled the measurement of the barrier function of BCECs through EIS in a 48 h experiment, the BCECs culture was extended to 7 days in both dynamic and static culture to conduct a more specific examination of electrical barrier function characterization. Each part comprising the chip bioreactor system, the TiN-coated tube electrodes, the BCECs layer, and the cell culture medium was modelled using known equivalent circuit elements to quantify useful electrical parameters. As shown in Figure 4.12, the equivalent circuits corresponding chip bioreactor system was constructed with a resistor (R_M) representing culture medium resistance and constant phase element (CPE) representing TiN-coated tube electrode impedance.

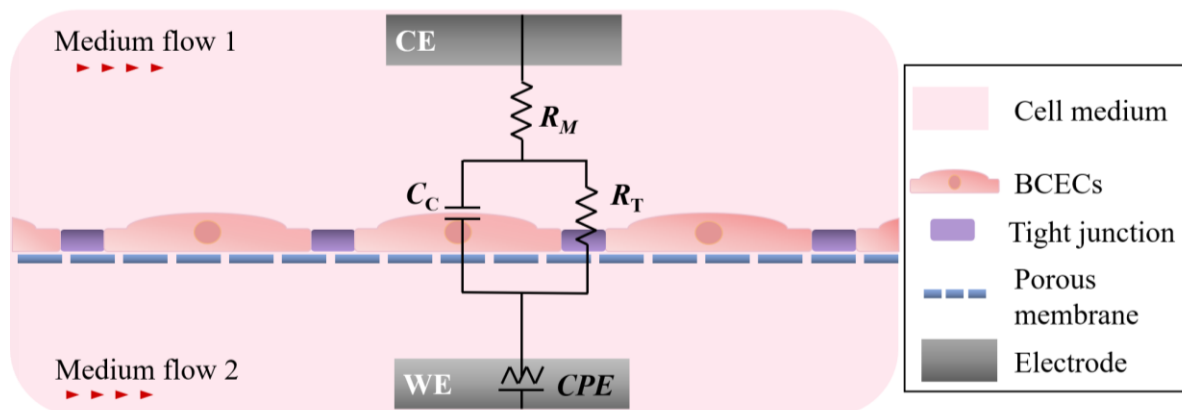


Figure 4.12. Illustration of the equivalent circuit model for bioreactor culture. It includes a constant phase element (CPE) to model the double layer capacitance of the electrode, a resistor (R_M) for the culture medium, and a parallel combination of a resistor (R_T) and a capacitance (C_C) to represent the electrical barrier function of the hiPSC-derived BCECs. These are connected in series with the CPE and R_M .

The BCECs layer was modelled with a parallel connection of a resistor (R_T) and a capacitor (C_C) where R_T is tight junction barrier resistance and C_C is cell membrane impedance. Therefore, the obtained impedance data from EIS measurement was fitted to the equivalent circuit using the Nova 2.1.4 software. Example raw data of fitting results for both dynamic and static cultures were captured and are depicted in Appendix B (Figure B.1).

As a result, the electrical parameters, R_T and C_C , were obtained. Due to resistance being inversely proportional to the cross-section area (Equation 1.18) the R_T was normalized by the geometrical surface area (chip insert membrane: 0.95 cm^2 , transwell inserts: 0.33 cm^2) of culture membrane to compare the static and dynamic culture. Conversely, the capacitance is proportional to the cross-section area (Equation 1.20), the C_C values were divided by the membrane surface area. The normalized R_T and C_C are represented in Figure 4.13A and B over the culture time.

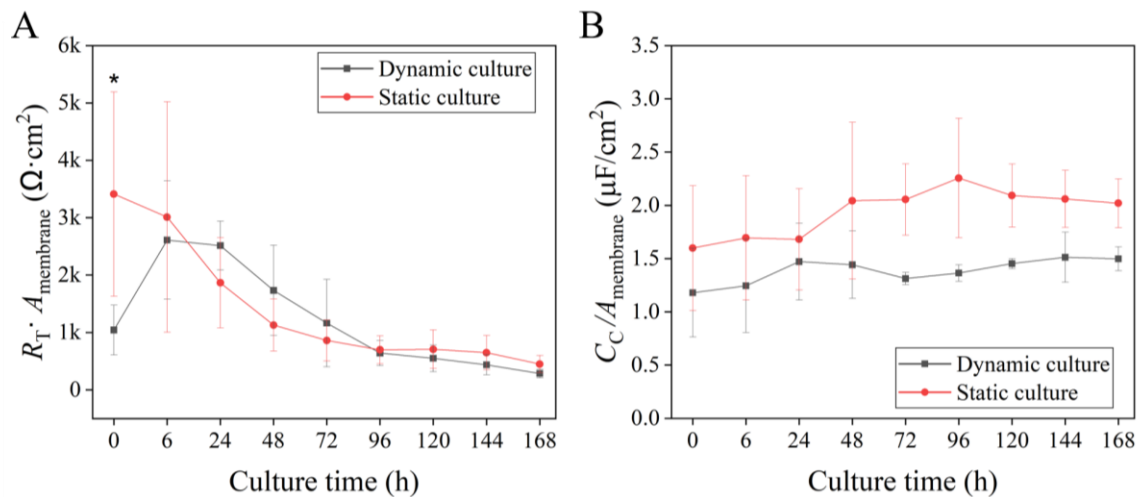


Figure 4.13. Barrier integrity of BCECs cultured in dynamic and static culture. (A) Tight junction resistance, R_T , were obtained over culture times by fitting and simulating EIS data with equivalent circuit model. (B) Cell membrane capacitance, C_C , were quantified over culture times by fitting and simulating EIS data. Normalized R_T and C_C values were plotted over time, with surface area of the porous membrane used for normalization. Except for the significant difference ($p < 0.05$) in R_T at 0 h between static and dynamic cultures, which can be attributed to the adaptation of BCECs to the dynamic culture environment, the R_T and C_C values were comparable between dynamic and static cultures during the 7-day culture period. The experiment was conducted with seven biological replicates from 0 to 48 h and three biological replicates from 48 h to 168 h. One-way ANOVA with Tukey's post hoc comparison test was conducted using OriginPro 2021b to compare electrical parameters over culture time in static and dynamic cultures, $p < 0.05$ (*). This figure has been reproduced the previous publication Choi et al., with under the terms of the Creative Commons Attribution (CC BY) license [156].

The EIS measurement started as soon as the bioreactor assembly, including BCECs cultured chip insert, was installed in the tailored incubator and filled the medium. Thus, the first measurement was designated to 0 h. At 0 h, there were substantial differences between static and dynamic culture. R_T of dynamic culture was $1.042 \pm 0.433 \text{ k}\Omega \cdot \text{cm}^2$. The static culture showed $3.411 \pm 1.779 \text{ k}\Omega \cdot \text{cm}^2$. The initial adaptation of BCECs to dynamic culture resulted in a significant reduction in tight junction resistance. The tight junction resistance recovered to

the originated state post-stabilization. Thereby, the R_T reached $2.609 \pm 1.029 \text{ k}\Omega \cdot \text{cm}^2$ at 6 h under the dynamic culture.

The R_T began to drop in both dynamic and static culture after 6 h, the value at 24 h was $1.865 \pm 0.786 \text{ k}\Omega \cdot \text{cm}^2$ and $2.513 \pm 0.424 \text{ k}\Omega \cdot \text{cm}^2$, respectively. Afterward, the R_T of dynamic culture decreased substantially until $641 \pm 219 \Omega \cdot \text{cm}^2$ at 96 h. The reduction of tight junction resistance was also shown in static culture, and reached to $697 \pm 244 \Omega \cdot \text{cm}^2$ at 96 h. The tight junction resistance kept dropping until 168 h in both dynamic and static conditions. Consequently, the final R_T value was $285 \pm 76 \Omega \cdot \text{cm}^2$ in dynamic culture and $449 \pm 149 \Omega \cdot \text{cm}^2$ in static culture.

Another equivalent circuit element, a capacitor, was modelled to represent the capacitance of the cell membrane. As with R_T , the capacitance of the cell membrane was quantified by fitting and simulating the impedance data (Figure 4.13B). The C_C of dynamic culture at 0 h was $1.18 \pm 0.42 \mu\text{F}/\text{cm}^2$. The value increased slightly to $1.47 \pm 0.36 \mu\text{F}/\text{cm}^2$ for 24 h and decreased to $1.31 \pm 0.06 \mu\text{F}/\text{cm}^2$ at 72 h. After that, C_C increased again reaching $1.49 \pm 0.11 \mu\text{F}/\text{cm}^2$ at 168 h. In static culture, C_C was raised from $1.59 \pm 0.58 \mu\text{F}/\text{cm}^2$ at 0 h via $1.68 \pm 0.47 \mu\text{F}/\text{cm}^2$ at 24 h through to $2.25 \pm 0.56 \mu\text{F}/\text{cm}^2$ at 96 h. After that, the capacitance decreased slightly to $2.02 \pm 0.22 \mu\text{F}/\text{cm}^2$ at 168 h. Compared to 0 h, the capacitance showed a high value at 168 h for both static and dynamic cultures. In addition, the average of the fitting error values for all results was calculated. The fitting errors for R_T and C_C were 0.7 % and 0.8 %, respectively, in static culture. In dynamic culture, the fitting errors were 6.59 % for R_T and 14.12 % for C_C .

Table 4.2. *CPE* parameters obtained from dynamic culture. The results were adapted from the previous publication Choi et al., under the terms of the Creative Commons Attribution (CC BY) license. (Biological replicates, $N = 7$)

Dynamic culture		
	Mean	SD
<i>CPE</i> admittance, Y_0 [$\text{S} \cdot \text{s}^n$]	8.84×10^{-4}	4.42×10^{-4}
n ($0 < n < 1$)	0.65	0.09

The mean of R_T and C_C from 7 replicates (4 replicates for 48 h and 3 replicates for 168 h in both dynamic and static cultures) were represented in the Appendix C (Table C.1). Additionally, the electrode capacitance remained stable with a mean of *CPE* admittance of $8.84 \times 10^{-4} \text{ S} \cdot \text{s}^n$ during 7 replicates (Table 4.2).

4.2.3. Analysis of Immunofluorescent Images

After 7 days of culture of BCECs under dynamic and static culture, the tight junction protein expression was investigated by immunofluorescent using specific protein markers such as Occludin, ZO-1, and GLUT-1.

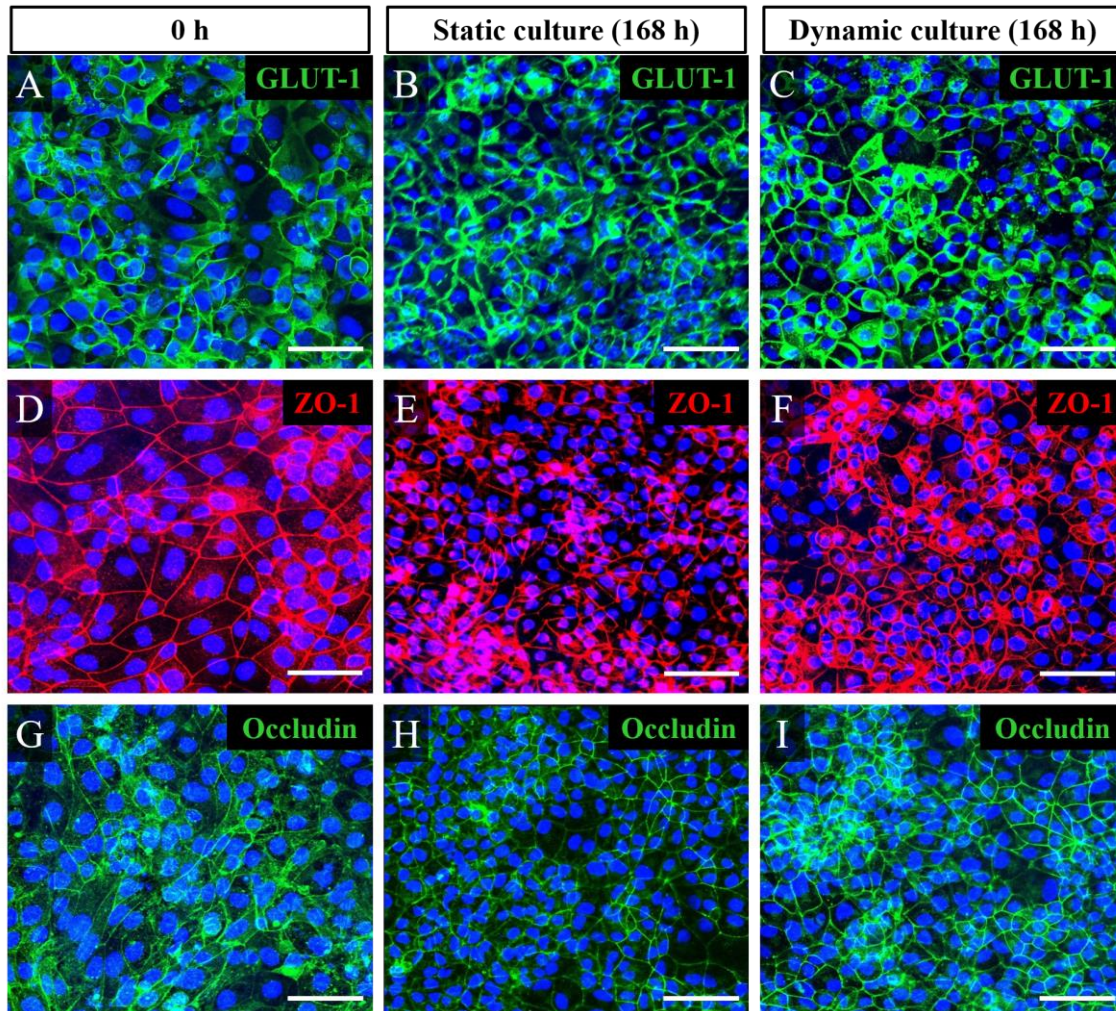


Figure 4.14. Immunofluorescence analysis of BCECs. Immunofluorescence staining of Glucose transporter-1 (GLUT-1, green), Zonula occludens (ZO-1, red), and Occludin (green) in static and dynamic cultures at 0 h and 168 h. (A, B, and C) GLUT-1 staining at (A) 0 h, (B) 168 h of static culture, and (C) 168 h of dynamic culture. (D, E, and F) ZO-1 staining at (D) 0 h, (E) 168 h of static culture, and (F) 168 h of dynamic culture. (G, H, and I) Occludin staining at (G) 0 h, (H) 168 h of static culture, and (I) 168 h of dynamic culture. In both static and dynamic conditions at 168 h, hiPSCs-derived BCECs exhibited an increase in nuclear condensation and upregulation of protein expressions of GLUT-1, ZO-1, and Occludin compared to 0 h. After 168 h of dynamic culture, the intensity of protein expression at the cell-cell borders was stronger and showed a continuous pattern compared to static culture. The fluorescent images were captured with 40 \times magnification and scale bar 50 μ m. The images presented in this figure are representative of three biological replicates ($N = 3$). This figure has been adapted from the previous publication Choi et al., under the terms of the Creative Commons Attribution (CC BY) license [156]. The histology and immunofluorescent imaging were performed by Dr. Sanjana Mathew.

Using immunofluorescence, the objective was to verify the stability of the chip bioreactor system and assess whether dynamic culture affects cellular barrier characteristics. The complete cell layers remained after 168 h dynamic culture on the chip insert. This observation proved that the bioreactor system is applicable and suitable for BCECs culture. In addition, the DAPI size of BCECs after 168 h dynamic culture (Figure 4.14C, F, and I) and static culture (Figure 4.14B, E, and H) became smaller, consequently, seemed more compact and tightly packed than BCECs at 0 h (Figure 4.14A, D, and G).

For detailed investigation, the DAPI 's number of each condition's images was counted using Fiji software program. According to DAPI counting (Table 4.3), the number of cells at 0 h was 204.22 ± 64.00 , while the cell number rose to 298.77 ± 30.00 after in 168 h static culture and to 291.77 ± 74.00 in 168 h dynamic culture. Furthermore, the expression pattern of ZO-1 (Figure 4.14F), and Occludin (Figure 4.14I) at the cellular border was smoother and thinner in 168 h dynamic conditions compared to 0 h (Figure 4.14D, and G).

Table 4.3. Analysis of DAPI counting of hiPSCs-derived BCECs. The results were adapted from the previous publication Choi et al., under the terms of the Creative Commons Attribution (CC BY) license [156].

DAPI counting		
	Mean	SD
0 h	204.22	64.00
Static culture (168 h)	298.77	30.00
Dynamic culture (168 h)	291.77	74.00

Moreover, the expression of GLUT-1 (Figure 4.14C) was less cytoplasmic localization in 168 h dynamic conditions than at 0 h (Figure 4.14A). The expression pattern shown in 168 h static conditions (Figure 4.14B, E, and H) was similar to 168 h dynamic conditions (Figure 4.14C, F, and I). However, the marker expression of 168 h static conditions (Figure 4.14B, E, and H) was not homogenous and was fragile at the membrane.

4.3. Electrode Application 2: A Miniature Hollow Fiber Bioreactor

TiN-coated tube electrode was also used in another type of perfusion bioreactor, namely the miniature HFBR. This was done to test the versatility of the TiN-coated electrode. Miniature HFBR consists of 15 hollow fibers that are securely fixed in a solid housing. However, due to its structure, verifying cell growth on the fibers while operating the bioreactor can be

challenging. In such cases, the bioreactor may run unnecessarily, leading to wasted operating costs and time. Therefore, a non-invasive method is necessary to avoid these disadvantages. The TiN-coated tube electrode was implemented to a miniature HFBR to inspect if the electrode system capable of monitoring cell growth during the HFBR culture. Cell lines of HUVECs and Caco-2 were used for the test. Before conducting EIS measurements on the miniature HFBR, EIS measurements on both HUVECs and Caco-2 cells in the transwell culture as a reference.

4.3.1. Barrier Integrity of Human Umbilical Vein Endothelial Cells

4.3.1.1. Reference Impedance Spectroscopy measurement for Barrier Integrity of Human Umbilical Vein Endothelial Cells

The bioreactor system is considered more complex than the transwell culture system due to the unavoidable long distance between two electrodes caused by the length of the bioreactor, the flow environment, and the high cell culture surface area. Consequently, the EIS measurements in the transwell culture were required as a reference to help interpret the EIS measurements in the miniature HFBR.

Electrochemical Impedance Spectroscopy Analysis

EIS measurement was performed on culture days 1, 2, 4, 6 and 9 in transwell culture. The frequency range of 1 Hz to 1 MHz was applied for EIS. Consequently, a Bode plot is demonstrated in Figure 4.15. It was confirmed that the impedance, equivalent to cellular barrier function (Tight junction resistance and cell membrane impedance), was detected dominantly between the frequency at approximately 1 kHz to 794 kHz (Figure 4.15A). The phase got lowered at the impedance of the cell membrane domain (frequency at 39 kHz to 794 kHz) as culture day increased (Figure 4.15C). To closely examine the detection of cell barriers, the phase plot represents frequencies ranging from 10 Hz to 1 MHz (Figure 4.15D). The phase was -0.63° on day 1 and decreased to -1.41° on day 4. Finally, the phase reached -2.2° on day 6 and was kept until culture day 9. As frequency decreased from 39 kHz to 1 kHz, the phase shifted close to 0° on all culture days, which meant of the tight junction resistance became dominant at the frequency ranges. Figure 4.15C shows that as the frequency decreased to 1 Hz, the phase approached a constant value of approximately -20° at all culture times, which can be attributed to the dominant electrode impedance. Figure 4.15A represents the impedance as a function of frequency. For better comparison, the impedance value at 794.33 kHz (baseline) was subtracted from the impedance values over the frequency range (1 Hz to 794.33 kHz).

As a result, the impedance values at 794.33 kHz set to 0 Ω . Figure 4.15B shows a frequency range of 10 Hz to 1 MHz for a more detailed examination of tight junction resistance changes over different culture times. At high frequencies (approximately 1 kHz to 794 kHz), the impedance of the barrier integrity increases as the frequency decreases compared to the control. In addition, the impedance gradually increased from day 1 to day 6 and then remained stable until day 9 of culture. Based on the EIS data in Figure 4.15, the electrical parameters were quantified through fitting and simulation using Nova 2.1.4 software.

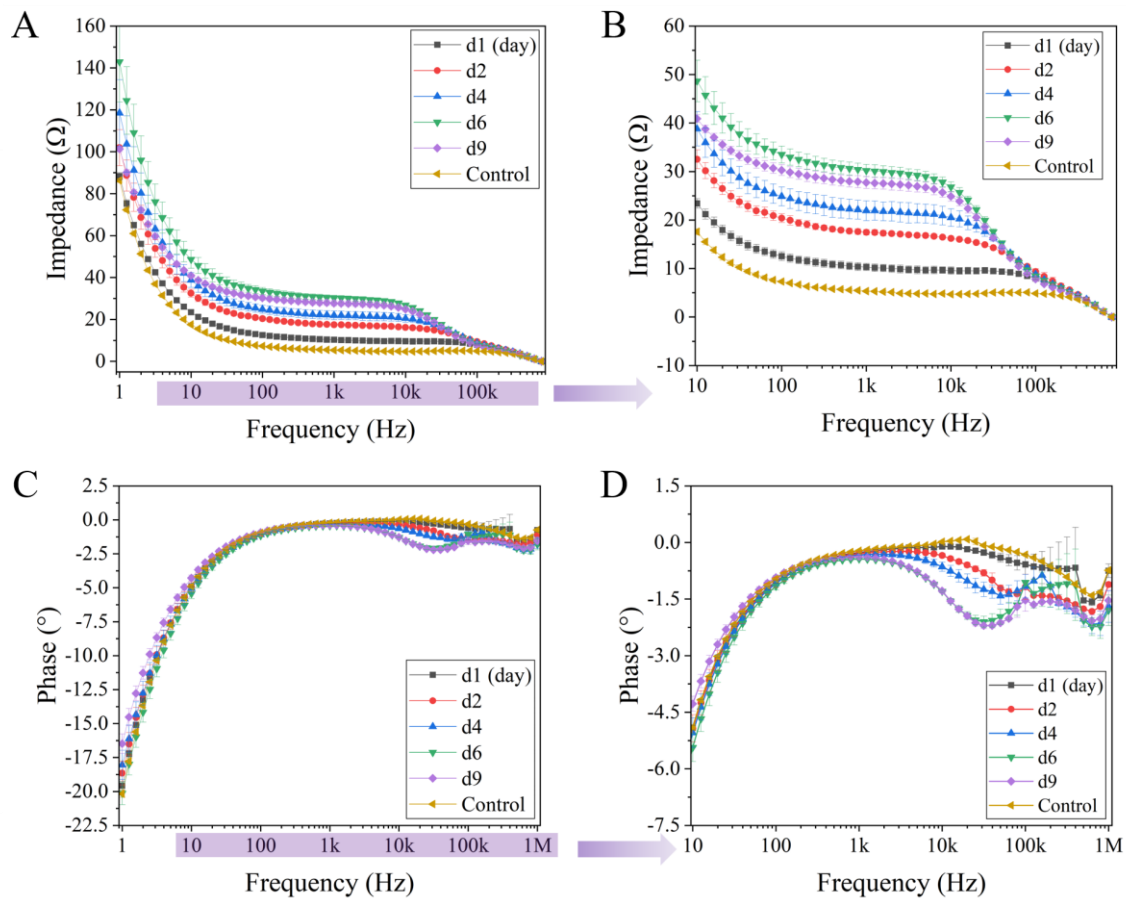


Figure 4.15. Referencing EIS results for HUVECs cultured in a transwell system. (A) The impedance was plotted as a function of frequency after subtracting the impedance baseline at 794 kHz. (B) To better observe the impedance corresponding to the barrier function, the impedance values between 10 Hz and 794 kHz were extracted from the Figure (A) and plotted separately. (C) The phase was plotted as a function of frequency from 1 Hz to 1 MHz. (D) The phase values between 10 Hz and 1 MHz were plotted separately to focus on the barrier function. The impedance and phase changes representing the electrical barrier function, tight junction resistance (R_T), and cell membrane capacitance (C_C) were detected between the frequency range of 39 kHz and 794 kHz from culture day 1 to day 9. The experiment was performed with three biological replicates ($N = 3$) and was represented by the mean and standard deviation.

The equivalent circuit had the same design as that of BCECs in static culture (Figure 3.5D). The fitting results are depicted in the Figure 4.16. Tight junction resistance, R_T , was $4.12 \Omega \cdot \text{cm}^2$ on day 1. The impedance kept rising to $6.55 \Omega \cdot \text{cm}^2$ on day 4 and reached $8.51 \Omega \cdot \text{cm}^2$ on day 6. After day 6, the impedance stayed stable, so the impedance was $8.08 \Omega \cdot \text{cm}^2$ on day 9.

The electrical parameter representing cell membrane capacitance, C_C , showed the same trends as R_T over culture times. Starting C_C from $0.10 \mu\text{F}/\text{cm}^2$ on day 1, it gradually increased over the next days until day 6 to $0.47 \mu\text{F}/\text{cm}^2$, then the value stayed until day 9.

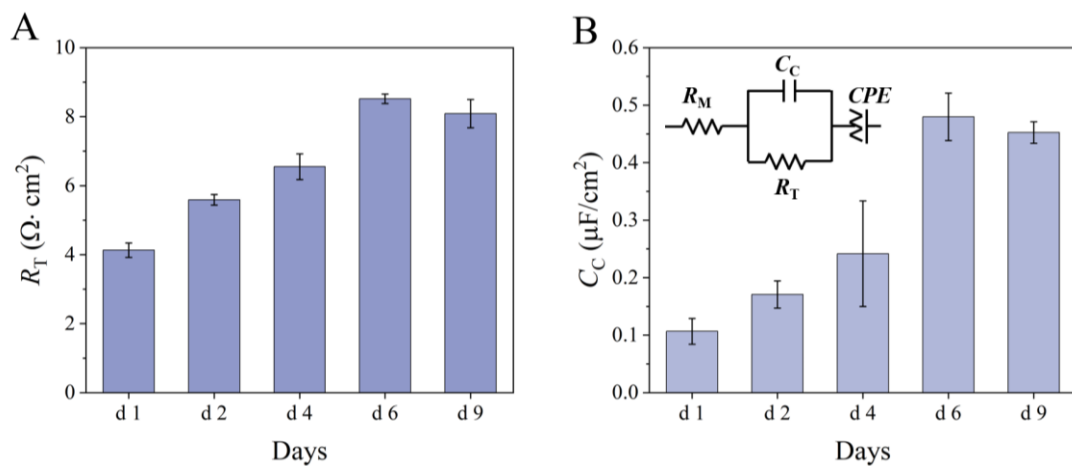


Figure 4.16. Fit and simulation of EIS data from HUVECs in static culture. The values obtained from fitting and simulation were normalized by the surface area (0.33 cm^2). (A) Tight junction resistance (R_T) as function of culture days. (B) Cell membrane capacitance (C_C) as function of culture days. The experiment was performed with three biological replicates ($N = 3$) and was represented by the mean and standard deviation.

Overall values, R_T and C_C , from Figure 4.16 were presented in Appendix D (Table D.1). In addition, Y_0 and n representing CPE elements were quantified. Y_0 containing electrode capacitance information was sustained with averaging $0.002 \text{ S} \cdot \text{s}^n$ during the cultures. The indicator of electrode inhomogeneity, n , was also stable, with an average value of 0.67 over culture time.

Analysis of Immunofluorescence Images

After finalizing EIS measurement on day 1 and 9, each cell samples were immunofluorescence using a ZO-1 protein marker and DAPI staining to analyze the cell's morphology over culture time. The immunofluorescent images were captured with magnification $20\times$ using immunofluorescence microscopy. The cell number increased day 9 (Figure 4.17B) compared

to day 1(Figure 4.17A). On day 1, although ZO-1 (green) was concentrated and localized in the cytoplasm, cell-cell contact had not yet been completely established (Figure 4.17C).

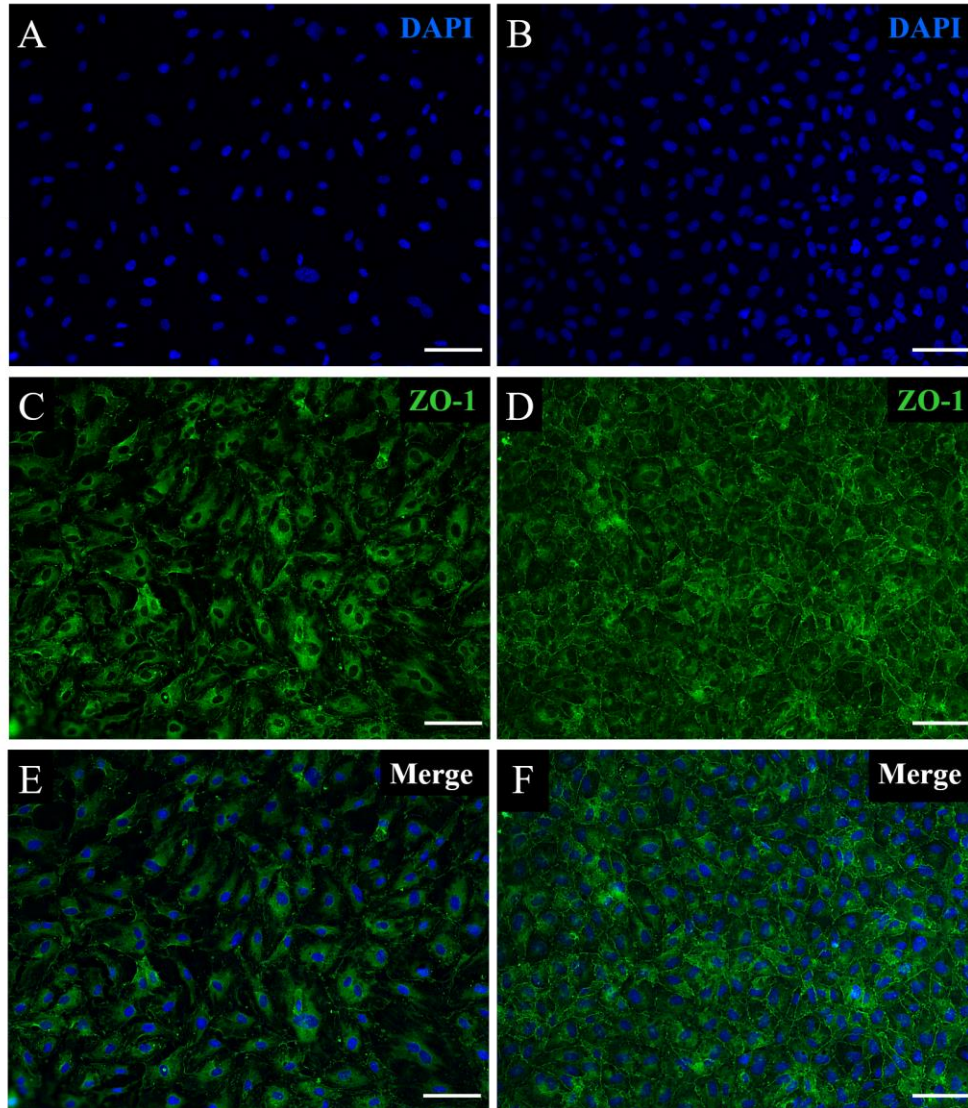


Figure 4.17. Immunofluorescence images of HUVECs in transwell culture. Day 1 images with channels for (A) DAPI staining (Blue), (C) Zonula Occludens-1 (ZO-1, Green), and (E) merged images. Day 9 images with channels for (B) DAPI staining (Blue), (D) ZO-1 (Green), and (F) merged images. The images were captured at a magnification of 20 \times and a scale bar of 100 μ m. The proliferation of HUVECs during day 9 cultures was observed by DAPI staining. On day 0, the ZO-1 protein was mostly expressed in the cytoplasm, whereas on day 9, its expression was prominent at the border of adherent cells, indicating the formation of tight junctions between cells.

On the other hand, on day 9, the ZO-1 was expressed in the tight junction of adjacent cells and the cytoplasm (Figure 4.17D). Despite the expression pattern of the tight junction observed at the overall adjacent cells, the boundary strands still had relatively thin and weak expressions.

4.3.1.2. Assessment of Barrier Integrity of Human Umbilical Vein Endothelial Cells in Miniature Hollow Fiber Bioreactor

TiN-coated tube electrodes were implemented to miniature HFBR. Miniature HFBR with TiN-coated tube electrodes were assembled in an incubator for long-term dynamic culture. The Figure 4.18A shows the miniature HFBR setup including electrodes in custom-made incubator.

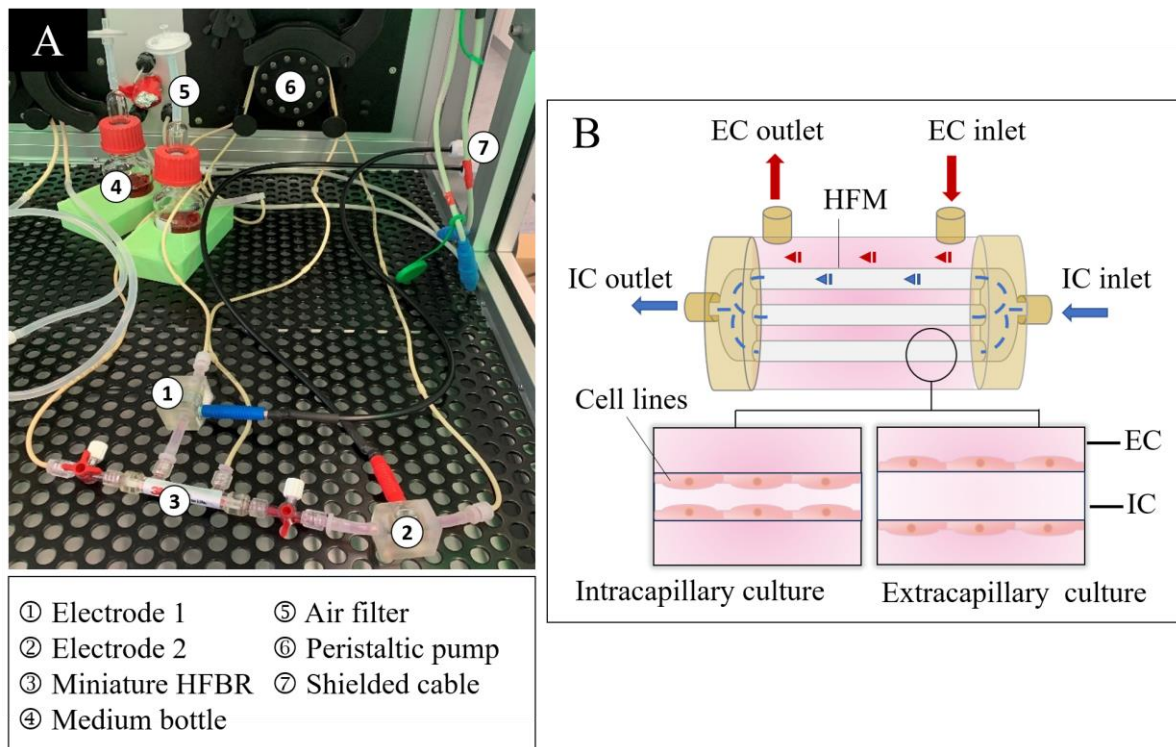


Figure 4.18. Miniature HFBR system setup incorporating TiN-coated tube electrodes. (A) Photograph of the miniature HFBR setup with TiN-coated tube electrodes. (B) Schematic representation of the structure of the HFBR and fluid flow direction. For EIS measurements, two electrodes were integrated into one at the intracapillary (IC) circuit, specifically at the IC inlet, and another at the extracapillary (EC) circuit, specifically at the EC outlet. In general, the cells can be seeded either intracapillary or extracapillary surface. In the HUVECs culture in the mini HFBR, cells were seeded on the intracapillary surface.

One electrode was placed in an EC outlet (Figure 4.18A ①), and the other was in an IC inlet (Figure 4.18A ②). The schematic of the miniature HFBR represented in Figure 4.18B. The miniature HFBR was composed of 15 hollow fiber membranes, and the direction of medium

passing through each IC and EC flowed in parallel. In the HUVECs culture, cells were seeded on the inner surface of the hollow fibers. EIS measurement ran daily, as a result, the Bode plot is depicted in the Figure 4.19A. The impedance value at 100 kHz (baseline) was subtracted from the impedance values at the frequency range (1 Hz to 100 kHz). Figure 4.19B represents the frequency range of 10 Hz to 100 kHz to focus on the cellular barrier impedance.

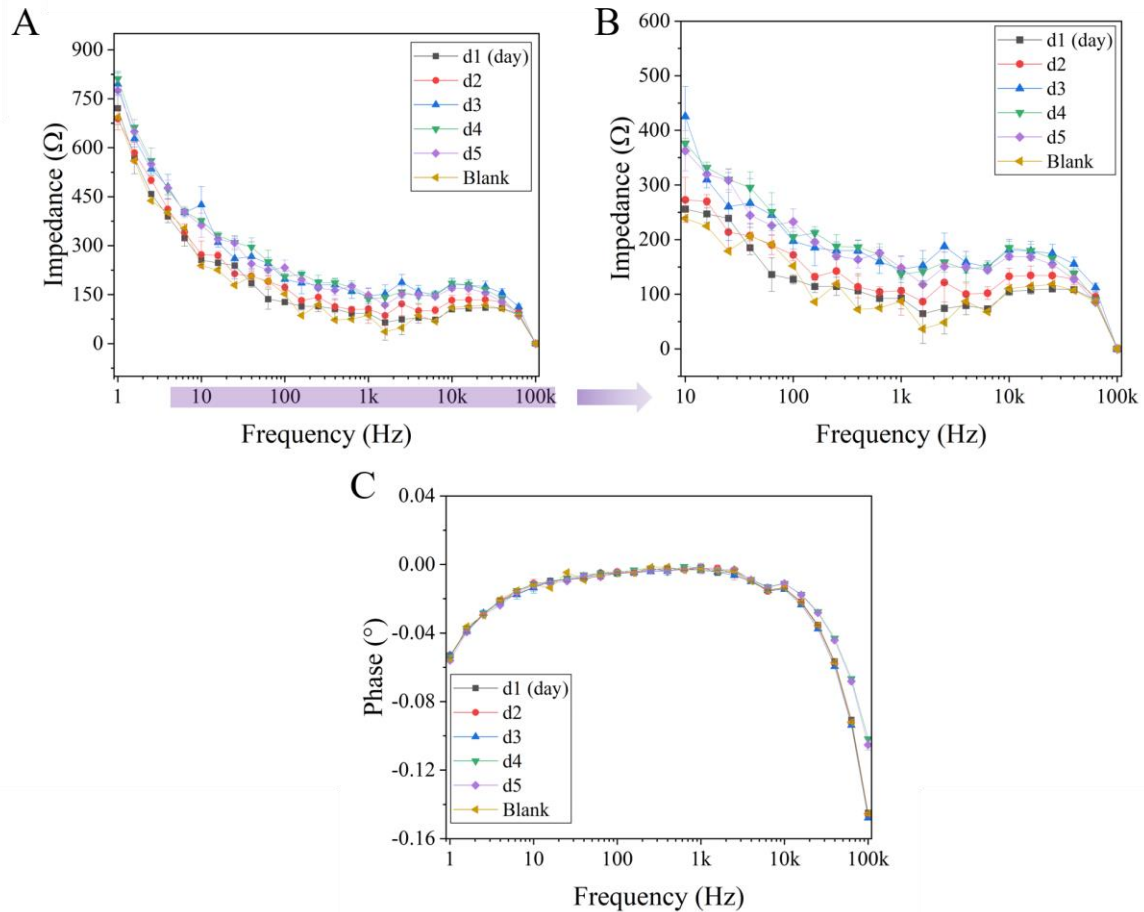


Figure 4.19. EIS analysis of HUVECs culture in miniature HFBR. (A) A Bode plot of impedance representing frequencies from 1 Hz to 100 kHz over 5 days of culture. The impedance at 100 kHz was subtracted from the impedance measured across the frequency range. (B) To closely examine the impedance differences between days, the impedance values within the frequency range of 10 Hz to 100 kHz were separately plotted. (C) A Bode plot of phase representing frequencies from 1 Hz to 100 kHz over 5 days of culture. There was no display of cell membrane capacitance behavior in the impedance spectrum, and no corresponding phase changes were observed. Although the impedance showed an increasing trend with increasing culture days, it was difficult to define it due to fluctuations. The experiment was performed with a biological replication of one ($N = 1$).

Impedance values extracted at 10 kHz for each culture time showed a trend of rising impedance until day 3, increasing by approximately 25 Ω from day 1 to day 2, followed by an additional

50 Ω increase on day 3. After 5 days of culture, the measurement result showed a decrease of 15 Ω compared to culture day 4. These trends appeared in most middle-frequency ranges (about 10 Hz to 16 kHz) except for fluctuation that could occur by disturbance. The phase shifts, indicative of barrier function, were anticipated, as observed in the reference static culture. However, there was no obvious phase shift compared to the blank (Figure 4.19C).

After finishing the bioreactor culture, Hoechst staining was performed to assess cell morphology. It was observed that the cells were well distributed in hollow fibers after dynamic cultures. The immunofluorescence image is represented in the Appendix E (Figure E.1).

4.3.2. Barrier Integrity of Cancer coli-2

Due to the relatively low barrier integrity of HUVECs, it seemed that EIS measurement was difficult to detect the barrier integrity of HUVECs on the miniature HFBR. To address this uncertainty, Caco-2 cell lines, which exhibit relatively higher barrier integrity compared to HUVECs, were tested using EIS measurements to evaluate the potential for non-invasive monitoring in miniature HFBR with TiN-coated tube electrodes.

4.3.2.1. Reference Impedance Spectroscopy Measurement in Transwell Culture

The barrier integrity of Caco-2 cells cultured in the transwell system was assessed as a reference before conducting experiments with the miniature HFBR. As mentioned above (Section 4.3.1.1), this was done to ensure the barrier integrity of cell lines in a simple system and to establish a standard value for interpretation in a complex system.

Electrochemical Impedance Spectroscopy Analysis

Caco-2 culture based on transwell culture was performed prior to miniature HFBR culture, and their impedance was used as a reference for EIS measurement of miniature HFBR. Three biological replicates (Passage 29, 30, and 31), each with three technical replicates, were carried out. Due to variations in culture time for each biological replicate, the results for each replicate are presented individually. Consequently, the Bode plot was obtained from EIS measurement (Figure 4.20). The impedance baseline was normalized to 0 by subtracting the impedance value at 100 kHz from all impedance within frequency ranges (Figure 4.20A, C, and E). Impedance and phase Bode plots of P29 Caco-2 culture is depicted in Figure 4.20A and B. The cellular barrier impedance was detected frequency range 10 Hz to 10 kHz.

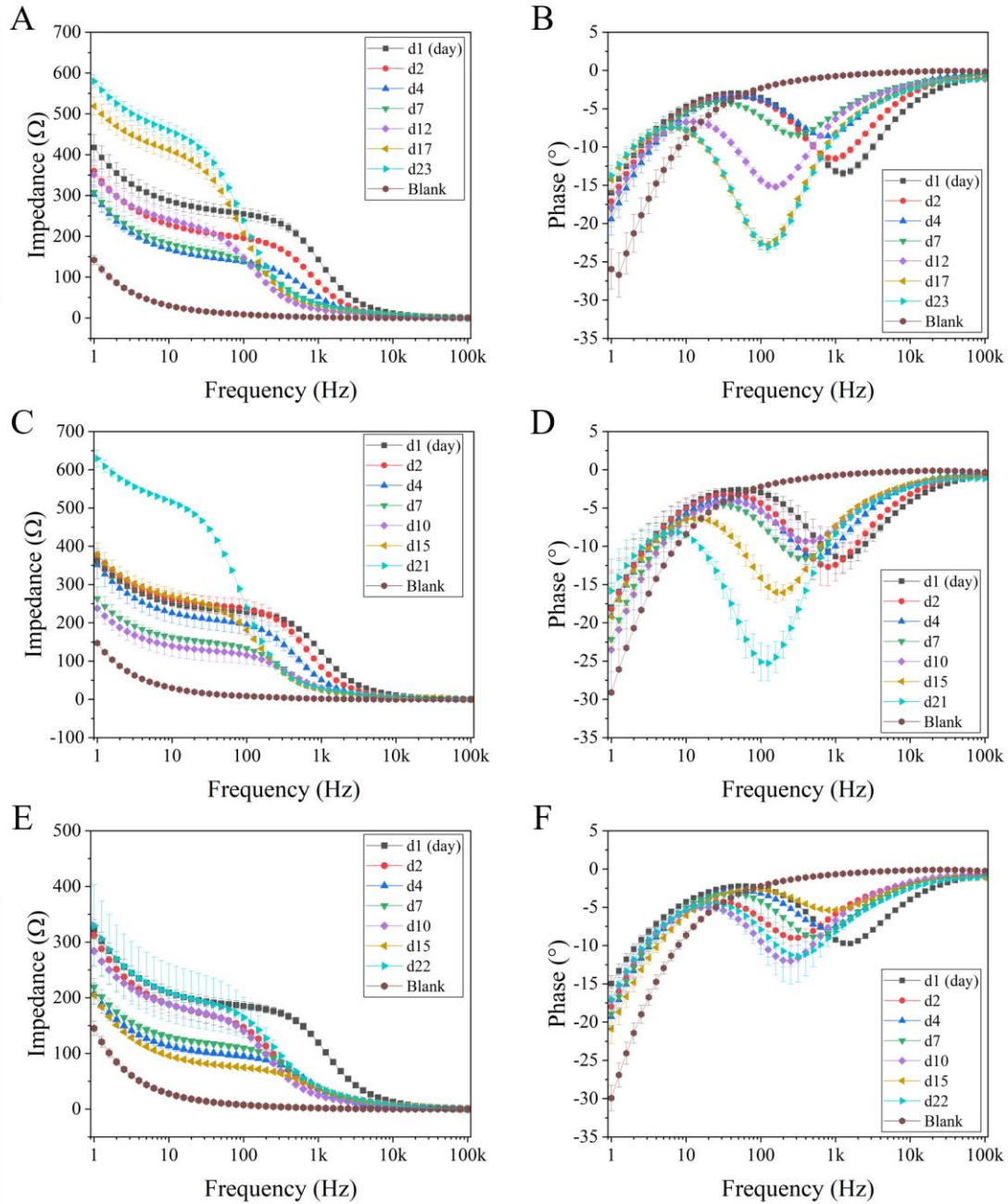


Figure 4.20. Referencing EIS results for Caco-2 cultured in a transwell system. The EIS measurements were conducted using three biological replicates ($N = 3$) with each of the cell passages, P29, P30, and P31. Each measurement, represented by the mean and standard deviation, includes three technical replicates. (A) Impedance Bode plot of P29. (B) Phase Bode plot of P29. (C) Impedance Bode plot of P30. (D) Phase Bode plot of P30. (E) Impedance Bode plot of P31 (F) Phase Bode plot of P31. The baseline impedance at 100 kHz was subtracted from the impedance measured over the frequency range of 1 Hz to 100 kHz prior to plotting it as a function of frequency. The electrical barrier function of cells was depicted at the middle frequency range (10 Hz to 100 kHz). The overall trend in cellular impedance showed a gradual decrease during the first 7 days, followed by an increase as the culture duration increased. The phase shift was observed according to the cell membrane capacitance.

The impedance exhibited a decrease from day 1 to day 7, followed by an increase until day 23, as depicted in Figure 4.20A. The phase showed an increase from -13.45° on day 1 to -8.41° on day 7, followed by a decrease to -23.07° on day 23 (Figure 4.20B). The impedance in the P30 experiment demonstrated a similar pattern, with a decrease in impedance until culture day 7, followed by an increase until day 21 (Figure 4.20C). The phase of culture day 1 was -11.54° which increased to -9.34° by day 10 (Figure 4.20D). However, it then decreased to -25.27° . The cellular barrier impedance of P31 dropped for 7 days and then increased on day 10 (Figure 4.20E). However, unlike P29 and P30, its impedance dropped again on day 15 but increased by day 22. The phase on day 1 began at -9.73° and increased to -7.60° by day 4 (Figure 4.20F). It then decreased to a value of -12.01° by day 10, increased to -5.3° on day 15, and ultimately ended with a value of -11.37° by day 22.

The obtained EIS data was further analyzed by fitting and simulation using Nova 2.1.4 software. The Figure 4.21 represents quantified values in R_T and C_C over culture days, and the values were normalized by the geometrical surface area of the insert membrane (0.33 cm^2). The R_T is equivalent to tight junction resistance and C_C is to cell membrane capacitance. The tight junction resistance of P29 (Figure 4.21A) was recorded as $78.79 \pm 4.37\ \Omega\cdot\text{cm}^2$ on day 1, then it continuously decreased to $36.62 \pm 1.38\ \Omega\cdot\text{cm}^2$. However, the R_T value was $60.40 \pm 3.36\ \Omega\cdot\text{cm}^2$ on day 12, increased to $94.57 \pm 8.28\ \Omega\cdot\text{cm}^2$ on day 17, and ultimately reached $106.30 \pm 6.74\ \Omega\cdot\text{cm}^2$ by day 23. The capacitance of the cell membrane was $1.92 \pm 0.02\ \mu\text{F}/\text{cm}^2$ on day 1, gradually increasing to $9.47 \pm 0.13\ \mu\text{F}/\text{cm}^2$ by day 7. Subsequently, it doubled in value and reached $19.02 \pm 0.17\ \mu\text{F}/\text{cm}^2$ by day 12. The value was sustained until day 17 at $19.44 \pm 0.5\ \mu\text{F}/\text{cm}^2$, then decreased to $16.75\ \mu\text{F}/\text{cm}^2$ on day 23. The results of P29 and P30 showed similar pattern in R_T and C_C . The R_T of P30 (Figure 4.21C) depicts decreasing trend for 10 days, from $71.40 \pm 3.38\ \Omega\cdot\text{cm}^2$ on day 1 to $37.05 \pm 9.41\ \Omega\cdot\text{cm}^2$ on day 10. Afterwards, the R_T increased until day 21, with a value of $73.76 \pm 4.14\ \Omega\cdot\text{cm}^2$ on day 15 and $131.30 \pm 3.84\ \Omega\cdot\text{cm}^2$ on day 21. The C_C of day 1 was $2.22 \pm 0.09\ \mu\text{F}/\text{cm}^2$, and reached $5.42 \pm 0.38\ \mu\text{F}/\text{cm}^2$ on day 4. Then, like P29, the C_C was doubled on day 7 from the value of day 4, hereby the capacitance was $10.98 \pm 0.19\ \mu\text{F}/\text{cm}^2$. After day 10, the capacitance increased further, and finalized $16.10 \pm 0.80\ \mu\text{F}/\text{cm}^2$ on day 21 (Figure 4.21D). The R_T of P31 (Figure 4.21E) on day 1 was relatively lower compared to the cultures of P29 and P30. It was recorded at $56.20 \pm 1.88\ \Omega\cdot\text{cm}^2$ and gradually decreased to $29.21 \pm 1.25\ \Omega\cdot\text{cm}^2$ by day 4. Thereafter, it increased to $48.84 \pm 4.67\ \Omega\cdot\text{cm}^2$ on day 10, but decreased again to $20.76 \pm 0.67\ \Omega\cdot\text{cm}^2$ on day 15. Finally, on day 22, the R_T increased to $51.50 \pm 15.52\ \Omega\cdot\text{cm}^2$.

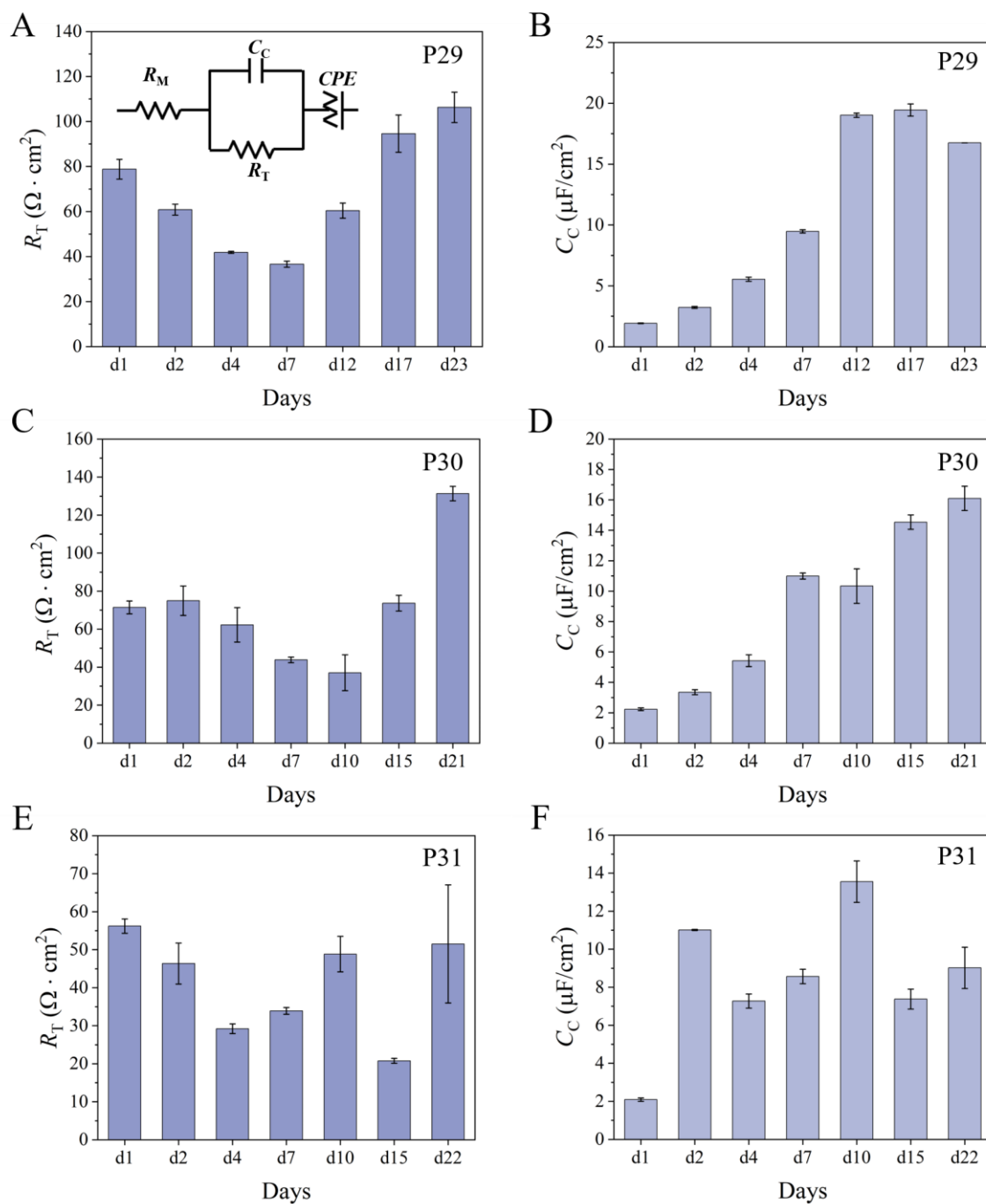


Figure 4.21. Fit and simulation of EIS data from Caco-2 in static culture. R_T and C_C were determined. Results from three different passages of Caco-2 cells were presented individually: (A and B) Passage 29 – R_T (A) and C_C (B), (C and D) Passage 30 – R_T (C) and C_C (D), (E and F) Passage 31 – R_T (E) and C_C (F). The equivalent circuit model used for fitting is described in the inset of graph (A). Each R_T and C_C were represented as normalized values based on the surface area of the porous membrane (0.33 cm^2). The mean and standard deviation values were calculated from three technical replicates ($N = 3$).

The C_C of P31 (Figure 4.21F) was increased relatively rapidly from $2.09 \pm 0.08 \mu\text{F}/\text{cm}^2$ on day 1 to $11.01 \pm 0.02 \mu\text{F}/\text{cm}^2$ on day 2. Subsequently, it decreased to $8.56 \pm 0.38 \mu\text{F}/\text{cm}^2$ on day 7. However, on day 10, the C_C value reached at maximum value with $13.55 \pm 1.09 \mu\text{F}/\text{cm}^2$, and finally recorded with $9.02 \pm 1.08 \mu\text{F}/\text{cm}^2$ on day 22.

Analysis of Immunofluorescence Images

After concluding the long-term transwell cell culture, the investigation of Caco-2 cell morphology was carried out using immunofluorescence staining. The immunofluorescent samples were visualized by confocal microscopy.

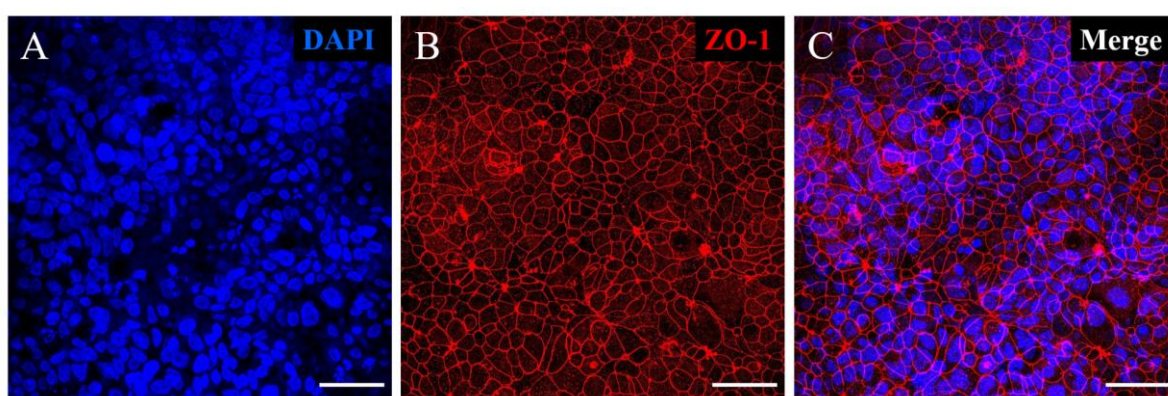


Figure 4.22. Immunofluorescence images of Caco-2 cells in static culture. The images depict cells following 21 days of transwell culture. (A) DAPI staining (Blue), (B) Zonula occludens- 1 (ZO-1, Red), and (C) merged image. The images were captured at a magnification of $40\times$ and a scale bar of $50 \mu\text{m}$. The cell nuclei are densely packed, and the expression of ZO-1 protein was highly localized at the adherent cell interface.

Figure 4.22A displays a DAPI-stained image captured at $40\times$ magnification from the P30 experiment on day 21, Figure 4.22B shows a ZO-1 stained image captured at the same magnification, and Figure 4.22C shows an overlay of both images for comparison. As seen in Figure 4.22B, the tight junction proteins, ZO-1, was localized along the border of adjacent cells. Furthermore, the ZO-1 expression was uniformly intense and well-defined along the boundaries.

4.3.2.2. Assessment of Barrier Integrity in Miniature Hollow Fiber Bioreactor

Electrochemical Impedance Spectroscopy Analysis

After the first trial with HUVECs, the miniature HFBR was tested and followed by Caco-2 cell culture. The bioreactor system setup, including the TiN-coated tube electrodes, was the same

as that used for the HUVECs culture (Figure 4.18A). The Caco-2 cell culture in miniature HFBR was performed for 14 days.

During the EIS measurement, it was observed that measurement failure often occurred due to a reduction in impedance, specifically in the middle frequency range. It seemed that tiny bubbles on the membranes disturbed the electrical signal. Figure 4.23A demonstrates the example of a measurement error, on the other hand, Figure 4.23B represents the Bode plot in general without any measurement error.

The graph in Figure 4.23A and B extracted the EIS results from day 6 and day 7, respectively. The assessment of cellular barrier function detection over culture time was accomplished by analyzing the phase Bode plot (Figure 4.24A). Beginning on day 6, with the frequency decreasing from 10 kHz to 100 Hz, a consistent trend of decreasing phase angle was observed as the detection of cell membrane capacity progressed, followed by a gradual increase in phase angle approaching 0° as tight junction resistance was detected.

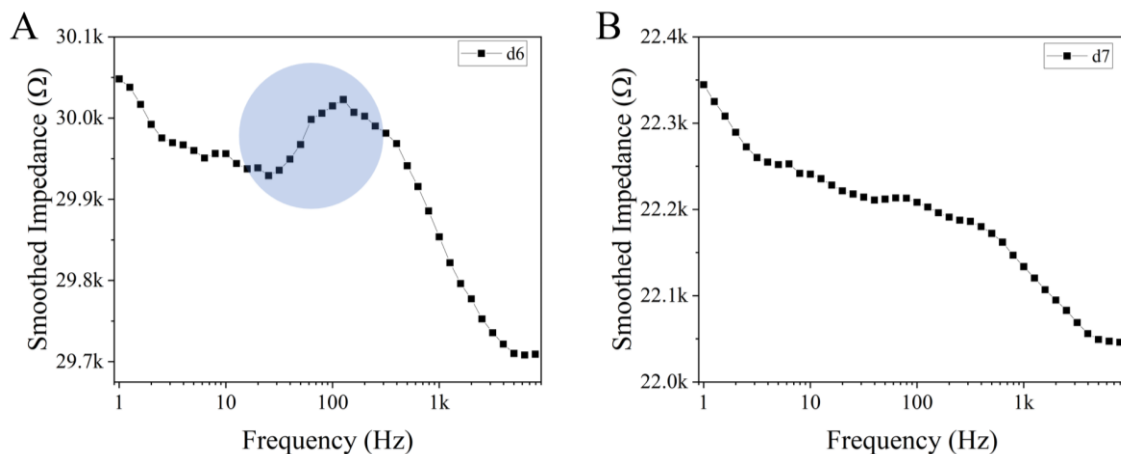


Figure 4.23. Error in EIS measurement during miniature HFBR culture of Caco-2. An abnormal drop in cellular impedance was observed in a specific frequency range. (A) Bode plot with the error highlighted. (B) Bode plot without error. The Bode plots were smoothed using the Nova 2.1.4 software program.

The phase was lowered to -0.2° at frequency 1.9953 kHz on day 7, even more got lowered to -0.33° at frequency 1.9953 kHz on day 14. Except the impedance data occurred the measurement error (d3 and d6), impedance Bode plot on day 7 and day 4 (Figure 4.24B) were subsequently quantified to obtain the R_T and C_C by fitting and simulation (Figure 4.24C and D). As a result, the R_T on day 7 was 163.08 Ω and increased to 293.48 Ω by day 14.

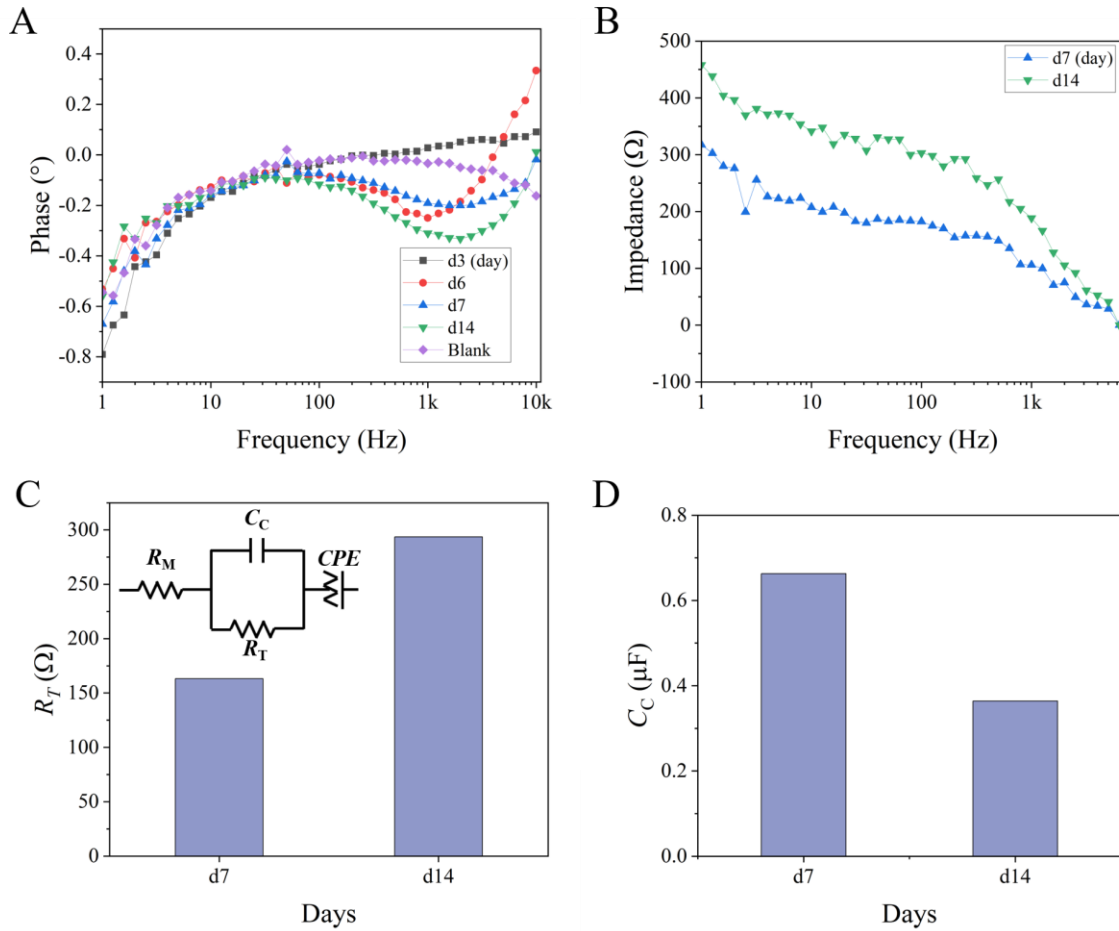


Figure 4.24. EIS monitoring of Caco-2 cells cultured in a miniature HFBR. (A) The phase was plotted as a function of frequency (1 Hz to 10 kHz) for different days of culture. Phase shifts due to the electrical properties of the cells began to be detected from day 6 in the frequency range of 100 Hz to 10 kHz. (B) Due to the errors indicated in Figure 4.23 occurring on day 3 and day 6, impedance results for day 7 and day 14 were depicted on a Bode plot. (C) The tight junction resistance and (D) the cell membrane capacitance of Caco-2 on day 7 and day 14 were quantified by fitting and simulation. The equivalent circuit depicted in the left corner of graph C was used for fitting and simulation. The results of the fitting and simulation graph are depicted in the Appendix B (Figure B.3). The experiment was performed with a biological replication of one ($N = 1$).

However, the cell membrane capacitance (C_C) decreased from 0.663 μF to 0.364 μF as the culture day increased from day 7 to day 14. Since provided surface area was an approximate value (approximately 12 cm²) for the surface area of the hollow fiber, the fitting results of R_T and C_C were not further normalized by surface area.

Immunofluorescence Analysis

On day 14 of Caco-2 culture in miniature HFBR, hollow fibers were taken for Hoechst staining to examine their morphology.

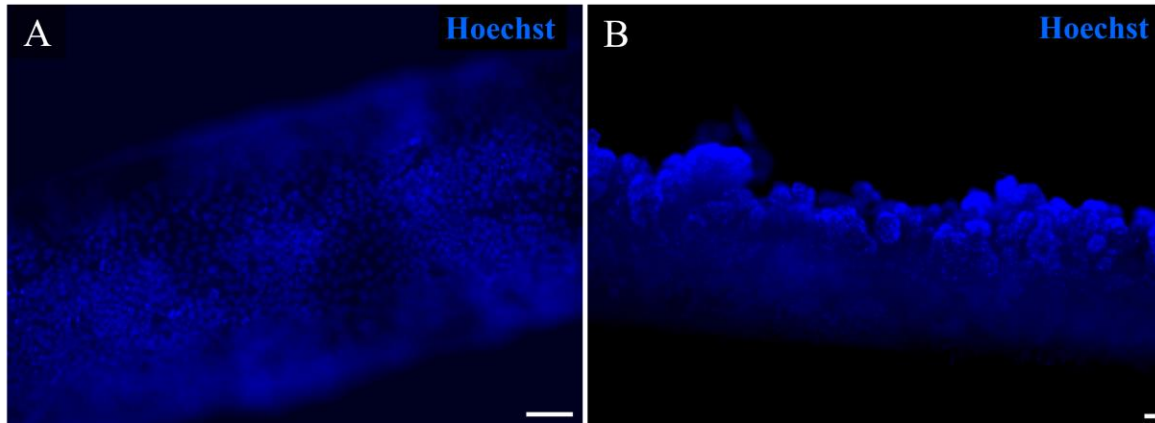


Figure 4.25. Immunofluorescence images of Caco-2 culture in miniature HFBR. Hoechst (Blue) staining images of Caco-2 cells on the hollow fiber after 14 days of culture. (A) The scale bar of the image is 100 μm . The cell nuclei are well spread out on the surface of the hollow fiber membrane. (B) The scale bar of the image is 50 μm . The presence of microvilli in the Caco-2 structure was observed.

The cell nuclei well distributed on hollow fiber membrane surface (Figure 4.25A). Furthermore, the microvilli structure was observed as shown in Figure 4.25B.

4.4. Electrode Application 3: Hemofiltration

The last application of the TiN-coated tube electrode was hemofiltration. Filter clotting and clogging reduce filter effectiveness leading to insufficient solute removal, costs, and greater workloads for medical staff. TMP is commonly used as an indicator for monitoring filter clogging. However, establishing absolute pressure guidelines for filter clotting or clogging can be challenging due to the possibility of misreading caused by pressure changes from chamber clotting or other factors, not just filter clotting or clogging. The hypothesis was based on the idea that, when current flows through the membrane, filter clogging might lead to a change in resistance, which could be detected using impedance spectroscopy. Therefore, EIS measurements correlated to four independent hemofiltration were analyzed and reviewed in this study.

4.4.1. Analysis of Electrochemical Impedance Spectroscopy and Pressure Data

Six TiN-coated tube electrodes were implemented in the flow circuit for EIS monitoring of hemofiltration. Each connected two electrodes at a distance of 5 cm were placed at each entrance where blood enters the hemofilter, blood leaves the filter, and effluent leaves from the filter (Figure 3.8). This electrode set allowed to measurement of impedance across the membrane (Z_{AM}), impedance along fibers (Z_{AF}), arterial impedance ($Z_{Arterial}$), venous impedance (Z_{Venous}), and effluent impedance ($Z_{Effluent}$). Depending on the impedance being focused on, particular two electrodes were connected with probes of Metrohm Autolab PGSTAT 204 for EIS measurement. The list of two electrodes used for measuring a specific impedance is presented in a square box in Figure 3.8. Four independent hemofiltration experiments were analyzed, designated as Hemofiltration 1, Hemofiltration 2, Hemofiltration 3, and Hemofiltration 4, in the order of the time sequence of the experiments.

As soon as hemofiltration began, EIS measurement continued until the end of the process. The focus during hemofiltration was on the changes in Z_{AM} , as per the hypothesis. Figure 4.26 illustrates the line graphs of three independent experiments: Hemofiltration 1, Hemofiltration 3, and Hemofiltration 4. These graphs represent Z_{AM} (Figure 4.26A, C, and E) as a function of time. Additionally, the pressure values (Figure 4.26B, D, and F) at the corresponding time points, where EIS was performed, is displayed.

Hemofiltration 1 (Figure 4.26A and B) ran for overnight. The initial Z_{AM} as soon as hemofiltration started was 28.89 k Ω . Then, the impedance dropped to 24.71 k Ω at 106 min. This decreasing pattern was also seen in $P_{arterial}$ and P_{venous} at the same time points as shown in the Figure 4.26B. After 106 min, Z_{AM} sustained until 231 min then increased to 25.49 k Ω at 357 min. Afterwards, the impedance was gradually decreased as reaching 19.81 k Ω at 1312 min. However, after about 1 h, it increased again to 23.26 k Ω . The $P_{Arterial}$ and P_{venous} were initially recorded as 240.96 mmHg and 60.36 mmHg, respectively, at 0 h. As mentioned above, the $P_{Arterial}$ and P_{Venous} had decreased patterns between 0 and 106 min. But they increased again, thereby, the $P_{Arterial}$ and P_{Venous} reached 291.97 mmHg and 57.37 mmHg at 357 min, respectively. Each pressure kept stable until 1312 min, but there was a certain dropped to 31.03 mmHg of $P_{Arterial}$ and 41.22 mmHg of P_{Venous} at 1389 min. Unlike the $P_{Arterial}$ and P_{Venous} pattern, the effluent pressure gradually decreased from starting pressure of 27.34 mmHg to - 142.60 mmHg until 422 min. The negative $P_{effluent}$ means the effluent moves out from the hemofilter not by convection but by a pump caused by the clogged filter.

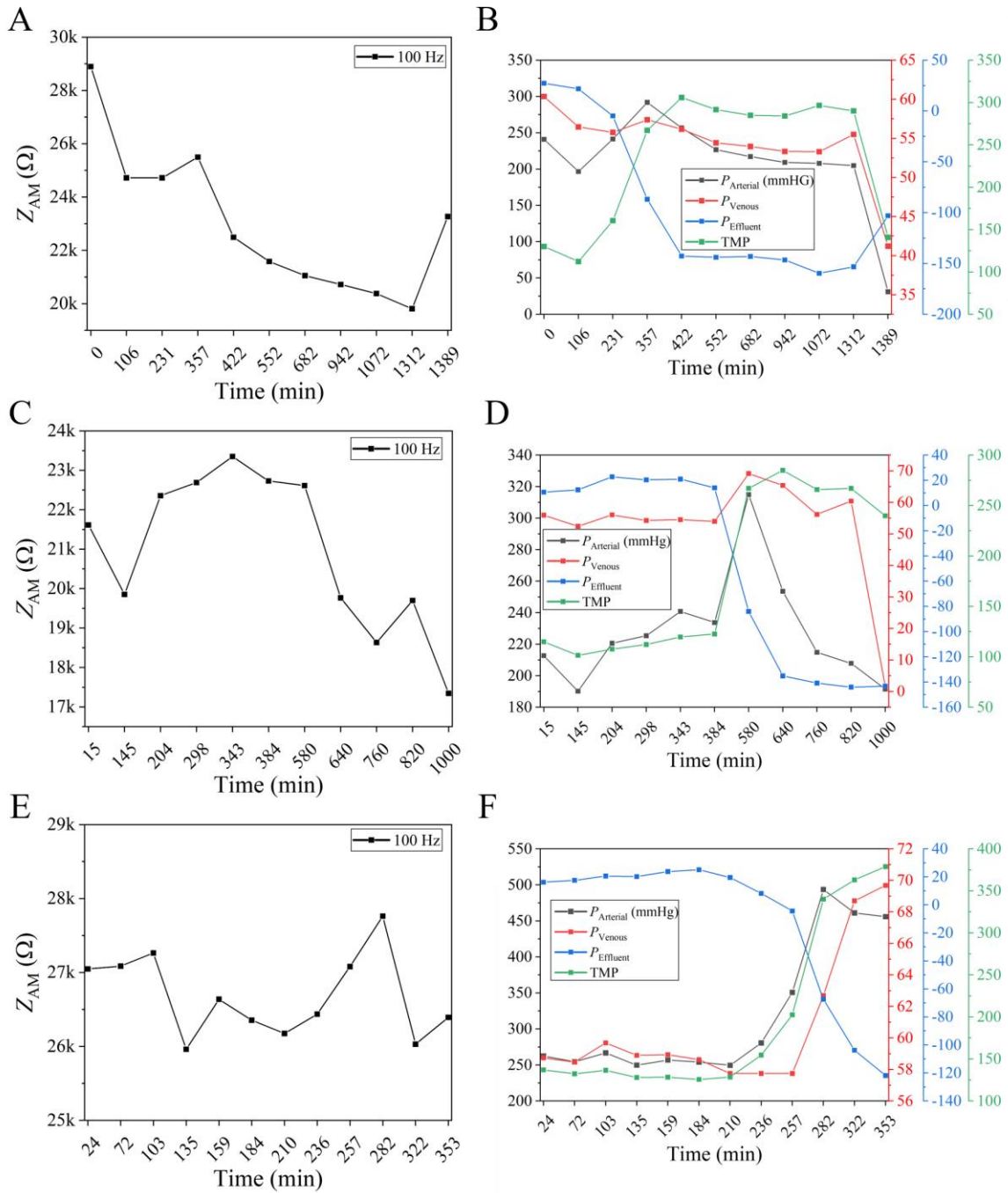


Figure 4.26. EIS and pressure measurement during hemofiltration. Three independent hemofiltration runs. Results of Hemofiltration 1 presented with (A) EIS and (B) pressure reading. Hemofiltration 3 results represented with (C) EIS and (D) pressure reading. Hemofiltration 4 results depicted with (E) EIS and (F) pressure reading. EIS was utilized to assess the impedance across the hollow fiber membrane. The impedance value at 100 Hz was extracted and plotted as a function of hemofiltration time (A, C, and E). Simultaneously, arterial, venous, and effluent pressures were monitored, and the transmembrane pressure (TMP) was calculated based on the measured pressures. The obtained pressure data was plotted as a function of hemofiltration time (B, D, and F).

The effluent value seemed to sustain until 1312 min but afterward increased, approaching - 102.95 mmHg at 1389 min. TMP, which is used as an indicator of filter clogging, is depicted in Figure 4.26B. It is not considered an absolute value indicating filter clogging, but still the only useful parameter in hemofiltration. Overall, the TMP trend was opposite to Z_{AM} except first dropping for 106 min. TMP was over 300 mmHg at 422 min, and usually, when TMP reaches above 300 mmHg which typically indicates filter clogging. After 422 min, TMP stayed near 300 mmHg until 1312 min, then dropped to 140.86 mmHg at 1389 min. Even though impedance-increasing trends were expected if there is a clogging of the hemofilter, most of the time, Z_{AM} showed decreasing trends. However, the overall TMP of Hemofiltration 1 was less than 300 mmHg, which was still below the filter clogging alarm range (above 300 mmHg) except for the value of 422 min.

Hemofiltration 3, was displayed in the Figure 4.26C and D. Hemofiltration 3 was performed overnight, and a first impedance drop similar to Hemofiltration 1 was observed from 15 min to 145 min, which might be the reason for early clotting, with values of 21.61 k Ω at 15 min and 19.85 k Ω at 145 min. The impedance then increased to 23.34 k Ω at 343 min. After 580 min, the impedance started to decrease again to 18.63 k Ω (760 min). Although it increased once more before 1000 min, the impedance dropped back to 17.34 k Ω on the last measurement. The $P_{Arterial}$ and P_{Venous} trends over hemofiltration were quite similar. Each pressure shows the first drop between 15 and 145 min even though the difference in P_{Venous} was minor. Afterward, the arterial and venous pressure increased and reached the highest value of 314.94 mmHg and 69.15 mmHg, respectively, at 580 min. The arterial value kept decreasing until the hemofiltration was terminated, dropping to 191.56 Ω at 1000 min over 253.61 Ω at 640 min. Unlike $P_{Arterial}$ started to decline right after 580 min, P_{Venous} showed later than 820 min. Thus, the P_{Venous} was 1.56 mmHg at 1000 min. Effluent pressure stayed stable at about 200 mmHg for 384 min, and began to drop from 14.06 mmHg at 384 min to - 135.1 mmHg at 640 min. The value was kept until the end of hemofiltration. TMP was kept stable for 384 min at an average of 113.09 ± 7.11 mmHg. After that, the pressure increased to 267.12 mmHg at 580 min and was stable until 1000 min. Like Hemofiltration 1, TMP at all time points was below 300 mmHg, which is not belonging to the filter clogging alarm zone. Also, after 580 min, the trends of TMP and Z_{AM} were opposite to each other.

Lastly, the Z_{AM} result of Hemofiltration 4 is represented in Figure 4.26E. Unlike the impedance drop between the first two time points (about 0 to 100 min) of Hemofiltration 1 and 3, the Z_{AM} began at 24 min with 27.04 k Ω , and increased slightly to 27.26 k Ω at 103 min. After 30 min,

it decreased to 25.96 k Ω but increased again to 26.63 k Ω at 159 min. Afterward, impedance seemed to drop again but rapidly raised to 27.76 k Ω , which is the highest value, at 282 min. The Z_{AM} dropped once more to 26.02 k Ω for the next about 45 min, and the Z_{AM} at 353 min was 26.39 k Ω . Opposite to Z_{AM} that showed fluctuation during hemofiltration, pressure was stable for 236 min of $P_{Arterial}$, for 257 min of P_{Venous} and $P_{Effluent}$. At 353 min, $P_{Arterial}$ increased to 455.82 mmHg and P_{Venous} increased to 69.7 mmHg, while the $P_{Effluent}$ dropped to -121.83 mmHg. TMP was calculated based on three measured pressure values, $P_{Arterial}$, P_{Venous} , and $P_{Effluent}$ using Equation 1.22. As a result, TMP stayed with an average pressure of 130.92 \pm 4.14 mmHg for 210 min. It continuously raised, the value of 282 min was 340.11 mmHg, and the TMP at 353 min even reached 378.85 mmHg. The pressure changes, which became apparent starting at 210 minutes, were observed in the arterial, venous, and effluent lines, indicating a potential issue with hemofiltration clogging. Thus consequently, TMP reached above 350 mmHg. Similarly, Z_{AM} showed increasing trends from 210 min to 282 min likely but suddenly dropped after 282 min. The same trend was observed previously in Hemofiltration 3.

To investigate the reason for the drop in Z_{AM} , the impedance of arterial, venous, and effluent lines was subsequently examined in Hemofiltration 1, 2, 3, and 4. To note, Hemofiltration 1, 3, and 4 were the same experiments mentioned above in Figure 4.26, and furthermore, an additional Hemofiltration 2 was conducted. The electrode pair that participated to measure arterial and venous impedance represents in the Figure 3.8.

The Figure 4.27 shows a double Y-axis graph depicting the impedance difference between arterial and venous blood, as well as the TMP, as a function of hemofiltration time. Hemofiltration 1, Hemofiltration 2, Hemofiltration 3, and Hemofiltration 4 are depicted in the Figure 4.27. Here, " ΔZ_{V-A} " refers to the impedance difference between arterial and venous. A single EIS device was used for the measurements, resulting in an interval of about 5 – 7 min between arterial and venous measurements. In Hemofiltration 1, the initial ΔZ_{V-A} filter was 16.32 k Ω and it was almost stable until 216 min, but then, ΔZ_{V-A} recorded with 2.76 k Ω at 1046 min. The TMP kept stable for 221 min starting with 142.43 mmHg, after that, it increased to 326.85 mmHg at 1046 min which was the opposite trend compared to the ΔZ_{V-A} . At the start, there was a notable impedance difference between venous and arterial measurements. However, over time, this difference decreased, suggesting a potential issue with membrane transport possibly due to filter clogging. TMP rising simultaneously with the decrease of ΔZ_{V-A} supported the explanation of filter clogging.

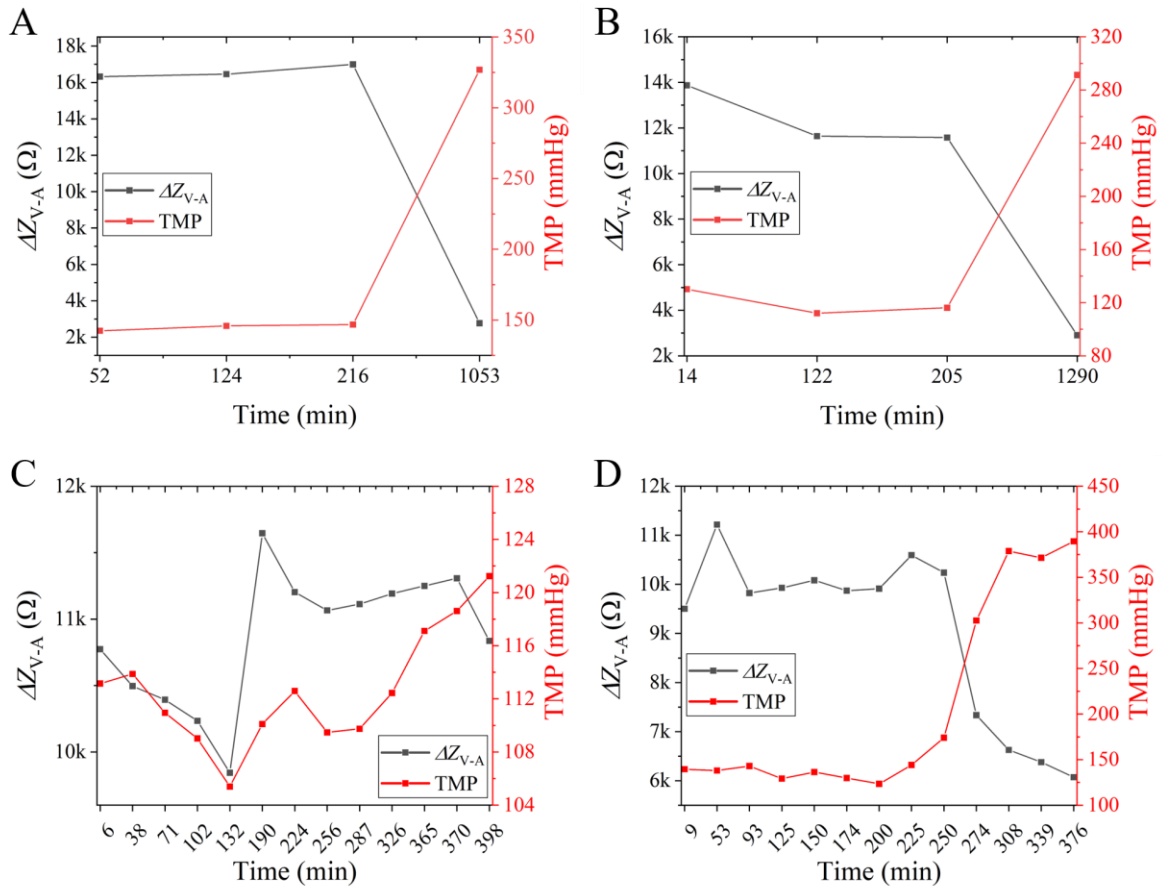


Figure 4.27. Comparison of ΔZ_{V-A} and TMP as function of time. Venous impedance (Z_V) and arterial impedance (Z_A) were measured at the entry and exit of the hemofilter, respectively, and their differences (ΔZ_{V-A}) were calculated. (A) ΔZ_{V-A} for Hemofiltration 1. (B) ΔZ_{V-A} for Hemofiltration 2. (C) ΔZ_{V-A} for Hemofiltration 3. (D) ΔZ_{V-A} for Hemofiltration 4. (A, B, C, and D) The blood impedance difference is shown on the left Y-axis, while TMP is plotted on the right Y-axis as a function of hemofiltration time. After a stable period lasting approximately 3 h, the blood impedance showed a decreasing trend, while the TMP displayed an increasing trend, suggesting potential hemofilter clogging.

When examining Hemofiltration 2 (Figure 4.27B), the ΔZ_{V-A} measured 13.87 k Ω initially, followed by a decrease to 11.64 k Ω at 122 min. Afterward, the ΔZ_{V-A} gradually dropped from 205 min to 1290 min resulting in a 2.90 k Ω . However, TMP was increased similar to hemofiltration 1.

The result of Hemofiltration 3 ran for 398 min represents in Figure 4.27C. Unlike Hemofiltration 1 (Figure 4.27A) and 2 (Figure 4.27B), TMP was not over 300 mmHg of all time, which means insignificant hemofilter clogging during hemofiltration.

In Hemofiltration 3, the initial ΔZ_{V-A} with 10.77 k Ω at 6 min dropped to 9.84 k Ω at 132 min. Afterward, it increased to 11.64 k Ω at 190 min, and decreased and reached to 11.06 k Ω at 256 min. After 256 min, the impedance slightly rising time to time, and the ΔZ_{V-A} was 11.30 k Ω at 370 min, though the final measurement was recorded as 10.83 k Ω . The graph of ΔZ_{V-A} and TMP trends over time was similar to each other.

Lastly, the ΔZ_{V-A} and TMP of Hemofiltration 4 was analyzed (Figure 4.27D). The impedance difference between arterial and venous was mostly stable for 250 min except for two peaks at 53 and 225 min. The ΔZ_{V-A} was 10.23 k Ω at 250 min. After 250 min, the ΔZ_{V-A} dropped remarkably in 25 min to 7.33 k Ω at 275 min. The decreasing trend continued until the last measurement recorded 6.07 k Ω at 376 min. The TMP was 139.43 mmHg initially, and the TMP was stable until 225 min, but then the value increased by 200 mmHg between 250 min and 308 min. Finally, the TMP reached to 389.49 mmHg at 376 min. As observed in Hemofiltration 1 and Hemofiltration 2, the time that TMP increased simultaneously happened when impedance decreased.

5. Discussion

Barrier tissue culture using a perfusion bioreactor is often preferred over conventional transwell culture due to its ability to provide *in-vivo* like tissue culture environment with continuous nutrient supply and mechanical stimulation, including shear stress [158-160]. However, a non-invasive monitoring system is necessary for investigating cellular functions when a perfusion bioreactor is operating in a closed system. The incorporation of EIS allows for non-invasive monitoring of cellular behavior in bioreactor cultures under dynamic flow conditions.

To manufacture a novel electrode material with low impedance suitable for biological experimentation, TiN coating material was fabricated using PVD technique. The TiN coating previously demonstrated and established by Schmitz et al. [86] was used in the fabrication process. This PVD method was beneficial to generate TiN layers on various substrates at a low cost. Primary, the even TiN coating could be checked by color change with a dark brownish color on all substrates such as polycarbonate Luer lock connectors, SS mesh, SS tubes, and glass plates. However, the observation revealed that the TiN coating on the polycarbonate Luer lock connector exhibited poor wear resistance, as it easily peeled off upon physical friction, distinguishing it from the TiN coating on glass or SS. As a result, TiN-coated Luer lock connector electrode could potentially result in a poor electrical connection and high electrode impedance. Moreover, there are risks associated with its long-term use as an electrode in fluidic flow cell culture environments. Hence, the Luer lock connectors were intentionally excluded from the process of identifying the most suitable options. After the primary check for TiN coating by color changes, the TiN coating on all different substrates was appraised by SEM. The TiN coating on the SS mesh, glass plate, and SS tube electrode has all demonstrated a rough nanostructured surface. The advantages of these fractal structures that offer highly effective surface properties needed as electrodes, such as high charge capacitive and low impedance, have been reported in several studies [161,162]. To investigate the impedance of TiN-coated electrodes with different substrates, EIS was conducted. As a result of EIS measurement, the electrode impedance was the highest with a TiN-coated glass plate. In contrast, the TiN-coated tube electrode had the lowest impedance which is preferable. Still, the impedance of all the electrodes was sufficiently low to ensure good performance as electrode sensors. In addition, their capacity was assessed by quantifying the electrical double layer capacitance occurring at the electrode/electrolyte interface. This was achieved by fitting and simulating the equivalent circuit model, comprising a series connection of R_e and CPE , to impedance data using the Nova 2.1.4 software. Consequently, the CPE admittance (Y_0)

containing capacitance information and n ($0 < n < 1$) constant associated with the double layer behavior of electrodes (Table 4.1) were obtained. The Y_0 of the TiN-coated tube electrode was the highest as $19.5 \times 10^{-4} \text{ S}\cdot\text{s}^n$. The TiN-coated SS mesh electrode was lower with $6.16 \times 10^{-4} \text{ S}\cdot\text{s}^n$ than the TiN-coated tube electrode, and the TiN-coated glass plate was even lower with $3.42 \times 10^{-4} \text{ S}\cdot\text{s}^n$. The higher Y_0 value observed in the TiN-coated tube electrode can be attributed to its larger geometric size. The capacitance of an electrode is directly proportional to its surface area of the electrode. Despite the challenges in comparing with the TiN-coated SS mesh electrode due to difficulties in precisely calculating its surface area, an observation indicates that the TiN-coated tube electrode, with a surface area twice that of the glass plate as depicted in Figure 4.1, demonstrates a higher Y_0 value. Therefore, the surface area may account for the observed increase in the Y_0 value. This relationship between capacitance and surface area is expressed in Equation 5.1, which is commonly used to calculate the capacitance of a capacitor [163].

$$C = \varepsilon \frac{A}{d} \quad 5.1$$

In this equation, C represents capacitance, ε denotes the permittivity of the electric field, A signifies the surface area of the electrode plate, and d represents the distance between the two electrodes. Therefore, it was examined that TiN coating can be applied to glass substrates and SS substrates, resulting in high wear resistance. TiN-coated glass plates, SS mesh, and SS tube electrodes were found to possess relatively high capacity and low impedance, although the TiN-coated SS tube electrodes had the lowest impedance.

To determine the optimum design for producing add-on types of electrodes, various designs of add-on types of electrodes were manufactured. The objective of the optimization is to ensure easy implementation and prevent fluid leakage under fluid flow conditions. In this study, the add-on electrodes with various designs were created by securely fixing the core electrode structure inside the PDMS shell. PDMS is a biocompatible material that has already been proven by using widely for microfabrication, such as microfluidic bioreactors [164-167]. Also, the casting method is relatively easy. Thereby, three different electrode designs, TiN-coated SS mesh, TiN-coated glass plate, and TiN-coated tube electrode, were completed using PDMS shell structure. Indeed, the 3D printing technique used to produce positive mold contributed to modifying design easily in need. Consequently, PDMS shells played an important role in insulating joints of either electrode, silicone tubing, or 3D-printed Luer lock connector to avoid leaking of fluid and electricity. At the subsequent leak test, there was no leak under conditions

with a low flow rate, whereas the leak occurred with TiN-coated SS mesh while increasing the flow rate (up to 280 mL/min), although it was minor. Also, air bubbles generated in a fluid flow were trapped on the mesh, causing raising the electrode impedance. This can lead to a measurement failure. Unlike, the TiN-coated glass plate and SS tube electrode did not have any leak even in high fluid flow rate. Therefore, in summary, the embedding of electrodes connected with a silicone tube in a PDMS shell has been demonstrated to create an independent and versatile electrode unit. Both the TiN-coated glass and SS tube electrodes have shown their suitability for integration into bioreactor systems with dynamic fluid flow and long-term operation. Notably, among the others, the TiN-coated tube electrode exhibits outstanding electrical properties without any leakage issues.

To investigate how influential parameters of a fluidic culture system impact EIS measurements, four independent tests were conducted, considering parameters such as the distance between electrodes, temperature, electrolyte concentration, and flow rate. Based on the electrode system setup, impedance consists of a real part and an imaginary part (Figure 4.4). The real part is determined by ohmic resistance, and the imaginary part is determined by double-layer capacitance. As the frequency decreased, the imaginary part, which represents double-layer capacitance, became dominant, while the real part approached zero. Conversely, as the frequency increased, the ohmic resistance, representing electrolyte resistance, became dominant, and the imaginary part approached zero. As the distance between the two electrodes increased, the electrolyte impedance also increased. Because as stated in the electrolyte resistance formula (Equation 5.2), the length of the material carrying current is proportional to electrolyte resistance [23].

$$R = \rho \frac{l}{A} \quad 5.2$$

Electrolyte resistance, R , is directly proportional to solution resistivity, ρ , and length of the material carrying current, l , while it is inversely proportional to cross sectional area, A . In the high frequency range, the impedance is raised by increased frequency. This trend began to appear at a 5 mm distance, and the rate of impedance increase became more pronounced as the distance increased further. Furthermore, the electrolyte impedance, primarily observed at high frequencies, decreases with increasing electrolyte concentration, temperature, and flow rate. Despite presenting results for a 10 % interval of electrolyte concentration testing, it was confirmed that EIS could detect a 2 % concentration difference in additional tests. Based on the test results, the TiN-coated tube electrode demonstrated high sensitivity as an electrode and

was found to be influenced by these parameters. Consequently, it is crucial to consider these parameters when interpreting the EIS data.

To integrate and test the applicability of a non-invasive monitoring system in a chip bioreactor, the configuration of the newly fabricated chip bioreactor was optimized, considering the quantity and placement of electrodes. The chip bioreactor was constructed using PDMS. Due to its biocompatibility and autoclavable properties, PDMS was a suitable material choice for bioreactors. In addition, the material cost is relatively low compared to bioreactors made of high-performance 3D printing material or glass. Furthermore, negative mold obtained through computer aided drawing (CAD) modelling, 3D printing, and silicon molding could be used multiple times, enabling rapid production after the first production. Another advantage of the bioreactor was that it is easy to assemble and handle, as no additional tools or screws are required to assemble the bioreactor. Moreover, the 3D-printed membrane frames enable it to be used for other scaffolds, such as biological matrices, electrospun carbon nanofiber mats, and 3D bioprinting scaffolds, by modifying their size. In other words, the bioreactor can be applied to various tissue cultures, not confined to particular tissue cultures. The objective of the test was to optimize the chip bioreactor setup with the TiN-coated tube electrode for EIS measurements and cell culture. Subsequently, it was to assess the capability of the TiN-coated tube electrode, in cooperation with EIS, to examine the barrier integrity of hiPSC-derived BCECs during bioreactor culture. Two TiN-coated tube electrodes were constructed in the chip bioreactor system, each positioned right next to the bioreactor chamber and diagonally from each other. In addition to the chip bioreactor, additional accessories that support the system were produced. The silicone medium bottle holder helped reduce the contamination rate caused by a wet air filter, which can occur due to the ease with which the medium inside the bottle can reach the air filter during handling. Surface modification of bioreactor chamber using oxygen plasma treatment prevented the trapping of air bubbles that might be generated during long-term cell culture in the chip bioreactor. For the EIS measurement, the applied voltage set for EIS measurement was $0.05 V_{RMS}$, resulting in an expected maximum current below $10 \mu A_{RMS}$. Since the electrodes were independent units, the distance between two electrodes was approximately 20 cm. Nonetheless, due to the superior material properties of TiN coating as an electrode with low impedance (approx. 80Ω (Figure 4.4)), the electrode impedance remained within the detected frequency range of 1 Hz to 10 Hz in the spectrum. This resulted in a lesser impact of electrode impedance on the high-frequency range where cell barrier impedance is detected.

As mentioned above, the hiPSC-derived BCECs were used for practical test the chip bioreactor providing non-invasive monitoring system. In the previous study [155], the promising *in vitro* hiPSC-derived BBB model based on transwell culture was established. The aim of this study was also to culture hiPSC-derived BCECs under dynamic conditions that generate mechanical shear stress while simultaneously monitoring the integrity of the BCECs barrier. As reported in the previously published paper [156], the chip bioreactor can supply the shear stress in the range of 1.76×10^{-3} dyne/cm² to approx. 8.34×10^{-2} dyne/cm². In this study, the shear stress of 1.76×10^{-3} dyne/cm² was applied for the dynamic culture of BCECs. The hiPSC-derived BCECs were cultured in the chip bioreactor system for 168 h. The EIS measurement started once the culture medium filled the whole bioreactor system, and the time point was designated as 0 h. Afterwards, EIS measurement was carried out every 24 h for 168 h. Based on the impedance results, it was possible to derive an equivalent circuit that accurately represented the BCECs bioreactor culture system. This circuit allowed for the quantification of important electrochemical parameters, including R_T (tight junction resistance), C_C (cell membrane capacitance), R_M (culture medium resistance), and CPE (electrode capacitance), as illustrated in Figure 4.12. The R_T of dynamic culture was comparable to static culture over 6 h to 168 h. Adapting BCECs to dynamic culture conditions had an impact on tight junction resistance, leading to low R_T value of 1.042 ± 0.433 k Ω ·cm² at 0 h compared to static culture. Nevertheless, the R_T value of dynamic culture was recovered after 6 h showing 2.609 ± 1.029 k Ω ·cm². From the 6 h, the R_T of dynamic culture remained above 1 k Ω ·cm² for 96 h, then continuously decreased and reached to 285 ± 76 Ω ·cm² at 168 h. However, the R_T of static culture remained above 1 k Ω ·cm² for 48 h, ultimately reaching 449 ± 149 Ω ·cm² at 168 h. This is in line with Vatine et al. [168], who demonstrated a decreasing trend in TEER values in an organ-on-chip model cultured with hiPSCs-derived brain microvascular endothelial-like cells (iBMECs) on the blood side, and separately with astrocytes and neurons on the brain side, after a few days of stabilization and increasing dynamic culture time. Also, Hollman et al. [169], reported a similar pattern of results in static culture. Nevertheless, there is a lack of research on the dynamic culture of hiPSCs-derived BBB. This study provides a direct comparison of the electrical properties of these cells under static and dynamic conditions over an extended period. The cell membrane capacitance was possibly quantified and compared between dynamic and static culture, in addition to tight junction resistance. The cell membrane capacitance showed an increasing trend with the culture times in both static and dynamic cultures. In dynamic culture, the cell membrane capacitance was 1.18 ± 0.42 μ F/cm² at 0 h and increased to 1.49 ± 0.11 μ F/cm² at 168 h. In static culture, it started at 1.59 ± 0.58 μ F/cm² at

0 h and rose to $2.02 \pm 0.22 \mu\text{F}/\text{cm}^2$ at 168 h. Consequently, the cell membrane capacitance in static culture consistently demonstrated higher values than that of dynamic culture throughout the entire culture period. Uncertainty remains regarding whether shear stress influences cell membrane capacitance in accordance with physiological changes. Further molecular studies, including ion channel assays and immunofluorescence with plasma membrane protein markers, are required. Although the tight junction resistance (R_T) decreased after 168 h in both static and dynamic culture systems, the expression of tight junction proteins (ZO-1 and Occludin) and Glut-1 in static and dynamic culture, as examined via immunofluorescence (Figure 4.14), exhibited further compaction in the cytoplasm after 168 h. Furthermore, cell nuclei numbers were verified to increase after 168 h of both static and dynamic culture using Fiji (Table 4.3). These morphological changes suggest potential maturation of BCECs. However, additional molecular-based studies are necessary to substantiate this hypothesis. Another aspect is that the increase in cell numbers might contribute to the electrical parameters of cell barrier, R_T and C_C , through changes in surface area. Basically, resistance is inversely proportional to the effective surface area. It can be assumed that as the number of cells increases, the area of tight junctions between cells increases and the R_T decreases accordingly [170]. On the contrary, the capacitance is proportional to the effective surface area. Thus, the observation of an increased trend of capacitance in continuing static and dynamic culture may be due to the growth of cell numbers. These results suggest the need for further investigation to explore morphological changes associated with BCECs maturation, including permeability tests with tracer molecules, while also examining electrical parameters.

Following the practical application of TiN-coated electrodes in a chip bioreactor, TiN-coated tube electrodes were integrated into a miniature HFBR to assess their applicability. The cell culture in a miniature HFBR is beneficial for mimicking the microenvironment in studies of tissue culture models related to the mammalian circulatory system, including endothelial, epithelial cells, and cardiomyocyte models [128,171-174]. Additionally, effective real-time and non-invasive monitoring of cell behavior, such as cell viability or barrier function, is required. Thus, the applicability of TiN-coated tube electrode for EIS measurements, a non-invasive method, was tested in the miniature HFBR. Prior to conducting the initial test to monitor HUVECs culture in miniature HFBR, EIS measurements were performed for transwell culture of HUVECs as a reference. As a result, the cellular barrier impedance, including tight junction resistance and cell membrane capacitance in HUVECs, was detected in a relatively higher frequency range (1 kHz to 794.33 kHz) than BCECs (5 Hz to 1 kHz) discussed in the previous

section. Here, emphasizing the importance of finding the optimal frequency range for objectives, which depends on cell types or EIS measurement setup. The R_T value on culture day 9 was $8.08 \pm 0.40 \Omega \cdot \text{cm}^2$. Meanwhile, the immunofluorescence image showed a confluent monolayer expressing TJ proteins (ZO-1) expression. The results are consistent with those reported by Beti Ernawati Dewi et al., who found that HUVECs demonstrates TEER values of $10 \Omega \cdot \text{cm}^2$ to $12 \Omega \cdot \text{cm}^2$ in transwell culture, when the cells reach confluence [175]. The cell membrane capacitance reached its highest point on day 9 at $0.45 \pm 0.01 \mu\text{F}/\text{cm}^2$. This result is comparable to the study by Pitsalidis et al., who reported a capacitance of $0.73 \pm 0.36 \mu\text{F}/\text{cm}^2$ for a co-cultured HUVEC model [176]. Although the typical range for cell membrane capacitance is around $1 \mu\text{F}/\text{cm}^2$, variations in membrane folding, cell layer thickness, the number of transmembrane proteins among cell lines can lead to differences in membrane capacitance [177-179]. For miniature HFBR culture, the two TiN-coated tube electrodes were positioned right next to the IC inlet and the EC outlet of miniature HFBR. Due to the length (approx. 10 cm) of miniature HFBR, the distance between two electrodes were approx. 7 cm. After subtracting the medium impedance, the observed impedance (from 1 kHz to 100 kHz) increased as the culture proceeded from day 1 to day 3, after which it remained stable until day 7 (Figure 4.19). However, the impedance and phase pattern related to cellular barrier impedance, which includes the parallel connection of the R_T and C_C , were missing. The relatively low tight junction resistance of HUVECs in transwell culture could explain the diminishing contribution of barrier impedance to total impedance as the system became more complex. Furthermore, for a total inner surface area of 15 hollow fibers with an approximate geometrical surface area of 7 cm^2 , the tight junction resistance value could be even lower due to the inverse relationship between resistance and surface area. Furthermore, based on the reference EIS measurement in transwell culture of HUVECs, the expectation was that the cellular barrier impedance would represent in high frequency range (1 kHz to 1 MHz). As observed in influential parameter test (Figure 4.6), the electrode system with a greater distance between electrodes shows an increase in impedance at high frequency ranges, with respect to the experimental setup. Hence, another potential explanation for the undetectability of cellular barrier impedance could be the predominant influence of impedance with respect to the experimental setup in the frequency range of 100 kHz to 1 MHz.

To further assess the applicability of the TiN-coated tube electrode in a miniature HFBR with Caco-2 cell lines, additional experiments were conducted. Before performing EIS measurements in the miniature HFBR culture of Caco-2 cells, the cellular barrier function was

initially assessed in a transwell culture of Caco-2 cells as a reference. The overall average R_T values in static culture showed a decreasing trend during the first seven days of differentiation, dropping from $68.79 \pm 9.4 \Omega \cdot \text{cm}^2$ on day 1 to $38.04 \pm 4.2 \Omega \cdot \text{cm}^2$ on day 7. Afterwards, as the Caco-2 cells became confluent and formed a polarized layer, R_T values steadily increased and reached $96.36 \pm 33.32 \Omega \cdot \text{cm}^2$ after day 21, indicating tight junction formation between adjacent cells. The R_T value after three weeks culture is comparable to the findings reported by Kannapin Felix et al. [170] and Balaji Srinivasan et al. [69]. Furthermore, the R_T value obtained in this study is within the TEER values, $12 \Omega \cdot \text{cm}^2$ to $120 \Omega \cdot \text{cm}^2$, reported for the small intestine *in vivo* [180,181]. In contrast to R_T value, the C_C value in static culture across all three replicates showed an increasing trend throughout the entire culture period, with overall average value of $2.07 \pm 0.12 \mu\text{F}/\text{cm}^2$ on day 1 that increased to $13.75 \pm 3.34 \mu\text{F}/\text{cm}^2$ after day 21. According to George Linz et al., the cell membrane capacitance varied between $3 \mu\text{F}/\text{cm}^2$ to $6 \mu\text{F}/\text{cm}^2$ on culture day 8 to day 10 depending on the ECM coatings used on the inserts [34]. Larissa Lefers et al. also reported that the capacitance of confluent monolayers was between $3.8 \mu\text{F}/\text{cm}^2$ to $5 \mu\text{F}/\text{cm}^2$ [182]. This study demonstrated a higher capacitance than those reported by Linz et al. and Lefers et al. The variation in capacitance values can be associated with the development of microvilli, as proposed by several studies, which have demonstrated an increase in surface area leading to higher capacitance values [114,183]. Supporting the impedance results, the immunofluorescent image revealed the formation of a Caco-2 monolayer after 21 days, with intensive tight junctions observed between adjacent cells. In the miniature HFBR culture of Caco-2, the tight junction resistance and cell membrane capacitance of Caco-2 cells were detectable within a given frequency range of 100 Hz to 10 kHz. However, difficulties were encountered due to measurement errors caused by air bubbles trapped between the hollow fibers. The abrupt drop in impedance occurring in the middle frequency range has disabled the precise extraction of tight junction resistance and cell membrane capacitance values, as the baseline cannot be accurately determined. The miniature HFBR possesses a small, compact space containing about 15 hollow fibers, making the removal of stacked air bubbles a challenging task. Therefore, when seeding cells by injection using a piston, it is important to be careful and avoid generating any air bubbles. Although the abrupt drop in impedance was significant in both the impedance Bode plot and Nyquist plot, the phase Bode plot remained unaffected. The phase pattern reflecting the parallel connection of a resistor, representing the resistance of the tight junction barrier, and a capacitor, representing the charging characteristic of the cell membrane, was observed throughout the culture days (day 3, 6, 7, and 14). The impedance results of days 7 and 14 didn't encounter any error issues, making it possible to

quantify the R_T and the C_C through fitting and simulation. The values of R_T and C_C on day 7 were 163.08Ω and $0.663 \mu\text{F}$, respectively, and increased to 293.48Ω and decreased to $0.364 \mu\text{F}$ on day 14. Because of incorporate biological replication, it may limit the generalizability of the findings to compare with those of other studies. However, the results still confirm the potential of using a TiN-coated tube electrode for non-invasive monitoring Caco-2 culture in miniature HFBR culture. Therefore, although this study has its limitations, its findings can still be valuable for future research and applications in this area.

To investigate the practicality of the electrode system in hemofiltration, TiN-coated electrodes were incorporated into a hemofilter system. The ultimate goal of this application is to test the hypothesis that EIS measurements can detect clogging on the filter membranes. Clogging of the hemofilter is a critical factor that reduces membrane effectiveness during hemofiltration. Continuing to operate hemofiltration with a clogged hemofilter can increase pressure, potentially causing damage to the filter or cells in blood and increasing the risk of infection [184,185]. Therefore, promptly detecting clogging is important to prevent those side effects. An investigation was conducted to determine whether EIS measurement, utilizing TiN-coated tube electrodes, could enable real-time monitoring of clogging on the hemofilter membrane based on the hypothesis. Connecting the six TiN-coated tube electrodes to the hemofilter was a simple and easy process using commercially available Luer lock connectors. The three entrances, blood inlet and outlet and effluent outlet connected each with two TiN-coated tube electrodes (Figure 3.8). Two electrodes were paired to perform a single EIS measurement, capable of measuring specific impedances such as impedance across the membrane (Z_{AM}), along the fibers (Z_{AF}), arterial ($Z_{Arterial}$) and venous (Z_{Venous}) blood impedance, as well as the impedance of effluent ($Z_{Effluent}$). Despite the complexity of the hemofiltration process, the TiN-coated electrodes were sensitive enough to detect impedance through the hemofilter, resulting in clear impedance readings in frequency spectrum. To test the hypothesis, the Z_{AM} value at 100 Hz was extracted and plotted as a function of the measurement time points to compare it with the pressure readings (Figure 4.26). The first impedance drop was observed within one hour, and simultaneously, a pressure drop was also noted in both $P_{Arterial}$ and P_{Venous} . This could be attributed to early clotting occurring as soon as hemofiltration begins. Clotting can potentially reduce the blood flow rate, and the changes in blood components due to clotting might contribute to the impedance drop. Furthermore, it was observed that the Z_{AM} mostly showed its highest value at the time point where the TMP reached its peak pressure around 300 mmHg. However, after the peak, while the TMP was sustained it until the end of the hemofiltration,

the Z_{AM} value dropped even lower than its initial value. Thus, trend was observed in all three individual hemofiltration tests. It was assumed that the contribution of blood impedance (electrolyte impedance) to total impedance might be higher than impedance occurred by clogging, where the Z_{AM} dropped after peak unlike TMP. To check the assumption, the calculation of the difference in blood impedance between arterial and venous (ΔZ_{V-A}) was conducted and subsequently compared with the TMP. As investigating three individual hemofiltration (Hemofilter 1,2, and 4), during the first 200 min, both the ΔZ_{V-A} and TMP values remained stable and comparable to their initial values, following a similar trend. However, as the hemofiltration process continued, the TMP steadily increased while the ΔZ_{V-A} value gradually decreased until the end. The initial values of the three hemofiltration experiments ranged from approximately 9.5 k Ω to 16 k Ω , while the final values were approximately 2 k Ω to 6 k Ω . This is likely due to the fiber membrane becoming clogged, resulting in reduced ionic permeability across the membrane and a subsequent decrease in ΔZ_{V-A} . As ions such as sodium (Na^+), bicarbonate (HCO_3^-), and chloride (Cl^-) that are removed from blood during hemofiltration are relatively smaller in size compared to other waste solutes such as urea and creatinine, lower ΔZ_{V-A} suggests impediment to ion permeation by the clogged membrane. Although TMP values are commonly used indicators for the clogging of a hemofilter, they are not absolute, as they can be impacted by other phenomena such as clotting or clogging of the venous drip chamber. Therefore, tracking the ions permeability using ΔZ_{V-A} may offer a more precise and absolute indication of membrane clogging during hemofiltration. The results suggest the potential for real-time non-invasive monitoring of hemofilter clogging through EIS measurements, but further research is necessary to establish a definitive conclusion. To improve understanding of the phenomenon, future studies should focus on investigating multiple results at various measurement time points (e.g., every minute) to capture the dynamics of the process. To achieve measurements at various time points, the frequency range can be narrowed (e.g., using 10 frequency points or even fewer), thereby reducing the measurement time from 8 min to 10 min down to 1 min to 3 min.

In summary, the independent add-on electrode unit ultimately suggests enhancing the versatility of the electrode in either perfusion bioreactors or a medical device to enable EIS, while providing precise EIS results for specific objectives. Recent studies have reported using electrodes inserted inside a bioreactor or directly affixed to it, as well as constructing four electrodes within a perfusion bioreactor [113-116,186,187]. However, the use of electrodes is limited in specific bioreactor, and especially, in microfluidic, the reproducibility is an issue.

Moreover, although four electrodes setup has preferred because it can eliminate the electrode resistance, which is not main object in biological experiments, it is a challenge to secure the space for electrodes in bioreactor. Here, the TiN-coated tube electrode achieved a relatively low impedance, resulting in a minor impact on the frequency spectrum of EIS measurements, allowing for a two-electrodes setup instead of four-electrodes setup. Consequently, it enables obtaining precise results with a simple setup using only two electrodes. Also, this independent add-on electrode design is reusable multiple times through autoclaving, and the simple fabrication process enables mass production. So, it could resolve the reproducibility issues, as electrode production is independent of bioreactor fabrication. Furthermore, its adaptability to various existing perfusion bioreactors has been confirmed, demonstrating versatility of the TiN-coated tube electrode in chip bioreactors, hollow fiber bioreactors, and hemofiltration for real-time and non-invasive EIS monitoring. While testing the applicability of TiN-coated tube electrodes in a chip bioreactor, this study proposes a novel bioreactor system that allows for non-invasive monitoring of cell barrier characteristics using EIS. Consequently, it enables the development of long-term shear stress-sensitive *in vitro* hiPSC-derived BCECs model. While Vatine et al. demonstrated long term TEER monitoring within a micro-organ-on-chip model that incorporates shear stress, the limited sample size remains as a concern in terms of reproducibility and the widespread applicability [168]. Regarding this, a millimeter-sized chip bioreactor could offer a greater number of cell samples for further analysis. In the next application of miniature HFBR, it was verified that non-invasive EIS monitoring of Caco-2 culture is feasible using a TiN-coated tube electrode, although it requires further experimentation for validation. There is a commercially available hollow fiber bioreactor facilitate four electrodes [116]. However, when considering studies like those presented on fiber modification aimed at enhancing the optimization of cell culture within a hollow fiber bioreactor [122,188-190], the use of commercial options is limited because they are associated with a single type of HFBR produced by company. On the other hand, the TiN-coated electrode can be adaptable in any type of HFBR. In the final application section involving the TiN-coated tube electrode, it was confirmed that the integration of the TiN-coated tube electrode into a hemofilter allows for real-time and non-invasive EIS monitoring of hemofilter clogging. TMP monitoring is only commonly used method for clogging monitoring during hemofiltration [191-194]. However, there is a possibility that pressures can be influenced by other factors, such as clogging on the venous drip chamber, making the definitive detection of clogging on the hemofilter membrane still a challenge [195]. Therefore, the EIS monitoring

proposed in this study, which tracks real-time blood conductivity, can complement the pressure monitoring methods in detecting clogging on the hemofilter.

6. Conclusion and Outlook

In conclusion, a modular add-on electrode, specifically a TiN-coated tube electrode, has been developed, demonstrating superior material quality and a robust structure suitable for use under fluid flow culture conditions. To verify the versatility of the electrodes, the TiN-coated tube electrodes were applied to two different bioreactor platforms and a medical device, including a newly fabricated perfusion bioreactor called the chip bioreactor, a hollow fiber bioreactor, and a hemofilter, for EIS monitoring. As a result of first application with chip bioreactor, the successful automated, real-time, and non-invasive EIS monitoring of barrier integrity of hiPSC-derived BCECs in dynamic culture was achieved using TiN-coated tube electrode. Moreover, the dynamic culture system is proposed to be capable of generating a flow-sensitive model of hiPSC-derived BCECs with potential applications in transport studies. The second application of a miniature HFBR indicated the potential for non-invasive EIS monitoring of Caco-2 cells in a miniature HFBR culture. However, the detection of HUVECs culture was limited due to the relatively low impedance associated with barrier integrity in the complex system. Lastly, TiN-coated tube electrodes were integrated into hemofiltration to test the hypothesis that EIS could be employed for detecting the clotting and clogging of the filter membrane. The results revealed that real-time monitoring of changes in ion concentration in the blood at the inlet and outlet of the filter was possible through EIS using TiN-coated tube electrodes, with the distinction in blood impedance may serve as an indicator of filter clogging.

It has been confirmed that the TiN-coated tube electrode can be easily integrated into existing perfusion bioreactor systems without the need for any construction processes. Consequently, various applications can be expected within dynamic barrier tissue culture models. As an example, the TiN-coated tube electrode can be adapted to microfluidic bioreactors or organ-on-chip systems by adjusting the diameter of the 3D-printed Luer lock connector and SS tube substrate. This could potentially offer a secure space within a micro-sized bioreactor while still delivering reliable EIS results. In future studies within the chip bioreactor system, additional analysis is required to explore the connection between the maturation and morphological changes observed in hiPSC-derived BCECs. As part of this analysis, it is essential to conduct a correlation between electrical parameters measured by EIS and the permeability of tracer molecules to effectively address the findings. Furthermore, the chip bioreactor system, incorporating TiN-coated tube electrodes, can be used for drug transport studies. For the monitoring of Caco-2 cells in the miniature HFBR experiment, additional experiment repetitions are necessary to verify the feasibility of EIS monitoring in miniature HFBR cell

culture. Also, other tissue cultures, such as the BBB, can be utilized for electrode verification in HFBR tissue culture. Through the EIS monitoring in hemofiltration, the finding real-time monitoring of blood impedance can be valuable indicator to detect clotting and clogging in the hemofilter. To find the standard value correlating clotting or clogging of hemofilter, enormous experiments need to be conducted. In addition, it is essential to conduct simultaneous EIS measurements of venous impedance and arterial impedance for further study by incorporating more impedance spectroscopy device. Additionally, the applied frequency range needs to be adjusted to enable measurements at one-minute intervals, reducing the measurement time to one minute.

7. Bibliography

1. Anusha, T.; Bhavani, K.S.; Kumar, J.S.; Brahman, P.K.; Hassan, R.Y. Fabrication of electrochemical immunosensor based on GCN- β -CD/Au nanocomposite for the monitoring of vitamin D deficiency. *Bioelectrochemistry* **2022**, *143*, 107935.
2. Zhang, X.; Wu, Y.; Tu, Y.; Liu, S. A reusable electrochemical immunosensor for carcinoembryonic antigen via molecular recognition of glycoprotein antibody by phenylboronic acid self-assembly layer on gold. *Analyst* **2008**, *133*, 485-492.
3. Easton, E.B.; Pickup, P.G. An electrochemical impedance spectroscopy study of fuel cell electrodes. *Electrochim Acta* **2005**, *50*, 2469-2474.
4. Hernández, H.H.; Reynoso, A.M.R.; González, J.C.T.; Morán, C.O.G.; Hernández, J.G.M.; Ruiz, A.M.; Hernández, J.M.; Cruz, R.O. Electrochemical impedance spectroscopy (EIS): A review study of basic aspects of the corrosion mechanism applied to steels. *Electrochemical Impedance Spectroscopy* **2020**, 137-144.
5. Liu, X.; Xiong, J.; Lv, Y.; Zuo, Y. Study on corrosion electrochemical behavior of several different coating systems by EIS. *Progress in Organic Coatings* **2009**, *64*, 497-503, doi:<https://doi.org/10.1016/j.porgcoat.2008.08.012>.
6. Schranzhofer, H.; Bugajski, J.; Santner, H.J.; Korepp, C.; Möller, K.-C.; Besenhard, J.O.; Winter, M.; Sitte, W. Electrochemical impedance spectroscopy study of the SEI formation on graphite and metal electrodes. *Journal of Power Sources* **2006**, *153*, 391-395.
7. Mansfeld, F.; Jeanjaquet, S.; Kendig, M. An electrochemical impedance spectroscopy study of reactions at the metal/coating interface. *Corrosion Science* **1986**, *26*, 735-742.
8. Macdonald, D.D.; Sun, A. An electrochemical impedance spectroscopic study of the passive state on Alloy-22. *Electrochim Acta* **2006**, *51*, 1767-1779.
9. Rondelli, G.; Torricelli, P.; Fini, M.; Giardino, R. In vitro corrosion study by EIS of a nickel-free stainless steel for orthopaedic applications. *Biomaterials* **2005**, *26*, 739-744.
10. Bertok, T.; Lorencova, L.; Chocholova, E.; Jane, E.; Vikartovska, A.; Kasak, P.; Tkac, J. Electrochemical impedance spectroscopy based biosensors: Mechanistic principles, analytical examples and challenges towards commercialization for assays of protein cancer biomarkers. *ChemElectroChem* **2019**, *6*, 989-1003.
11. Moysidou, C.M.; Pitsalidis, C.; Al-Sharabi, M.; Withers, A.M.; Zeitler, J.A.; Owens, R.M. 3D bioelectronic model of the human intestine. *Advanced Biology* **2021**, *5*, 2000306.
12. Mitamura, Y.; Ogulur, I.; Pat, Y.; Rinaldi, A.O.; Ardicli, O.; Cevhertas, L.; Brüggem, M.C.; Traidl-Hoffmann, C.; Akdis, M.; Akdis, C.A. Dysregulation of the epithelial barrier by environmental and other exogenous factors. *Contact Dermatitis* **2021**, *85*, 615-626.
13. Fernández-Sánchez, C.; McNeil, C.J.; Rawson, K. Electrochemical impedance spectroscopy studies of polymer degradation: application to biosensor development. *TrAC Trends in Analytical Chemistry* **2005**, *24*, 37-48.
14. Dean, D.; Ramanathan, T.; Machado, D.; Sundararajan, R. Electrical impedance spectroscopy study of biological tissues. *Journal of electrostatics* **2008**, *66*, 165-177.
15. Pan, J.; Thierry, D.; Leygraf, C. Electrochemical impedance spectroscopy study of the passive oxide film on titanium for implant application. *Electrochim Acta* **1996**, *41*, 1143-1153.
16. Allen J. Bard, L.R.F. *Electrochemical Methods: Fundamentals and Applications, 2nd Edition*; John Wiley & Sons: 2001.
17. Pan, J.; Leygraf, C.; Thierry, D.; Ektessabi, A. Corrosion resistance for biomaterial applications of TiO₂ films deposited on titanium and stainless steel by ion-beam-

- assisted sputtering. *Journal of Biomedical Materials Research: An Official Journal of The Society for Biomaterials and The Japanese Society for Biomaterials* **1997**, *35*, 309-318.
18. Bolat, G.; Izquierdo, J.; Santana, J.J.; Mareci, D.; Souto, R.M. Electrochemical characterization of ZrTi alloys for biomedical applications. *Electrochim Acta* **2013**, *88*, 447-456, doi:<https://doi.org/10.1016/j.electacta.2012.10.026>.
 19. Adumitrăchioaie, A.; Tertiş, M.; Cernat, A.; Săndulescu, R.; Cristea, C. Electrochemical methods based on molecularly imprinted polymers for drug detection. A review. *Int. J. Electrochem. Sci* **2018**, *13*, 2556-2576.
 20. Narang, J.; Malhotra, N.; Singh, G.; Pundir, C. Electrochemical impedimetric detection of anti-HIV drug taking gold nanorods as a sensing interface. *Biosensors and Bioelectronics* **2015**, *66*, 332-337.
 21. Kim, T.; Kang, J.; Lee, J.-H.; Yoon, J. Influence of attached bacteria and biofilm on double-layer capacitance during biofilm monitoring by electrochemical impedance spectroscopy. *Water Research* **2011**, *45*, 4615- 4622, doi:<https://doi.org/10.1016/j.watres.2011.06.010>.
 22. Mohammad-Razdari, A.; Ghasemi-Varnamkhashti, M.; Izadi, Z.; Ensafi, A.A.; Rostami, S.; Siadat, M. An impedimetric aptasensor for ultrasensitive detection of Penicillin G based on the use of reduced graphene oxide and gold nanoparticles. *Microchimica Acta* **2019**, *186*, 1-10.
 23. Basics of Electrochemical Impedance Spectroscopy. Available online: <https://www.gamry.com/application-notes/EIS/basics-of-electrochemical-impedance-spectroscopy/> (accessed on December. 2022).
 24. Peroff, A. Electrochemical Impedance Spectroscopy (EIS) Basics. Available online: <https://pineresearch.com/shop/kb/theory/eis-theory/eis-basics/> (accessed on April. 2023).
 25. EIS Mathematical Theory. Available online: <https://pineresearch.com/shop/kb/theory/eis-theory/eis-mathematical-theory/> (accessed on April.2023).
 26. Lazanas, A.C.; Prodromidis, M.I. Electrochemical Impedance Spectroscopy—A Tutorial. *ACS Measurement Science Au* **2023**, *3*, 162- 193, doi:10.1021/acsmesuresci.au.2c00070.
 27. Magar, H.S.; Hassan, R.Y.A.; Mulchandani, A. Electrochemical Impedance Spectroscopy (EIS): Principles, Construction, and Biosensing Applications. *Sensors (Basel)* **2021**, *21*, doi:10.3390/s21196578.
 28. Abdul Halim, S.I.; Chan, C.H.; Apotheker, J. Basics of teaching electrochemical impedance spectroscopy of electrolytes for ion-rechargeable batteries – part 1: a good practice on estimation of bulk resistance of solid polymer electrolytes. *Chemistry Teacher International* **2021**, *3*, 105-115, doi:10.1515/cti-2020-0011.
 29. Bandarenka, A.S. Exploring the interfaces between metal electrodes and aqueous electrolytes with electrochemical impedance spectroscopy. *The Analyst* **2013**, *138*, 5540, doi:10.1039/c3an00791j.
 30. Juttner, K. Electrochemical Impedance Spectroscopy (Eis) of Corrosion Processes on Inhomogeneous Surfaces. *Electrochim Acta* **1990**, *35*, 1501- 1508, doi: Doi 10.1016/0013-4686(90)80004-8.
 31. Sriraman, K.R.; Brahimi, S.; Szpunar, J.A.; Osborne, J.H.; Yue, S. Characterization of corrosion resistance of electrodeposited Zn-Ni Zn and Cd coatings. *Electrochim Acta* **2013**, *105*, 314-323, doi:10.1016/j.electacta.2013.05.010.

32. Norlin, A.; Pan, J.; Leygraf, C. Investigation of interfacial capacitance of Pt, Ti and TiN coated electrodes by electrochemical impedance spectroscopy. *Biomolecular Engineering* **2002**, *19*, 67-71, doi:[https://doi.org/10.1016/S1389-0344\(02\)00013-8](https://doi.org/10.1016/S1389-0344(02)00013-8).
33. Rengaraju, S.; Neelakantan, L.; Pillai, R. Investigation on the polarization resistance of steel embedded in highly resistive cementitious systems – An attempt and challenges. *Electrochim Acta* **2019**, *308*, doi:10.1016/j.electacta.2019.03.200.
34. Linz, G.; Djeljadini, S.; Steinbeck, L.; Köse, G.; Kiessling, F.; Wessling, M. Cell barrier characterization in transwell inserts by electrical impedance spectroscopy. *Biosensors and Bioelectronics* **2020**, *165*, 112345, doi:10.1016/j.bios.2020.112345.
35. Rajabzadeh, M.; Ungethuen, J.; Herkle, A.; Schilpp, C.; Fauler, M.; Wittekindt, O.; Ortmanns, M. A 24-Ch. Multi-Electrode Array Allowing Fast EIS to Determine Transepithelial Electrical Resistance. In Proceedings of the 2019 IEEE Biomedical Circuits and Systems Conference (BioCAS), 17-19 Oct. 2019, 2019; pp. 1-4.
36. Vigh, J.P.; Kincses, A.; Ozgür, B.; Walter, F.R.; Santa-Maria, A.R.; Valkai, S.; Vastag, M.; Neuhaus, W.; Brodin, B.; Dér, A. Transendothelial electrical resistance measurement across the blood–brain barrier: A critical review of methods. *Micromachines* **2021**, *12*, 685.
37. De León, S.E.; Pupovac, A.; McArthur, S.L. Three-Dimensional (3D) cell culture monitoring: Opportunities and challenges for impedance spectroscopy. *Biotechnology and bioengineering* **2020**, *117*, 1230-1240.
38. Zeng, A.; Liu, E.; Annergren, I.F.; Tan, S.N.; Zhang, S.; Hing, P.; Gao, J. EIS capacitance diagnosis of nanoporosity effect on the corrosion protection of DLC films. *Diamond and Related Materials* **2002**, *11*, 160-168, doi:[https://doi.org/10.1016/S0925-9635\(01\)00568-4](https://doi.org/10.1016/S0925-9635(01)00568-4).
39. K'Owino, I.O.; Sadik, O.A. Impedance Spectroscopy: A Powerful Tool for Rapid Biomolecular Screening and Cell Culture Monitoring. *Electroanalysis* **2005**, *17*, 2101-2113, doi:<https://doi.org/10.1002/elan.200503371>.
40. Mansfeld, F. Electrochemical impedance spectroscopy (EIS) as a new tool for investigating methods of corrosion protection. *Electrochim Acta* **1990**, *35*, 1533-1544, doi:[https://doi.org/10.1016/0013-4686\(90\)80007-B](https://doi.org/10.1016/0013-4686(90)80007-B).
41. EIS Data fitting – How to obtain good starting values of equivalent circuit elements. Available online:<https://translate.google.com/translate?hl=de&sl=en&u=https://www.metrohm.com/en/applications/application-notes/autolab-applikationen-anautolab/an-eis-007.html&prev=search&pto=ae> (accessed on
42. Chang, B.-Y. Conversion of a constant phase element to an equivalent capacitor. *Journal of Electrochemical Science and Technology* **2020**, *11*, 318-321.
43. Brug, G.; van den Eeden, A.L.; Sluyters-Rehbach, M.; Sluyters, J.H. The analysis of electrode impedances complicated by the presence of a constant phase element. *Journal of electroanalytical chemistry and interfacial electrochemistry* **1984**, *176*, 275-295.
44. Córdoba-Torres, P.; Mesquita, T.J.; Devos, O.; Tribollet, B.; Roche, V.; Nogueira, R.P. On the intrinsic coupling between constant-phase element parameters α and Q in electrochemical impedance spectroscopy. *Electrochim Acta* **2012**, *72*, 172-178, doi:<https://doi.org/10.1016/j.electacta.2012.04.020>.
45. Schiller, C.A.; Strunz, W. The evaluation of experimental dielectric data of barrier coatings by means of different models. *Electrochim Acta* **2001**, *46*, 3619-3625, doi:[https://doi.org/10.1016/S0013-4686\(01\)00644-2](https://doi.org/10.1016/S0013-4686(01)00644-2).
46. Darowicki, K.; Ślepski, P.; Szociński, M. Application of the dynamic EIS to investigation of transport within organic coatings. *Progress in Organic Coatings* **2005**, *52*, 306-310, doi:<https://doi.org/10.1016/j.porgcoat.2004.06.007>.

47. Nguyen, T.Q.; Breitkopf, C. Determination of Diffusion Coefficients Using Impedance Spectroscopy Data. *Journal of The Electrochemical Society* **2018**, *165*, E826, doi:10.1149/2.1151814jes.
48. Randviir, E.P.; Banks, C.E. Electrochemical impedance spectroscopy: an overview of bioanalytical applications. *Analytical methods* **2013**, *5*, 1098-1115.
49. Magin, R.; Ovadia, M. Modeling the cardiac tissue electrode interface using fractional calculus. *Journal of Vibration and Control* **2008**, *14*, 1431-1442.
50. Brett, C.M.A. Electrochemical Impedance Spectroscopy in the Characterisation and Application of Modified Electrodes for Electrochemical Sensors and Biosensors. *Molecules* **2022**, *27*, doi:10.3390/molecules27051497.
51. Schwan, H.P. Electrical Properties of Tissue and Cell Suspensions* *This work was supported in part by grants from the United States Public Health Service, H-1253(c2-4) and in part by the Office of Naval Research, 119–289. In *Advances in Biological and Medical Physics*, Lawrence, J.H., Tobias, C.A., Eds.; Elsevier: 1957; Volume 5, pp. 147-209.
52. Miklavčič, D.; Pavšelj, N.; Hart, F.X. Electric properties of tissues. *Wiley encyclopedia of biomedical engineering* **2006**.
53. Amini, M.; Hisdal, J.; Kalvøy, H. Applications of bioimpedance measurement techniques in tissue engineering. *Journal of Electrical Bioimpedance* **2018**, *9*, 142-158.
54. Anderson, J.M.; Van Itallie, C.M. Physiology and function of the tight junction. *Cold Spring Harbor perspectives in biology* **2009**, *1*, a002584.
55. Alberts, B.; Johnson, A.; Lewis, J.; Raff, M.; Roberts, K.; Walter, P. Blood vessels and endothelial cells. In *Molecular Biology of the Cell. 4th edition*; Garland Science: 2002.
56. Yeste, J.; Illa, X.; Alvarez, M.; Villa, R. Engineering and monitoring cellular barrier models. *Journal of biological engineering* **2018**, *12*, 1-19.
57. Lampugnani, M.G. Endothelial cell-to-cell junctions: adhesion and signaling in physiology and pathology. *Cold Spring Harbor perspectives in medicine* **2012**, *2*, a006528.
58. Ussing, H.H. The active ion transport through the isolated frog skin in the light of tracer studies. *Acta Physiol Scand* **1949**, *17*, 1-37, doi:10.1111/j.1748-1716.1949.tb00550.x.
59. Ussing, H.H. The distinction by means of tracers between active transport and diffusion: The transfer of iodide across the isolated frog skin. *Acta physiologica scandinavica* **1949**, *19*, 43-56.
60. Tsukita, S.; Furuse, M.; Itoh, M. Multifunctional strands in tight junctions. *Nature reviews Molecular cell biology* **2001**, *2*, 285-293.
61. Ussing, H.H. Epithelial transport: frog skin as a model system. *Membrane Transport: People and Ideas* **1989**, 337-362.
62. Volpe, D.A. Variability in Caco-2 and MDCK cell-based intestinal permeability assays. *Journal of pharmaceutical sciences* **2008**, *97*, 712-725.
63. Sambuy, Y.; De Angelis, I.; Ranaldi, G.; Scarino, M.; Stamatii, A.; Zucco, F. The Caco-2 cell line as a model of the intestinal barrier: influence of cell and culture-related factors on Caco-2 cell functional characteristics. *Cell biology and toxicology* **2005**, *21*, 1-26.
64. Odijk, M.; van der Meer, A.D.; Levner, D.; Kim, H.J.; van der Helm, M.W.; Segerink, L.I.; Frimat, J.-P.; Hamilton, G.A.; Ingber, D.E.; van den Berg, A. Measuring direct current trans-epithelial electrical resistance in organ-on-a-chip microsystems. *Lab on a Chip* **2015**, *15*, 745-752.
65. Elbrecht, D.H.; Long, C.J.; Hickman, J.J. Transepithelial/endothelial Electrical Resistance (TEER) theory and applications for microfluidic body-on-a-chip devices. *Journal of Rare Diseases Research & Treatment* **2016**, *1*.

66. Sill, H.W.; Chang, Y.S.; Artman, J.R.; Frangos, J.; Hollis, T.; Tarbell, J.M. Shear stress increases hydraulic conductivity of cultured endothelial monolayers. *American Journal of Physiology-Heart and Circulatory Physiology* **1995**, *268*, H535-H543.
67. Suttorp, N.; Hessz, T.; Seeger, W.; Wilke, A.; Koob, R.; Lutz, F.; Drenckhahn, D. Bacterial exotoxins and endothelial permeability for water and albumin in vitro. *American Journal of Physiology-Cell Physiology* **1988**, *255*, C368-C376.
68. Benson, K.; Cramer, S.; Galla, H.-J. Impedance-based cell monitoring: barrier properties and beyond. *Fluids and Barriers of the CNS* **2013**, *10*, 1-11.
69. Srinivasan, B.; Kolli, A.R.; Esch, M.B.; Abaci, H.E.; Shuler, M.L.; Hickman, J.J. TEER measurement techniques for in vitro barrier model systems. *J Lab Autom* **2015**, *20*, 107-126, doi:10.1177/2211068214561025.
70. Haorah, J.; Schall, K.; Ramirez, S.H.; Persidsky, Y. Activation of protein tyrosine kinases and matrix metalloproteinases causes blood-brain barrier injury: Novel mechanism for neurodegeneration associated with alcohol abuse. *Glia* **2008**, *56*, 78-88.
71. Andjelkovic, A.V.; Stamatovic, S.M.; Phillips, C.M.; Martinez-Revollar, G.; Keep, R.F. Modeling blood-brain barrier pathology in cerebrovascular disease in vitro: current and future paradigms. *Fluids and Barriers of the CNS* **2020**, *17*, 1-21.
72. Lengauer, W.; Binder, S.; Aigner, K.; Ettmayer, P.; Guillou, A.; Debuigne, J.; Groboth, G. Solid state properties of group IVb carbonitrides. *Journal of Alloys and Compounds* **1995**, *217*, 137-147, doi:[https://doi.org/10.1016/0925-8388\(94\)01315-9](https://doi.org/10.1016/0925-8388(94)01315-9).
73. Terence, B. Electrical Conductivity of Metals. Available online: thoughtco.com/electrical-conductivity-in-metals-2340117 (accessed on
74. Datta, S.; Das, M.; Balla, V.K.; Bodhak, S.; Murugesan, V. Mechanical, wear, corrosion and biological properties of arc deposited titanium nitride coatings. *Surface and Coatings Technology* **2018**, *344*, 214-222.
75. Dion, I.; Roques, X.; More, N.; Labrousse, L.; Caix, J.; Lefebvre, F.; Rouais, F.; Gautreau, J.; Baquey, C. Ex vivo leucocyte adhesion and protein adsorption on TiN. *Biomaterials* **1993**, *14*, 712-719.
76. Tamura, Y.; Yokoyama, A.; Watari, F.; Kawasaki, T. Surface properties and biocompatibility of nitrated titanium for abrasion resistant implant materials. *Dental materials journal* **2002**, *21*, 355-372.
77. Serro, A.; Completo, C.; Colaço, R.; Dos Santos, F.; Da Silva, C.L.; Cabral, J.; Araújo, H.; Pires, E.; Saramago, B. A comparative study of titanium nitrides, TiN, TiNbN and TiCN, as coatings for biomedical applications. *Surface and Coatings Technology* **2009**, *203*, 3701-3707.
78. Cui, W.; Qin, G.; Duan, J.; Wang, H. A graded nano-TiN coating on biomedical Ti alloy: Low friction coefficient, good bonding and biocompatibility. *Materials Science and Engineering: C* **2017**, *71*, 520-528.
79. Piscanec, S.; Ciacchi, L.C.; Vesselli, E.; Comelli, G.; Sbaizero, O.; Meriani, S.; De Vita, A. Bioactivity of TiN-coated titanium implants. *Acta Materialia* **2004**, *52*, 1237-1245.
80. Khatkhatay, F.; Jiao, L.; Jian, J.; Zhang, W.; Jiao, Z.; Gan, J.; Zhang, H.; Zhang, X.; Wang, H. Superior corrosion resistance properties of TiN-based coatings on Zircaloy tubes in supercritical water. *Journal of Nuclear Materials* **2014**, *451*, 346-351.
81. Was, G.S.; Ampornrat, P.; Gupta, G.; Teyseyre, S.; West, E.A.; Allen, T.R.; Sridharan, K.; Tan, L.; Chen, Y.; Ren, X.; et al. Corrosion and stress corrosion cracking in supercritical water. *Journal of Nuclear Materials* **2007**, *371*, 176-201, doi:<https://doi.org/10.1016/j.jnucmat.2007.05.017>.
82. Subramanian, B.; Muraleedharan, C.; Ananthakumar, R.; Jayachandran, M. A comparative study of titanium nitride (TiN), titanium oxy nitride (TiON) and titanium

- aluminum nitride (TiAlN), as surface coatings for bio implants. *Surface and Coatings Technology* **2011**, *205*, 5014-5020.
83. Curtis, H.J.; Cole, K.S. Transverse electric impedance of Nitella. *The Journal of general physiology* **1937**, *21*, 189-201.
 84. Kappenman, E.S.; Luck, S.J. The effects of electrode impedance on data quality and statistical significance in ERP recordings. *Psychophysiology* **2010**, *47*, 888-904.
 85. Picton, T.W.; Bentin, S.; Berg, P.; Donchin, E.; Hillyard, S.; Johnson Jr, R.; Miller, G.; Ritter, W.; Ruchkin, D.; Rugg, M. Guidelines for using human event-related potentials to study cognition: Recording standards and publication criteria. **2000**.
 86. Schmitz, T.; Schweinlin, M.; Kollhoff, R.T.; Engelhardt, L.; Lotz, C.; Groeber-Becker, F.; Walles, H.; Metzger, M.; Hansmann, J. Nanostructured TiN-Coated Electrodes for High-Sensitivity Noninvasive Characterization of in Vitro Tissue Models. *Acs Appl Nano Mater* **2018**, *1*, 2284-2293, doi:10.1021/acsanm.8b00345.
 87. Schmitz, T. Functional coatings by physical vapor deposition (PVD) for biomedical applications. Universität Würzburg, 2016.
 88. Mattox, D.M. Physical vapor deposition (PVD) processes. *Metal Finishing* **2002**, *100*, 394-408.
 89. Rossnagel, S. Thin film deposition with physical vapor deposition and related technologies. *Journal of Vacuum Science & Technology A: Vacuum, Surfaces, and Films* **2003**, *21*, S74-S87.
 90. Probst, J.; Gbureck, U.; Thull, R. Binary nitride and oxynitride PVD coatings on titanium for biomedical applications. *Surface and Coatings Technology* **2001**, *148*, 226-233.
 91. Zarka, M.; Dikici, B.; Niinomi, M.; Ezirmik, K.; Nakai, M.; Yilmazer, H. A systematic study of β -type Ti-based PVD coatings on magnesium for biomedical application. *Vacuum* **2021**, *183*, 109850.
 92. Uddin, G.M.; Jawad, M.; Ghufuran, M.; Saleem, M.W.; Raza, M.A.; Rehman, Z.U.; Arafat, S.M.; Irfan, M.; Waseem, B. Experimental investigation of tribo-mechanical and chemical properties of TiN PVD coating on titanium substrate for biomedical implants manufacturing. *The International Journal of Advanced Manufacturing Technology* **2019**, *102*, 1391-1404.
 93. Heo, C.H.; Lee, S.-B.; Boo, J.-H. Deposition of TiO₂ thin films using RF magnetron sputtering method and study of their surface characteristics. *Thin solid films* **2005**, *475*, 183-188.
 94. Lee, B.H.; Kim, I.G.; Cho, S.W.; Lee, S.-H. Effect of process parameters on the characteristics of indium tin oxide thin film for flat panel display application. *Thin Solid Films* **1997**, *302*, 25-30.
 95. Chawla, V.; Jayaganthan, R.; Chandra, R. Structural characterizations of magnetron sputtered nanocrystalline TiN thin films. *Materials characterization* **2008**, *59*, 1015-1020.
 96. Patsalas, P.; Charitidis, C.; Logothetidis, S. The effect of substrate temperature and biasing on the mechanical properties and structure of sputtered titanium nitride thin films. *Surface and Coatings Technology* **2000**, *125*, 335-340.
 97. Jones, M.; McColl, I.; Grant, D. Effect of substrate preparation and deposition conditions on the preferred orientation of TiN coatings deposited by RF reactive sputtering. *Surface and Coatings Technology* **2000**, *132*, 143-151.
 98. Kavitha, A.; Kannan, R.; Sreedhara Reddy, P.; Rajashabala, S. The effect of annealing on the structural, optical and electrical properties of Titanium Nitride (TiN) thin films prepared by DC magnetron sputtering with supported discharge. *Journal of Materials Science: Materials in Electronics* **2016**, *27*, 10427-10434.

99. Merie, V.; Bîrleanu, C.; Pustan, M.; Negrea, G.; Pinteau, I. Analysis on temperature effect on the mechanical and tribological properties of titanium nitride thin films. In Proceedings of the IOP Conference Series: Materials Science and Engineering, 2016; p. 012019.
100. Vasu, K.; Krishna, M.G.; Padmanabhan, K. Substrate-temperature dependent structure and composition variations in RF magnetron sputtered titanium nitride thin films. *Applied Surface Science* **2011**, *257*, 3069-3074.
101. Kim, T.-S.; Park, S.-S.; Lee, B.-T. Characterization of nano-structured TiN thin films prepared by RF magnetron sputtering. *Materials Letters* **2005**, *59*, 3929-3932.
102. Dhanaraj, R.; Mohamed, S.; Kamruddin, M.; Kaviyarasu, K.; Manojkumar, P. Structural properties of TiN thin films prepared by RF reactive magnetron sputtering. *Materials Today: Proceedings* **2021**, *36*, 146-149.
103. Gastfriend, B.D.; Palecek, S.P.; Shusta, E.V. Modeling the blood–brain barrier: Beyond the endothelial cells. *Current Opinion in Biomedical Engineering* **2018**, *5*, 6-12, doi:<https://doi.org/10.1016/j.cobme.2017.11.002>.
104. Hatherell, K.; Couraud, P.-O.; Romero, I.A.; Weksler, B.; Pilkington, G.J. Development of a three-dimensional, all-human in vitro model of the blood–brain barrier using mono-, co-, and tri-cultivation Transwell models. *Journal of Neuroscience Methods* **2011**, *199*, 223-229, doi:<https://doi.org/10.1016/j.jneumeth.2011.05.012>.
105. Hilgers, A.R.; Conradi, R.A.; Burton, P.S. Caco-2 Cell Monolayers as a Model for Drug Transport Across the Intestinal Mucosa. *Pharmaceutical Research* **1990**, *7*, 902-910, doi:10.1023/A:1015937605100.
106. Partyka, P.P.; Godsey, G.A.; Galie, J.R.; Kosciuk, M.C.; Acharya, N.K.; Nagele, R.G.; Galie, P.A. Mechanical stress regulates transport in a compliant 3D model of the blood-brain barrier. *Biomaterials* **2017**, *115*, 30-39.
107. Ghaemmaghami, A.M.; Hancock, M.J.; Harrington, H.; Kaji, H.; Khademhosseini, A. Biomimetic tissues on a chip for drug discovery. *Drug discovery today* **2012**, *17*, 173-181.
108. Tarbell, J.M. Shear stress and the endothelial transport barrier. *Cardiovascular research* **2010**, *87*, 320-330.
109. DeStefano, J.G.; Jamieson, J.J.; Linville, R.M.; Searson, P.C. Benchmarking in vitro tissue-engineered blood–brain barrier models. *Fluids and Barriers of the CNS* **2018**, *15*, 1-15.
110. Ménard, O.; Cattenoz, T.; Guillemin, H.; Souchon, I.; Deglaire, A.; Dupont, D.; Picque, D. Validation of a new in vitro dynamic system to simulate infant digestion. *Food chemistry* **2014**, *145*, 1039-1045.
111. Kulthong, K.; Hooiveld, G.J.; Duivenvoorde, L.; Miro Estruch, I.; Marin, V.; van der Zande, M.; Bouwmeester, H. Transcriptome comparisons of in vitro intestinal epithelia grown under static and microfluidic gut-on-chip conditions with in vivo human epithelia. *Scientific reports* **2021**, *11*, 3234.
112. Instruments, G. Two-, three-, and four-electrode experiments. *Application Note* **2011**.
113. Griep, L.M.; Wolbers, F.; de Wagenaar, B.; ter Braak, P.M.; Weksler, B.B.; Romero, I.A.; Couraud, P.O.; Vermes, I.; van der Meer, A.D.; van den Berg, A. BBB on chip: microfluidic platform to mechanically and biochemically modulate blood-brain barrier function. *Biomedical microdevices* **2013**, *15*, 145-150.
114. Van Der Helm, M.W.; Henry, O.Y.F.; Bein, A.; Hamkins-Indik, T.; Cronce, M.J.; Leineweber, W.D.; Odijk, M.; Van Der Meer, A.D.; Eijkel, J.C.T.; Ingber, D.E.; et al. Non-invasive sensing of transepithelial barrier function and tissue differentiation in organs-on-chips using impedance spectroscopy. *Lab on a Chip* **2019**, *19*, 452-463, doi:10.1039/c8lc00129d.

115. Linz, G.; Rauer, S.B.; Kuhn, Y.; Wennemaring, S.; Siedler, L.; Singh, S.; Wessling, M. 3D-Printed Bioreactor with Integrated Impedance Spectroscopy for Cell Barrier Monitoring. *Advanced Materials Technologies* **2021**, *6*, 2100009.
116. Cacopardo, L.; Costa, J.; Giusti, S.; Buoncompagni, L.; Meucci, S.; Corti, A.; Mattei, G.; Ahluwalia, A. Real-time cellular impedance monitoring and imaging of biological barriers in a dual-flow membrane bioreactor. *Biosens Bioelectron* **2019**, *140*, 111340, doi:10.1016/j.bios.2019.111340.
117. Santaguida, S.; Janigro, D.; Hossain, M.; Oby, E.; Rapp, E.; Cucullo, L. Side by side comparison between dynamic versus static models of blood–brain barrier in vitro: a permeability study. *Brain research* **2006**, *1109*, 1-13.
118. De Bartolo, L.; Salerno, S.; Curcio, E.; Piscioneri, A.; Rende, M.; Morelli, S.; Tasselli, F.; Bader, A.; Drioli, E. Human hepatocyte functions in a crossed hollow fiber membrane bioreactor. *Biomaterials* **2009**, *30*, 2531-2543.
119. Jauregui, H.O.; Mullon, C.J.P.; Trenkler, D.; Naik, S.; Santangini, H.; Press, P.; Muller, T.E.; Solomon, B.A. In vivo evaluation of a hollow fiber liver assist device. *Hepatology* **1995**, *21*, 460-469.
120. Zhang, S.; Chen, L.; Liu, T.; Wang, Z.; Wang, Y. Integration of single-layer skin hollow fibers and scaffolds develops a three-dimensional hybrid bioreactor for bioartificial livers. *Journal of Materials Science: Materials in Medicine* **2014**, *25*, 207-216.
121. Neuhaus, W.; Lauer, R.; Oelzant, S.; Fringeli, U.P.; Ecker, G.F.; Noe, C.R. A novel flow based hollow-fiber blood–brain barrier in vitro model with immortalised cell line PBMEC/C1–2. *Journal of biotechnology* **2006**, *125*, 127-141.
122. Mantecón-Oria, M.; Diban, N.; Berciano, M.T.; Rivero, M.J.; David, O.; Lafarga, M.; Tapia, O.; Urtiaga, A. Hollow fiber membranes of PCL and PCL/graphene as scaffolds with potential to develop in vitro blood—brain barrier models. *Membranes* **2020**, *10*, 161.
123. Humes, H.D.; Buffington, D.A.; MacKay, S.M.; Funke, A.J.; Weitzel, W.F. Replacement of renal function in uremic animals with a tissue-engineered kidney. *Nature biotechnology* **1999**, *17*, 451-455.
124. Humes, H.D.; Fissell, W.H.; Weitzel, W.F.; Buffington, D.A.; Westover, A.J.; MacKay, S.M.; Gutierrez, J.M. Metabolic replacement of kidney function in uremic animals with a bioartificial kidney containing human cells. *American journal of kidney diseases* **2002**, *39*, 1078-1087.
125. Humes, H.D.; Weitzel, W.F.; Bartlett, R.H.; Swaniker, F.C.; Paganini, E.P.; Luderer, J.R.; Sobota, J. Initial clinical results of the bioartificial kidney containing human cells in ICU patients with acute renal failure. *Kidney international* **2004**, *66*, 1578-1588.
126. Oo, Z.Y.; Kandasamy, K.; Tasnim, F.; Zink, D. A novel design of bioartificial kidneys with improved cell performance and haemocompatibility. *Journal of cellular and molecular medicine* **2013**, *17*, 497-507.
127. Ng, C.P.; Zhuang, Y.; Lin, A.W.H.; Teo, J.C.M. A fibrin-based tissue-engineered renal proximal tubule for bioartificial kidney devices: development, characterization and in vitro transport study. *International Journal of Tissue Engineering* **2012**, *2013*.
128. Eghbali, H.; Nava, M.M.; Mohebbi-Kalhari, D.; Raimondi, M.T. Hollow fiber bioreactor technology for tissue engineering applications. *The International journal of artificial organs* **2016**, *39*, 1-15.
129. Morelli, S.; Piscioneri, A.; Salerno, S.; De Bartolo, L. Hollow fiber and nanofiber membranes in bioartificial liver and neuronal tissue engineering. *Cells Tissues Organs* **2022**, *211*, 447-476.

130. Mueller, D.; Tascher, G.; Damm, G.; Nüssler, A.K.; Heinzle, E.; Noor, F. Real-time in situ viability assessment in a 3D bioreactor with liver cells using resazurin assay. *Cytotechnology* **2013**, *65*, 297-305.
131. Gloeckner, H.; Jonuleit, T.; Lemke, H.-D. Monitoring of cell viability and cell growth in a hollow-fiber bioreactor by use of the dye Alamar Blue™. *Journal of immunological methods* **2001**, *252*, 131-138.
132. Lavogina, D.; Lust, H.; Tahk, M.-J.; Laasfeld, T.; Vellama, H.; Nasirova, N.; Vardja, M.; Eskla, K.-L.; Salumets, A.; Rinken, A.; et al. Revisiting the Resazurin-Based Sensing of Cellular Viability: Widening the Application Horizon. *Biosensors* **2022**, *12*, 196.
133. Cucullo, L.; Hossain, M.; Tierney, W.; Janigro, D. A new dynamic in vitro modular capillaries-venules modular system: cerebrovascular physiology in a box. *BMC neuroscience* **2013**, *14*, 1-12.
134. Grimnes, S.; Martinsen, Ø.G. Sources of error in tetrapolar impedance measurements on biomaterials and other ionic conductors. *Journal of Physics D: Applied Physics* **2006**, *40*, 9.
135. Forni, L.; Hilton, P. Continuous hemofiltration in the treatment of acute renal failure. *New England Journal of Medicine* **1997**, *336*, 1303-1309.
136. Brunet, S.; Leblanc, M.; Geadah, D.; Parent, D.; Courteau, S.; Cardinal, J. Diffusive and convective solute clearances during continuous renal replacement therapy at various dialysate and ultrafiltration flow rates. *American journal of kidney diseases* **1999**, *34*, 486-492.
137. Bellomo, R.; Ronco, C. Continuous renal replacement therapy in the intensive care unit. *Intensive Care Medicine* **1999**, *25*, 781.
138. Oda, S.; Hirasawa, H.; Shiga, H.; Nakanishi, K.; Matsuda, K.i.; Nakamura, M. Continuous hemofiltration/hemodiafiltration in critical care. *Therapeutic Apheresis* **2002**, *6*, 193-198.
139. Baldwin, I. Factors affecting circuit patency and filter 'life'. *Acute Kidney Injury* **2007**, *156*, 178-184.
140. Luai, A.; Abdulelah, N.; Ankush, M.; Mujeeb, S. Effectiveness of Ultrafiltration in Patients with Congestive Heart Failure. In *Advances in Hemodiafiltration*, Ayman, K., Ed.; IntechOpen: Rijeka, 2016; p. Ch. 5.
141. Davenport, A. The coagulation system in the critically ill patient with acute renal failure and the effect of an extracorporeal circuit. *American journal of kidney diseases* **1997**, *30*, S20-S27.
142. Tangvoraphonkchai, K.; Riddell, A.; Davenport, A. Platelet activation and clotting cascade activation by dialyzers designed for high volume online hemodiafiltration. *Hemodialysis International* **2018**, *22*, 192-200.
143. Schetz, M. Anticoagulation for continuous renal replacement therapy. *Current Opinion in Anesthesiology* **2001**, *14*, 143-149.
144. Fiaccadori, E.; Maggiore, U.; Rotelli, C.; Minari, M.; Melfa, L.; Cappè, G.; Cabassi, A. Continuous haemofiltration in acute renal failure with prostacyclin as the sole anti-haemostatic agent. *Intensive care medicine* **2002**, *28*, 586-593.
145. Gabutti, L.; Marone, C.; Colucci, G.; Duchini, F.; Schönholzer, C. Citrate anticoagulation in continuous venovenous hemodiafiltration: a metabolic challenge. *Intensive Care Medicine* **2002**, *28*, 1419-1425.
146. Oudemans-van Straaten, H.M.; Bosman, R.J.; Koopmans, M.; Van Der Voort, P.H.; Wester, J.P.; Van Der Spoel, J.I.; Dijksman, L.M.; Zandstra, D.F. Citrate anticoagulation for continuous venovenous hemofiltration. *Critical care medicine* **2009**, *37*, 545-552.

147. Schilder, L.; Nurmohamed, S.A.; Bosch, F.H.; Purmer, I.M.; den Boer, S.S.; Kleppe, C.G.; Vervloet, M.G.; Beishuizen, A.; Girbes, A.R.; Ter Wee, P.M. Citrate anticoagulation versus systemic heparinisation in continuous venovenous hemofiltration in critically ill patients with acute kidney injury: a multi-center randomized clinical trial. *Critical care* **2014**, *18*, 1-9.
148. Gashti, C.N.; Salcedo, S.; Robinson, V.; Rodby, R.A. Accelerated venovenous hemofiltration: early technical and clinical experience. *American journal of kidney diseases* **2008**, *51*, 804-810.
149. Uchino, S.; Fealy, N.; Baldwin, I.; Morimatsu, H.; Bellomo, R. Pre-dilution vs. post-dilution during continuous veno-venous hemofiltration: impact on filter life and azotemic control. *Nephron Clinical Practice* **2003**, *94*, c94-c98.
150. Kobayashi, K.; Kurihara, Y.; Ueki, S.; Kokubo, K.; Kubota, M.; Kobayashi, H. Effects of hydrophilic polymer-embedded membrane on permeability and cell adhesion during continuous hemofiltration. *Renal Replacement Therapy* **2022**, *8*, 1-9.
151. Kokubo, K.; Kurihara, Y.; Tsukao, H.; Maruyama, N.; Kobayashi, K.; Shinbo, T.; Hirose, M.; Kobayashi, H. Effects of increased surface coverage of polyvinylpyrrolidone over a polysulfone hemofilter membrane on permeability and cell adhesion during continuous hemofiltration. *Journal of Artificial Organs* **2015**, *18*, 257-263.
152. Fissell, W.H.; Dubnisheva, A.; Eldridge, A.N.; Fleischman, A.J.; Zydney, A.L.; Roy, S. High-performance silicon nanopore hemofiltration membranes. *Journal of membrane science* **2009**, *326*, 58-63.
153. Neri, M.; Villa, G.; Garzotto, F.; Bagshaw, S.; Bellomo, R.; Cerda, J.; Ferrari, F.; Guggia, S.; Joannidis, M.; Kellum, J.; et al. Nomenclature for renal replacement therapy in acute kidney injury: basic principles. *Critical Care* **2016**, *20*, 318, doi:10.1186/s13054-016-1489-9.
154. Graves, G.D. Arterial and venous pressure monitoring during hemodialysis. *Nephrology Nursing Journal* **2001**, *28*, 23.
155. Appelt-Menzel, A.; Cubukova, A.; Gunther, K.; Edenhofer, F.; Piontek, J.; Krause, G.; Stuber, T.; Walles, H.; Neuhaus, W.; Metzger, M. Establishment of a Human Blood-Brain Barrier Co-culture Model Mimicking the Neurovascular Unit Using Induced Pluri- and Multipotent Stem Cells. *Stem Cell Rep* **2017**, *8*, 894-906, doi:10.1016/j.stemcr.2017.02.021.
156. Choi, J.; Mathew, S.; Oerter, S.; Appelt-Menzel, A.; Hansmann, J.; Schmitz, T. Online Measurement System for Dynamic Flow Bioreactors to Study Barrier Integrity of hiPSC-Based Blood-Brain Barrier In Vitro Models. *Bioengineering (Basel)* **2022**, *9*, doi:10.3390/bioengineering9010039.
157. Schindelin, J.; Arganda-Carreras, I.; Frise, E.; Kaynig, V.; Longair, M.; Pietzsch, T.; Preibisch, S.; Rueden, C.; Saalfeld, S.; Schmid, B.; et al. Fiji: an open-source platform for biological-image analysis. *Nature Methods* **2012**, *9*, 676-682, doi:10.1038/nmeth.2019.
158. Hansmann, J.; Egger, D.; Kasper, C. Advanced dynamic cell and tissue culture. **2018**, *5*, 65.
159. Hansmann, J.; Groeber, F.; Kahlig, A.; Kleinhans, C.; Walles, H. Bioreactors in tissue engineering—principles, applications and commercial constraints. *Biotechnology journal* **2013**, *8*, 298-307.
160. Martin, I.; Wendt, D.; Heberer, M. The role of bioreactors in tissue engineering. *TRENDS in Biotechnology* **2004**, *22*, 80-86.

161. Bolz, A.; Hubmann, M.; Hardt, R.; Riedmüller, J.; Schaldach, M. Low polarization pacing lead for detecting the ventricular-evoked response. *Med Prog Technol* **1993**, *19*, 129-137.
162. Janders, M.; Egert, U.; Stelzle, M.; Nisch, W. Novel thin film titanium nitride micro-electrodes with excellent charge transfer capability for cell stimulation and sensing applications.
163. Tutorials, E. Available online: <https://www.electronics-tutorials.ws> (accessed on
164. Wu, M.H.; Urban, J.P.; Cui, Z.; Cui, Z.F. Development of PDMS microbioreactor with well-defined and homogenous culture environment for chondrocyte 3-D culture. *Biomedical microdevices* **2006**, *8*, 331-340.
165. Leclerc, E.; Sakai, Y.; Fujii, T. Perfusion culture of fetal human hepatocytes in microfluidic environments. *Biochemical engineering journal* **2004**, *20*, 143-148.
166. Brown, J.A.; Pensabene, V.; Markov, D.A.; Allwardt, V.; Neely, M.D.; Shi, M.; Britt, C.M.; Hoilett, O.S.; Yang, Q.; Brewer, B.M. Recreating blood-brain barrier physiology and structure on chip: A novel neurovascular microfluidic bioreactor. *Biomicrofluidics* **2015**, *9*.
167. Zhang, B.; Korolj, A.; Lai, B.F.L.; Radisic, M. Advances in organ-on-a-chip engineering. *Nature Reviews Materials* **2018**, *3*, 257-278.
168. Vatine, G.D.; Barrile, R.; Workman, M.J.; Sances, S.; Barriga, B.K.; Rahnama, M.; Barthakur, S.; Kasendra, M.; Lucchesi, C.; Kerns, J.; et al. Human iPSC-Derived Blood-Brain Barrier Chips Enable Disease Modeling and Personalized Medicine Applications. *Cell Stem Cell* **2019**, *24*, 995-1005.e1006, doi:10.1016/j.stem.2019.05.011.
169. Hollmann, E.K.; Bailey, A.K.; Potharazu, A.V.; Neely, M.D.; Bowman, A.B.; Lippmann, E.S. Accelerated differentiation of human induced pluripotent stem cells to blood-brain barrier endothelial cells. *Fluids Barriers CNS* **2017**, *14*, 9, doi:10.1186/s12987-017-0059-0.
170. Felix, K.; Tobias, S.; Jan, H.; Nicolas, S.; Michael, M. Measurements of transepithelial electrical resistance (TEER) are affected by junctional length in immature epithelial monolayers. *Histochem Cell Biol* **2021**, *156*, 609-616, doi:10.1007/s00418-021-02026-4.
171. Jansen, J.; De Napoli, I.; Fedecostante, M.; Schophuizen, C.; Chevchik, N.; Wilmer, M.; Van Asbeck, A.; Croes, H.; Pertijs, J.; Wetzels, J. Human proximal tubule epithelial cells cultured on hollow fibers: living membranes that actively transport organic cations. *Scientific reports* **2015**, *5*, 16702.
172. Wung, N.; Acott, S.M.; Tosh, D.; Ellis, M.J. Hollow fibre membrane bioreactors for tissue engineering applications. *Biotechnology letters* **2014**, *36*, 2357-2366.
173. Deng, X.; Zhang, G.; Shen, C.; Yin, J.; Meng, Q. Hollow fiber culture accelerates differentiation of Caco-2 cells. *Applied microbiology and biotechnology* **2013**, *97*, 6943-6955.
174. Unger, R.E.; Peters, K.; Huang, Q.; Funk, A.; Paul, D.; Kirkpatrick, C. Vascularization and gene regulation of human endothelial cells growing on porous polyethersulfone (PES) hollow fiber membranes. *Biomaterials* **2005**, *26*, 3461-3469.
175. Dewi, B.E.; Takasaki, T.; Kurane, I. In vitro assessment of human endothelial cell permeability: effects of inflammatory cytokines and dengue virus infection. *J Virol Methods* **2004**, *121*, 171-180, doi:10.1016/j.jviromet.2004.06.013.
176. Pitsalidis, C.; van Niekerk, D.; Moysidou, C.-M.; Boys, A.J.; Withers, A.; Vallet, R.; Owens, R.M. Organic electronic transmembrane device for hosting and monitoring 3D cell cultures. *Science Advances* **2022**, *8*, eabo4761.

177. Bagnaninchi, P.O.; Drummond, N. Real-time label-free monitoring of adipose-derived stem cell differentiation with electric cell-substrate impedance sensing. *Proceedings of the National Academy of Sciences* **2011**, *108*, 6462-6467.
178. Wegener, J.; Sieber, M.; Galla, H.-J. Impedance analysis of epithelial and endothelial cell monolayers cultured on gold surfaces. *Journal of biochemical and biophysical methods* **1996**, *32*, 151-170.
179. Zimmermann, D.; Zhou, A.; Kiesel, M.; Feldbauer, K.; Terpitz, U.; Haase, W.; Schneider-Hohendorf, T.; Bamberg, E.; Sukhorukov, V. Effects on capacitance by overexpression of membrane proteins. *Biochemical and biophysical research communications* **2008**, *369*, 1022-1026.
180. Fleischer, D. Biological Transport Phenomena in the Gastrointestinal Tract: Cellular Mechanisms. In *Transport Processes in Pharmaceutical Systems*, Gordon L. Amidon, P.I.L., Elizabeth M. Topp, Ed.; Boca Raton, 1999; p. 38.
181. Ayejunie, S.; Landry, T.; Stevens, Z.; Armento, A.; Hayden, P.; Klausner, M. Human Primary Cell-Based Organotypic Microtissues for Modeling Small Intestinal Drug Absorption. *Pharm Res* **2018**, *35*, 72, doi:10.1007/s11095-018-2362-0.
182. Leffers, L.; Wehe, C.A.; Hüwel, S.; Bartel, M.; Ebert, F.; Taleshi, M.S.; Galla, H.J.; Karst, U.; Francesconi, K.A.; Schwerdtle, T. In vitro intestinal bioavailability of arsenosugar metabolites and presystemic metabolism of thio-dimethylarsinic acid in Caco-2 cells. *Metallomics* **2013**, *5*, 1031-1042, doi:10.1039/c3mt00039g.
183. Gerasimenko, T.; Nikulin, S.; Zakharova, G.; Poloznikov, A.; Petrov, V.; Baranova, A.; Tonevitsky, A. Impedance Spectroscopy as a Tool for Monitoring Performance in 3D Models of Epithelial Tissues. *Front Bioeng Biotechnol* **2019**, *7*, 474, doi:10.3389/fbioe.2019.00474.
184. Boyle, M.; Baldwin, I. Understanding the continuous renal replacement therapy circuit for acute renal failure support: a quality issue in the intensive care unit. *AACN advanced critical care* **2010**, *21*, 367-375.
185. Acierno, M.J.; Maeckelbergh, V. Continuous renal replacement therapy. *COMPENDIUM ON CONTINUING EDUCATION FOR THE PRACTISING VETERINARIAN-NORTH AMERICAN EDITION-* **2008**, *30*, 264.
186. Riahi, R.; Shaegh, S.A.M.; Ghaderi, M.; Zhang, Y.S.; Shin, S.R.; Aleman, J.; Massa, S.; Kim, D.; Dokmeci, M.R.; Khademhosseini, A. Automated microfluidic platform of bead-based electrochemical immunosensor integrated with bioreactor for continual monitoring of cell secreted biomarkers. *Scientific Reports* **2016**, *6*, 24598, doi:10.1038/srep24598.
187. Salih, A.R.C.; Farooqi, H.M.U.; Kim, Y.S.; Lee, S.H.; Choi, K.H. Impact of serum concentration in cell culture media on tight junction proteins within a multiorgan microphysiological system. *Microelectronic Engineering* **2020**, *232*, 111405, doi:<https://doi.org/10.1016/j.mee.2020.111405>.
188. Ho Ye, S.; Watanabe, J.; Takai, M.; Iwasaki, Y.; Ishihara, K. High functional hollow fiber membrane modified with phospholipid polymers for a liver assist bioreactor. *Biomaterials* **2006**, *27*, 1955- 1962, doi:<https://doi.org/10.1016/j.biomaterials.2005.09.041>.
189. Bettahalli, N.; Steg, H.; Wessling, M.; Stamatialis, D. Development of poly (l-lactic acid) hollow fiber membranes for artificial vasculature in tissue engineering scaffolds. *Journal of membrane science* **2011**, *371*, 117-126.
190. Gray, S.G.; Weinberg, P.D. Biomechanical determinants of endothelial permeability assessed in standard and modified hollow-fibre bioreactors. *Journal of the Royal Society Interface* **2023**, *20*, 20230222.

191. Honore, P.M.; Spapen, H.D. What a clinician should know about a renal replacement membrane? *Journal of translational internal medicine* **2018**, *6*, 62-65.
192. Michel, T.; Ksouri, H.; Schneider, A.G. Continuous renal replacement therapy: understanding circuit hemodynamics to improve therapy adequacy. *Current opinion in critical care* **2018**, *24*, 455-462.
193. Tan, C.-S.; Tan, H.K.; Choong, H.L. Real-Time Circuit Pressures Correlate Poorly with Circuit Longevity in Anticoagulant-Free, Predilution Continuous Venovenous Hemofiltration. *Blood purification* **2011**, *32*, 15-20.
194. Joannidis, M.; Oudemans-van Straaten, H.M. Clinical review: patency of the circuit in continuous renal replacement therapy. *Critical Care* **2007**, *11*, 1-10.
195. Ejaz, A.A.; Komorski, R.M.; Ellis, G.H.; Munjal, S. Extracorporeal circuit pressure profiles during continuous venovenous haemofiltration. *Nurs Crit Care* **2007**, *12*, 81-85, doi:10.1111/j.1478-5153.2006.00192.x.

8. Appendix

Appendix A. Unstable Coating Issue on Luer Lock Connectors

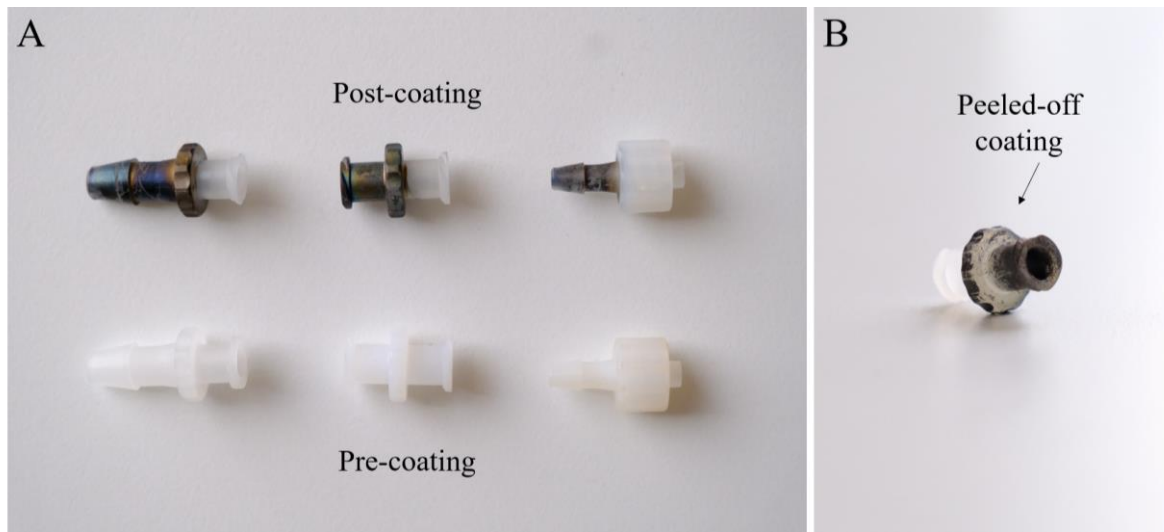


Figure A.1. Coating imperfections revealed: Titanium nitride (TiN) coating flaws on Luer lock connectors. Our observations indicate that the TiN coating on Luer lock connector is prone to peeling off due to physical friction. (A) displays TiN pre-coating and post-coating on Luer lock connectors, with the post-coating samples shown after use. (B) A close-up view. This appendix figure is relevant to Section 4.1.2.

Appendix B. Equivalent Circuit Fitting on Electrochemical Impedance Data

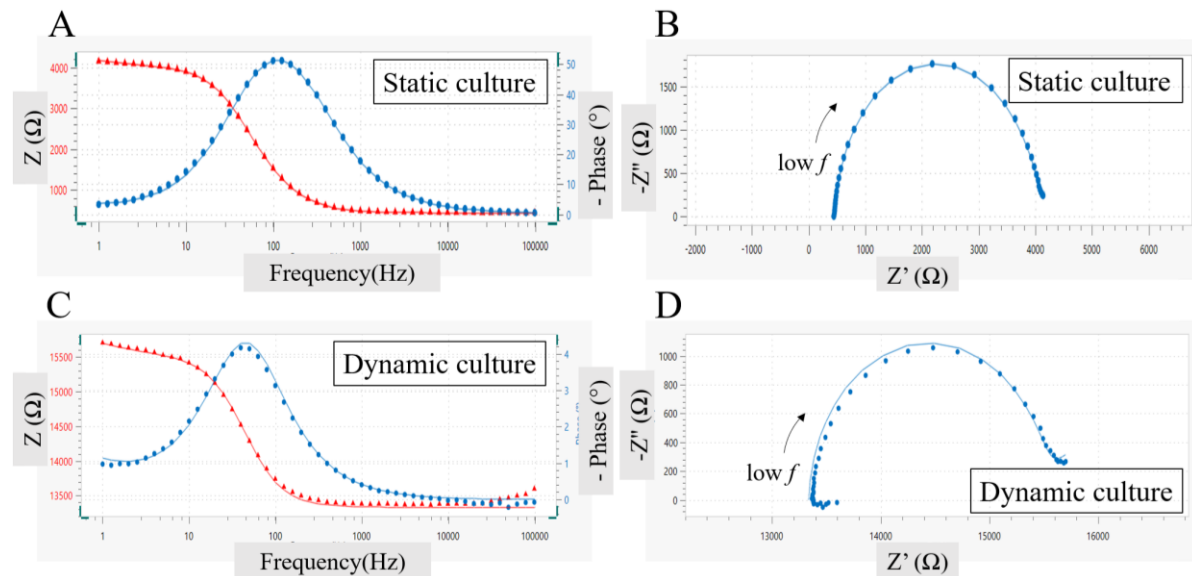


Figure B.1. Fitted and simulated EIS data results using NOVA software program for BCECs in static and dynamic culture. (A and B) Bode (A) and Nyquist (B) plot of fitted and simulated EIS data results for BCECs in static culture. (C and D) Bode (C) and Nyquist (D) plot of fitted and simulated EIS data results for BCECs in dynamic culture. The equivalent circuit model used for fitting the EIS data for dynamic (Figure 3.5) and static (Figure 4.12) cultures was ultimately same. The data points in the plot represent the original EIS measurements, while the lines represent the fitted curves. The fitting lines of both static and dynamic cultured EIS data demonstrate accurate fitting with minimal errors. This appendix figure is relevant to section 4.2.2.2.

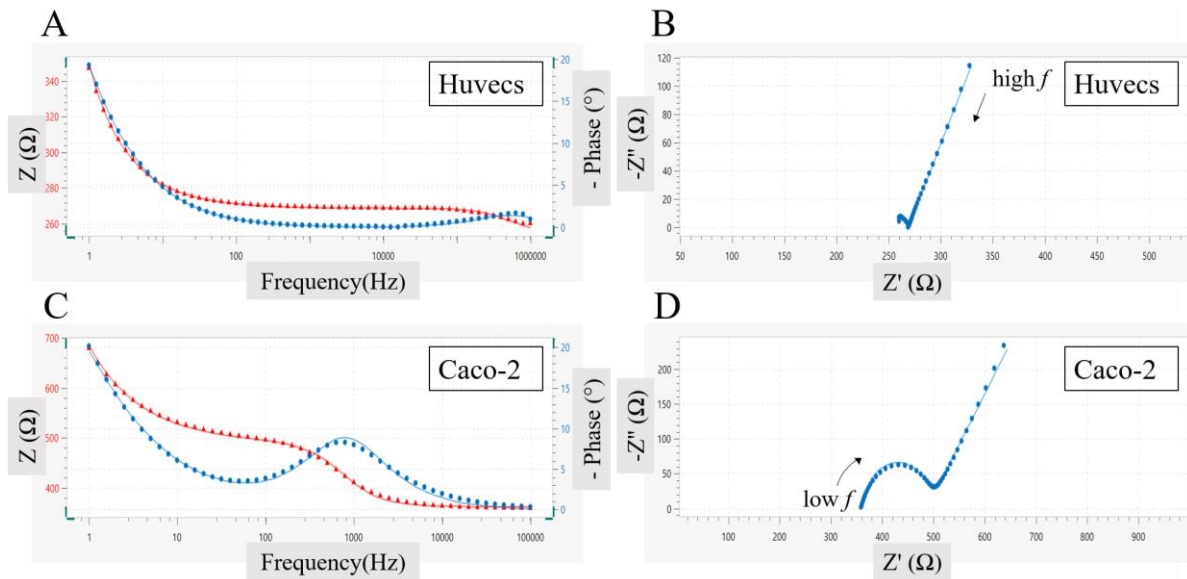


Figure B.2. Fitted and simulated EIS data results using NOVA software program for HUVECs and Caco-2 in a transwell culture. (A and B) Bode (A) and Nyquist (B) plot of fitted and simulated EIS data results for HUVECs in a transwell culture. (C and D) Bode (C) and Nyquist (D) plot of fitted EIS data results for Caco-2 in transwell culture. The equivalent circuit model represented Figure 3.5 was used to fit the EIS data for all. The data points in the plot represent the original EIS measurements, while the lines represent the fitted curves. The fitting lines of HUVECs and Caco-2 cells in the transwell culture EIS data demonstrate a perfect fit. These appendix figures (A and B) serve as supplements to section 4.3.1.1, while figures (C and D) serve as supplements to Section 4.3.2.1, respectively.

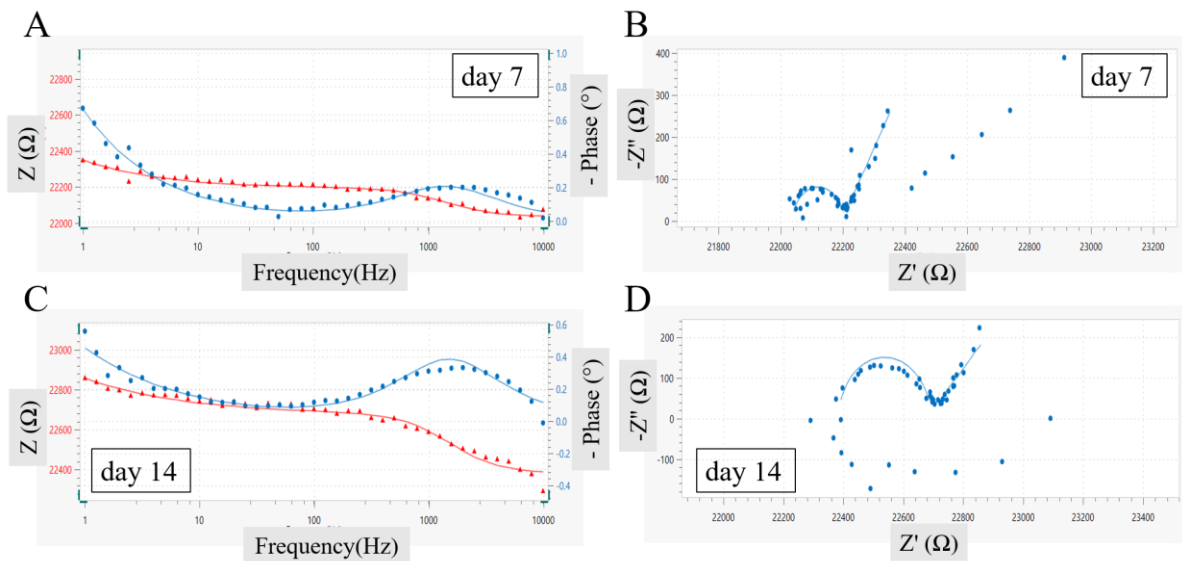


Figure B.3. Fitted and simulated EIS data results using NOVA software program for Caco-2 culture in miniature HFBR. Fitting and simulation was performed in frequency range 1 Hz to 10 kHz. The data points in the plot represent the original EIS measurements, while the lines represent the fitted curves. (A and B) Fitted and simulated EIS data of Caco-2 culture in miniature HFBR on day 7 represented in Bode plot (A) and Nyquist plot (B). (C and D) Fitted and simulated EIS data of Caco-2 culture in miniature HFBR on day 14 represents in Bode plot (C) and Nyquist plot (D). The estimated error of fitting was below 10 %. This appendix figure is relevant to section 4.3.2.2

Appendix C. Barrier Resistance and Capacitance of Human Induced Pluripotent Stem Cell-derived Brain Capillary Endothelial Cells

Table C.1. Overall values of tight junction resistance (R_T) and cell membrane capacitance (C_C) in static and dynamic cultures using EIS data fitted with an equivalent circuit over a culture period of 7 days. Biological replicates ($N = 7$ (0 h – 48 h) and $N = 3$ (72 h – 168 h)). This table has been reprinted our previous publication Choi et al., with under the terms of the Creative Commons Attribution (CC BY) license [156]. This appendix includes raw data for Figure 4.13.

hours (h)	R_T [$\Omega \cdot \text{cm}^2$]				C_C [$\mu\text{F}/\text{cm}^2$]			
	Dynamic culture		Static culture		Dynamic culture		Static culture	
	Mean	SD	Mean	SD	Mean	SD	Mean	SD
0	1042	433	3411	1779	1.18	0.42	1.59	0.58
6	2609	1029	3010	2008	1.25	0.44	1.69	0.58
24	2513	424	1865	786	1.47	0.36	1.68	0.47
48	1733	785	1129	451	1.44	0.32	2.04	0.73
72	1165	762	860	358	1.31	0.06	2.05	0.33
96	641	219	697	244	1.36	0.08	2.25	0.56
120	550	232	706	336	1.45	0.04	2.09	0.29
144	437	176	648	298	1.51	0.23	2.06	0.26
168	285	76	449	149	1.49	0.11	2.02	0.22

Appendix D. Barrier Resistance and Capacitance of Human Umbilical Vein Endothelial Cells in Transwell Culture

Table D.1. The overall values of tight junction resistance (R_T) and cell membrane capacitance (C_C) of HuveCs in transwell culture were obtained by fitting an equivalent circuit to the EIS data. The obtained values of R_T and C_C were normalized by the surface area of the porous membrane (0.33 cm^2) and the mean and standard deviation were calculated from three biological replicates. This appendix includes raw data for Figure 4.16.

Culture time (day)	R_T [$\Omega \cdot \text{cm}^2$]		C_C [$\mu\text{F}/\text{cm}^2$]	
	Mean	SD	Mean	SD
d1	4.12	0.20	0.10	0.02
d2	5.59	0.15	0.17	0.02
d4	6.55	0.37	0.24	0.09
d6	8.51	0.13	0.47	0.04
d9	8.08	0.40	0.45	0.01

Appendix E. Hoechst Staining Images of Human Umbilical Vein Endothelial Cells in Miniature Hollow Fiber Reactor

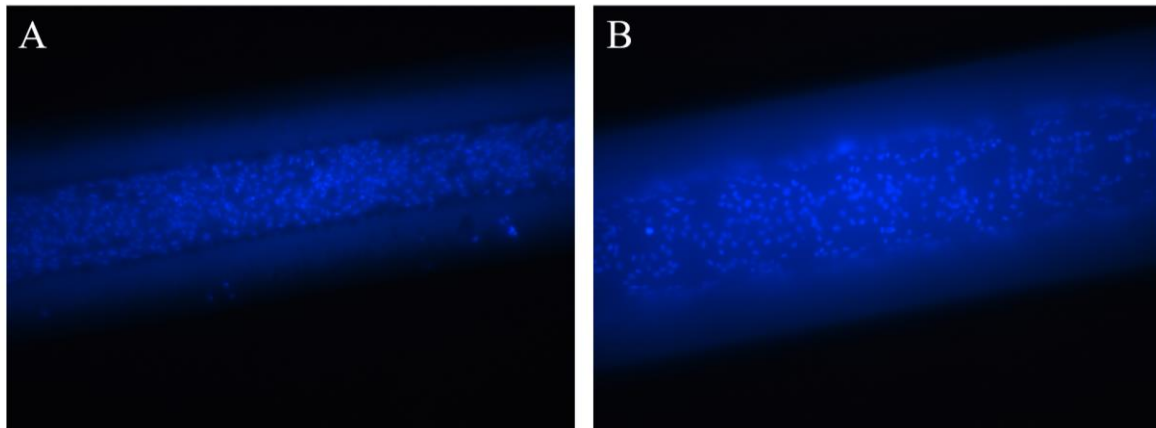


Figure E.1. Fluorescent image analysis of HUVECs in a miniature HFBR. (A) Hoechst staining images were captured after 5 days of culture. The distribution of HUVECs within the hollow fiber appears to be even. (B) There are concerns regarding the formation of tight junctions, as the distance between cell-cell junctions seems relatively larger. To further investigate this, future studies may include immunofluorescence analysis using tight junction protein markers such as Occludin or Zonula occludens (ZO-1). The scale bar for the image is not provided. This appendix figure is relevant to section 4.3.1.2. The Hoechst staining preparation and imaging were conducted by Dr. Moritz Tulke from eXcorlab.

Appendix F. Barrier Resistance and Capacitance of Cancer Coli-2 in Transwell Culture

Table F.1. The overall values of tight junction resistance (R_T) and cell membrane capacitance (C_C) which were quantified by fitting equivalent circuit. The quantified values of R_T and C_C were then normalized by the surface area of the porous membrane (0.33 cm^2). The mean and standard deviation were calculated from three technical replicates ($N = 3$). This Appendix includes law date for Figure 4.21.

$R_T [\Omega \cdot \text{cm}^2]$								
P29			P30			P31		
Day (d)	Mean	SD	Day (d)	Mean	SD	Day (d)	Mean	SD
1	78.79	4.37	1	71.40	3.38	1	56.20	1.88
2	60.80	2.41	2	74.96	7.73	2	46.36	5.38
4	41.84	0.46	4	62.26	9.06	4	29.21	1.25
7	36.62	1.38	7	43.82	1.49	7	33.90	0.87
12	60.40	3.36	10	37.05	9.41	10	48.84	4.67
17	94.57	8.28	15	73.67	4.14	15	20.76	0.67
23	106.30	6.74	21	131.30	3.84	22	51.50	15.52

$C_C [\mu\text{F}/\text{cm}^2]$								
P29			P30			P31		
Day (d)	Mean	SD	Day (d)	Mean	SD	Day (d)	Mean	SD
1	1.92	0.02	1	2.22	0.09	1	2.09	0.08
2	3.23	0.07	2	3.35	0.16	2	11.01	0.02
4	5.54	0.17	4	5.42	0.38	4	7.27	0.37
7	9.47	0.13	7	10.98	0.19	7	8.56	0.38
12	19.02	0.17	10	10.33	1.13	10	13.55	1.09
17	19.44	0.50	15	14.53	0.47	15	7.37	0.52
23	16.75	0	21	16.10	0.80	22	9.02	1.08

Appendix G. Photography of Hemofiltration

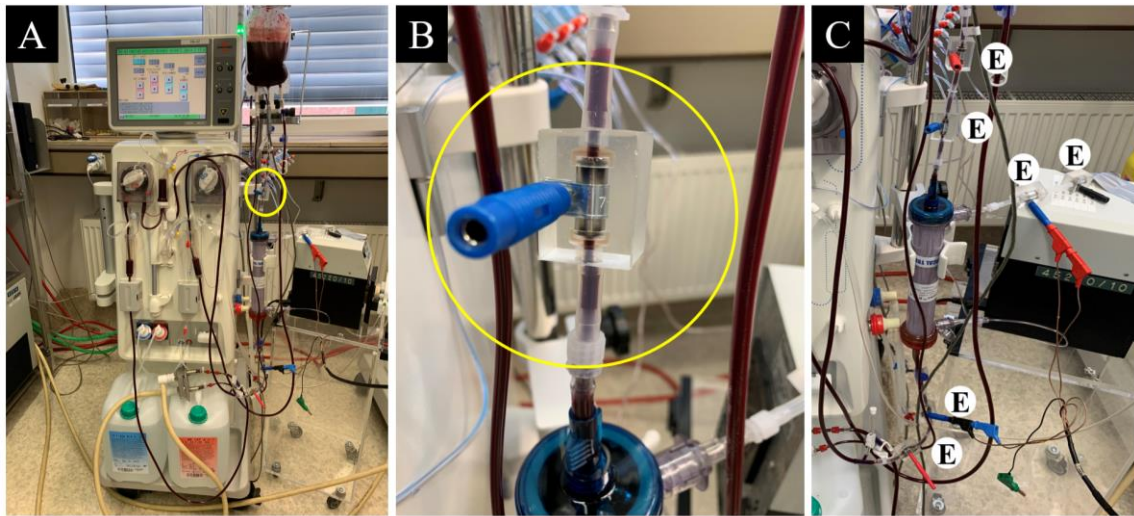


Figure G.1. Photograph of hemofiltration operation. (A) presents an overview of the hemofilter setup, which includes TiN-coated tube electrodes that are incorporated into an EIS device. (B) provides a close-up view of the TiN-coated tube electrode, marked by a yellow circle in Figure A. The electrode structure maintained its solidity and structural integrity even under high flow rates, highlighting its well-constructed. (C) depicts the locations of the six integrated electrodes within the hemofilter setup. The specific positions of these electrodes were described in section 3.5.1.

Publications

Publication

Choi, Jihyoung, Sanjana Mathew, Sabrina Oerter, Antje Appelt-Menzel, Jan Hansmann, and Tobias Schmitz. 2022. "Online Measurement System for Dynamic Flow Bioreactors to Study Barrier Integrity of hiPSC-Based Blood–Brain Barrier In Vitro Models" *Bioengineering* 9, no. 1: 39. <https://doi.org/10.3390/bioengineering9010039>

Poster presentations

Choi, J et al. “Development of an Impedance Spectrometric Method for Automated Control of Cell Growth”, 56th Annual Meeting of the Society for Laboratory Animal Science GV-SOLAS and 18th Advanced Training Course of the IGTP, virtual conference, September 16th to 17th 2020.

Choi, J et al. “Development of an Impedance Spectrometric Method for Online Monitoring of Barrier Integrity in Dynamic Flow Culture Systems”, EUREKA! 2021, virtual conference, October 7th and 8th 2021

Choi, J et al. “Establishing a Novel Online Monitoring System Based on Electrochemical Impedance Spectroscopy to Examine Barrier Integrity in Dynamic Flow Culture”, KSSCR 2022 Annual Meeting, SEOUL in Republic of Korea, August 11th -12th 2022

Acknowledgement

First and foremost, I would like to express my sincere gratitude to my primary supervisor, Prof. Dr.-Ing. Jan Hansmann, for granting me the invaluable opportunity to work within the bioreactor group at the Tissue Engineering and Regenerative Medicine Institute. I am deeply appreciative of your guidance, invaluable advice, and persistent support, accompanied by warm encouragement, throughout the entire duration of my research.

In addition, I deeply appreciate to my thesis committee members, Prof. Dr. Heike Walles and Priv.-Doz. Dr. Vladimir Soukhoroukov. Thank you, Prof. Dr. Heike Walles, for your consistent support and valuable advice, not only in research but also regarding institute life. And thank you, Priv.-Doz. Dr. Vladimir Soukhoroukov, for your invaluable support, advice, and kind words of encouragement.

I would like to express my appreciation to Dr. Tobias Schmitz for your invaluable guidance throughout my PhD studies. Your support and mentorship have greatly contributed to the value of all my research work. Furthermore, I am immensely grateful that you were willing to share your expertise with me. Your passion for research has been a constant source of motivation throughout my PhD studies.

I would like to express my gratitude to my collaboration partners. I appreciate Dr. Antje Appelt- Menzel, Dr. Sabrina Oerter, and Sanjana Mathew from the BBB group at TERM for their valuable support, biological knowledge, and collaboration. I am also grateful to Dr. rer. nat. Horst-Dieter Lemke, Dr. rer. medic. Marieke R uth, Dr. Moritz Tulke, and Dominik K hler from eXcorelab for their expertise in hollow fiber bioreactor culture and hemodialyzer, as well as their helpful advice and support. It was a wonderful working experience in such an interesting field.

A special thank you goes to Marc M llmann for his technical help with bioreactor facilities and 3D printing techniques, helpful suggestions, and enjoyable small talks at the workshop. Additionally, I would like to thank Philip Stahlhut at FMZ for the SEM examination. I would like to acknowledge the support and kind care I have received from Sabine Getzner during my time working in the bioreactor lab. Also, I would like to express my thanks to Tobias Weigel for your willingness to help and support starting from master's studies. I truly appreciate your assistance.

I would like to thank my colleagues and friends, Ives Bernardelli de Mattos and Thomas Düllary, for their willingness to listen, share my concerns, and provide helpful advice. I also feel incredibly lucky to have kind and friendly officemates who create an enjoyable environment alongside our hard work. A special thank you goes to Lisa Kieseletter, Christoph Markus, Anna Leikam, Christina Fey, Merignac-Lacombe Jeanne, Lukas Königer, and Leon Volk for their kindness and friendly cooperation. I would like to extend a big hug and express my deepest gratitude to Rinu Sivarajan, Philipp Ockerman, and David Komla Kessie. You have consistently been there to lend an ear, listen to my thoughts and feelings, and provide unwavering support and encouragement both within the institute and in everyday life. Thank you to the bioreactor group, Thomas Schwarz, Shahbaz Tareq Bandesha, and Dalia Mahdy as well as all my colleagues in the department for all the support and engaging discussions.

Thank to friends Reem Alhijialan, Barbara Tabisz, Melva Suarez, Claudia Siverino, Markus Mühlemann, Jennifer Heubusch, Florentin Baur, Sebastian Schürlein, Songi Lee, Meejin Kim, Eunjeong park, Kyuryoung Kim, Jinyoung Park for undoubtable support and encouragement.

Lastly, I would like to express my deepest appreciation and heartfelt thanks to my family, specifically my parents, Youngju Choi and Dongsuk Shin, my sister, Jieun Choi, and my grandmothers, Sunjo Park and Yongno Kim. Your unwavering love, constant support, and understanding have been the driving force behind my progress and accomplishments throughout my PhD journey. Your unwavering belief in my abilities has been instrumental in making my achievements possible.

Curriculum Vitae

Affidavit

I hereby confirm that my thesis entitled “Development of Add-On Electrode for Non-Invasive Monitoring in Bioreactor Cultures and Medical Devices” is the result of my own work. I did not receive any help or support from commercial consultants. All sources and / materials applied are listed and specified in the thesis.

Furthermore, I confirm that this thesis has not yet been submitted as part of another examination process neither in identical nor in similar form.

Place, Date

Signature

Eidesstattliche Erklärung

Hiermit erkläre ich an Eides statt, die Dissertation “Entwicklung einer Zusatzelektrode für die nicht-invasive Überwachung in Bioreaktorkulturen und medizinischen Geräten” eigenständig, d.h insbesondere selbständig und ohne Hilfe eines kommerziellen Promotionsberaters, angefertigt und keine anderen als die von mir angegebenen Quellen und Hilfsmittel verwendet zu haben.

Ich erkläre außerdem, dass die Dissertation weder in gleicher noch in ähnlicher Form bereits in einem anderen Prüfungsverfahren vorgelegen hat.

Ort, Datum

Unterschrift